

AD-A173 412

AFOSR-TR- 86-0818

(Q)

DYNAMIC FRACTURE BEHAVIOR OF STRUCTURAL MATERIALS

July 1986

AIR FORCE OFFICE OF SCIENTIFIC RESEARCH (AFSC)
NOTICE OF TRANSMISSION TO DTIC

This technical report has been reviewed and is
approved for public release in accordance with AFM 190-12.
Distribution is unlimited.

Final Report

MATTHEW J. KEPPEL

Chief, Technical Information Division

By: J. H. Giovanola and D. A. Shockey
Principal Investigators
(415) 859-3252 / 859-2587

Approved for public release;
distribution unlimited.

Prepared for:

AIR FORCE OFFICE OF SCIENTIFIC RESEARCH
AFOSR/NE, Bldg. 410
Bolling Air Force Base
Washington, DC 20332

Attention: Dr. Alan Rosenstein

DTIC FILE COPY

Contract No. AFOSR/F49620-81-K-0007

SRI Project PYU-2777

DTIC
ELECTED
OCT 15 1986
S D

SRI International
333 Ravenswood Avenue
Menlo Park, California 94025-3493
(415) 326-6200
TWX: 910-373-2046
Telex: 334486



86 10 10 056

UNCLASSIFIED

SECURITY CLASSIFICATION OF THIS PAGE

REPORT DOCUMENTATION PAGE

1a. REPORT SECURITY CLASSIFICATION Unclassified		1b. RESTRICTIVE MARKINGS							
2a. SECURITY CLASSIFICATION AUTHORITY		3. DISTRIBUTION/AVAILABILITY OF REPORT Approved for public release; distribution unlimited.							
2b. DECLASSIFICATION/DOWNGRADING SCHEDULE									
4. PERFORMING ORGANIZATION REPORT NUMBER(S) BYU-2777		5. MONITORING ORGANIZATION REPORT NUMBER(S) AFOSR-TR. 88-0818							
6a. NAME OF PERFORMING ORGANIZATION SRI International		6b. OFFICE SYMBOL (If applicable) NE							
6c. ADDRESS (City, State and ZIP Code) 333 Ravenswood Avenue Menlo Park, CA 94025		7a. NAME OF MONITORING ORGANIZATION Air Force Office of Scientific Research							
6d. ADDRESS (City, State and ZIP Code) Bldg 410 Bolling AFB DC 20332		7b. ADDRESS (City, State and ZIP Code) Bolling Air Force Base Washington, DC 20332							
8a. NAME OF FUNDING/SPONSORING ORGANIZATION AFOSR		8b. OFFICE SYMBOL (If applicable) NE							
8c. ADDRESS (City, State and ZIP Code)		9. PROCUREMENT INSTRUMENT IDENTIFICATION NUMBER AFOSR/F49620-81-K-0007							
11. TITLE (Include Security Classification) Dynamic Fracture Behavior of Structural Materials		10. SOURCE OF FUNDING NOS. PROGRAM ELEMENT NO. 61102F PROJECT NO. 2306 TASK NO. A1 WORK UNIT NO.							
12. PERSONAL AUTHOR(S) J. H. Ciovanola and D. A. Shockey									
13a. TYPE OF REPORT Final Report		13b. TIME COVERED FROM 2/81 TO 1/86							
14. DATE OF REPORT (Yr., Mo., Day) 86 07		15. PAGE COUNT 226							
16. SUPPLEMENTARY NOTATION									
17. COSATI CODES <table border="1"><tr><td>FIELD 20</td><td>GROUP "11</td><td>SUB. GR. </td></tr><tr><td>11</td><td>06</td><td> </td></tr></table>		FIELD 20	GROUP "11	SUB. GR. 	11	06		18. SUBJECT TERMS (Continue on reverse if necessary and identify by block number) Dynamic Fracture, Mixed-Mode Fracture, One-Point-Bend Test, Dynamic Initiation Toughness, Dynamic Propagation Toughness, Dynamic Fracture Criterion	
FIELD 20	GROUP "11	SUB. GR. 							
11	06								
19. ABSTRACT (Continue on reverse if necessary and identify by block number) The new directed energy and advanced kinetic energy weapons have placed a renewed emphasis on the importance of dynamic fracture in evaluating the vulnerability of airborne and spaceborne structures. These weapons can subject targets to high amplitude load pulses at very high loading rates and for short durations.									
This report presents the results of a five-year program to improve our understanding of dynamic fracture behavior by investigating both the crack tip loading conditions and the material properties for fracture at high loading rates. A new test procedure, the one- point-bend test, conceived by Kalthoff and co-workers, was analyzed and further developed to test a wide range of materials at impact loading rates (10^5 to 10^6 MPa m $^{1/2}$ s $^{-1}$). The test uses inertial loading to load the crack tip and affords an unambiguous measurement of the dynamic initiation toughness. The usefulness of the test in producing small controlled increments of crack extension and in crack propagation studies was also demonstrated.									
20. DISTRIBUTION/AVAILABILITY OF ABSTRACT UNCLASSIFIED/UNLIMITED <input checked="" type="checkbox"/> SAME AS RPT. <input type="checkbox"/> DTIC USERS <input type="checkbox"/>		21. ABSTRACT SECURITY CLASSIFICATION UNCLASSIFIED							
22a. NAME OF RESPONSIBLE INDIVIDUAL Dr. Alan Rosenstein		22b. TELEPHONE NUMBER (Include Area Code) (202) 767-4933	22c. OFFICE SYMBOL Elec. & Mat. Sci.						

UNCLASSIFIED

SECURITY CLASSIFICATION OF THIS PAGE

Moreover, the concept of inertial loading was extended to study dynamic mixed-mode crack initiation under controlled mixed mode I and II conditions.

These new test techniques were used to establish the dynamic fracture behavior of 4340 steel (HRC 50). It was shown that, for loading times to fracture as short as 20 μ s, no time-modified criterion is necessary to predict crack initiation. The classical fracture criterion equating the applied stress intensity to the dynamic fracture toughness is adequate, provided the dynamically applied stress intensity is correctly evaluated. Under mixed mode I and II loading with K_{II}/K_I values between 0 and 0.5, it was demonstrated that dynamic crack initiation is essentially controlled by the mode I stress intensity and by the mode I dynamic fracture toughness. A lower bound for the failure envelope was established.

The propagation toughness K_{ID} was estimated for crack velocities up to 600 m s^{-1} by means of strain gages and temperature measurements and compared with the initiation toughness K_{Id} . It was shown that K_{ID} can be up to two and a half times larger than K_{Id} . For the specimen thicknesses investigated (9.8 mm and 12.7 mm), K_{ID} depends both on the amount of crack extension and on the crack velocity. The large values of the propagation toughness are attributed to the formation of small shear lips and to the bowing of the crack front that occur during the first millimeters of crack extension and thus introduce a resistance curve effect.

The results of this research program can now be applied to evaluate dynamic fracture properties of materials and to establish the influence of microstructure on these properties. They also permit more reliable predictions of crack instability under complex impact loading conditions.

UNCLASSIFIED

SECURITY CLASSIFICATION OF THIS PAGE

SUMMARY

The new directed energy and advanced kinetic energy weapons have placed a renewed emphasis on the importance of dynamic fracture in evaluating the vulnerability of airborne and spaceborne structures. These weapons can subject targets to high amplitude load pulses at very high loading rates and for short durations.

This report presents the results of a five-year program to improve our understanding of dynamic fracture behavior by investigating both the crack tip loading conditions and the material properties for fracture at high loading rates. A new test procedure, the one-point-bend test, conceived by Kalthoff and co-workers, was analyzed and further developed to test a wide range of materials at impact loading rates (10^5 to 10^6 MPa $\text{m}^{1/2} \text{s}^{-1}$). The test uses inertial loading to load the crack tip and affords an unambiguous measurement of the dynamic initiation toughness. The usefulness of the test in producing small controlled increments of crack extension and in crack propagation studies was also demonstrated. Moreover, the concept of inertial loading was extended to study dynamic mixed-mode crack initiation under controlled mixed mode I and II conditions.

These new test techniques were used to establish the dynamic fracture behavior of 4340 steel (HRC 50). It was shown that, for loading times to fracture as short as 20 μs , no time-modified criterion is necessary to predict crack initiation. The classical fracture criterion equating the applied stress intensity to the dynamic fracture toughness is adequate, provided the dynamically applied stress intensity is correctly evaluated. Under mixed mode I and II loading with K_{II}/K_I values between 0 and 0.5, it was demonstrated that dynamic crack

Approved by:

1. SECRET

Distribution Codes	
Dist	Avail and/or Special
A1	

initiation is essentially controlled by the mode I stress intensity and by the mode I dynamic fracture toughness. A lower bound for the failure envelope was established.

The propagation toughness K_{ID} was estimated for crack velocities up to 600 m s^{-1} by means of strain gages and temperature measurements and compared with the initiation toughness K_{Id} . It was shown that K_{ID} can be up to two and a half times larger than K_{Id} . For the specimen thicknesses investigated (9.8 mm and 12.7 mm), K_{ID} depends both on the amount of crack extension and on the crack velocity. The large values of the propagation toughness are attributed to the formation of small shear lips and to the bowing of the crack front that occur during the first millimeters of crack extension and thus introduce a resistance curve effect.

The results of this research program can now be applied to evaluate dynamic fracture properties of materials and to establish the influence of microstructure on these properties. They also permit more reliable predictions of crack instability under complex impact loading conditions.

CONTENTS

SUMMARY.....	iii
LIST OF ILLUSTRATIONS.....	vii
LIST OF TABLES.....	xi
1. INTRODUCTION.....	1
2. RESEARCH OBJECTIVES AND ACCOMPLISHMENTS.....	3
3. SUMMARY OF RESULTS.....	5
Development of New Dynamic Fracture Testing Techniques.....	5
The 1PBT for Mode I Dynamic Crack Initiation.....	5
The Modified 1PBT for Dynamic Mixed Mode I and II Crack Initiation.....	8
The 1PBT for Dynamic Crack Propagation Experiments.....	10
Dynamic Mode I Crack Initiation for Short Loading Times.....	12
Dynamic Mixed-Mode Crack Initiation.....	14
Relationship Between Dynamic Initiation and Propagation Toughness.....	18
PERSONNEL ACTIVITIES, PUBLICATIONS, AND PRESENTATIONS.....	21
REFERENCES.....	27
APPENDICES	
A INVESTIGATION AND APPLICATION OF THE ONE-POINT-BEND IMPACT TEST.....	A-1
B ONE-POINT-BEND TEST.....	B-1
C DETERMINATION OF DYNAMIC STRESS INTENSITY HISTORIES BY STRAIN GAGE MEASUREMENTS.....	C-1
D MODEL FOR ESTIMATING THE STRESS INTENSITY FACTOR AT THE TIP OF A RUNNING CRACK IN ONE-POINT-BEND TEST.....	D-1
E CRACK INITIATION AND EXTENSION IN STEEL FOR SHORT LOADING TIMES.....	E-1
F DYNAMIC MIXED-MODE CRACK INITIATION.....	F-1
G INVESTIGATION OF THE INITIAL PHASE OF DYNAMIC CRACK EXTENSION FOR IMPACT LOADING CONDITIONS.....	G-1
H INVESTIGATION OF DYNAMIC CRACK EXTENSION BY MEANS OF HEAT OF FRACTURE MEASUREMENTS.....	H-1

LIST OF ILLUSTRATIONS

1. Test Arrangement and Loading Mechanism for the One-Point-Bend Test.....	7
2. Typical Stress-Intensity and Load Histories Obtained in the One-Point-Bend Test.....	7
3. Test Arrangements for Dynamic Mixed-Mode Fracture Experiments.....	9
4. Stress Intensity Histories for Mixed-Mode Fracture Experiment (K_{II}/K_I) _{init} = 0.51.....	11
5. Summary of Fracture Test Results on 4340 Steel for Four Stress Intensity Rates.....	15
6. Results of Dynamic Mixed-Mode Fracture Experiments on 4340 Steel.....	17
7. Propagation Toughness of 4340 Steel as a Function of Crack Velocity.....	20
C-1 Definition of Coordinates and Strain Gage Position.....	C-3
C-2 Estimate of Gage Integration Error.....	C-12
C-3 Histories of Mode I Stress Intensity Factor K_I and First Order Term Coefficient A_1 Measured in IPBT.....	C-14
C-4 Ratio of First order Term Coefficient A_1 to Mode I Stress Intensity Factor K_I for Histories Plotted in Figure C-3.....	C-17
C-5 Simulation of Strain History at Initial Crack Tip For Two Gage Positions x and for Several Propagation Toughness Assumptions.....	C-20
C-6 Simulations of Strain History at Initial Crack Tip For Two Gage Positions x and for Several Propagation Toughness Assumptions.....	C-22
C-7 Normalized Experimental Strain History Near Initial Crack Tip for Two Gage Positions x	C-24

C-8	Normalized Experimental Strain History Near Initial Crack Tip for Two Gage Positions x.....	C-25
C-9	Normalized Experimental Strain History Near the Initial Crack Tip for Side-Grooved and Ungrooved Specimens.....	C-27
D-1	Normalized Stress Intensity History for Specimens with Different Crack Lengths.....	D-3
D-2	Schematic of Crack Mouth Opening History for 1PB Specimens with Different Crack Lengths.....	D-7
D-3	Simplified Kinematic Model of 1PB Specimen.....	D-8
D-4	Schematic of Crack Mouth Opening Behavior Assumed in 1PBT Model for Specimen With Propagating Crack.....	D-12
D-5	Positions Where ϵ_y Strain is Evaluated and Definition of Coordinates.....	D-15
D-6	Crack Face Displacement and Stress Intensity Histories For Specimens with Different Crack Lengths.....	D-19
D-7	Hammer Load Histories for Two Specimen Geometries Each With Two Different Crack Lengths.....	D-21
D-8	Comparison of Experimental and Predicted Stress Intensity Histories for Specimens of Different Crack Lengths.....	D-22
F-1	Possible Specimen Configuration to Obtain Mixed-Mode Loading in 1PBT.....	F-3
F-2	Stress Intensity Histories for 1PB Double-Crack Specimen with $2D = 10-2$ mm, $a/w = 0.6$	F-4
F-3	Stress Intensity Histories for Double-Crack 1 PB Specimens with Different Crack Spacings $2D$ ($a/W = 0.3$, $V_{imp} = 4.3 \text{ m s}^{-1}$).....	F-6
F-4	Stress Intensity Histories for Double-Crack 1PB Specimens with Different Crack Lengths ($2D = 50$ mm, $V_{imp} = 4.3 \text{ m s}^{-1}$).....	F-8
F-5	Arrangements to Control Mixed-Mode Ratio.....	F-11
F-6	Stress Intensity Histories for Three Mixed-Mode Fracture Experiments.....	F-14
F-7	Results of Dynamic Mixed-Mode Fracture Experiments on 4340 Steel.....	F-15

F-8	Crack Path in Mixed-Mode Fracture Specimens.....	F-17
F-9	Fracture Surface of Mixed-Mode Specimens.....	F-18
G-1	Stress Intensity History for Crack Jump Specimen with Stationary Crack.....	G-5
G-2	Results of Crack Jump Experiments and Comparison with 1PBT Model Simulations.....	G-7
G-3	Normalized Strain Histories for CJ Experiments.....	G-10
G-4	Normalized Strain Histories for Completely Fractured Specimens.....	G-11
G-5	Simulation of Normalized Strain Histories for CJ Experiments Shown in Figure G-3.....	G-13
G-6	Simulation of Normalized Strain Histories for Fracture Experiments Shown in Figure G-4.....	G-14
G-7	Comparison of Experimental and Simulated Strain Histories in Specimen H7.....	G-17
G-8	Crack Velocity \dot{a} as a Function of Crack Extension Δa for Test H7.....	G-19
G-9	Propagation Toughness Measured in Test H7.....	G-20
G-10	Normalized Strain History for 12.7-mm-Thick Specimen Loaded at Low Rate.....	G-22
G-11	Arrested Crack Shape and Shear Lips.....	G-23
G-12	Normalized Strain History for 12.7-mm-Thick Specimen Loaded at Intermediate Rate.....	G-25
G-13	Normalized Strain History for 12.7-mm-Thick Specimen Loaded at High Rate.....	G-27
G-14	Normalized Strain History for Smooth and Side-Grooved Specimens.....	G-28
H-1	Coordinates at a Running Crack Tip.....	H-3
H-2	Nondimensional Function H Used in Calculating K_I^{dyn} From Strain Gage Measurements.....	H-5
H-3	Crack Propagation Specimen Dimensions in mm (inch), and Instrumentation.....	H-9

H-4	Electronic Instrumentation for Crack Propagation Experiments.....	H-10
H-5	Loading Arrangement for Crack Propagation Experiments.....	H-12
H-6	Strain Histories Along Crack Paths.....	H-15
H-7	Crack Velocity \dot{a} as a Function of Crack Jump Distance Δa	H-17
H-8	Temperature Histories for Specimen CT3.....	H-18
H-9	Temperature Histories for Specimen CT6.....	H-19
H-10	Normalized Temperature Histories at Several Locations y for Line Heat Source and Finite Width Heat Source.....	H-22
H-11	K_I^{dyn} and K_{ID} as a Function of Crack Speed \dot{a}	H-24
H-12	K_I^{stat} , K_I^{dyn} , and K_{ID} as a Function of Crack Length.....	H-25

LIST OF TABLES

C-1 Comparison of Stress Intensity Estimates by the Static Calibration (SC) Method and the Singularity Solution (SS) Method.....	C-9
F-1 Results of Mixed-Mode Fracture Experiments.....	F-13
G-1 Static and Dynamic Fracture Toughness.....	G-3
G-2 Average Crack Velocities for First Millimeters of Crack Extension.....	G-16
H-1 Angle θ_{\max} for Maximum Strain ϵ_y^{\max}	H-6
H-2 Experimental Parameters for Six Wedge-Loaded Compact Tension Tests.....	H-14
H-3 Comparison of Thermistor (TH) and Thermouple (TC) Data....	H-27

1. INTRODUCTION

Recent developments in directed energy and in advanced kinetic energy weapons have placed a renewed emphasis on the importance of dynamic fracture processes in evaluating the vulnerability of airborne and spaceborne structures. These new weapon systems can subject targets to high amplitude load pulses of very high rate and very short duration. Under such conditions, the concepts of classical static fracture mechanics can no longer characterize the conditions for initiation and propagation of preexisting flaws and new methods must be applied. As shown in a previous AFOSR-sponsored program,¹ the highly transient nature of the stress and strain fields surrounding the crack tip must be taken into account, and the effect of extremely high loading rates on the material deformation and microdamage response must be evaluated.

This report summarizes the results of a five-year research program to improve our understanding of dynamic fracture behavior by investigating both the crack tip loading conditions and the material fracture properties for high loading rates. Section 2 reviews the objectives and highlights accomplishments of the program. The results are summarized in Section 3 and discussed in detail in the appendices. Section 4 lists the project personnel and describes special activities during the program. A list of publications and presentations resulting from this and the previous programs is also presented in Section 4.

2. RESEARCH OBJECTIVES AND ACCOMPLISHMENTS

The objectives of this research were to establish the conditions controlling dynamic crack initiation and extension and to generate reliable experimental data to validate proposed dynamic fracture theories. To accomplish these objectives, the following tasks were performed during the five-year program:

- Task 1: Develop a simple test procedure for obtaining reliable initiation fracture toughness values K_{Id} at strain rates representative of impact loading.
- Task 2: Using the test procedure developed in Task 1, generate the necessary data to verify and extend time modified theories for dynamic crack instability.
- Task 3: Measure critical conditions and establish criteria for crack instability under dynamic mixed-mode I and II loading.
- Task 4: Obtain values of the propagation toughness K_{ID} and establish the relationship between K_{ID} and the dynamic initiation toughness K_{Id} .

The successful completion of these tasks has resulted in the following significant accomplishments:

- A simplified impact fracture test, the one-point-bend test (1PBT), was developed and fully characterized. The new test permits reliable dynamic fracture toughness measurements at rates in excess of $10^6 \text{ MPa m}^{1/2} \text{ s}^{-1}$. This testing procedure is now documented in the ASM Metals Handbook, Ninth Edition, Volume 8 on Mechanical Testing.
- The 1PBT procedure was modified to permit dynamic mixed-mode I and II fracture experiments with controlled ratios of mode I and mode II loading.
- We established experimentally that, for high strength steels and similar alloys, no time-modified fracture criterion is necessary when the loading time to crack initiation is greater than 20 μs . In these situations, the classical fracture criterion is adequate to predict crack

initiation, provided the correct dynamically applied stress intensity factor is equated to the dynamic fracture toughness.

- The dynamic mixed-mode I and II failure curve was determined for a high strength steel for mode II/mode I ratios between 0 and 0.5. Mixed-mode fracture in this range appears essentially controlled by the mode I dynamic fracture toughness. A lower bound mixed-mode failure envelop was also established for higher mixed-mode ratios.
- For specimen thicknesses up to 12.7 mm, we demonstrated that the propagation toughness of high strength steel can be over twice the value of the dynamic initiation toughness. This large increase in toughness was attributed in part to a resistance curve effect associated with the formation of small shear lips and with the bowing of the crack front during extension.

3. SUMMARY OF RESULTS

The results of the research are summarized below according to the four main tasks of our work. We first report on the development of new experimental techniques necessary to investigate fracture at high loading rates. Then we review how these techniques were used to investigate dynamic crack initiation under pure mode I loading, mixed-mode I and II loading, and dynamic crack propagation. Detailed discussions of each topic are presented in Appendices A through H.

DEVELOPMENT OF NEW DYNAMIC FRACTURE TESTING TECHNIQUES.

One main achievement of the research program was the development and analysis of a novel impact fracture test, the one-point-bend test (1PBT), for measuring reliable dynamic initiation fracture toughness. The concept of the 1PBT was used further to develop an impact test capable of producing crack initiation under controlled conditions of mixed mode I (tensile opening) and mode II (in-plane shear) loading and to investigate dynamic crack propagation.

The 1PBT for Mode I Dynamic Crack Initiation

A testing method that produces an adjustable and smoothly varying load history is desirable to obtain reliable measurements of the dynamic initiation fracture toughness. Unfortunately, conventional tests such as the Charpy impact test or the dynamic tear test do not produce a smoothly varying stress intensity history. Thus, interpretation of the test results is not straightforward. To circumvent these difficulties we investigated a test configuration in which a simple edge-cracked specimen is loaded in bending by impacting it at the midsection, but without supporting it at the outer edges.

The test arrangement and the loading mechanism for this one-point-bend test are shown in Figure 1. The loading at the crack tip is achieved strictly by inertial effects. The resulting stress intensity history, shown in Figure 2, has approximately a sinusoidal time dependence, with the period of oscillation given by the first natural frequency of vibration of the specimen. The maximum stress intensity amplitude K_I^{Max} is controlled in part by the specimen geometry and density, but mainly by the impact velocity. The stress intensity history can easily be measured during the test by placing a strain gage a short distance from the crack tip.

We investigated, analytically and experimentally, how the stress intensity duration T_o and amplitude K_I^{Max} vary with impact conditions, specimen geometry, dimensions and material properties (Appendix A and Appendix B). We showed that T_o and K_I^{Max} can be expressed as:

$$T_o = W \sqrt{\rho/E} h_1(L/W, a/W, v) \quad (1)$$

$$K_I^{Max} = V_{imp} \sqrt{W\rho E} h_2(L/W, a/W, v) \quad (2)$$

where W , L , and a are the width, length, and crack depth of the specimen, respectively; ρ , E , and v are the mass density, Young's modulus, and Poisson's ratio, respectively; V_{imp} is the impact velocity; and h_1 and h_2 are nondimensional functions. We also investigated the reliability of the strain gage technique for measuring the stress intensity history and established procedures for determining the point of crack initiation (Appendix C).

The 1PBT can be performed on a pendulum impact tester, on a drop-weight tester, or on any other apparatus capable of impact velocities greater than 3 m s^{-1} . Its primary advantage is that the measured stress intensity history varies smoothly and incorporates dynamic effects completely. Therefore, in contrast to other dynamic fracture tests, no limits need to be imposed on the impact velocity and the test duration to

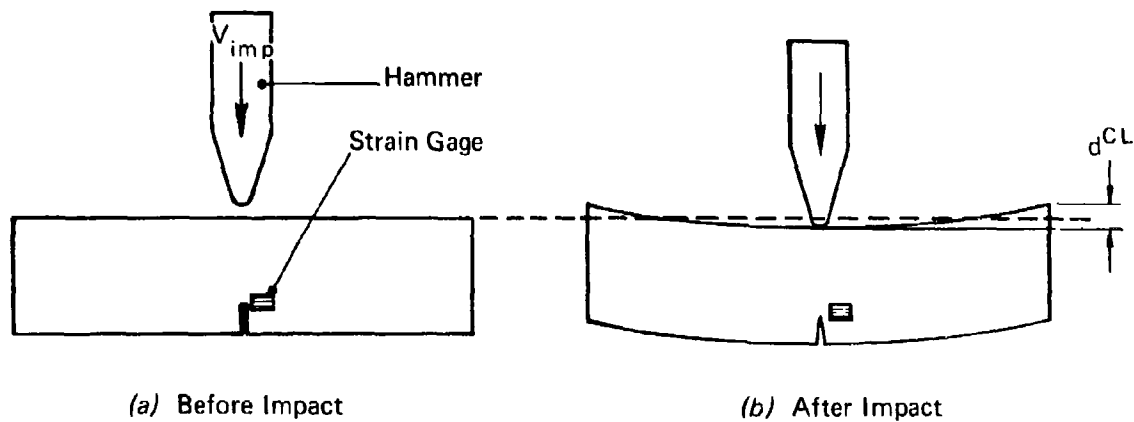


FIGURE 1 TEST ARRANGEMENT AND LOADING MECHANISM FOR THE ONE-POINT-BEND TEST

JA-2777-16

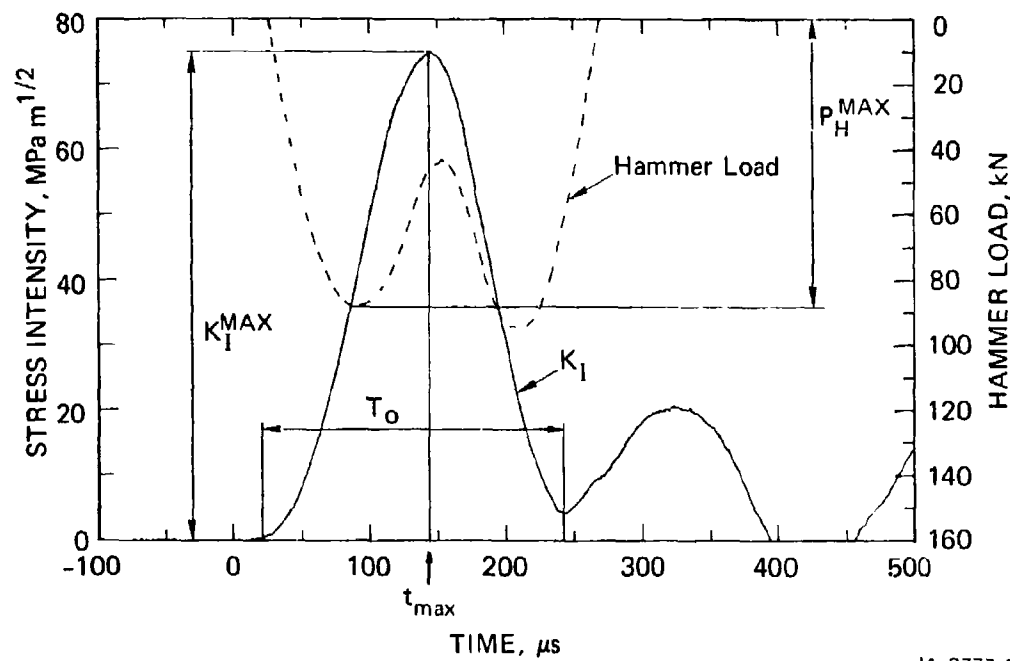


FIGURE 2 TYPICAL STRESS-INTENSITY AND LOAD HISTORIES OBTAINED IN THE ONE-POINT-BEND TEST

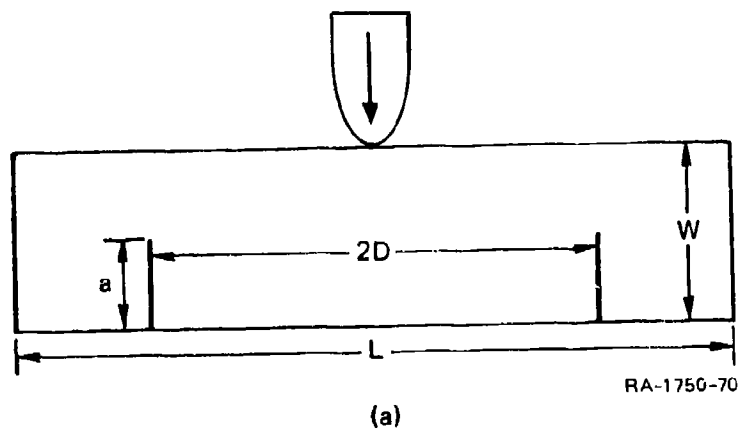
fracture. Another advantage of the 1PBT is that the test duration T_0 and the stress intensification rate \dot{K}_I can be varied over an order of magnitude range (80 to 800 μs and 3×10^5 to $3 \times 10^6 \text{ MPa m}^{1/2} \text{ s}^{-1}$) by changing the specimen geometry and the impact velocity.

The 1PBT is now a well-established technique for simply and reliably measuring dynamic initiation fracture toughness values. Its use has also been extended recently to nonmetallic materials,² and it has been successful in discriminating between two commercial alumina ceramics in terms of their dynamic fracture toughness.

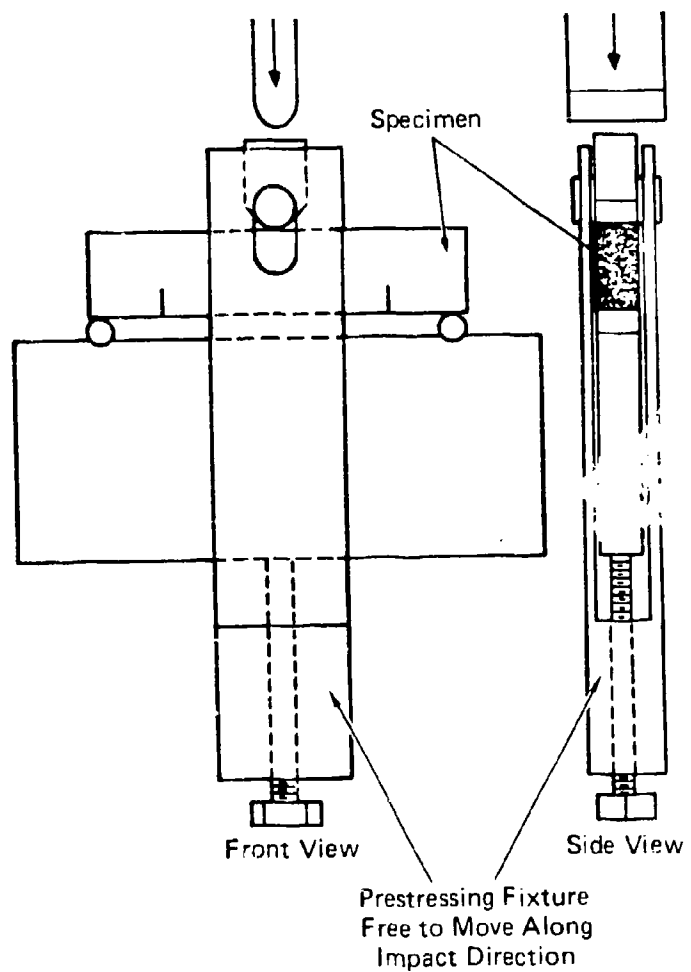
The Modified 1PBT for Dynamic Mixed-Mode I and II Crack Initiation

To investigate dynamic crack initiation under mixed-mode loading conditions, it is necessary to control the mixed-mode ratio K_{II}/K_I that is achieved during the experiment. Controlling this ratio can be particularly difficult because, due to structural and stress wave dynamics, the mixed-mode ratio generally varies continuously in a dynamic mixed-mode experiment. To overcome this difficulty, we chose the double-crack 1PBT configuration shown in Figure 3(a) (Appendix F). This configuration presents the advantage that the specimen dynamics are relatively simple and easy to understand: inertia will cause shear stresses on the ligaments ahead of the off-centered cracks and bending as in the single crack one-point-bend test. By controlling the shear stresses, we can adjust the mode II stress intensity, and by controlling the bending, we can adjust the mode I stress intensity. The straight crack configuration also makes it easier to fatigue precrack the specimens than it is with the slanted crack configurations used in other investigations.

To achieve control of the mixed-mode ratio K_{II}/K_I , we modified the configuration in Figure 3(a) by statically prestressing the specimen using the arrangement shown in Figure 3(b). Prestressing introduces a mode I loading component during the early times of the experiments when the mode II loading due to the inertia of the specimen is maximum. The inertia of the prestressing fixture itself permits maintaining this mode



(a)



(b)

JA-2777-44A

FIGURE 3 TEST ARRANGEMENTS FOR DYNAMIC MIXED-MODE FRACTURE EXPERIMENTS

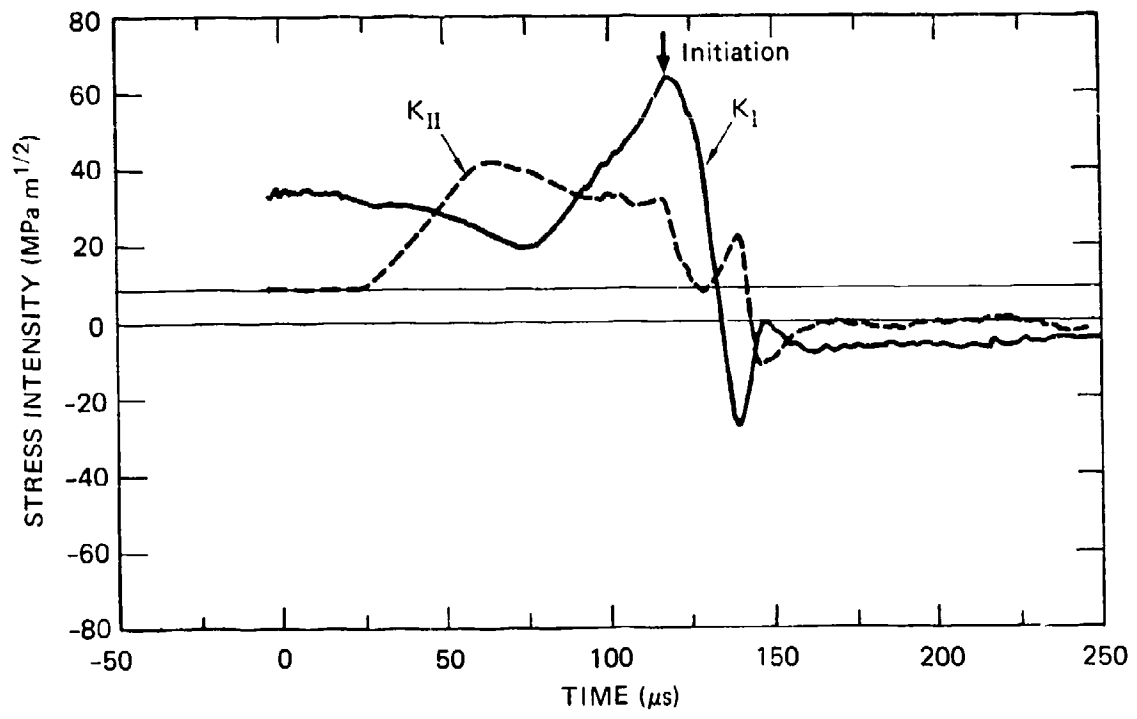
II loading component at later times when the dynamic mode I loading component due to specimen inertial bending becomes significant. Stress intensity histories obtained with this arrangement are shown in Figure 4 for an experiment in which the specimen fractured at a mixed-mode ratio of 0.51.

We investigated the dependence of the stress intensity histories in the double-crack one-point-bend specimen on the crack length, the crack separation, and the impact conditions. Three strain gages were positioned at different angles near the crack tip to measure the stress intensity histories (Appendix C). It was found that beyond a limit impact velocity for which vibrational model transition occurs, the stress intensity amplitudes are proportional to the impact velocity and increase with increasing initial crack length. The distance between the two cracks has little effect on the mode II stress intensity and is chosen to facilitate fatigue-precracking.

With the arrangement shown in Figure 3(b), we were able to produce controlled stress intensity histories with mixed-mode ratios varying from 0 to 0.5, with maximum K_{II} amplitudes in excess of $50 \text{ MPa m}^{1/2}$. Therefore, a simple and reliable technique is now available for dynamic mixed-mode fracture investigations. Further studies are required to fully understand the double-crack 1PBT specimen dynamics. In particular, the effect of the impact velocity on the specimen response needs to be examined. Moreover, adjustment of the prestressing support mass and position, as well as modifications of the impact hammer geometry, will result in increased mixed-mode ratios and improved control of the experiment.

The 1PBT for Dynamic Crack Propagation Experiments

The one-point-bend test is also attractive for crack propagation investigations. The simplicity of inertial crack tip loading and the good control over the loading amplitude and duration permit the crack extension distance and the crack velocity to be adjusted precisely. Further, the simplicity of the boundary conditions in the 1PBT makes



RA-1750-34

FIGURE 4 STRESS INTENSITY HISTORIES FOR MIXED-MODE FRACTURE EXPERIMENT
 $(K_{II}/K_I)_{init} = 0.51$

numerical simulations of the experiment particularly easy. Finally, the one-point-bend test permits the investigation of propagating cracks initiated under impact conditions in contrast to most other test procedures, which use quasi-static initiation conditions.

During this program, we demonstrated that very small, controlled crack jumps can be produced with the 1PBT (Appendix G). With this technique we were able to investigate the very first increments of crack extension to relate dynamic initiation toughness and propagation toughness. We developed an empirical model of the 1PBT to obtain first order estimates of the stress intensity at the tip of the extending crack (Appendix D). The model is based on the stress intensity history measurements for specimens with stationary cracks of various lengths. It assumes that the 1PBT is displacement controlled, with the first flexural mode of the specimen controlling the stress intensity at the crack tip. The model accounts for the effect of crack extension and for the effect of material inertia on the stress intensity at the crack tip. The model is implemented on a microcomputer and calculates the stress intensity and history using the propagation toughness or the crack velocity as input variables.

The model was used to evaluate the first increments of crack extension during the 1PBT experiments. We also used it to analyze the strain history at the original crack tip after crack initiation (Appendix C, Appendix G), and we demonstrated that the strain history can yield crack velocity and propagation toughness information.

DYNAMIC MODE I CRACK INITIATION FOR SHORT LOADING TIMES

In a previous AFOSR-sponsored research program,¹ it was experimentally established that, for very short duration pulse loads (less than $2.2\text{-}\mu\text{s}$ duration), the classical quasi-static linear elastic fracture mechanics criterion for crack instability must be modified to account for microstructural rate effects. Kalthoff and Shockley³ postulated that cracks would become unstable only after the dynamic fracture toughness has been exceeded for a minimum time (minimum time

theory). Based on fracture tests with pulse loads of several durations (18 to 80 μ s), Homma et al.⁴ have estimated that, for 4340 steel in the HRC 50 condition, the minimum time for fracture should be about 7 μ s. This value is somewhat uncertain, however, because the fracture toughness reported by Homma et al. is only about half the value reported in the literature for similar loading rates.

More recently, Ravi-Chandar and Knauss⁵ in experiments with Homalite, and Kalthoff⁶ in experiments with high strength steel, found that when the time to monotonically load a crack to fracture is gradually decreased below about 30 μ s, the stress intensity value at which the crack becomes unstable increases rapidly. For a loading time to fracture of 5 to 10 μ s, the stress intensity factor at instability is about twice the value when the loading time is 50 μ s or more. Kalthoff rationalized this behavior by suggesting that a so-called incubation time is necessary to nucleate, grow, and coalesce microdefects ahead of the macrocrack. Conceptually, the incubation time is similar to the minimum time postulated by Kalthoff and Shockley.

We attempted to establish whether fracture incubation time has a significant influence on crack instability conditions in high strength steel at conventional impact loading rates, that is, for fracture times down to 20 μ s (Appendix E). For this investigation, we used the 1PBT, varying the impact velocity. In tests at low stress intensity rate, the specimens were impacted at a velocity sufficient to produce a maximum stress intensity slightly above the anticipated critical value. The loading times to fracture were about 100 μ s, well above the anticipated incubation time. Thus these tests provided a measure of the dynamic fracture toughness, K_{Id} .

Tests at high loading rates were designed to determine a possible incubation time. In these tests the specimens were grossly overloaded by increasing the impact velocity to achieve times to fracture of 20 to 25 μ s. Thus, if fracture incubation time is important, and of the order of several microseconds, we expected fracture to occur at significantly higher stress intensity values than the value measured in the low rate

tests. The difference between the time at which K_{Id} was reached and the time of instability would provide an estimate of the incubation time. Intermediate rate tests provided additional data to monitor the influence of the loading rate on the value of the stress intensity factor at crack initiation.

The results of the dynamic fracture tests are summarized in Figure 5. Within the range of loading rates studied, the stress intensity factor at initiation is $58.5 \text{ MPa m}^{1/2}$ and essentially constant. This value is about 92% of the static toughness and represents the dynamic initiation fracture toughness K_{Id} . The results therefore demonstrate that a fracture incubation time is unimportant for these loading rates. Further, our results imply that, if a fracture incubation time exists, it is much smaller than 20 to 25 μs .

We conclude that, for fracture times in excess of 20 μs , crack initiation predictions for 4340 steel in the HRC 50 condition (and probably for similar high strength alloys) do not require a time modified fracture criterion. Rather, our work indicates that the initiation conditions can be determined solely by using the classical concepts of fracture mechanics, provided the correct dynamic stress intensity history is used.

DYNAMIC MIXED-MODE CRACK INITIATION

In most practical situations, cracks are not only loaded in the tensile opening mode, i.e., mode I loading, but also experience in-plane shear, i.e., mode II loading. Crack initiation conditions under mixed-mode loading no longer depend on a single parameter, but rather must be expressed in terms of a failure curve in the K_I - K_{II} plane, where K_I and K_{II} represent the mode I and mode II stress intensity factors, respectively. Several attempts have been made to establish the mixed-mode failure locus under quasi-static loading conditions. These investigations suggest that a failure curve based on a critical maximum tangential stress at a critical distance ahead of the crack tip may be adequate. However, they also suggest that the failure locus depends

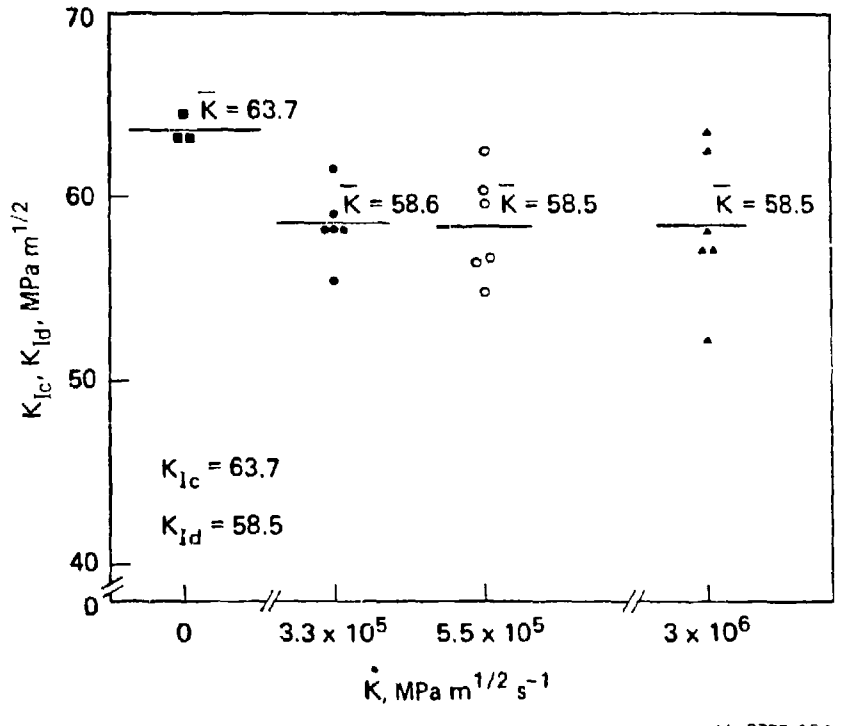


FIGURE 5 SUMMARY OF FRACTURE TEST RESULTS ON 4340 STEEL FOR FOUR STRESS INTENSITY RATES

on the specific material and on the micromode of fracture. In contrast to the static mixed-mode case, very few data are available for dynamic mixed-mode crack initiation, and the lack of these data prevents the development and evaluation of reliable mixed-mode initiation criteria. To remedy this lack of information, we performed mixed-mode initiation experiments using the impact test technique to establish the failure curve for 4340 steel in the HRC 50 condition (Appendix F).

The results of these experiments are summarized in Figure 6, which plots the mode I stress intensity factor normalized by the dynamic mode I initiation toughness, K_{Id} , versus the mode II stress intensity factor, also normalized by K_{Id} . In the dynamic experiments the mixed-mode ratio does not stay constant but varies continuously with time. The open circles in Figure 6 therefore represent mixed-mode states that have been traversed during the tests, but did not cause initiation; the solid circles represent the mixed-mode states that resulted in crack instability. The lines connecting the symbols represent typical loading paths followed during the experiments.

We draw several conclusions from the results in Figure 6. First, for K_{II}/K_I between 0 and 0.5, crack initiation appears essentially controlled by the mode I stress intensity factor. Initiation occurs when $K_I = K_{Id}$. (The two isolated points on the far right of Figure 6 are believed to be shifted artificially to higher values of K_I at initiation because of the difficulty of detecting the precise point of crack initiation for higher mixed-mode ratios, see Appendix F.)

Further, based on the points of the K_I-K_{II} plane traversed during the fracture experiments, but for which no failure occurred, a tentative lower bound mixed-mode failure curve can be drawn for 4340 steel HRC 50. We estimate that the pure mode II dynamic toughness K_{IId} is at least equal to the pure mode I initiation toughness K_{Id} ; i.e., $K_{IId} \geq 58 \text{ MPa m}^{1/2}$. Assuming that K_{IId} has the same low rate sensitivity as K_{Id} , and taking for the static mode II fracture toughness the value reported by Shah,⁷ $88 \text{ MPa m}^{1/2}$, we estimate that K_{IId} should be about $85 \text{ MPa m}^{1/2}$. This value is consistent with the proposed lower bound failure curve.

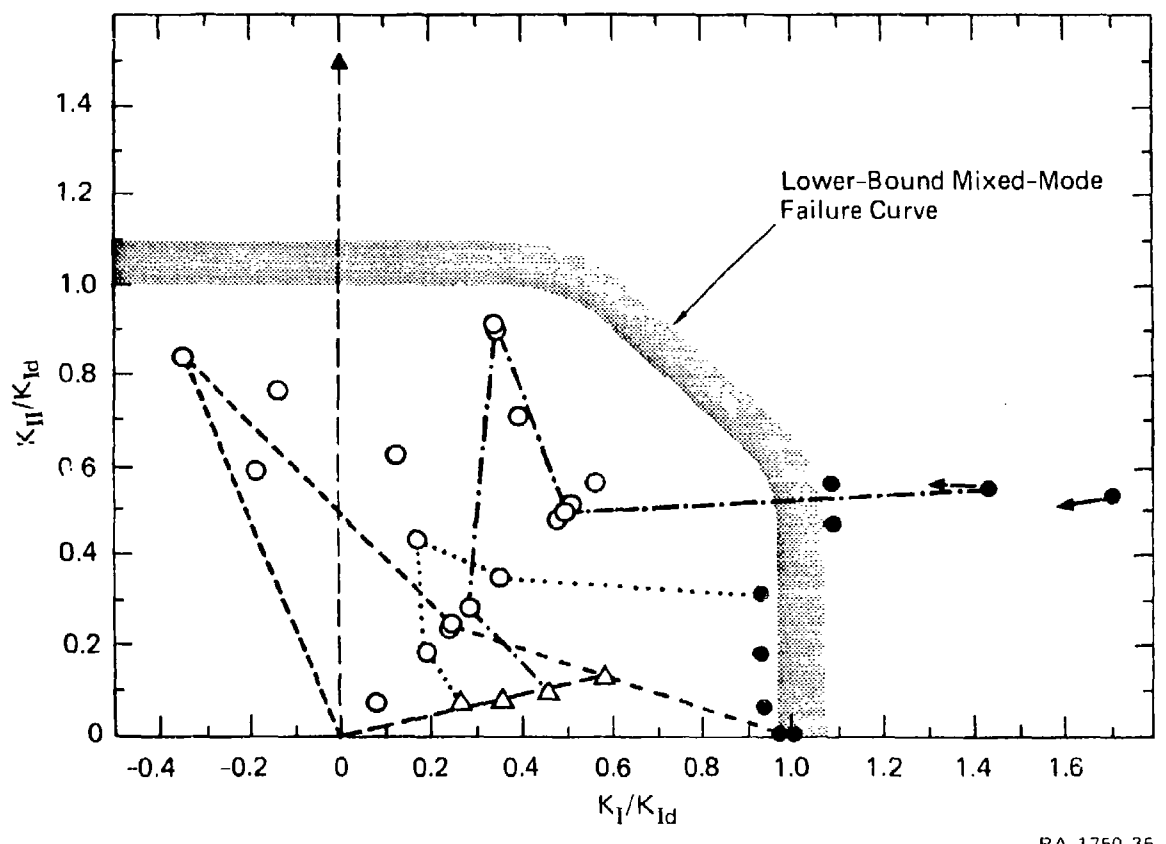


FIGURE 6 RESULTS OF DYNAMIC MIXED-MODE FRACTURE EXPERIMENTS ON 4340 STEEL

For specimens tested with the highest mixed mode ratio, we noticed a significant difference in both the macroscopic and microscopic fracture surface appearance. These specimens exhibited a much rougher fracture surface, with large inclined steps, possibly formed by grain pullout. These differences in the fracture surface morphology suggest that the micromechanisms of dynamic mixed-mode fracture will have to be understood first before physically relevant initiation and extension models and criteria can be formulated.

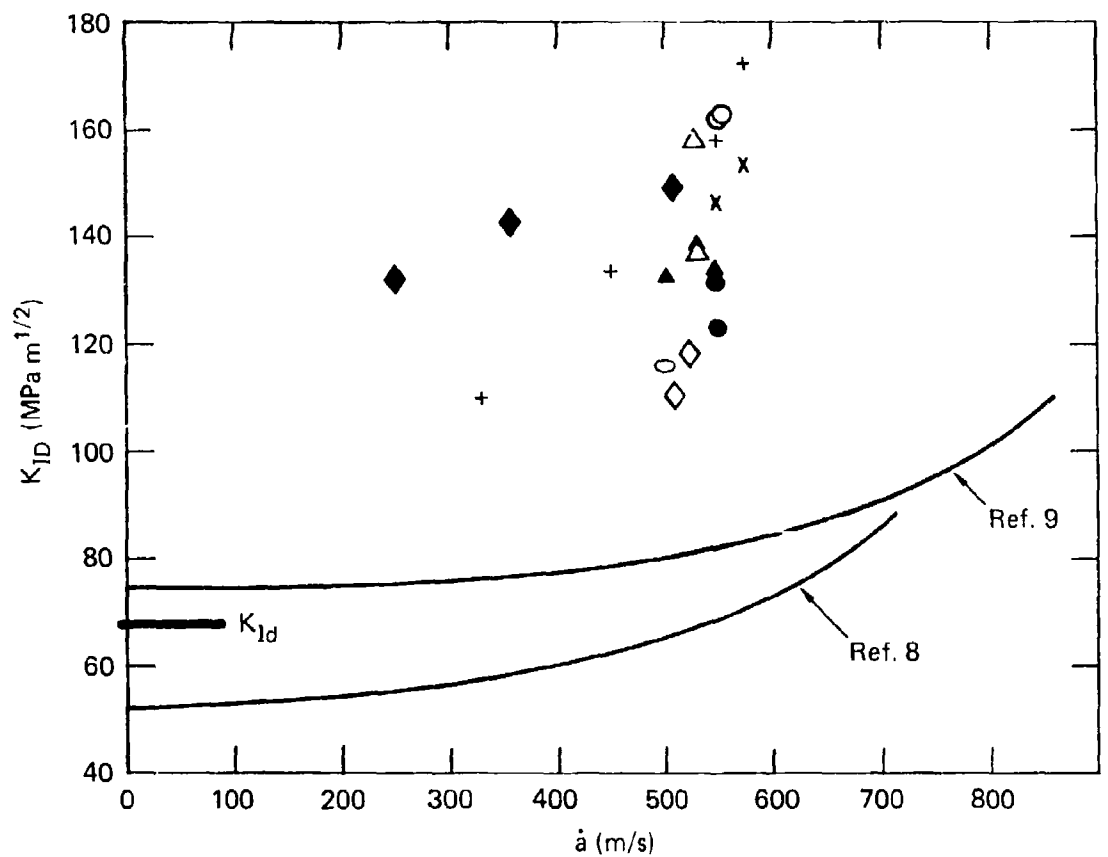
RELATIONSHIP BETWEEN DYNAMIC INITIATION AND PROPAGATION TOUGHNESS

Knowledge of the intrinsic resistance of a material to dynamic crack extension (dynamic propagation toughness, K_{ID}) is an important element in predicting how far a crack will propagate once it has initiated, and where and when it will arrest. To investigate the relationship between the resistance to dynamic crack extension and the dynamic initiation toughness in 4340 HRC 50 steel, we used two approaches. In the first approach, we observed the crack extension behavior immediately after crack initiation from a sharp fatigue crack (Appendix G). We estimated the crack velocity and the propagation toughness by analyzing the strain history measured near the initial crack tip and by comparing the experimental results with simulations obtained with the simple 1PBT model described in Appendix D. In the second approach, we derived the propagation toughness either by measuring the heat dissipated during the fracture process, using thermocouples or by measuring strains using strain gages mounted along the crack path (Appendix G and Appendix H).

We established that, during the first millimeter or so of dynamic crack extension, the crack speed is not constant but increases, slowly at first, then more rapidly. The crack speed history is a function of the loading rate. The resistance to crack extension increases significantly (up to 50 %) above the dynamic initiation fracture toughness during the first millimeter of extension. For crack velocities of 400 to 600 m s^{-1} , we measured values of K_{ID} that are more than twice the value of the initiation toughness.

These results are shown in Figure 7, which plots K_{ID} as a function of the crack velocity, as is customary in crack propagation investigations, to show the strong crack velocity dependence of the propagation toughness. Also shown in Figure 7 are results for the same material published in the literature.^{8,9} At the crack velocities investigated, our results fall significantly above the published results. However, Figure 7 is somewhat misleading because part of the elevation of the resistance to crack extension above the initiation toughness is due to a resistance curve effect, whereby the propagation toughness increases above the initiation toughness as a function of crack extension distance. The mechanism for this elevation is the formation of small shear lips and the bowing of the crack front, which occur during the first millimeter or so of crack extension in the relatively thin specimens used for our investigation (9.8 and 12.7 mm). Moreover, we believe that the velocity dependence of the propagation toughness is also influenced by the formation of shear lips and by crack tunneling, but this crack velocity dependence could not be assessed independently from the resistance curve effect.

Our findings have four practical implications. First, they indicate that cracks initiated by pulse loads in structures less than 25 mm thick may not necessarily be unstable, because of the resistance curve effect, which requires an increasing applied stress intensity factor to sustain crack extension at an appreciable crack velocity. The second implication is that the thickness requirements to obtain thickness independent propagation toughness values are much more stringent than the thickness requirements for the measurement of dynamic initiation toughness. The third implication is that, because of the three-dimensional nature of the crack propagation process, caution should be applied in interpreting experimental data obtained from surface measurements. Finally, a comparison of propagation toughness data obtained with cracks initiated from blunt notches or from sharp cracks suggests that the initiation conditions may affect the extension behavior over distances that are significant compared with the plastic zone size at the initial notch or crack tip.



RA-1750-38

FIGURE 7 PROPAGATION TOUGHNESS OF 4340 STEEL AS A FUNCTION OF CRACK VELOCITY
Solid curves are published experimental results.

PERSONNEL ACTIVITIES, PUBLICATIONS, AND PRESENTATIONS

The following professional personnel were associated with this research effort.

D. A. Shockey, principal investigator
J. H. Giovanola, co-principal investigator
T. Kobayashi
A. T. Werner
H. Yamada
W. Klemm
H. Homma
J. F. Kalthoff.

The work performed in this program was presented at several technical meetings and resulted in two technical journal articles, three conference proceedings articles, and two handbook articles. Dr. A. H. Rosenstein and I. Caplan of the Air Force Office of Scientific Research were given extensive oral reviews of the program results on the occasions of their yearly visits to SRI and during a one day visit in Washington. Contact was also maintained with Dr. T. Nicholas, Metals Behavior Branch of the Air Force Materials Laboratory at Wright-Patterson Air Force Base, and he visited SRI International in February 1986 to obtain a complete first-hand presentation of the program accomplishments.

The work performed in this and the previous program continues to attract the attention of the technical and scientific community. The Principal Investigator, D. A. Shockey, was invited to participate in a workshop on dynamic fracture sponsored by the National Science Foundation and the Army Research Office and a special session on dynamic fracture organized by the Society for Experimental Mechanics. The co-principal investigator, J. H. Giovanola, made presentations at the 17th ASTM

National Symposium on Fracture Mechanics in Albany, New York, and at the DYMAT International Conference on Mechanical and Physical Behavior of Materials under Dynamic Loading, in Paris. D. A. Shockey was editor of the chapter on dynamic fracture testing of Volume 8, Mechanical Testing, of the ASM Metals Handbook, Ninth Edition, and both D. A. Shockey and J. H. Giovanola contributed articles to this chapter. Moreover, J.H. Giovanola has been invited several times to lecture on the subject of material failure at high strain rates at Stanford University and at the University of California in Berkeley.

A list of papers published and presentations made during this and the previous contracts is given on the following pages.

PUBLICATIONS

J. F. Kalthoff and D. A. Shockey, "Instability of Cracks Under Impulse Loads," *J. Appl. Phys.* 48, 984-993 (March 1977)

D. A. Shockey, J. F. Kalthoff, H. Homma, and D. C. Erlich, "Criterion for Crack Instability Under Short Pulse Loads," Advances in Fracture Research, D. Francois et al., Eds. (Oxford and Pergamon Press, New York, 1980), pp. 415-423.

D. A. Shockey, J. F. Kalthoff, and D. C. Erlich, "Evaluation of Dynamic Crack Instability Criteria," *Int. J. Fract. Mech.* 22, 217-229 (1983).

D. A. Shockey, J. F. Kalthoff, W. Kleemann, and S. Winkler, "Simultaneous Measurements of Stress Intensity and Toughness for Fast Running Cracks in Steel," *Exp. Mech.* 23, 140-145 (1983).

H. Homma, D. A. Shockey, and Y. Murayama, "Response of Cracks in Structural Materials to Short Pulse Loads," *J. Mech. Phys. Solids* 31, 261-279 (1983)

D. A. Shockey, J. F. Kalthoff, H. Homma, and D. C. Erlich, "Response of Cracks to Short Pulse Loads," Proceedings of the Workshop on Dynamic Fracture, W. G. Knauss, Ed., held at the California Institute of Technology, Pasadena, CA, under sponsorship of the National Science Foundation and the Army Research Office, Feb. 17-18, 1983. pp. 57-71.

J. H. Giovanola, "Investigation and Application of the One-Point-Bend Impact Test," in Fracture Mechanics: Seventeenth Volume, ASTM STP 905, J. G. Underwood, R. Chait, C. W. Smith, D. P. Wilhelm, W. A. Andrews, and J. Newman, Eds. (American Society for Testing and Materials, Philadelphia, 1986), pp. 307-328.

J. H. Giovanola, "The One-Point-Bend Test," in ASM Metals Handbook, 9th Edition, Volume 8, Mechanical Testing (American Society for Metals, Metals Park, OH, 1985) pp. 271-275.

D. A. Shockey, "Short-Pulse-Duration Tests," in ASM Metals Handbook, 9th Edition, Volume 8, Mechanical Testing (American Society for Metals, Metals Park, OH 1985), pp. 282-284.

D. A. Shockey, J. F. Kalthoff, H. Homma, and D. C. Erlich, "Short Pulse Fracture Mechanics," in Dynamic Fracture, The Albert S. Kobayashi Anniversary Volume of the International Journal of Fracture, M. F. Kanninen and S. N. Atluri, Eds (Pergamon Press, New York, 1986), pp. 311-319.

J. H. Giovanola, "Crack Initiation and Extension in Steel for Short Loading Times," in the Proceedings of DYMAT '85, International Conference on Mechanical and Physical Behavior of Materials under Dynamic Loading, Paris, September 2-5 (1985) (Les Editions de Physique, France, 1985), pp. C5-171 through C5-178.

PRESENTATIONS

D. C. Erlich and D. A. Shockey, "Instability Conditions for Cracks Under Short-Duration Pulse Loads," Topical Conference on Shock Waves in Condensed Matter, Meeting of the American Physical Society, Washington State University, Pullman, WA, June 11-13, 1979.

D. A. Shockey, "Instability Conditions for Cracks Loaded by Short Stress Pulses," Poulter Laboratory Seminar, SRI International, Menlo Park, CA, December 12, 1979.

D. A. Shockey, "Dynamic Crack Instability," Institut CERAC, Ecublens, Switzerland, May 19, 1980.

D. A. Shockey, "Dynamic Crack Instability," Institut für Werkstoffmechanik, Freiburg, Germany, May 21, 1980.

D. A. Shockey, "Simultaneous Measurements of Stress Intensity and Toughness for Fast Running Cracks in Steel," Poulter Laboratory Seminar, SRI International, Menlo Park, CA, June 1980.

D. A. Shockey, "Criterion for Crack Instability Under Short Pulse Loads," Fifth International Conference on Fracture (ICF5), Cannes, France, March 29-April 3, 1981.

D. A. Shockey, "Simultaneous Measurements of Stress Intensity and Toughness for Fast Running Cracks in Steel," 18th Annual Meeting of the Society for Engineering Science, Inc., Brown University, Providence, RI, September 2-4, 1981.

D. A. Shockey, "Short Pulse Fracture Mechanics," Seminar for the Department of Applied Mechanics, Stanford University, Stanford, CA, March 3, 1983, C. Steele, Chairman.

D. A. Shockey, "Short Pulse Fracture Mechanics," Poulter Laboratory Seminar, SRI International, Menlo Park, CA, April 11, 1983.

J. H. Giovanola, "Mechanics of Fracture Under Pulse Loads; Minimum Time Theory Revisited," Poulter Laboratory Seminar, SRI International, Menlo Park, CA, April 1984.

J. H. Giovanola, "Material Failures at High Strain Rates," two lectures given at the Department of Materials Science and Engineering of Stanford University, May 1984.

J. H. Giovanola, "Material Failures at High Strain Rate," Materials Science and Engineering Graduate Seminar, University of California Berkeley, November 1984.

J. H. Giovanola, "Investigation and Analysis of the One-Point-Bend Impact Test," presented at the ASTM Seventeenth National Symposium on Fracture Mechanics, Albany, NY, August 7-9, 1984.

D. A. Shockey, D. R. Curran, and L. Seaman, "Fracture Under Impact Loads," presented at the International Conference on Dynamic Fracture Mechanics, San Antonio, November 7-9, 1984.

J. H. Giovanola, "The One-Point-Bend Test: Experiment and Analysis," Poulter Laboratory Seminar, SRI International, Menlo Park, CA, March 1985.

D. A. Shockey, J. F. Kalthoff, H. Homma, and J. H. Giovanola, "Recent Results in Short Pulse Fracture Mechanics," presented at the SEM Spring Meeting, Las Vegas, June 1985.

J. H. Giovanola, "Crack Initiation and Extension in Steel for Short Loading Times," presented at DYMAT International Conference on Mechanical and Physical Behavior of Materials under Dynamic Loading, Paris, September 2-5 (1985).

J. H. Giovanola: "Fracture of High Loading Rates," to be presented at the University of California Berkeley Short Course, Fracture and Fatigue: Approaches for Analysis and Control of Failure, June 1986.

REFERENCES

1. D. A. Shockey, "Fracture of Structural Materials under Dynamic Loading," Final Technical Report Prepared for the Air Force Office of Scientific Research, Contract AFOSR/F49620-77-C-0059, SRI International, Menlo Park (March 1981).
2. J. H. Giovanola and R. D. Caligiuri, "Evaluation of Rate Effects on Mechanical Properties of Ceramics," Final Report to FMC Corporation, SRI International, Menlo Park (January 1986).
3. J. F. Kalthoff and D. A. Shockey, "Instability of Cracks Under Impulse Loads," *J. Appl. Phys.*, 48, 984-993 (1977).
4. H. Homma, D. A. Shockey, and Y. Murayama, "Response of Cracks in Structural Materials to Short Pulse Loads," *J. Mech. Phys. Solids*, 31, 261-279, 1983.
5. K. Ravi-Chandar and W. G. Knauss, "An Experimental Investigation into Dynamic Fracture: I. Crack Initiation and Arrest," *Int. J. Fract.*, 25, 247-262 (1984).
6. J. F. Kalthoff, "Fracture Behavior under High Rates of Loading," *Eng. Fract. Mech.*, 23 289-298 (1986).
7. R. C. Shah, "Fracture under Combined Modes in 4340 Steel," *ASTM STP 650*, pp. 29-52 (1974).
8. T. Kobayashi and J. W. Dally, "Dynamic Photoelastic Determination of the $\dot{\epsilon}$ -K Relation for 4340 Steel," Crack Arrest Methodology and Applications, ASTM STP 711, G. T. Hahn and M. F. Kanninen, Eds. (American Society for Testing and Materials, 1980), pp. 189-210.
9. A. J. Rosakis, J. Duffy, and L. E. Freund, "The Determination of Dynamic Fracture Toughness of AISI 4340 Steel by the Shadow Spot Method," *J. Mech. Phys. Solids*, 32, 443-460 (1984).

Appendix A

INVESTIGATION AND APPLICATION OF THE ONE-POINT-BEND IMPACT TEST

Paper appeared in Fracture Mechanics: Seventeenth Volume, ASTM STP 905, J. H. Underwood, R. Chait, C. W. Smith, D. P. Wilhelm, W. A. Andrews, and J. C. Newman, Eds., American Society for Testing and Materials, Philadelphia, 1986, pp. 307-328.

Jacques H. Giovanola¹

Investigation and Application of the One-Point-Bend Impact Test

Authorized Reprint from Special Technical Publication 905
Copyright American Society for Testing and Materials 1916 Race Street, Philadelphia, PA 19103 1986

REFERENCE: Giovanola, J. H., "Investigation and Application of the One-Point-Bend Impact Test," *Fracture Mechanics: Seventeenth Volume, ASTM STP 905*, J. H. Underwood, R. Chait, C. W. Smith, D. P. Wilhem, W. A. Andrews, and J. C. Newman, Eds., American Society for Testing and Materials, Philadelphia, 1986, pp. 307-328.

ABSTRACT: This paper investigates a dynamic fracture test that produces smoothly varying stress intensity histories of controlled amplitude and duration. A test configuration has been adopted in which a simple edge-cracked specimen is loaded in bending by impacting it at the midsection without supporting it at the outer edges. The stress intensity history is measured by a strain gage near the crack tip and has approximately a sinusoidal time dependence.

The dependence of stress intensity amplitude and duration on the impact velocity and on the specimen material and dimensions has been determined both analytically and experimentally. The limit on the specimen aspect ratio to obtain a smooth stress intensity history controlled only by the first mode of vibration of the specimen has also been established. Stress intensity pulses of durations varying between 90 and 500 μs can be readily achieved, and the maximum amplitude can be independently adjusted over an order of magnitude (20 to 200 MPa $\text{m}^{1/2}$).

The new experimental procedure has been used to measure the dynamic fracture toughness of 4340 steel (HRC 50) at three loading rates. Comparison of the dynamic results with the value of the static toughness indicates little strain-rate sensitivity of the fracture toughness of 4340 steel in the range of loading rates investigated (quasi-static to 3×10^6 MPa $\text{m}^{-2} \text{s}^{-1}$).

KEY WORDS: dynamic fracture, stress intensity history, impact bend test, unsupported bend specimen, dynamic fracture toughness, 4340 steel, rate sensitivity

Nomenclature

- a* Crack length
- a* Crack velocity
- B* Specimen thickness
- C_{CR}* Elastic compliance of bend specimen due to crack

¹Research Engineer, Department of Metallurgy and Fracture Mechanics, SRI International, Menlo Park, CA 94025.

C_{UN}	Elastic compliance of uncracked bend specimen
$d(x, r)$	Specimen deflection
d_{CR}^{CL}	Specimen deflection along center line due to crack
d_{UN}^{CL}	Uncracked specimen deflection along center line
E	Young's modulus
E^{KIN}	Maximum kinetic energy of specimen
E^{STR}	Maximum strain energy of specimen
$K_1(t)$	Dynamic stress intensity factor
K_{lc}	Static fracture toughness
K_{ld}	Dynamic initiation fracture toughness
K_1^{MAX}	Maximum stress intensity amplitude
m	Specimen mass
M	Hammer mass
P_H	Hammer load
P_H^{MAX}	Maximum hammer load
P_{EFF}^{MAX}	Maximum effective dynamic load on the specimen
S	Specimen length
t	Time
t^{MAX}	Time at which maximum stress intensity amplitude is reached
T_0	Duration of stress intensity history
T_1	First natural period of oscillation of specimen
T_{UN}	First natural period of oscillation of the uncracked specimen
V_H	Hammer velocity at t^{MAX}
V_{imp}	Hammer impact velocity
V_S	Velocity of the specimen center of mass at t^{MAX}
W	Specimen width
x	Coordinate along specimen axis
ρ	Mass density of specimen material
ν	Poisson's ratio

Introduction

A dynamic fracture test having an adjustable and smoothly varying load history is desirable for unambiguous determination of dynamic fracture behavior. Unfortunately, conventional tests, such as the Charpy impact test or the dynamic tear test, do not produce a smoothly varying stress intensity history. Thus interpretation of the results is not straightforward. This paper discusses a modification of the conventional impact bend test, first proposed and investigated by Kalthoff and co-workers [1-3], which produces a smoothly varying stress intensity history. The amplitude and duration of the stress intensity history are easily varied by varying the impact velocity and the specimen dimensions.

We have investigated the influence of specimen dimensions and impact velocity on the stress intensity history both analytically and experimentally. We

have then used the new test procedure to measure the dynamic fracture toughness of 4340 steel at three strain rates.

Background

Dynamic effects in impact-loaded, three-point-bend specimens (3PBS) have been discussed in several recent publications. In particular, Kalthoff and co-workers have shown that the stress intensity history results from the superposition of the specimen free oscillations on the fundamental oscillation of the hammer-specimen-support system [1,2,4-6]. Böhme [6] has proposed a semi-analytical description of the behavior of the hammer-specimen-support system to predict the influence of specimen dimensions, impact velocity, and material properties on the stress intensity history. He has further demonstrated that the dynamic effects due to the specimen oscillations can be estimated for specimens of arbitrary size and material from a set of normalized master curves. Each master curve depends only on the ratios of crack length to width, a/W , and specimen length to width, S/W .

Böhme and Kalthoff [1] have also observed that soon after impact the 3PB specimen momentarily loses contact with the supports. Therefore, during the initial phase of the test, the supports do not influence the loading, and the stress intensity history obtained for specimens impacted with or without supports is identical. The crack tip loading is then strictly achieved by inertia. Only at later times, when the specimen makes contact with the supports again, does its behavior differ from that of the unsupported specimen; the stress intensity history for the supported specimen continues to rise, whereas that for the unsupported specimen decreases to zero.

On the basis of these observations, Kalthoff and co-workers [2,3] have demonstrated that the bend specimen impacted without supports—called *one-point-bend test* (1PBT)—provides a convenient configuration to obtain controlled and smoothly varying stress intensity histories.

The test arrangement and loading mechanism for the 1PBT are illustrated in Fig. 1. Figure 2 shows the resulting stress intensity history in a specimen with a blunt notch, as measured with a strain gage placed near the notch tip. This stress intensity history is roughly sinusoidal and is characterized by the half period T_0 and the maximum amplitude K_I^{MAX} . Figure 2 also shows the corresponding hammer load. On impact, the center portion of the specimen is accelerated away from the hammer, whereas the end portions of the specimen lag behind because of inertia. This causes the specimen to bend and to load the crack tip. The specimen deflection also progressively unloads the hammer tip until the maximum deflection (and hence the maximum stress intensity) is reached. As the specimen bends back, the stress intensity decreases, whereas the hammer load increases again because the relative displacement of the hammer and of the specimen's center portion are now in opposite directions [1].

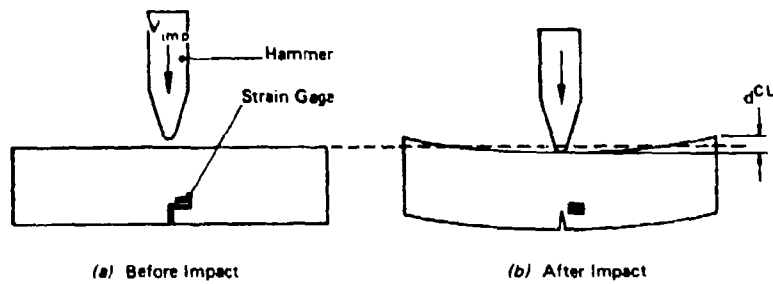


FIG. 1—Test arrangement and loading mechanism for the 1PBT.

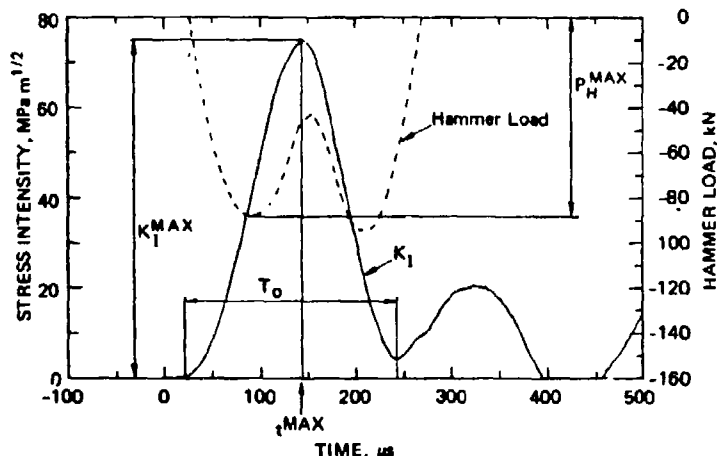


FIG. 2—Typical stress intensity and load histories obtained in 1PBT.

According to this interpretation of the stress intensity records, the first natural period of oscillation of the specimen controls the duration of the approximately sinusoidal stress intensity history. Thus the test duration can be controlled by changing the dimensions of the specimen to change the natural frequency. Furthermore, the results of Böhme [6] suggest that the maximum stress intensity amplitude is proportional to the impact velocity.

The purpose of the present investigation was to verify the foregoing predictions, to establish the range of load durations that could be achieved with the 1PBT, to determine more precisely the role of specimen dimensions and material properties on the stress intensity history, and to apply the 1PBT to dynamic fracture toughness testing.

Investigation of the Dynamic Behavior of the 1PBT

Analysis

Here we assume that the stress intensity history is sinusoidal with a period $2T_0$ equal to the first natural period of the specimen and with an amplitude K_i^{MAX} . We then determine how these two parameters depend on the specimen material and dimensions and on the impact velocity.

Details of this approximate analysis are presented in the Appendix together with references to earlier analyses. We find that T_0 and K_i^{MAX} are given by

$$T_0 = T_{\text{UN}} h_1 \left(\frac{S}{W}, \frac{a}{W}, \nu \right) = W \sqrt{\frac{\rho}{E}} h_2 \left(\frac{S}{W}, \frac{a}{W}, \nu \right) \quad (1)$$

and

$$K_i^{\text{MAX}} = V_{\text{imp}} \sqrt{W} \sqrt{\rho E} h_3 \left(\frac{S}{W}, \frac{a}{W}, \nu \right) \quad (2)$$

where T_{UN} is the first natural period of oscillation of the uncracked beam with free ends; h_1 , h_2 , and h_3 are dimensionless functions of the specimen dimensions and of Poisson's ratio; and the other symbols are as defined in the Nomenclature section of this paper. In Eq 2, it has been assumed that the hammer mass, M , is much larger than the specimen mass, m .

Equations 1 and 2 show that for geometrically similar specimens (and neglecting a mild dependence on Poisson's ratio), T_0 scales with the specimen size and with the square root of the ratio of mass density to elastic modulus; K_i^{MAX} is proportional to the impact velocity and scales with the square root of specimen size, mass density, and elastic modulus. Both T_0 and K_i^{MAX} are independent of specimen thickness and increase with crack length for given values of S , W , and V_{imp} . Equations 9 and 18 in the Appendix can be used to obtain estimates of T_0 and K_i^{MAX} . The estimates of K_i^{MAX} will only yield approximate trends, however, because two coefficients are not known precisely in Eq 18.

Experimental Verification

To verify the predictions of Eqs 1 and 2, we have tested several steel and aluminum specimens. Table 1 gives a matrix of the specimens tested and their dimensions and aspect ratios. The specimens had a blunt notch of 0.5 mm (20 mil) tip radius to prevent fracture during the tests. We measured the stress intensity history with a single element strain gage placed a small distance—3 to 5 mm (0.1 to 0.2 in.)—away from and directly above the notch tip. The gage was oriented to measure strains perpendicular to the crack. The stress

TABLE I—Specimen dimensions and material, and impact conditions for experimental investigation of IPBT.

Specimen Size Number	Materials Tested	S		W		B		a		A/W		S/W		V_{imp} (ft/s)
		mm	(in.)	mm	(in.)	mm	(in.)	mm	(in.)	mm	(in.)	mm	(in.)	
1	steel aluminum	177.8	(7)	25.4	(1)	12.7	(0.5)	7.6	(0.3)	7	0.3	5.3	117.4	
2	steel aluminum	355.6	(14)	25.4	(1)	12.7	(0.5)	7.6	(0.3)	14	0.3	5.3	117.4	
3a	steel aluminum	241.3	(9.5)	63.5	(2.5)	12.7	(0.5)	19.1	(0.75)	3.8	0.3	5.3	117.4	
3b	steel	241.3	(9.5)	63.5	(2.5)	12.7	(0.5)	25.4	(1.0)	3.8	0.4	5.3	117.4	
3c	steel	241.3	(9.5)	63.5	(2.5)	12.7	(0.5)	31.8	(1.25)	3.8	0.5	5.3	117.4	
4	steel aluminum	355.6	(14)	63.5	(2.5)	12.7	(0.5)	19.1	(0.75)	5.6	0.3	3.5, 5.3	(11.5, 17.4)	
5	steel aluminum	101.6	(4)	38.1	(1.5)	12.7	(0.5)	12.7	(0.5)	2.7	0.33	1.0 to 5.3	(3.3 to 17.4)	
6	steel	228.6	(9)	86.0	(3.5)	9.5	(0.375)	26.9	(1.06)	2.6	0.3	3.5	(11.5)	

intensity can be calculated from the strain measurement by two methods. In the first method, stress intensity and strain are related using a static calibration procedure developed by Loss [7,8]. In the second method, the elastic singularity solution [9,10] is used to relate near-crack-tip strain and stress intensity factor; a plane stress situation is assumed at the gage location. Böhme and Kalthoff have discussed the uncertainties associated with this approach [11]. By comparing K values measured simultaneously with either of the two methods, we have found that for the specimen geometries considered here, the two methods agree to within 5%. Because of its simplicity, we used the singularity solution method for the blunt notch experiments. The impact tests were performed on a standard pendulum impact machine modified to accommodate the IPBT specimen and a redesigned instrumented hammer. Figure 3 shows a schematic of the test setup. In some experiments we varied the impact velocity between 1 and 5.3 m/s by changing the drop height of the hammer. The impact velocity was measured by two pairs of light-emitting diodes/photodiodes. For each specimen and test condition, we repeated the experiment several times to check reproducibility. Figures 4 to 7 summarize the experi-

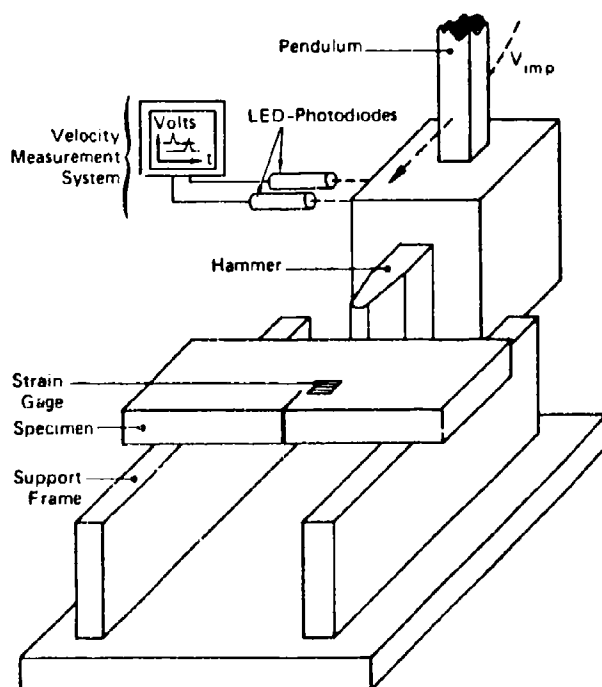


FIG. 3—Experimental setup used to perform IPBT.

mental results. They agree well with the analytical predictions (Eqs 1 and 2) and demonstrate that the interpretation of the specimen behavior in the one-point-bend test and the assumptions made in the analysis are correct.

Figure 4 represents the stress intensity history for several steel and aluminum specimens impacted at 5.3 m/s. First we observe that for specimens with high S/W values, higher modes of oscillation also significantly affect the

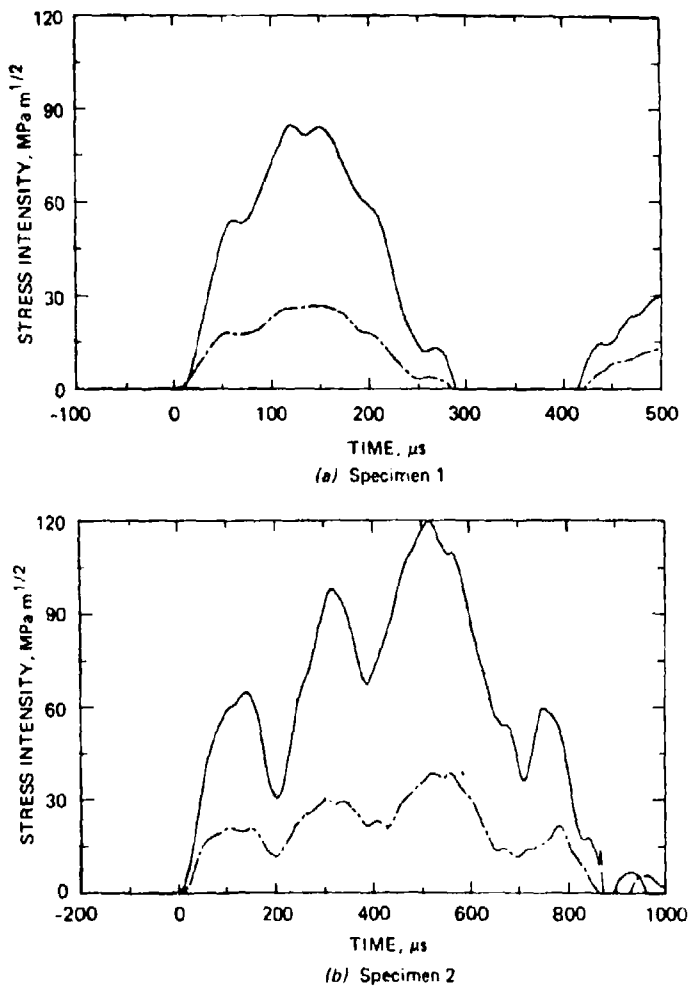


FIG. 4—Stress intensity histories obtained for six different geometries. Legend—Solid line: steel specimen; dash line: aluminum specimen. Specimen numbers refer to numbers in Table 1. $V_{imp} = 5.3 \text{ m/s}$.

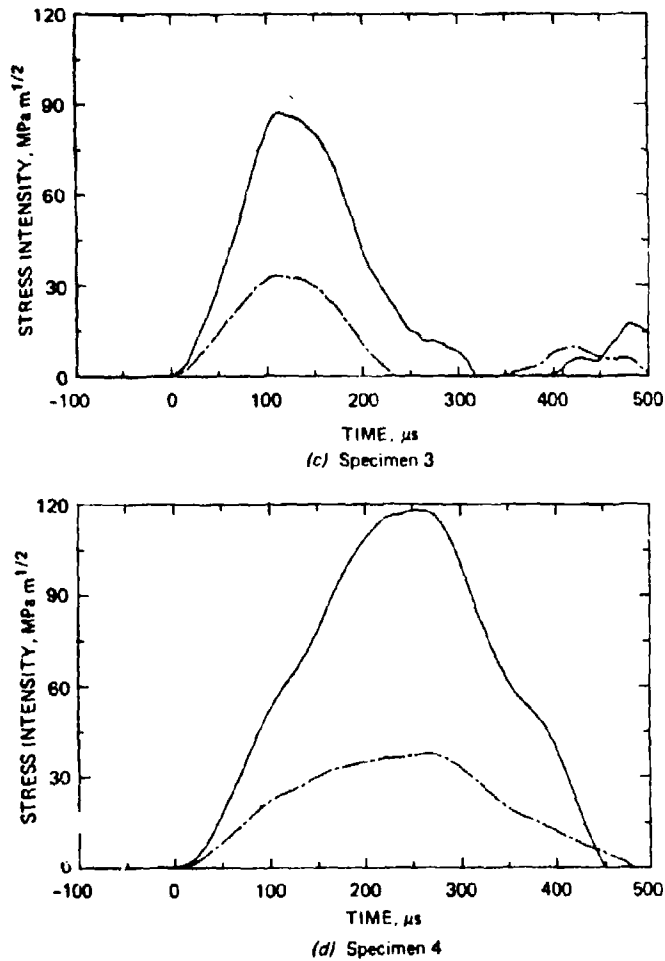


FIG. 4—(continued).

stress intensity history. Beyond a value of $S/W = 7$, the stress intensity history displays large oscillations superimposed on the fundamental oscillation (Fig. 4b). This behavior complicates the interpretation of fracture tests. Thus specimens with S/W values less than seven are preferable. (We have not investigated whether a/W ratios higher than 0.3 would suppress the higher oscillations in geometries with $S/W > 7$). By taking into account this limitation on S/W , test durations T_0 in the range of 90 to 500 μs can be readily achieved with 1PB specimens of practical size.

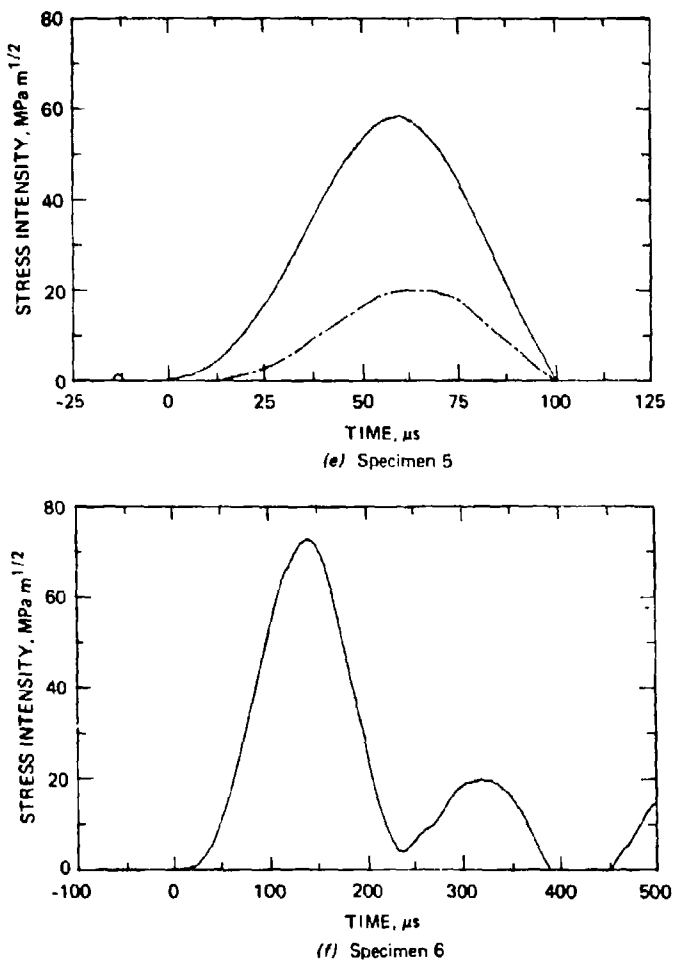


FIG. 4—(continued).

Test durations measured in Fig. 4 and predictions from Eq 9 in the Appendix are compared in Table 2. Estimates are given only for specimens for which the compliance can be evaluated with reasonable confidence from handbook tabulations. The agreement between predictions and measurements is sufficiently good to confirm that the first mode of oscillation of the specimen largely controls the test duration for specimens with $S/W < 7$. The largest error is on the order of 30%. The greatest discrepancies arise for those stress intensity histories that show marked inflections, and they may be attributable to the influence of higher mode oscillations.

TABLE 2—Comparison of predicted and measured 1PBT durations.

Specimen Size Number	Predicted Half Period ($T_1/2$, μs)	Measured Duration 1PBT (T_0 , μs)	$\frac{T_0 - 1/2 T_1}{T_0} \times 100$	S/W
1	300	284	-6.0	7.0
2	1123	854	-31.5	14.0
3a	261	304	14.3	3.8
3b	294	300	2.0	3.8
3c	345	340	-1.5	3.8
4	508	434	-17.1	5.6

Figure 4 further demonstrates that the stress intensity histories for steel and aluminum specimens are remarkably similar except for the amplitude. Again, this finding is expected from Eqs 1 and 2. Because the ratio ρ/E is about the same for steel and aluminum, specimens with the same dimensions will have the same fundamental period. Because higher oscillations are multiples of the fundamental, we anticipate that steel and aluminum specimens will have a stress intensity history with the same global shape. According to Eq 2, K_1^{MAX} values for steel and aluminum specimens of identical geometry should be approximately in the ratio of 3 to 1. The measured ratios for specimen sizes 1 to 5 in Table 1 are 3.2, 3.1, 2.6, 3.1, and 2.9 to 1, respectively.

Tests on the same specimen at several impact velocities show that K_1^{MAX} is proportional to V_{imp} , as predicted by Eq 2. This is illustrated in Fig. 5, which shows the stress intensity histories for steel specimen 4 tested at 3.5 and 5.3 m/s, plotted after scaling with the impact velocity.

The effect of geometrical scaling is represented in Fig. 6. The stress inten-

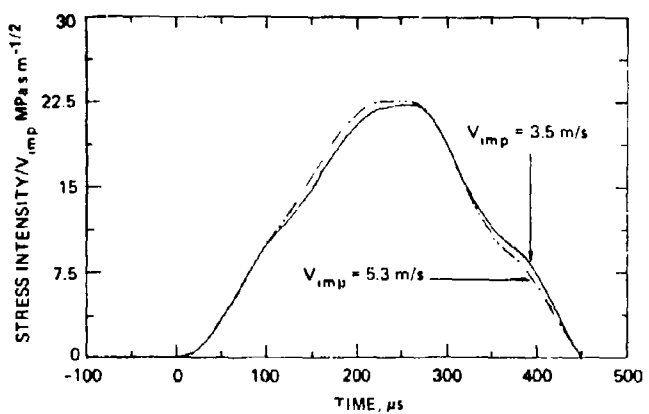


FIG. 5—Normalized stress intensity histories for specimen 4 impacted at 3.5 and 5.3 m/s.

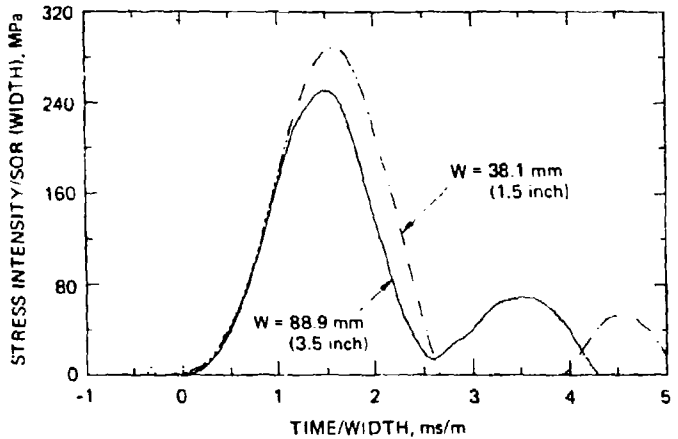


FIG. 6—Normalized stress intensity histories for two geometrically similar specimens of different sizes.

sity divided by the square root of the specimen width has been plotted as a function of time divided by the specimen width for two similar specimens (5 and 6). The agreement of the two curves is relatively good considering that the scaling of the in-plane dimensions, in particular of the crack length, was not exact (see Table 1).

Figure 7 shows the influence of increasing the crack length on the stress intensity history when all other dimensions are kept constant. Both $T_0/2$ and

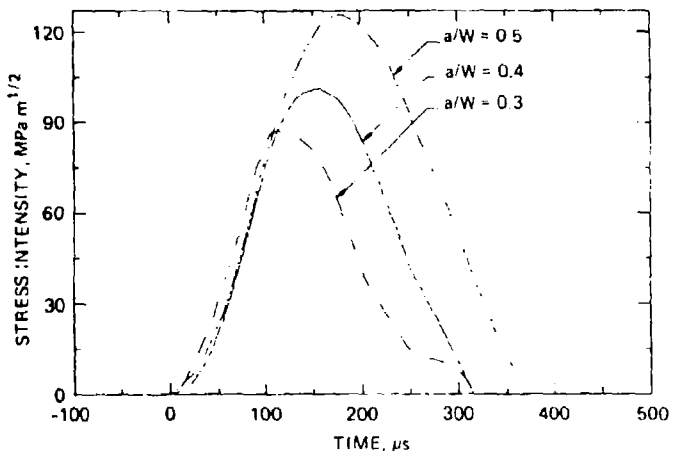


FIG. 7—Stress intensity histories for specimen 3 with three different crack lengths.

K_I^{MAX} increase with crack length as predicted by the analysis. Note, however, that the initial portion of the stress intensity histories is the same for all three crack lengths. This result occurs because in the early part of the loading, the dynamic stress intensity factor depends on time and not on crack length. Only after elastic waves have traversed the crack length several times does the stress intensity become proportional to the square root of crack length [12,13].

Finally, multiple tests on the same specimen at the same impact velocity have demonstrated that the stress intensity histories are quite reproducible for large specimens (less than 6% deviation on K_I^{MAX}). For small specimens, the scatter increases somewhat (15% deviation on K_I^{MAX}), presumably because small specimens are more sensitive to misalignment errors.

Dynamic Fracture Tests

As part of an investigation of dynamic crack instability criteria, we have used the 1PBT to determine the dynamic fracture toughness of commercial aircraft-quality 4340 steel at three different strain rates. Specimens corresponding to sizes 3 and 4 in Table 1 were cut from 63.5 by 12.7 mm (2.5 by 0.5 in.) bars, and quenched and tempered to a Rockwell C hardness of 50. The specimens were notched, fatigue precracked in accordance with ASTM Standard Test Method for Plane-Strain Fracture Toughness of Metallic Materials (E 399), and instrumented with a strain gage.

Six tests were performed at each of three impact velocities—3.5, 5.3, and 50 m/s (11.5, 17.4, and 164 ft/s)—to achieve stress intensity rates of 3.3×10^5 , 5×10^5 , and 3×10^6 MPa $\text{m}^{1/2} \text{s}^{-1}$ (3.0×10^5 , 4.6×10^5 , and 2.7×10^6 ksi $\text{in.}^{1/2} \text{s}^{-1}$). The experiments at impact velocities of 3.5 and 5.3 m/s were performed on the modified pendulum tester with specimens of size 4 with $a/W = 0.3$ and 0.38, respectively. To achieve the 50 m/s impact velocity, we resorted to a compressed air launcher to accelerate a steel hammer plate. The test arrangement remained otherwise the same as for the experiments on the pendulum tester. The high-impact-velocity specimens were of size 3. For comparison, we also measured the static fracture toughness in triplicate following the standard procedure in ASTM E 399.

For the dynamic fracture tests, we obtained the stress intensity from the strain measurements using the static calibration method. The dynamic initiation fracture toughness, $K_{I\text{d}}$, was determined from the experimental stress intensity history as the stress intensity value at the point where crack extension is first noticeable on the record. Crack extension manifests itself by either a clear drop in the measured strain or by a gradual deviation from an essentially linearly rising stress intensity curve.

Figures 8 to 10 show typical stress intensity histories measured at the three loading rates, together with the point of crack initiation. The curves in Figs. 8 to 10 represent the true stress intensity history only up to the point of crack initiation, because once the crack propagates the stress intensity is no longer

directly proportional to the recorded strain. Figure 8 shows that for the tests at $3.3 \times 10^5 \text{ MPa m}^{1/2} \text{ s}^{-1}$, the crack started to propagate and then arrested after extending 2 to 5 mm (0.1 to 0.2 in.). At the higher rates, the specimens fractured completely.

At low impact velocities, crack initiation causes a clear drop in the measured strain, and the point at which K_{Ic} is evaluated can therefore be easily determined (Fig. 8). At the highest impact velocity, the strain record has a smoother appearance; thus the point of crack initiation was chosen as the point of separation of the recorded strain history from a straight line fitted to the main portion of this curve (Fig. 9). For the intermediate impact velocity, some test records showed a significant departure from linearity before a sharp drop in strain; others only showed a rapid drop in strain. Therefore, for the intermediate impact velocity, either one or the other definition of the point of crack initiation was used, as appropriate for the particular test record (Fig. 10).

The results of the static and dynamic fracture experiments are summarized in Fig. 11. Although the scatter in data increases with loading rate, the average value of the dynamic fracture toughness K_{Id} , $58.5 \text{ MPa m}^{1/2}$ ($53.5 \text{ ksi in.}^{1/2}$), is essentially the same for the three rates, and it is only slightly lower than the static K_{Ic} value, $63.7 \text{ MPa m}^{1/2}$ ($58 \text{ ksi in.}^{1/2}$).

Discussion

Results of the Fracture Tests

The dynamic fracture toughness measurements reported here demonstrate that in the relatively narrow range of strain rates 3.3×10^5 to $3.0 \times 10^6 \text{ MPa}$

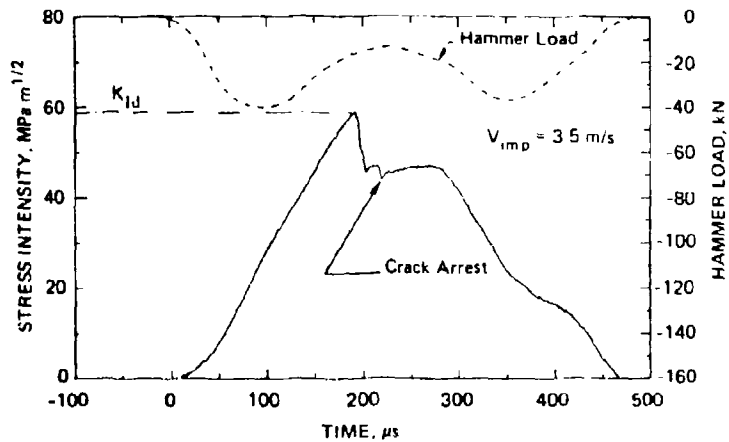


FIG. 8—Stress intensity and hammer load histories for fracture test at low stress intensity rate.

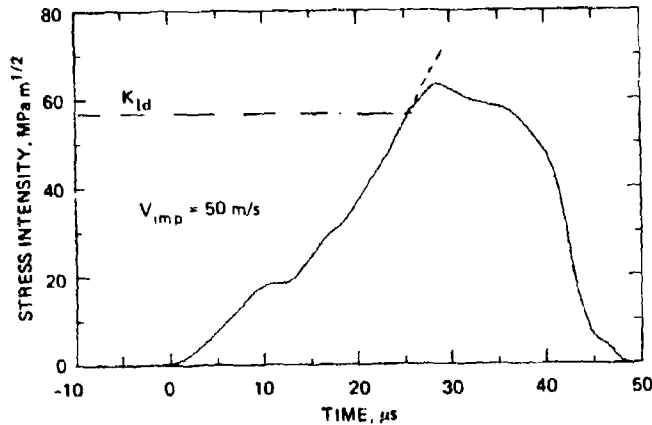


FIG. 9—Stress intensity history for fracture test at high stress intensity rate.

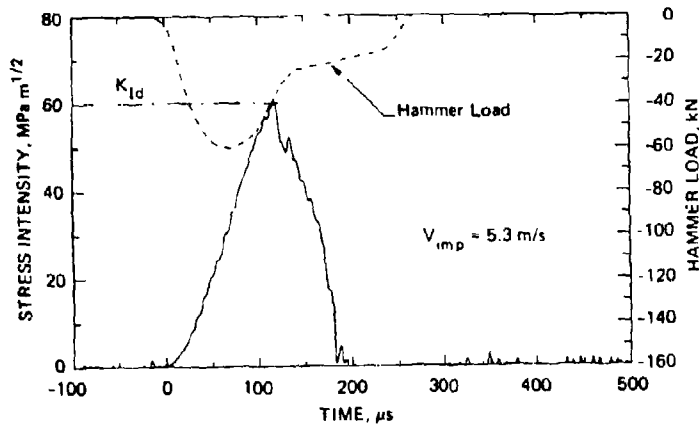


FIG. 10—Stress intensity and hammer load histories for fracture test at intermediate stress intensity rate.

$\text{m}^{1/2} \text{s}^{-1}$ (3×10^5 to 2.7×10^6 ksi in. $^{1/2}$ s $^{-1}$), K_{Id} for 4340 steel HRC 50 is not sensitive to changes in loading rate. Furthermore, comparison of the dynamic fracture toughness value $58.5 \text{ MPa m}^{1/2}$ (53.3 ksi in. $^{1/2}$) with the static fracture toughness value $63.7 \text{ MPa m}^{1/2}$ (58.0 ksi in. $^{1/2}$) shows that the overall strain-rate sensitivity of the fracture toughness is only mild. If it is assumed that the strain-rate sensitivity of the fracture toughness is a consequence of the strain-rate sensitivity of the flow stress, then our results are consistent

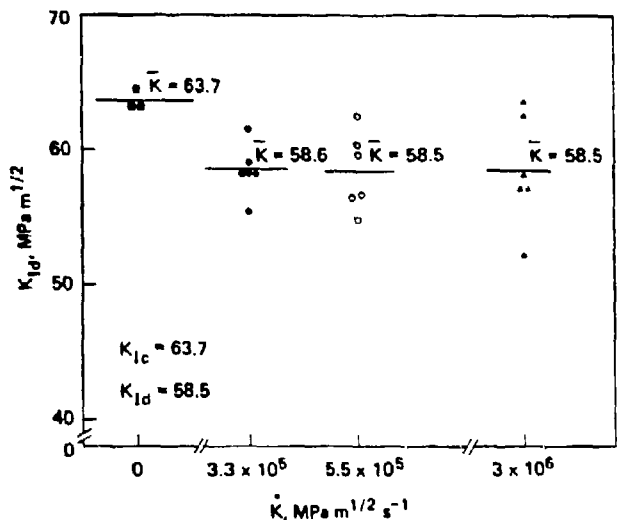


FIG. 11.—Summary of fracture test results for four stress intensity rates.

with dynamic flow stress data for 4340 steel [14,15]. These data, obtained for lower hardnesses (HRC 40 and HRC 30), indicate little strain-rate sensitivity for the flow stress over a range of strain rates from 10^{-4} s^{-1} to 10^4 s^{-1} .

However, our results contradict the dynamic fracture data of Homma et al [16,17] for nominally the same material and for comparable loading rates. Homma et al [16,17] report a K_{I_d} value of $31.7 \text{ MPa m}^{1/2}$, more than 30% lower than the static toughness. This discrepancy may reflect differences in microfailure modes. Homma et al [16] observed a transition from fully dimple fracture at low strain rates to a mixture of dimples and cleavage facets at high strain rates. Scanning electron microscope (SEM) observations did not reveal a change in microfracture mode in our experiments. Under both static and dynamic conditions, fracture occurred by what appears a mixture of dimple, intergranular, and transgranular failures.

The difference between the results of Homma et al and the present results may also be due to a difference in the definition of the point of crack initiation. Homma et al measure K_{I_d} after 20 to $50 \mu\text{m}$ of crack extension, whereas the K_{I_d} value we report probably corresponds to 200 to $500 \mu\text{m}$ of crack extension.

Significance of the 1PBT

The present investigation has confirmed the suggestion by Kalthoff et al [2,3] that the 1PBT provides an attractive test configuration for dynamic frac-

ture experiments. It produces a smoothly varying stress intensity history that can be easily characterized in a calibration experiment. Furthermore, the loading rate and the pulse amplitude and duration can be readily adjusted over an order of magnitude range for each parameter. The analytical and experimental results given in this paper provide the information necessary to choose the appropriate combination of specimen dimensions and impact velocity to achieve desired test conditions.

The results for the 1PBT expressed in Eqs 1 and 2 also supplement the results obtained for the impacted 3PBT reported by Böhme [6]. They provide an independent analysis of the free specimen oscillations that were shown to play an important role in the impacted 3PBT, and they yield the same conclusion regarding the representation of these dynamic effects by master curves that depend only on specimen aspect ratios.

The maximum stress intensity amplitude that can be obtained in a 1PBT using a conventional pendulum impact tester is rather low, particularly in experiments with lighter alloys such as aluminum or titanium alloys. For these materials, devices capable of higher impact velocities are required. This problem may also be circumvented by attaching ballast plates to the specimen extremities. The high-strain-rate fracture experiments also showed that the point of crack initiation is not always clearly defined on the records of strain as a function of time. Further study of this problem is desirable to obtain an unambiguous definition of the point of dynamic crack initiation.

An interesting aspect of the 1PBT was brought to light by the fracture experiments in which crack arrest occurred. They indicated that the one-point-bend test could provide a convenient experimental procedure to study not only dynamic crack initiation but also crack propagation and arrest. The advantage of the one-point-bend test for crack propagation investigations would be that because of the inertial loading, the driving force on the running crack tip and the crack velocity could be easily controlled by changing the impact velocity. Further, because of its very simple boundary conditions, the one-point-bend test should be much easier to simulate in numerical calculations than the conventional wedge-loaded compact tension crack arrest test configuration.

Summary and Conclusions

The stress intensity history obtained by impacting an unsupported, cracked, bend specimen has been investigated. A combination of experiments and analysis was used to establish the influence of specimen material and dimensions and impact velocity on the maximum stress intensity amplitude and the test duration. Stress intensity pulses of durations varying between 90 and 500 μ s can be readily achieved. For steel, maximum amplitudes exceeding 100 MPa $m^{1/2}$ have been produced with a pendulum impact tester.

The applicability of the test procedure has been illustrated by measuring the dynamic fracture toughness of 4340 steel (HRC 50) at three different

strain rates. The tests indicated little strain-rate sensitivity for the fracture toughness of this material.

Finally, it is suggested that the one-point-bend test could also conveniently serve to investigate dynamic crack propagation and arrest.

Acknowledgments

This work was supported by the Air Force Office of Scientific Research under Contract AFOSR/F49620-81-K-0007 and was monitored by Dr. Alan H. Rosenstein. The author would like to thank Drs. J. F. Kalthoff, and W. Böhme, Fraunhofer Institut für Werkstoffmechanik, Freiburg, West Germany, for suggesting the use of the one-point-bend test and for supplying preliminary information about the test. Many helpful discussions during the course of this study with Dr. D. A. Shockley are also gratefully acknowledged.

APPENDIX

Over the years several authors have presented analyses of the impacted-bend specimen to help in evaluating dynamic fracture experiments [6,18-22]. Here we present simple derivations to obtain the test duration T_0 and the maximum stress intensity amplitude K_I^{MAX} for the 1PBT. The resulting expressions are to be considered more as a dimensional analysis than as precise quantitative predictions.

Estimation of the Duration T_0

To evaluate the test duration T_0 , we assume that it is equal to one half the fundamental period of oscillation T_1 of the cracked beam. Ireland has previously proposed an empirical formula to estimate the period of inertial oscillation in the impacted 3PBT [21]. We estimate T_1 using Rayleigh's method. To do so, we assume for the deflection d of the beam the following function of position x along the axis:

$$d(x) = d_{\text{UN}}^{\text{CL}} \sin\left(\frac{\pi}{S}x\right) + 2 \frac{x}{S} d_{\text{CR}}^{\text{CL}}; \quad 0 < x < \frac{S}{2} \quad (3)$$

The first term on the right of Eq 3 represents the center line deflection of the un-cracked beam, and the second term represents an estimate of the deflection due to the crack.

Next we express $d_{\text{UN}}^{\text{CL}}$ and $d_{\text{CR}}^{\text{CL}}$ in terms of the respective elastic compliances C_{UN} and C_{CR} , and of an effective dynamic load amplitude $P_{\text{MAX}}^{\text{EFF}}$, where $P_{\text{MAX}}^{\text{EFF}}$ can be regarded as the maximum hammer load corrected to account for the inertia forces in the sense of the analysis reported in Refs 19 and 20. Thus

$$d_{\text{UN}}^{\text{CL}} = C_{\text{UN}} P_{\text{MAX}}^{\text{EFF}} \quad \text{and} \quad d_{\text{CR}}^{\text{CL}} = C_{\text{CR}} P_{\text{MAX}}^{\text{EFF}} \quad (4)$$

The beam deflection at any point x and time t is given by

$$d(x,t) = \left[C_{\text{UN}} \sin\left(\frac{\pi}{S}x\right) + C_{\text{CR}} \frac{2x}{S} \right] P_{\text{MAX}}^{\text{EFF}} \sin\left(\frac{2\pi}{T_1}t\right); \quad 0 < x < \frac{S}{2} \quad (5)$$

Using Eq 5, we calculate the maximum kinetic energy of the specimen

$$E_{\text{MAX}}^{\text{KIN}} = \rho B W (P_{\text{MAX}}^{\text{EFF}})^2 \left(\frac{2\pi}{T_1} \right)^2 \left[C_{\text{UN}}^2 \frac{S}{4} + \frac{4S}{\pi^2} C_{\text{UN}} C_{\text{CR}} + \frac{S}{6} C_{\text{CR}}^2 \right] \quad (6)$$

The maximum strain energy is simply

$$E_{\text{MAX}}^{\text{STR}} = \frac{1}{2} (P_{\text{MAX}}^{\text{EFF}})^2 (C_{\text{UN}} + C_{\text{CR}}) \quad (7)$$

Equating kinetic energy and strain energy yields

$$T_1 = 2\pi \sqrt{2\rho B W \frac{\left(\frac{C_{\text{UN}}^2}{4} + \frac{4C_{\text{UN}} C_{\text{CR}}}{\pi^2} + \frac{C_{\text{CR}}^2}{6} \right)}{(C_{\text{CR}} + C_{\text{UN}})}} \quad (8)$$

Substituting

$$C_{\text{UN}} = \frac{S^3}{4EBW^3} \left[1 + 3(1 + \nu) \left(\frac{W}{S} \right)^2 \right]$$

and rearranging yields

$$T_1 = T_{\text{UN}} \sqrt{\frac{\pi^4}{24}} \sqrt{\frac{\frac{1}{4} + \frac{4}{\pi^2} \beta + \frac{1}{6} \beta^2}{(1 + \beta)}} \sqrt{1 + 3(1 + \nu) \left(\frac{W}{S} \right)^2} \quad (9)$$

where $\beta = C_{\text{CR}}/C_{\text{UN}}$ and $T_{\text{UN}} = (4S^2/\pi W)\sqrt{3\rho/E}$ is the fundamental period of the uncracked beam.

The dependence of T_1 on specimen dimensions and material properties given by Eq 9 is the same as the dependence anticipated from Ireland's formula [27].

Estimation of the Maximum Amplitude K_1^{MAX}

To estimate the maximum stress intensity amplitude, we express it as

$$K_1^{\text{MAX}} = \frac{3}{2} \frac{S\sqrt{\pi a}}{BW^2} F(a/W) P_{\text{MAX}}^{\text{EFF}} \quad (10)$$

where $F(a/W)$ is the handbook-tabulated stress intensity calibration appropriate for the given S/W ratio [23]. We then proceed to express $P_{\text{MAX}}^{\text{EFF}}$ using Newton's law and conservation of momentum and energy.

At every instant t , the force P_H on the hammer is given by

$$P_H(t) = P_H^{\text{MAX}} g \left(\frac{t}{T_1} \right) \quad (11)$$

where P_H^{MAX} is defined in Fig. 2 and $g(t/T_1)$ is a nondimensional function that can be obtained experimentally.

Integration of Newton's law for the hammer from the initial time of impact $t = 0$ to the time t_{MAX} at which the specimen deflection, and hence the stress intensity, is maximum gives

$$\int_0^{t_{\text{MAX}}} P_{\text{H}}^{\text{MAX}} g\left(\frac{t}{T_1}\right) dt = T_1 P_{\text{H}}^{\text{MAX}} \left[G\left(\frac{t_{\text{MAX}}}{T_1}\right) - G(0) \right] = T_1 P_{\text{H}}^{\text{MAX}} \alpha = M(V_{\text{imp}} - V_{\text{H}}) \quad (12)$$

where M is the hammer mass, V_{imp} is the initial impact velocity, V_{H} is the residual hammer velocity at time t_{MAX} , and α is a coefficient resulting from the integration of $g(t/T_1)$. Considering the approximately sinusoidal shape of the hammer load in Fig. 2 (period $\approx T_0 \approx T_1/2$), we see that α is on the order of $1/2\pi \approx 0.15$.

From Eq 12 we obtain

$$V_{\text{H}} = V_{\text{imp}} - \frac{\alpha T_1 P_{\text{H}}^{\text{MAX}}}{M} \quad (13)$$

Application of momentum conservation to the hammer-specimen system, with substitution of Eq 13 for V_{H} , yields

$$V_s = \frac{\alpha T_1 P_{\text{H}}^{\text{MAX}}}{m} \quad (14)$$

where m is the specimen mass and V_s is the velocity of the center of mass of the specimen, which at t_{MAX} is also the uniform velocity of the whole specimen.

Finally, the energy conservation equation can be written

$$\frac{1}{2} V_{\text{imp}}^2 M = \frac{1}{2} V_{\text{H}}^2 M + \frac{1}{2} m V_s^2 + \frac{1}{2} (P_{\text{MAX}}^{\text{EFF}})^2 (C_{\text{UN}} + C_{\text{CR}}) \quad (15)$$

where the last term of the right-hand side represents the strain energy. $P_{\text{MAX}}^{\text{EFF}}$, C_{UN} , and C_{CR} have been defined above.

We now write $P_{\text{MAX}}^{\text{EFF}}$ as a multiple of $P_{\text{H}}^{\text{MAX}}$:

$$P_{\text{MAX}}^{\text{EFF}} = \frac{1}{\lambda} P_{\text{H}}^{\text{MAX}} \quad (16)$$

The results of Ref 20 indicate that $1/\lambda$ should be between 0 and 1.

By substitution of Eqs 13, 14, and 16 in Eq 15 we obtain

$$P_{\text{MAX}}^{\text{EFF}} = 2V_{\text{imp}} T_1 \alpha \left[\frac{1}{\lambda T_1^2 \alpha^2 \frac{1}{M} + \frac{1}{m} + \frac{1}{\lambda} (C_{\text{UN}} + C_{\text{CR}})} \right] \quad (17)$$

Finally, combining Eqs 9, 10, and 17, we obtain

$$K_I^{\text{MAX}} = V_{\text{imp}} \sqrt{\pi a} \sqrt{12\rho E} \frac{3\alpha}{\pi^2} F(a/w) \left(\frac{S}{W}\right)^3 \sqrt{1 + 3(1 + \nu) \left(\frac{W}{S}\right)^2} L(\beta) \\ \times \frac{1}{\frac{1}{M} EB(C_{\text{UN}} + C_{\text{CR}}) + \lambda\alpha^2 \left[1 + \frac{m}{M} \left| \frac{12}{\pi^4} L^2(\beta) \left(\frac{S}{W}\right)^3 \left[1 + 3(1 + \nu) \left(\frac{W}{S}\right)^2\right] \right|\right]} \quad (18)$$

where

$$L(\beta) = \sqrt{\frac{\pi^4}{24} \left(\frac{1/4 + 4/\pi^2\beta + 1/6\beta^2}{1 + \beta} \right)}$$

Equations 9 and 18 are the expanded versions of Eqs 1 and 2. The assumption $T_0 = T_i/2$ has been made in writing Eq 1.

References

- [1] Bohme, W. and Kalthoff, J. F., *International Journal of Fracture*, Vol. 20, No. 1, 1982, pp. 139-143.
- [2] Kalthoff, J. F., Winkler, S., Bohme, W., and Shockley, D. A. in *Proceedings, International Conference on the Dynamical Properties and Fracture Dynamics of Engineering Materials*, Brno, Czechoslovakia, June 1983.
- [3] Kalthoff, J. F., Bohme, W., and Winkler, S., "Verfahren zum Bestimmen mechanischer Werkstoffkennwerte und Vorrichtung zur Durchföhrung des Verfahrens," Patent Disclosure Deutsches Patentamt, June 1983.
- [4] Kalthoff, J. F., Winkler, S., and Beinert, J., *International Journal of Fracture*, Vol. 13, No. 4, Aug. 1977, pp. 528-531.
- [5] Kalthoff, J. F., Winkler, S., Klemm, W., and Beinert, J., in *Instrumented Impact Tests*, Proceedings of 5th International Conference on Structural Mechanics in Reactor Technology, Berlin, Vol. G (4/5), North-Holland, Amsterdam, 1979.
- [6] Bohme, W., "Eine Einfache Methode zur Bestimmung der dynamischen Risspitzenbeanspruchung bei Schlagbelasteten Dreipunktbiegeproben," FhG Report Z 2/84, Fraunhofer-Institut für Werkstoffmechanik, Freiburg, W. Germany, March 1984.
- [7] Loss, J. F., Hawthorne, J. R., and Griffis, C. A., "Fracture Toughness of Light Water Reactor Pressure Vessel Materials," Naval Research Laboratory Memorandum Report 3036, Washington, D.C., April 1975.
- [8] Loss, J. F., paper presented to Third Water Reactor Safety Research Information Meeting, Oct. 1975.
- [9] Sneddon, I. N., *Proceedings of the Physical Society, London*, Vol. 187, 1946, pp. 229-260.
- [10] Williams, M. L., *Journal of Applied Mechanics*, Vol. 24, 1957, pp. 109-114.
- [11] Bohme, W. and Kalthoff, J. F., "Der Einfluss der Probengroße auf dynamische Effekte bei der K_{Ic} -Bestimmung in Kerbschlagbiegetest," FhG Report W 3/83, Fraunhofer-Institut für Werkstoffmechanik, Freiburg, W. Germany, 1983.
- [12] Freund, L. B., *Journal of the Mechanics and Physics of Solids*, Vol. 21, 1973, pp. 47-61.
- [13] Shockley, D. A., Kalthoff, J. F., and Erlich, D. C., *International Journal of Fracture*, Vol. 22, 1983, pp. 217-229.
- [14] Duffy, J., Brown University, Providence, R.I., private communication, 1983.
- [15] Chariagnac, P. F., "Analysis of the SRI Symmetric Taylor Test Data on 4340 Steels," SRI International Internal Report, Menlo Park, Calif., 1983.

328 FRACTURE MECHANICS: SEVENTEENTH VOLUME

- [16] Homma, H., Shockey, D. A., and Murayama, Y., *Journal of the Mechanics and Physics of Solids*, Vol. 31, No. 3, 1983, pp. 261-279.
- [17] Homma, H., Shockey, D. A., and Hada, S., this publication, pp. 683-696.
- [18] Nash, G. E., *International Journal of Fracture Mechanics*, Vol. 5, No. 4, 1969, pp. 269-286.
- [19] Radon, J. C. and Turner, C. E., *Engineering Fracture Mechanics*, Vol. 1, No. 3, 1969, pp. 411-428.
- [20] Turner, C. E. in *Impact Testing of Metals*, ASTM STP 466, American Society for Testing and Materials, Philadelphia, 1970, pp. 93-114.
- [21] Ireland, D. R. in *Proceedings, International Conference on Dynamic Fracture Toughness*, London, England, July 1976.
- [22] Gudmundson, P., *Journal of the Mechanics and Physics of Solids*, Vol. 31, No. 4, 1983, pp. 329-345.
- [23] Tada, H., Paris, P. C., and Irwin, G. R., *The Stress Analysis of Cracks Handbook*, Del Research Corp., Hellertown, Pa., 1973.

Appendix B

ONE-POINT-BEND TEST

Article appeared in Metals Handbook Ninth Edition, Volume 8,
Mechanical Testing, American Society for Metals, Metals Park,
Ohio, 1985, pp. 271-275.

One-Point Bend Test

By Jacques Henri Joseph Giovanola
Research Engineer
SRI International

INVESTIGATIONS of the dynamic behavior of the impacted three-point bend specimen have shown that immediately after impact by the hammer, the ends of the specimen lose contact with the supports (Ref 71). Consequently, the initial part of the response curve discussed in the preceding section is strictly the result of inertial loading, without contribution from the reactions at the supports. Therefore, if high impact velocities are applied to achieve high loading rates and short times-to-fracture, it becomes unnecessary to support the bend specimen during impact, and a so-called one-point bend test can be performed (Ref 72-74).

The one-point bend test allows reliable toughness data to be obtained at loading rates one to two orders of magnitude higher than the maximum loading rate considered in ASTM E 399 for fracture tests (Ref 1). Several tests performed with different specimen sizes and impact velocities on high-strength 4340 steel have demonstrated the usefulness of the one-point bend test and have provided dynamic fracture toughness values in good agreement with values obtained with more complicated tests.

Test Principle

The one-point bend test uses a single-edge cracked specimen and the same testing arrangement as a conventional three-point bend test, except that the end supports are removed. The procedure is illustrated in Fig. 13. When the hammer strikes the specimen, the center portion of the specimen is accelerated away from the hammer; the end portions

of the specimen lag behind by an amount d^{CL} because of inertia. This causes the specimen to bend and to load the crack tip.

A typical stress-intensity history resulting from such inertial loading is shown in Fig. 14. The impact conditions for the test were such that no crack extension occurred. The stress-intensity history is approximately sinusoidal; it increases monotonically up to the maximum amplitude and then decreases monotonically. Later oscillations in the stress-intensity history are of much smaller amplitude. For comparison, the hammer load is also shown in Fig. 14. It is apparent that there is no direct relationship between the hammer load history and the crack tip stress-intensity history in the one-point bend test.

The stress-intensity history obtained in the one-point bend test depends only on the impact velocity and on the specimen geometry, size, and material. It is independent of the fracture properties of the material tested. Therefore, the concepts of response curve and time-to-fracture described earlier in this article can also be applied to the one-point bend test when used for dynamic fracture toughness measurements in the small-scale yielding regime.

As described previously, dynamic fracture measurements involve two steps: determination of the response curve, i.e., the stress-intensity history, for a given specimen geometry and class of material and measurement of the time-to-fracture with a fatigue pre-cracked specimen. The dynamic fracture toughness is then evaluated using Eq 23.

Alternatively, the stress-intensity history and the stress-intensity level at which crack

where r and θ are the polar coordinates of the center of the strain gage with origin at the crack tip, and E and ν are Young's modulus and Poisson's ratio, respectively. Both methods work equally well if the strain gage is positioned properly. This aspect is discussed in a subsequent section.

Dependence of Stress-Intensity History on Test Parameters. As illustrated in Fig. 14, the stress-intensity history is characterized by the duration of loading, T_o , and the maximum stress-intensity amplitude, K_I^{\max} . It has been shown (Ref 74) that T_o and K_I^{\max} can be expressed as:

$$T_o = W \sqrt{\frac{\rho}{E}} h_1 \left(\frac{L}{W}, \frac{a}{W}, \nu \right) \quad (\text{Eq } 26)$$

$$K_I^{\max} = V_{\text{imp}} \sqrt{W} \sqrt{\rho E} h_2 \left(\frac{L}{W}, \frac{a}{W}, \nu \right) \quad (\text{Eq } 27)$$

where W , L , and a are the width, length, and crack depth of the specimen, respectively; ρ , E , and ν are the mass density, Young's modulus, and Poisson's ratio, respectively; V_{imp} is the impact velocity; and h_1 and h_2 are non-dimensional functions.

Equations 26 and 27 have been verified experimentally (Ref 74) and provide the scaling rules for the one-point bend test stress-intensity history. Given the stress-intensity history for one material, one specimen size and geometry, and one impact velocity, Eq 26 and 27 allow construction of the stress-intensity history for any material, impact velocity, and specimen size as long as geometrical similarity of the specimen is preserved. In particular, for given specimen dimensions and material, the one-point bend test stress-intensity history is proportional to the impact velocity and is independent of specimen thickness. For a specimen and impact velocity, it can further be shown that both K_I^{\max} and T_o increase with an increase in crack length.

The experimental one-point bend test stress-intensity histories for several specimen geometries, normalized according to Eq 26 and 27, are shown in Fig. 15 and 16. These curves were obtained from steel specimens with blunt notches. Figure 15 illustrates the effect of changing the length-over-width ratio. Figure 16 presents the normalized stress-intensity curves for a specimen with the standard ASTM E 399 (Ref 1) proportions ($L/W = 4.2$) and for four ratios of crack length to specimen width ($a/W = 0.3, 0.4, 0.5$, and 0.6).

Advantages and Limitations

The primary advantage of the one-point bend test is that the measured stress-intensity

initiation occurs can be measured for each specimen by measuring the crack tip strain intensification with a calibrated strain gage placed near the crack tip. The measured strain histories can be related to the stress-intensity histories by two methods. In the first method, the strain gage signal is calibrated against a known applied stress intensity in a static three-point bend experiment. It is then assumed that the static calibration also applies in the dynamic case. In the second

method, the strain history $\epsilon_s(t)$ is related directly to the stress-intensity history by means of the elastic singularity solution. The stress intensity is then given by:

$$K_I(t) = \frac{\epsilon_s(t) E \sqrt{2\pi r}}{\cos \frac{\theta}{2} \left[1 + \sin \frac{\theta}{2} \sin \frac{3\theta}{2} - \nu \left(1 - \sin \frac{\theta}{2} \sin \frac{3\theta}{2} \right) \right]} \quad (\text{Eq } 25)$$

Fig. 15 Normalized stress-intensity histories for two specimens with different L/W ratios

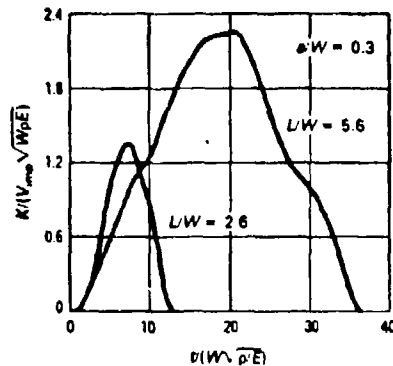


Fig. 16 Normalized stress-intensity histories for ASTM standard bend specimen with four different crack lengths

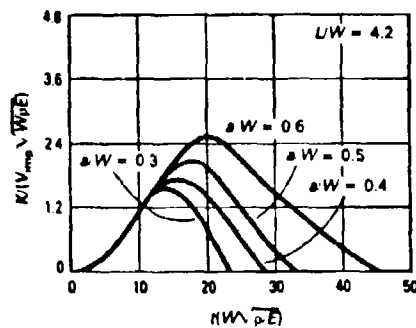


Fig. 13 Test arrangement and loading mechanism for the one-point bend test

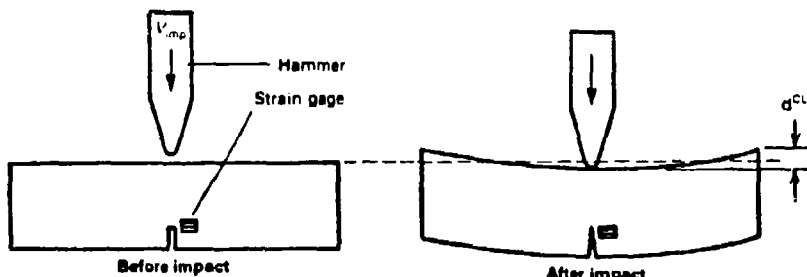
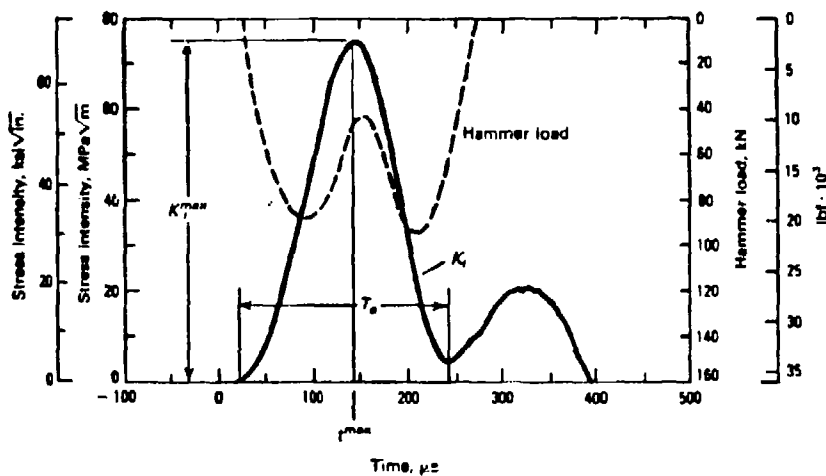


Fig. 14 Typical stress-intensity and load histories obtained in the one-point bend test



history incorporates dynamic effects completely. Therefore, no limits need to be imposed on the impact velocity and the test duration to fracture.

Combined use of the one-point bend test and the impact response curve concept produces a simple, smoothly varying response curve. For a given specimen geometry, the response curve must be measured experimentally only once. It can then be extended to other specimen sizes (of same aspect ratios), impact velocities, and materials by using the scaling rules of Eq 26 and 27.

Another advantage of the one-point bend test is that the test duration, T_0 , and the stress intensification rate can be varied over an order of magnitude range (80 to 800 μ s and 3×10^5 to 3×10^6 $\text{MPa}\sqrt{\text{m}} \cdot \text{s}^{-1}$, or 2.7×10^5 to 2.7×10^6 $\text{ksi}\sqrt{\text{in.}} \cdot \text{s}^{-1}$) by changing the specimen geometry and the impact velocity. Because loading occurs by inertia only, the one-point bend test response curve is insensitive to the characteristics of

274/High Strain Rate Testing

the loading machine, provided the hammer mass is much larger than the specimen mass.

When measurement of the stress-intensity history is direct, the test procedure to obtain dynamic fracture toughness using the one-point bend test is also simple. It requires only limited instrumentation, and interpretation of the test data is straightforward.

Use of the one-point bend test currently is restricted to small-scale yielding conditions. Furthermore, the maximum stress-intensity amplitude that can be obtained using convenient specimen sizes and a conventional pendulum impact tester is rather low, particularly for lighter alloys such as aluminum and titanium alloys. For these materials, devices capable of higher impact velocities are required. This problem can also be circumvented by attaching ballast plates to the ends of the specimen.

Test Setup and Instrumentation

Figure 17 illustrates the typical test setup for performing a one-point bend test on a pendulum impact tester. The specimen holder used in a Charpy or Izod test is replaced by a simple frame that supports the specimen, while allowing it to move freely in the horizontal plane. Depending on the design of the original pendulum and hammer, the impact tester may require retrofitting with a new hammer and striker that will not interfere with the specimen edges or the support frame. The striker should be instrumented with two foil gages—one on each lateral side—to record the impact load on the hammer.

In the response curve time-to-fracture approach, the time-to-fracture is defined as the interval between the time of impact and the time at which crack extension occurs. The time of impact can be determined conveniently from the leading edge of the hammer load signal, whereas the time of crack extension can be measured by an uncalibrated strain gage placed near the crack tip, or by a magnetic pickup. If the response curve is to be used later in conjunction with other impact velocities, it is also necessary to measure the hammer impact velocity.

When calibrated strain gages are used to perform a direct measurement of the stress-intensity history, the gage element should be approximately 2 by 2 mm (0.08 by 0.08 in.) or smaller. The center of the gage should be positioned 3 to 4 mm (0.12 to 0.16 in.) above the crack plane, on a line normal to the crack path and passing through the crack tip.

Two amplifiers with a frequency response greater than 100 kHz are required to process the hammer and specimen gage signal for

recording. These signals are best recorded on a digital storage oscilloscope with a time resolution of 1 μ s or better. If this recording instrument has the capability to store signals that occur before the trigger time, the hammer or specimen gage signals can be used as a trigger. Otherwise, a trigger source must be incorporated into the test setup. A laser beam interrupted by the hammer in conjunction with a photodiode is one option. Another is a simple electrical circuit closed by the contact of hammer and specimen; however, this method may cause transient noise on the strain gage signals.

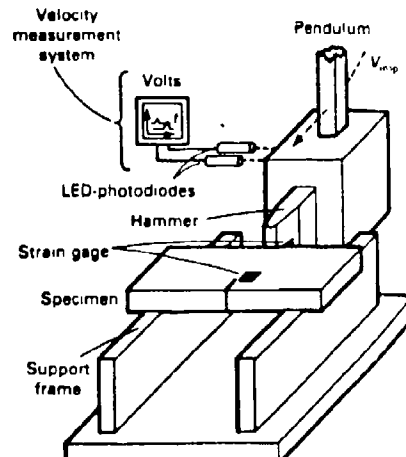
Specimen Size and Geometry. To guarantee small-scale yielding conditions, specimens used in the one-point bend test are subject to the same size requirements as specimens used for static fracture measurements according to ASTM E 399 (Ref 1). In addition, restrictions on the value of the length-to-width ratio, L/W , must be imposed because of the natural modes of vibration of the specimen. It has been shown experimentally that for large values of L/W , higher mode frequencies are excited when the specimen is impacted, thus causing large oscillations in the stress-intensity history (Ref 74). To avoid this undesirable tendency, values of L/W should not exceed 7.

In principle, there is no limit to the absolute size of the specimens beyond those dictated by the development of plasticity. In practice, however, small samples are more susceptible to misalignment errors than large ones. For a given impact velocity, small samples show more test-to-test variability in the maximum amplitude of the stress-intensity history. Consequently, samples less than 100 mm (4 in.) in length are not recommended.

Determination of Dynamic Toughness From Strain Gage Records. As mentioned previously, there are two methods of determining dynamic toughness from strain gage records: the static calibration method and the direct method using Eq 25. The direct method is simpler, but requires care in positioning the strain gage to measure r and θ . The gage should be far enough from the crack tip to avoid the plastic zone, but close enough to the tip to remain in the zone dominated by the singular term of the elastic solution.

Test results show that the recommended distance of 3 to 4 mm (0.12 to 0.16 in.) meets both requirements, even for the smallest recommended specimen size. Furthermore, the crack front obtained from fatigue precracking invariably exhibits a slight curvature. Thus, when determining r and θ , it must be determined whether the origin of the coordinate system should be taken at the location of a virtual average crack front (following the averaging procedure detailed in

Fig. 17 Experimental setup used to perform the one-point bend test



ASTM E 399), or at the actual position of the crack tip on the side of the specimen where the strain gage is mounted. Although further verification is required, experience shows that measuring r and θ from the actual crack tip on the gage side of the specimen provides more consistent results. This practice is therefore recommended.

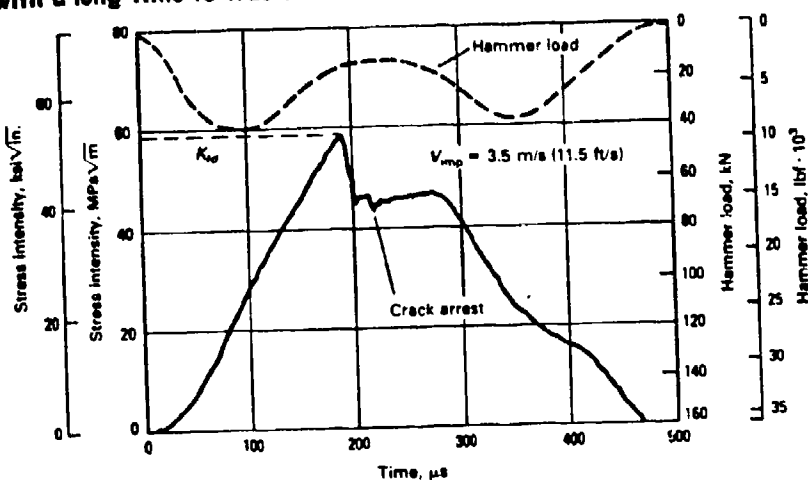
Another concern is the determination of the point of crack initiation when the test is performed with strain gages. For experiments with long times-to-fracture ($>50 \mu$ s), crack initiation causes a clear drop in the measured strain, and the point at which K_{Ic} is evaluated can therefore be determined unambiguously (Fig. 18). For experiments with short times-to-fracture ($<50 \mu$ s), experimental results and simulations indicate that the strain recorded by the strain gage may continue to increase once the crack has begun to extend. This may result in overestimates of the dynamic fracture toughness.

To determine the correct point of crack initiation, the procedure illustrated in Fig 19 should be followed. The reference stress-intensity history for the specimen—i.e., the complete history untruncated by crack extension—is first scaled to the appropriate test conditions. The scaled reference stress-intensity history is then superimposed on the curve recorded during the fracture test. The point where the two curves begin separating is then selected as the point of crack initiation.

If the reference stress-intensity history is not available, a tangent straight line can be fitted to the fracture test record. As before, the point of separation of the experimental record from the tangent line determines crack initiation.

Performing Tests With Ballast at the Specimen Ends. When testing low-density

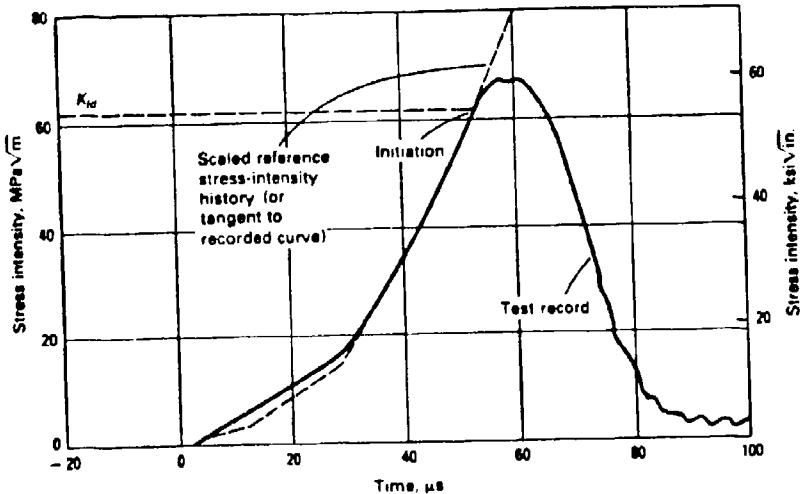
Fig. 18 Stress-intensity and hammer-load histories for fracture test with a long time-to-fracture



materials such as aluminum or titanium alloys, the inertial loading capacity of the one-point bend test may be insufficient to initiate crack propagation. To circumvent this limitation, ballast may be affixed to the specimen ends, as illustrated in Fig. 20. The stress-intensity history for an aluminum specimen outfitted with ballast plates is illustrated in Fig. 21 along with the stress-intensity history for the same specimen without ballast plates. The tests were performed at an impact velocity of 5.3 m/s (17.4 ft/s).

The dimensions of the specimen are $L = 241 \text{ mm (9.5 in.)}$, $W = 63.5 \text{ mm (2.5 in.)}$, $B = 12.7 \text{ mm (0.5 in.)}$, and $a = 19 \text{ mm (0.75 in.)}$. Two ballast plates of steel (89 by 25.4 by 6.4 mm, or 3.5 by 1.0 by 0.25 in.) were attached on each side of the specimen. The maximum stress-intensity amplitude is significantly higher for the specimen with ballast.

Fig. 19 Stress-intensity history for a fracture test with a short time-to-fracture and procedure for determining K_{Id}



276/High Strain Rate Testing

Fig. 20 Specimen and ballast plates used to obtain response curve in Fig. 21

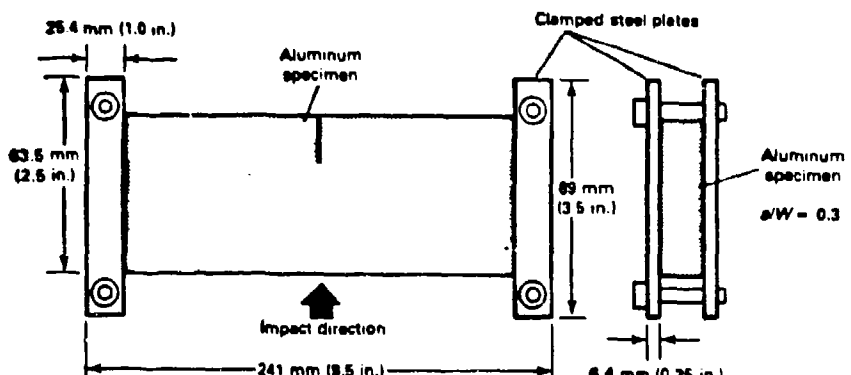
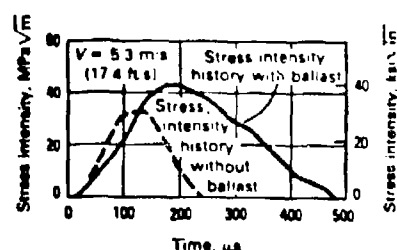


Fig. 21 Stress-intensity histories for an aluminum specimen with and without ballast plates



REFERENCES

1. "Standard Test Method for Plane-Strain Fracture Toughness of Metallic Materials," E 399, *Annual Book of ASTM Standards*, Vol 03.01, ASTM, Philadelphia, 1984, p 519-554
71. W. Böhme and J.F. Kalthoff, The Behavior of Notched Bend Specimens in Impact Testing, *Int. J. Fract.*, Vol 20 (No. 1), 1982, p 139-143
72. J.F. Kalthoff, S. Winkler, W. Böhme, and D.A. Shockley, Mechanical Response of Cracks to Impact Loading, in *Proceedings of the International Conference on the Dynamical Mechanical Properties and Fracture Dynamics of Engineering Materials*, Czechoslovak Academy of Sciences, Institute of Physical Metallurgy, Brno, Czechoslovakia, June 1983
73. J.F. Kalthoff, W. Böhme, and S. Winkler, "Verfahren zum Bestimmen mechanischer Werkstoff-Kennwerte und Vorrichtung zur Durchführung des Verfahrens," patent disclosure, Deutsches Patentamt, Munich, June 1983
74. J.H. Giovanola, "Investigation and Application of the One-Point-Bend Impact Test," *ASTM 17th National Symposium on Fracture Mechanics*, Albany, NY, Aug 1984

Appendix C

DETERMINATION OF DYNAMIC STRESS INTENSITY HISTORIES BY STRAIN GAGE MEASUREMENTS

INTRODUCTION

The major difficulty in measuring the mode I dynamic initiation fracture toughness is the lack of a direct relationship between the stress intensity history at the crack tip and the history of the load applied away from the crack tip. Therefore, measurements must be performed in the immediate vicinity of the crack tip to obtain the stress intensity history. Optical techniques, such as photoelasticity¹ and the shadow optical method of caustic² have been successfully used for these measurements. Unfortunately, these techniques are complex, and hence not suitable for routine testing.

Simpler, yet reliable techniques, are required for dynamic initiation toughness measurements. One such technique uses strain gages to measure strain histories near the crack tip. The stress intensity history is then related to the strain histories using either of two methods: the singularity solution method or the static calibration method.

In this appendix, we first review the principle of the strain gage technique and discuss its limitations. Then we use experimental results to evaluate the effect of these limitations on the measurements of stress

¹A. S. Kobayashi, "Experimental Techniques in Fracture Mechanics," Chapter 6, Monograph No. 1 (Society for Experimental Stress Analysis, Iowa State Press, Ames, Iowa, 1973), pp. 126-145.

²J. Beinert, J. F. Kalthoff, and M. Maier, "Neuer Ergebnisse zur Anwendung des Schattenfleckverfahrens auf stehende und schnell-laufende Brüche," VDI-Berichte, Vol. 313, pp. 791-798 (1978).

intensity histories for pure mode I and mixed mode I and mode II dynamic loading. Finally, we discuss the parameters affecting the strain history records once the crack has started to extend, with the purpose of defining crack initiation and to estimate the crack velocity and the propagation toughness on the basis of the strain gage records.

PRINCIPLE AND LIMITATIONS OF THE STRAIN GAGE TECHNIQUE

The strain gage technique for determining the stress intensity history is based on the assumption that, up to the point of crack initiation, the strain at a given location in the vicinity of the crack tip is directly proportional to the stress intensity. Two methods for relating the strain to the stress intensity are discussed below: the singularity solution method and the static calibration method.

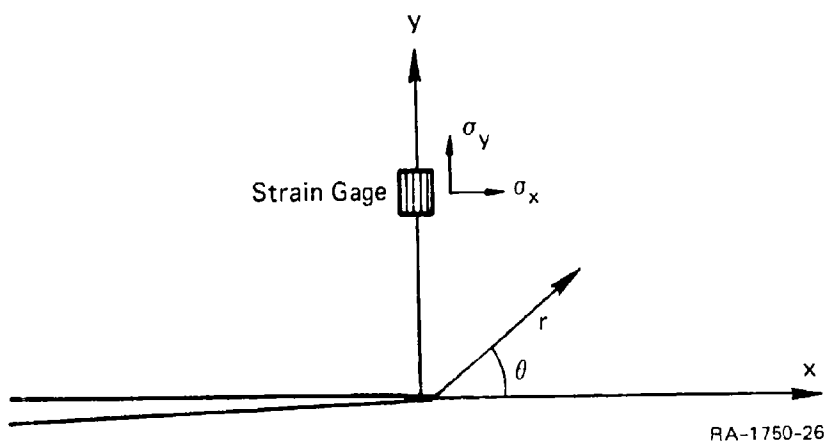
Singularity Solution Method

The singularity solution method relies on the analytical elastodynamic solution for the stress field around a crack tip to relate the strain to the stress intensity factor. Referring to Figure C-1 for the definition of the coordinate systems, the stresses are given in terms of a series expansion in the polar coordinates r and θ centered at the crack tips as

$$\sigma_x = \frac{K_I(t)}{\sqrt{2\pi r}} \cos \frac{\theta}{2} \left(1 - \sin \frac{\theta}{2} \sin \frac{3}{2} \theta\right) + \sum_{i=1,2,\dots}^{i-1} A_i(t) r^{\frac{i-1}{2}} f_i(\theta) \quad (C-1)$$

$$\sigma_y = \frac{K_I(t)}{\sqrt{2\pi r}} \cos \frac{\theta}{2} \left(1 + \sin \frac{\theta}{2} \sin \frac{3}{2} \theta\right) + \sum_{i=1,2,\dots}^{i-1} A_i(t) r^{\frac{i-1}{2}} g_i(\theta) \quad (C-2)$$

where $K_I(t)$ is the time-dependent mode I stress intensity factor and $A_i(t)$ are the time-dependent coefficients of the higher order terms of



RA-1750-26

FIGURE C-1 DEFINITION OF COORDINATES AND STRAIN GAGE POSITION
AT INITIAL CRACK TIP

the expansion. Equations (C-1) and (C-2) have the same form as the elastostatic solution, except that the coefficients are now time dependent. In particular, the angular functions, $f_1(\theta)$ and $g_1(\theta)$, are the same as in the static case. Assuming plane stress conditions at the specimen surface, the strain measured by the strain gage, positioned as shown in Figure C-1, can be expressed as

$$\epsilon_y = \frac{1}{E} (\sigma_y - v \sigma_x) \quad (C-3)$$

Inserting (C-1) and (C-2) into (C-3) yields

$$\begin{aligned} \epsilon_y(t) &= \frac{1}{E} \frac{K_I(t)}{\sqrt{2\pi r}} [1 - v + (1 + v) \sin \theta \sin \frac{3}{2} \theta] \\ &+ \sum_{i=1,2,\dots}^{i-1} A_i(t) r^{\frac{i-1}{2}} (g_i(\theta) - v f_i(\theta)) \end{aligned} \quad (C-4)$$

Very near the crack tip, the first (singular) term in equation (C-4) dominates over the other terms, so the strain is approximately given by

$$\epsilon_y(t) = \frac{1}{E} \frac{K_I(t)}{\sqrt{2\pi r}} [1 - v + (1 + v) \sin \theta \sin \frac{3}{2} \theta] \quad (C-5)$$

Knowing the coordinates r and θ of the center of the gage with respect to the initial crack tip, equation (C-5) can be used to calculate the stress intensity history from a single strain history record taken during the dynamic fracture test. In dynamic fracture tests, the strain gage is usually located as shown in Figure C-1 with the gage element oriented in the y -direction. The advantages of this configuration will be discussed below.

The singularity solution method introduces four sources of error in the measurement of the stress intensity history. First, the singular

term in equation (C-4) dominates only very close to the crack tip. For practical reasons, however, the strain gage has to be positioned a finite distance from the crack tip, if only to avoid the plastic zone. As the distance from the crack tip is increased, the contribution of the higher order terms to the strain may become important. Thus the use of equation (C-5) may introduce a nonnegligible error in the estimate of the stress intensity history.

A second source of error is introduced by the finite size of the strain gage active grid. This causes the strain gage to measure a strain averaged over an area rather than the strain at a point, as assumed when using equation (C-5). In the presence of a strong strain gradient, such as near the crack tip, the average strain measured by the gage could be significantly different from the strain at the nominal point of measurement (the center of the gage) and this difference could introduce an error in the estimate of the stress intensity.

A third type of error arises if the position of the gage with respect to the crack tip is not measured precisely. In particular, when the crack front is slightly curved, there is a question of whether the polar coordinate system should be defined by the average crack length or by the length of the crack on the face where the strain gage is mounted. Also, small angular misalignments of the gage element with respect to the y-direction may cause some error when using equation (C-5) to obtain the stress intensity factor.

Estimates of the importance of these four error sources are discussed in a later section.

Static Calibration Method

In the static calibration method, first proposed by Loss³, the proportionality factor between strain and stress intensity is determined experimentally. The specimens, with the strain gage mounted at the crack tip, are loaded quasi-statically using a test configuration for which the stress intensity calibration is available in handbooks. During this calibration test, the applied load and the strain gage output are recorded simultaneously. The proportionality factor between strain and stress intensity factor is calculated from these two records using the handbook calibration function.

It is then assumed that the relationship between strain gage output and stress intensity factor obtained under quasi-static conditions is also valid under dynamic conditions and can be used to relate the strain history to the stress intensity history. This assumption implies that the time-dependent coefficients of the higher order terms in equation C-4 all vary in proportion to the stress intensity history, and that the proportionality factors are the same as for the static case. However, this may not be true, particularly in experiments where stress waves play an important role and interact both with the boundaries and the crack tip.

Thus, similarly to the singularity solution method, the static calibration method could introduce an error related to the way higher order terms are taken into account. The static calibration method, however, avoids the potential error associated with the strain integration over a finite area and with the positioning of the strain gage because these effects are automatically accounted for in the calibration procedure. From this point of view, the static calibration

³J. F. Loss, J. R. Hawthorne, and C. A. Griffis, "Fracture Toughness of Light Water Reactor Pressure Vessel Materials," Naval Research Laboratory Memorandum Report 3036 (April 1975).

method appears to be more reliable than the singularity solution, although it has the disadvantage of being more complicated to implement.

USE OF THE STRAIN GAGE METHOD IN MIXED-MODE DYNAMIC FRACTURE

The singularity solution method can be applied to mixed-mode dynamic fracture experiments. In the case of mixed mode I and II loading, the stress field is given by

$$\sigma_x = \frac{K_I(t)}{\sqrt{2\pi r}} \cos \frac{\theta}{2} (1 - \sin \frac{\theta}{2} \sin \frac{3}{2} \theta) - \frac{K_{II}(t)}{\sqrt{2\pi r}} \sin \frac{\theta}{2} (2 + \cos \frac{\theta}{2} \cos \frac{3}{2} \theta) + \sum_{i=1,2,\dots}^{i-1} A_i(t) r^{\frac{i-1}{2}} f_i(\theta) \quad (C-6)$$

$$\sigma_y = \frac{K_I(t)}{\sqrt{2\pi r}} \cos \frac{\theta}{2} (1 + \sin \frac{\theta}{2} \sin \frac{3}{2} \theta) + \frac{K_{II}(t)}{\sqrt{2\pi r}} \sin \frac{\theta}{2} (\cos \frac{\theta}{2} \cos \frac{3}{2} \theta) + \sum_{i=1,2,\dots}^{i-1} A_i(t) r^{\frac{i-1}{2}} g_i(\theta) \quad (C-7)$$

where $K_{II}(t)$ is the dynamic mode II stress intensity factor.

As in the pure mode I case, the strain at any location and in any direction can be expressed in terms of equation C-7. In the immediate vicinity of the crack tip, the singular terms will dominate and the strain, say, in the y-direction, can be written as

$$\epsilon_y(t) = \frac{K_I(t)}{\sqrt{2\pi r}} \cos \frac{\theta}{2} [1 - \nu + (1 + \nu) \sin \frac{\theta}{2} \sin \frac{3}{2} \theta] + \frac{K_{II}}{\sqrt{2\pi r}} \sin \frac{\theta}{2} [(1 - \nu) \cos \frac{\theta}{2} \cos \frac{3}{2} \theta - 2\nu] \quad (C-8)$$

Therefore, given two independent strain history records, the mode I and mode II stress intensity factors can be determined at each instant by solving two algebraic equations in the form of equation C-8. If

additional strain gages are introduced, higher order coefficients can also be determined using the strain gage method.

This multiple strain gage approach has been used to measure the mode I and mode II stress intensity histories in mixed mode fracture experiments and to evaluate the first higher order term in the series expansion, A_1 .

ESTIMATION OF ERRORS IN THE DETERMINATION OF STRESS INTENSITY HISTORIES USING STRAIN GAGE MEASUREMENTS

Comparison of Singularity Solution and Static Calibration Methods

A first approach to evaluate the reliability of the strain gage method of measuring the dynamic stress intensity factor is to compare the estimates obtained with the singularity solution and with the static calibration methods for the same experiment. In doing so, we assume that the static calibration method will provide a more accurate estimate of the stress intensity history than the singularity solution method for the reasons discussed in the preceding section. Hence, the static calibration method will provide a reference with which to compare the singularity solution results.

We have compared estimates of the stress intensity based on the singularity solution method and estimates based on the static calibration method for several specimen geometries impacted in 1PBT experiments. Some specimens had a fatigue precrack, others contained a blunt notch with a notch root radius of approximately 0.5 mm. All the strain measurements were performed with the same type of strain gage, with a gage element length of 1.57 mm and width of 1.57 mm. The gages were mounted as shown in Figure C-1, 3 to 4 mm above the crack tip. In one case two gages were used, one mounted 1.6 mm and the other 5.6 mm from the fatigue crack tip.

The results of the comparisons, summarized in Table C-1, show that the difference between estimates from one data reduction method and the other never exceeds 16%. If we consider only the data obtained from fatigue-precracked experiments, the differences are even smaller and do

Table C-1

COMPARISON OF STRESS INTENSITY ESTIMATES BY THE STATIC CALIBRATION (SC) METHOD
AND THE SINGULARITY SOLUTION (SS) METHOD

Specimen No.	W [mm]	S/R [mm]	a/W	Gage Position $y = r [mm]$	$(K_I^{\max})_{SC}$	$(K_I^{\max})_{SS}$	Specimen Type
					[MPa m ^{1/2}]	[MPa m ^{1/2}]	
K _{Id} -16-2	63.5	5.6	0.42	6.2 (1.6)*	60.4 (63.9)*	62.7	1.9%
F-1	31.75	4.2	0.41	3.2	68.6	65.2	5%
F-2†	31.75	4.2	0.41	3.0	66.7	66.9	-0.3%
ASTM-small-1	25.4	4.2	0.3	3.7	37.2	35.7	4%
ASTM-small-2	25.4	4.2	0.4	3.8	40.80	42.4	-3.9%
ASTM-small-3	25.4	4.2	0.5	3.5	56.4	47.6	15.6
ASTM-small-4		0.6	3.6	64.1	58.5	8.7%	Notched (p = 0.5 mm)
ASTM-large-1	63.5	4.2	0.3	3.8	62.2	71.5	-15%

*Second gage.

†Fracture test.

not exceed 5%. In particular, very good agreement was obtained for the test where two independent strain histories were recorded (specimen K_{Id}-16-2). For the gage closest to the crack tip, the maximum stress intensity value estimated with the singularity solution method agreed closely with the value estimated from the static calibration method (1.9% difference). A comparison between the stress intensity values obtained from gage 1 and 2 using the static calibration method gives an estimate of the error associated with this method. This error is about 6% and probably corresponds to the random error associated with the static calibration procedure itself. From these data, we conclude that, for sharp cracks, the singularity solution method gives results that are as reliable as the static calibration method.

Larger differences are observed between the two methods when specimens with blunt notches are tested. No particular trend in the differences could be established with specimen size and geometry. Because the notch root radius used was relatively large compared with the distance from the gage center to the notch tip, we believe that the observed differences are due to the influence of the notch on the near tip strain field. As a result of the finite root radius of the notch, the strains at the gage location are different from the strains given by the elastic solution for the sharp crack, and an error is introduced when this solution is used to reduce the experimental data. The variability in the magnitude of this error may be due to the differences in geometry and surface finish from notch to notch, because these parameters were not closely controlled. Nevertheless, the data of Table C-I demonstrate that the singularity solution method provides acceptable estimates of the stress intensity history, even for blunt notches.

Estimate of the Gage Integration Error

To assess in more detail the error associated with the singularity solution method, we estimated the error due to the strain integration by the strain gage over a surface, using an approach proposed by Böhme and

Kalthoff.⁴ They estimated the strain measured by the strain gage by integrating the singularity solution over the area of the strain gage, that is

$$\epsilon_y^{\text{gage}} = \frac{1}{E} \int_{r - \lambda/2}^{r + \lambda/2} \int_{-b/2}^{b/2} \frac{\sigma_y(r', \theta) - v\sigma_x(r', \theta)}{bl} dx dy \quad (\text{C-9})$$

where λ is the length of the active strain gage element and b is its width.

Dividing equation C-9 by equation C-5 gives an estimate of the ratio of measured strain to true strain.

$$\frac{\epsilon_y^{\text{gage}}}{\epsilon_{\text{true}}} = \frac{2\sqrt{2}}{3-v} \frac{\sqrt{r}}{bl} \int_{r - \frac{\lambda}{2}}^{r + \lambda/2} \int_{-b/2}^{b/2} \frac{1}{\sqrt{r'}} \cos \frac{\theta}{2} [(1-v) + (1+v) \sin \frac{\theta}{2} \sin \frac{3\theta}{2}] dx dy \quad (\text{C-10})$$

Equation C-10 has been evaluated numerically for the values of $\lambda = 1.57$ mm and $b = 1.57$ mm, corresponding to the dimensions of the gages used in our experiments. The results are plotted in Figure C-2 as a function of gage distance from the crack tip, r . It can be seen that the strain integration causes an underestimate of the strain and that the error drops off rapidly with r . For r equal to 3 mm or greater, the error is less than 2%. Therefore, even with relatively large strain gages, the gage integration error is small.

⁴W. Bohme and J. F. Kalthoff, "Der Einfluss der Probengrösse auf dynamische Effekte bei der K_{Ic} -Bestimmung im Kerbschlagtest," Report W3/83, Fraunhofer-Institut für Werkstoffmechanik, Freiburg, West Germany, (1983).

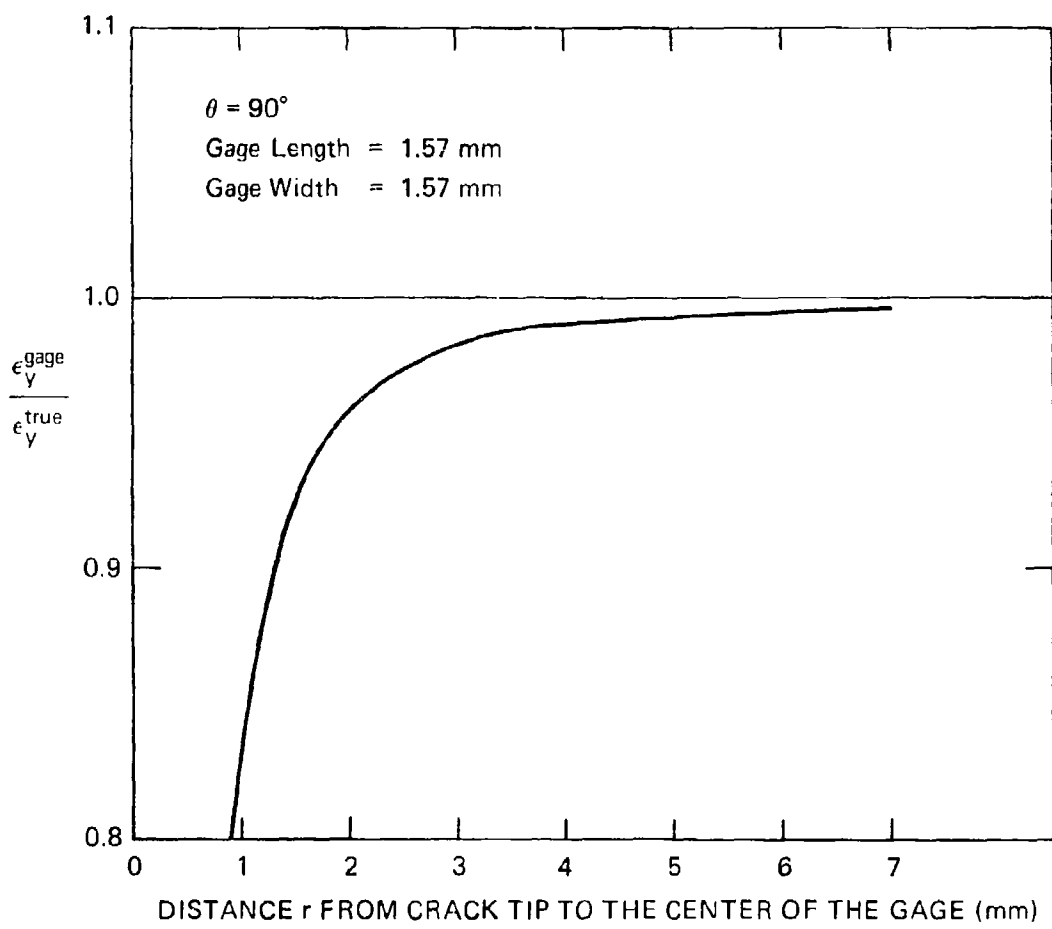


FIGURE C-2 ESTIMATE OF GAGE INTEGRATION ERROR

Effect of First Higher Order Term in the Elastic Solution

Böhme and Kalthoff⁴ estimated the error introduced in the singularity solution method by neglecting the influence of the first two higher order terms. They found that, for a three-point-bend specimen with aspect ratio $S/W = 4$, and a relative crack length a/W between 0.2 and 0.7, the error was always smaller than 10% for relative gage positions r/W smaller than 0.005. Their estimate, however, is based on the values of the higher order coefficients for the static case. Therefore, there is some question whether it can be extended to the dynamic case, where wave reflections may play a significant role.

To investigate this question, we performed pure mode I experiments using the 1PBT and specimens instrumented with two strain gages, positioned at $\theta = 45$ and 90 degrees. Using the procedure outlined above, we calculated the histories of the mode I stress intensity and of the coefficient of the first higher order term A_1 (the r -independent term) in the series expansion solution from the measured strain histories. The stress intensity history resulting from using only the singular term in the solution was also calculated based on the strain measurement of a single gage, the gage positioned at 90° from the crack plane. By comparing the stress intensity histories obtained from single gage and two gage strain measurements, we obtain an estimate of the error introduced by neglecting higher order terms when evaluating strain gage data.

Figure C-3 shows the results of an experiment in which both $K_I(t)$ and $A_1(t)$ were evaluated for a specimen with a length of 267 mm, a width of 63 mm, and a crack length to width ratio of 0.6. The A_1 history is negative, indicating a compressive stress acting parallel to the crack plane, which is consistent with the hammer load history. Similar results were obtained for a specimen with a crack length to width ratio of 0.3. Comparison of the stress intensity histories obtained with and without taking into account the A_1 term shows that the difference between the two curves is small: the maximum amplitudes differ by no more than 2% for the specimen with $a/W = 0.6$ and no more than 10% for the specimen with $a/W =$

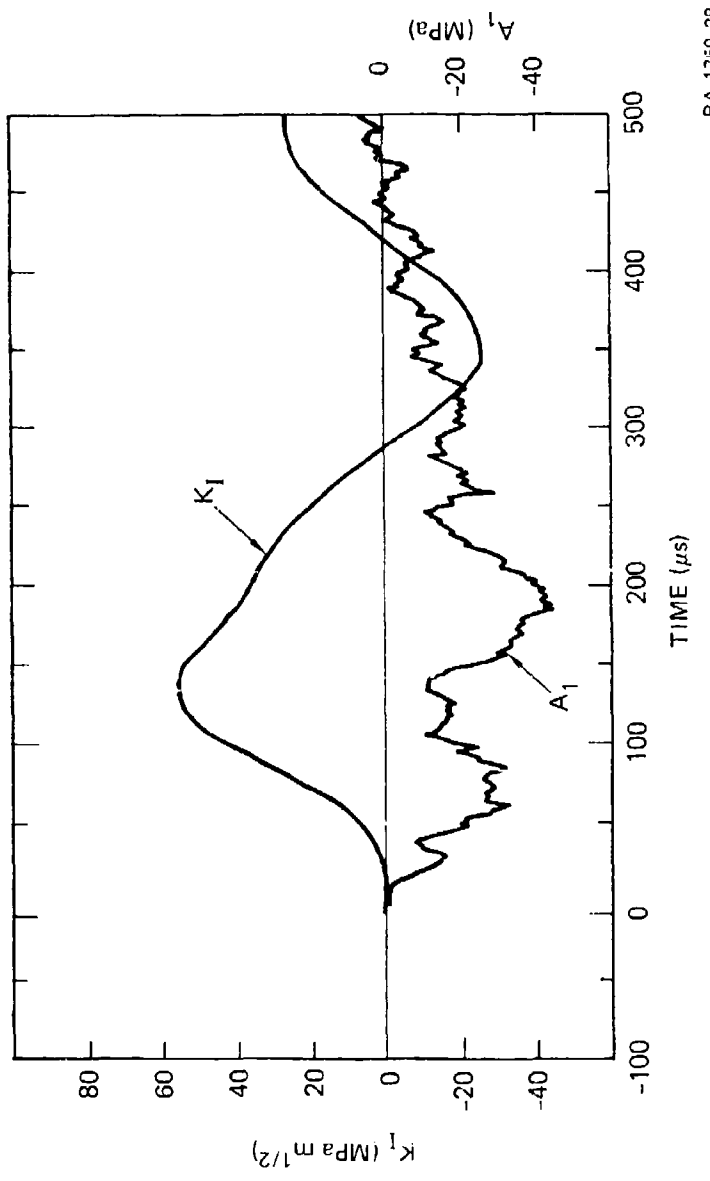


FIGURE C-3 HISTORIES OF MODE I STRESS INTENSITY FACTOR K_I AND FIRST ORDER TERM COEFFICIENT A_1 MEASURED IN 1PBT

RA-1750-28

0.3. We think that the 10% difference is due to the larger value of the notch root radius (approximately 0.75 mm compared with 0.125 mm for the other specimen). Such an influence of the root radius was reported earlier in this section in connection with the data in Table C-1.

We also evaluated the effect of A_1 and K_I and K_{II} in mixed-mode experiments, using a double-crack IPBT technique described in Appendix F and two or three gages to measure strains near the crack tip. For the mode I experiments, we found that neglecting A_1 for the strain data reduction has little influence on the K_I history and introduces differences of about 2%. The effect on K_{II} appears more significant. We calculated differences up to 35% in the maximum amplitudes as well as differences in the overall shape of the K_{II} histories. This observation is consistent with photoelastic results reported by Kobayashi et al.⁵ Therefore, in the mixed-mode experiments reported in Appendix F, we always used three strain gages to determine, K_I , K_{II} , and A_1 .

Our assessment of the influence of higher order terms on the strain gage technique for measuring stress intensity histories is only approximate because we have performed it for a limited number of specimen sizes and geometries. Furthermore, the accuracy of the multiple gage approach itself has not been assessed against other techniques or against numerical simulations. Nevertheless, we conclude that, in the dynamic case and for the size and position of the strain gages that we used, neglecting the first higher order term in calculating the mode I stress intensity history introduces an error of less than 5%. This result is consistent with the conclusions based on the comparison of the static calibration method and the singularity solution method.

⁵A. S. Kobayashi and M. Ramulu, "Dynamic Mixed-Mode Fracture," in Mixed-Mode Crack Propagation, G. C. Sih and P. S. Theocaris, Eds., Sijthoff and Noordhoff, Rockville, Maryland, 1981), pp. 163-172.

Our conclusion can be rationalized by considering the elastic solution for $\theta = 90^\circ$. Taking only the singular term and the first higher order term, the strain in the y-direction at a distance $r = 2.5$ mm is

$$\epsilon_y = \frac{1}{E} (7.61 K_I - 0.28 K_{II} - 0.3 A_1) \quad (C-11)$$

where a value of 0.3 has been assumed for Poisson's ratio. Equation (C-11) indicates that, if the strain gage is positioned immediately above the crack tip, the y-strain will be controlled predominantly by the mode I stress intensity factor, unless the mode II stress intensity factor and the coefficient of the first higher order term are large. Thus, the position of the measuring strain gage in Figure C-1 represents an optimum position.

To verify the basic assumption underlying the static calibration method namely, that the higher order coefficients vary proportionally to $K_I(t)$, we consider the ratio $A_1(t)/K_I(t)$. This ratio, obtained from the data in Figure C-3, is plotted in Figure C-4. Clearly, the ratio A_1/K_I is not constant during the experiment, so the assumption underlying the static calibration method is violated. However, from equation (C-11), we estimate that the variation around a mean value of the ratio of -1.5 will cause errors of $\pm 6\%$ in the value of K_I . What remains to be shown is whether the mean value of A_1/K_I is consistent with the value of the ratio in the static case.

Gage Position Error in Singularity Solution Method

We have not directly assessed the gage position error (coordinates and angular position with respect to the y-axis). Nevertheless, the good agreement between the results of the static calibration method (which does not introduce a gage position error) and the results of the singularity solution method indicates that this error is only a few percent. When the fatigue crack front of the fracture specimen displays a significant curvature or is not absolutely perpendicular to the

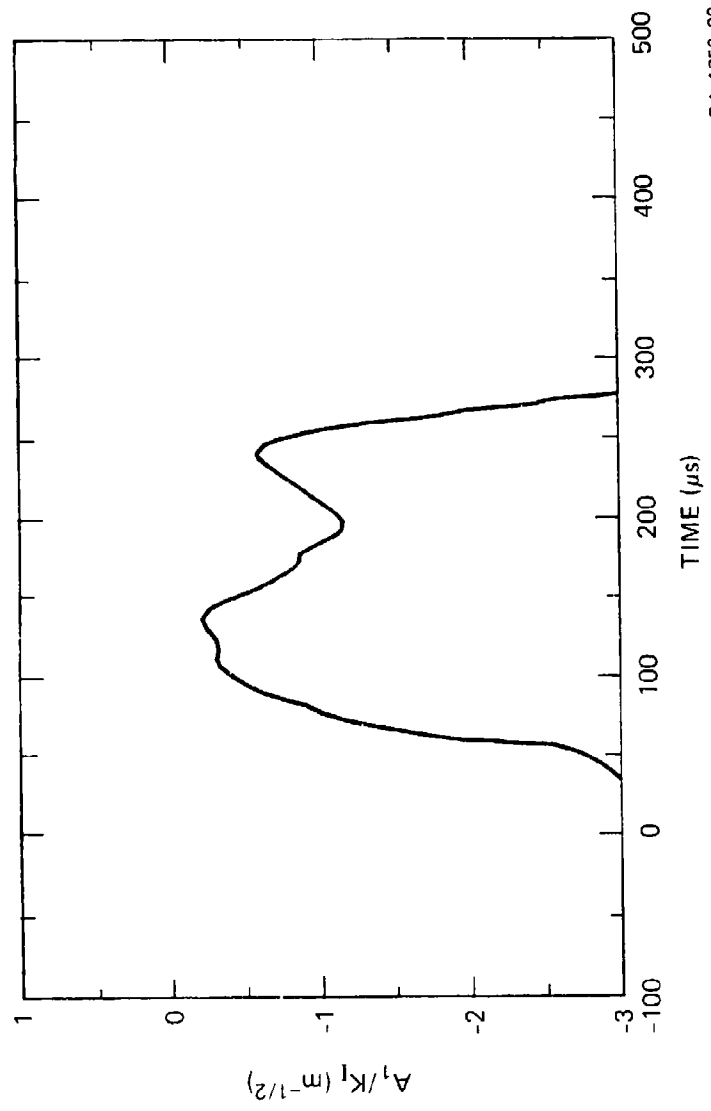


FIGURE C-4 RATIO OF FIRST ORDER TERM COEFFICIENT A_1 TO MODE 1
STRESS INTENSITY FACTOR K_1 FOR HISTORIES PLOTTED
IN FIGURE C-3

specimen faces, experience has shown that referring the gage position to the actual crack tip position (on the specimen side where the gage is mounted), rather than to an average crack tip position, yields more consistent data with less scatter.

Summary of Results

The evaluations of the two strain gage methods of measuring dynamic stress intensity histories discussed above show that neglecting the effect of the higher order terms introduces an error in both the singularity solution method and the static calibration method. However, this error is small (~ 5%) for the mode I stress intensity factor. For the singularity solution method, the combined effect of the integration error and the gage position error is also only a few percent, as assessed by comparison with the static calibration method results. Therefore, the strain gage method provides an attractive alternative to the more involved stress optic methods for determining dynamic initiation toughness values. Furthermore, at a comparable degree of accuracy, the singularity solution method is simpler to apply than the static calibration method and is therefore more advantageous to use.

FACTORS AFFECTING THE STRAIN HISTORY AFTER INITIATION AND DETECTION OF THE POINT OF CRACK INITIATION ON THE STRAIN RECORDS

An important step in estimating the dynamic fracture toughness with the 1PBT is determining the instant of crack initiation from the near crack tip strain history record. The basis for determining the instant of crack initiation is that crack extension will cause a clear change in the slope of the strain history record. As the crack moves away from the strain gage position, the strain will decrease rapidly and this drop can be used to pinpoint the instant of crack initiation. Once the crack starts to extend, however, the following factors can influence the strain history:

- The gage position with respect to the crack tip.

- The crack speed and the resistance of the material to crack extension.
- The applied stress intensity rate.
- Plasticity effects, residual strains, and the formation of shear lips.
- Nonsingular terms in the series expansion solution.

In general, the effect of all these factors will be combined in a complex way to yield the experimental strain history record.

We have investigated how these factors influence the strain history record, using an approximate model of the IPBT to simulate the strain history after the crack has started to extend. A detailed description of the model is given in Appendix D. The model allows us to load the crack at different rates and to vary the behavior of the dynamic propagation toughness. The near crack tip strain history is calculated using the singular term of the elastic series expansion for a stationary crack.

Figure C-5 shows the results of simulations of the strain at the tip of a crack in a 1PB specimen 63.5 mm wide and 241 mm long with a crack length of 19 mm. The simulated impact velocity was 50 m s^{-1} .

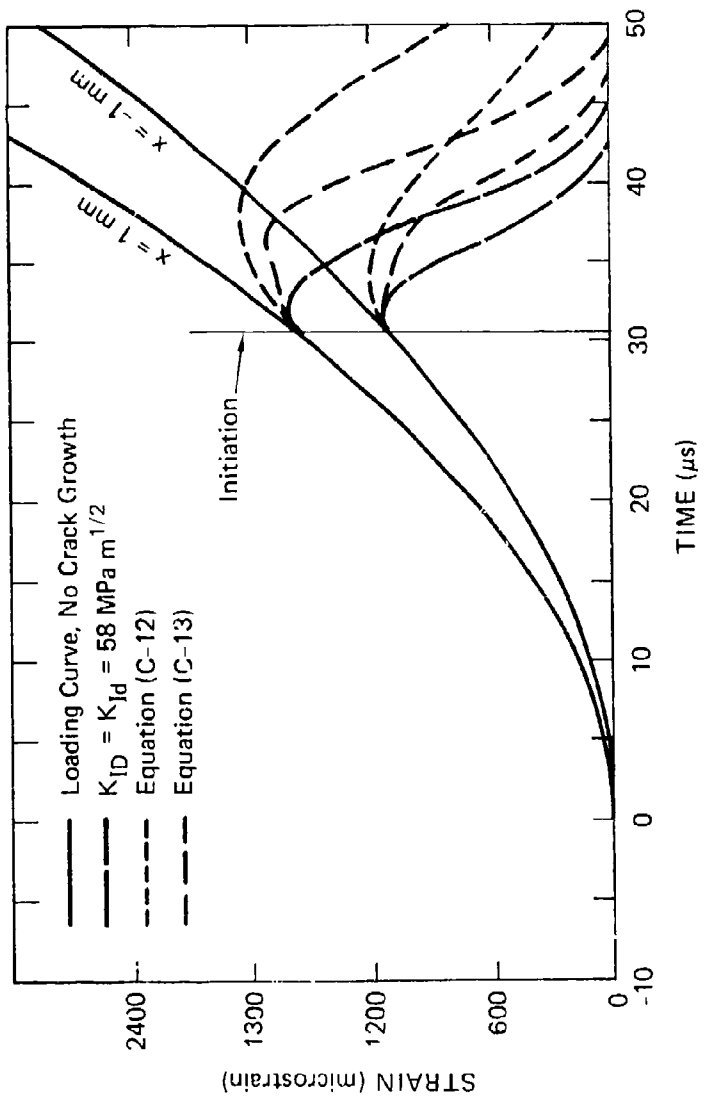
Simulations were performed to calculate the strain at two positions near the crack tip ($x = -1 \text{ mm}$, $y = 5.9 \text{ mm}$, and $x = 1 \text{ mm}$, $y = 5.9 \text{ mm}$) assuming three different behaviors for the propagation toughness K_{ID} . In the first case, K_{ID} was assumed constant and equal to the initiation toughness K_{Id} . A value of $58 \text{ MPa m}^{1/2}$ was chosen for K_{Id} , representing the initiation toughness of 4340 steel heat treated to HRC50. In the second case, the propagation toughness varied with velocity as

$$K_{ID} = 58 \times 10^6 + 395 \text{ } \text{Å}^2 \quad (\text{C-12})$$

In the third case, the propagation toughness was assumed to rise with crack extension over the first millimeter of crack growth as

$$K_{ID} = 58 \times 10^6 (1 + \Delta a / 250), \Delta a < 1 \text{ mm} \quad (\text{C-13})$$

$$K_{ID} = 72.5 \times 10^6, \Delta a > 1 \text{ mm}$$



RA-1750-30

FIGURE C-5 SIMULATION OF STRAIN HISTORY AT INITIAL CRACK TIP
FOR TWO GAGE POSITIONS x AND FOR SEVERAL
PROPAGATION TOUGHNESS ASSUMPTIONS
Test at high impact velocity.

Beyond 1 mm, K_{ID} was assumed constant equal to $72.5 \text{ MPa m}^{1/2}$. The K_{ID} behaviors represented by equations C-12 and C-13 were chosen arbitrarily and are not intended to be those of 4340 steel.

For the first case of a constant propagation toughness, the simulation shows that the strain can still increase slightly after crack initiation. If the strain is measured 1 mm ahead of the crack tip, the overshoot will be somewhat larger and last longer than when the strain is measured 1 mm behind the crack tip. This behavior becomes more pronounced for the propagation toughness assumptions in equations C-12 and C-13. There is a significant overshoot of the strain measured 1 mm ahead of the crack tip, whereas very little or no overshoot is observed for the strain measured 1 mm behind the crack tip. More important, there is a considerable delay in the drop in strains when we assume an increasing propagation toughness with crack extension or crack velocity, compared with the case of a constant K_{ID} .

Figure C-6 shows a set of simulations similar to those plotted in Figure C-5, but for a specimen 63 mm wide and 356 mm long with a crack length of 19 mm. The simulated impact velocity was 3.5 m s^{-1} , resulting in a much smaller stress intensity rate than in Figure C-5. Therefore, a comparison of Figure C-5 and C-6 illustrates the effect of changes in the stress intensity rate. In the simulations of Figure C-6, the applied stress intensity history was such that crack arrest was predicted in all the simulations after an amount of crack extension varying depending on the propagation toughness assumption. For the case of the constant propagation toughness and the case of the toughness varying according to equation C-13, the strain drop appears sharper than for the simulation at higher rate. However, this difference is essentially due to the change in the time scale of the plots associated with the different stress intensity rates. For the case of the propagation toughness rising with the amount of crack extension, very little crack extension occurred, and the simulated strain history lies very close to the strain history for the specimen with a stationary crack. In such a case, the instant of crack initiation would be difficult to establish unambiguously.

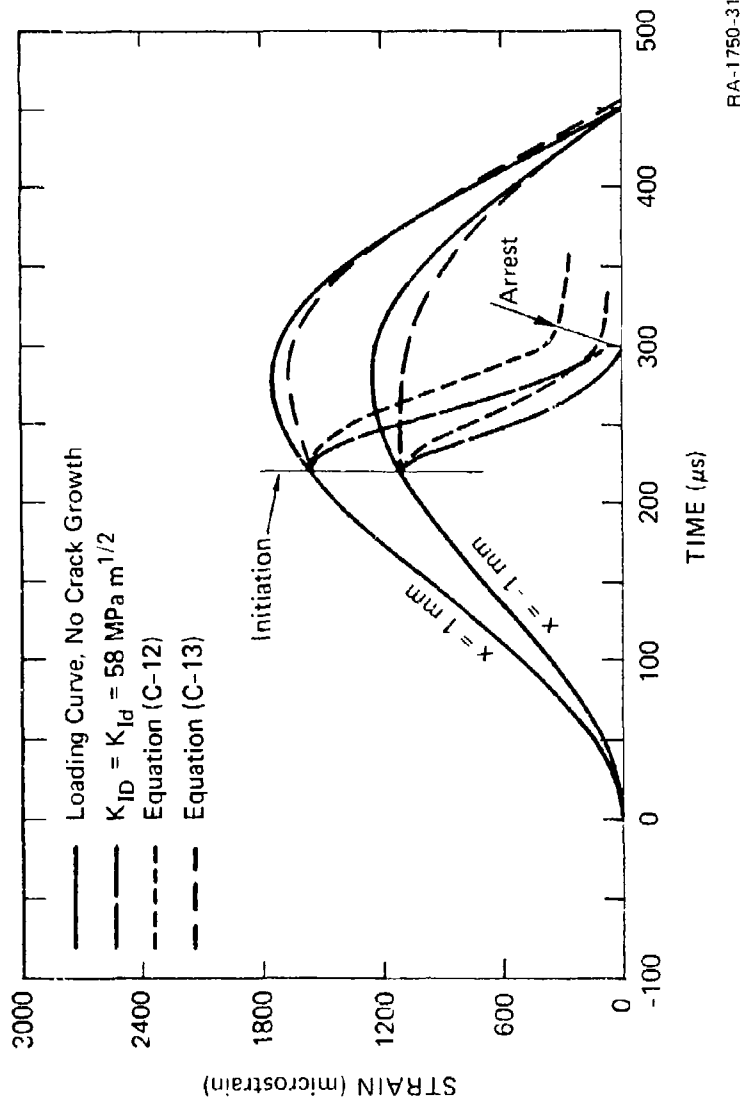


FIGURE C-6 SIMULATION OF STRAIN HISTORY AT INITIAL CRACK TIP
FOR TWO GAGE POSITIONS x AND FOR SEVERAL
PROPAGATION TOUGHNESS ASSUMPTIONS
Test at low impact velocity.

RA-1750-31

Features similar to those predicted by the strain simulations in Figures C-5 and C-6 have been observed in the experimental strain history records. Figures C-7 and C-8 show examples of strain records for experiments with the same specimen geometries as the specimens simulated in Figures C-5 and C-6. In Figures C-7 and C-8, each of the curves was obtained from identical but separate tests with different gage positions with respect to the crack tip. The experimental strain records have also been normalized by the strain at initiation. In these records, the strain history after initiation is significantly affected by the gage position. Moreover, some of the experimental records also display a strain overshoot and a delayed drop in the strain, compared with the strain simulations for the constant propagation toughness.

Several conclusions can be drawn from the strain record simulations. First, because of the potential for a strain overshoot after crack initiation, we must be careful in determining the instant of crack initiation from the strain history records to avoid overestimating the dynamic initiation toughness. In particular, the instant of maximum strain may not correspond to the point of crack initiation. Rather, the point of separation of the strain record from the reference curve for the specimen without crack extension is a better indication of the instant of crack initiation. If the reference curve is not available, it can be approximated by a tangent to the strain record in the region immediately preceding the point of inflection.

The second conclusion drawn from the strain record simulations is that the toughness characteristics of the material tested strongly affect the strain history after crack initiation. However, the simulations also indicate that, given a particular gage location, the amount of crack extension required to drop the strain to zero depends only mildly on the propagation toughness characteristics and hence can be assumed constant in first approximation. These observations indicate that, as suggested by Bönme and Kalthoff,⁴ information about the dynamic propagation toughness and the initial crack velocity can be obtained from the analysis of the strain records.

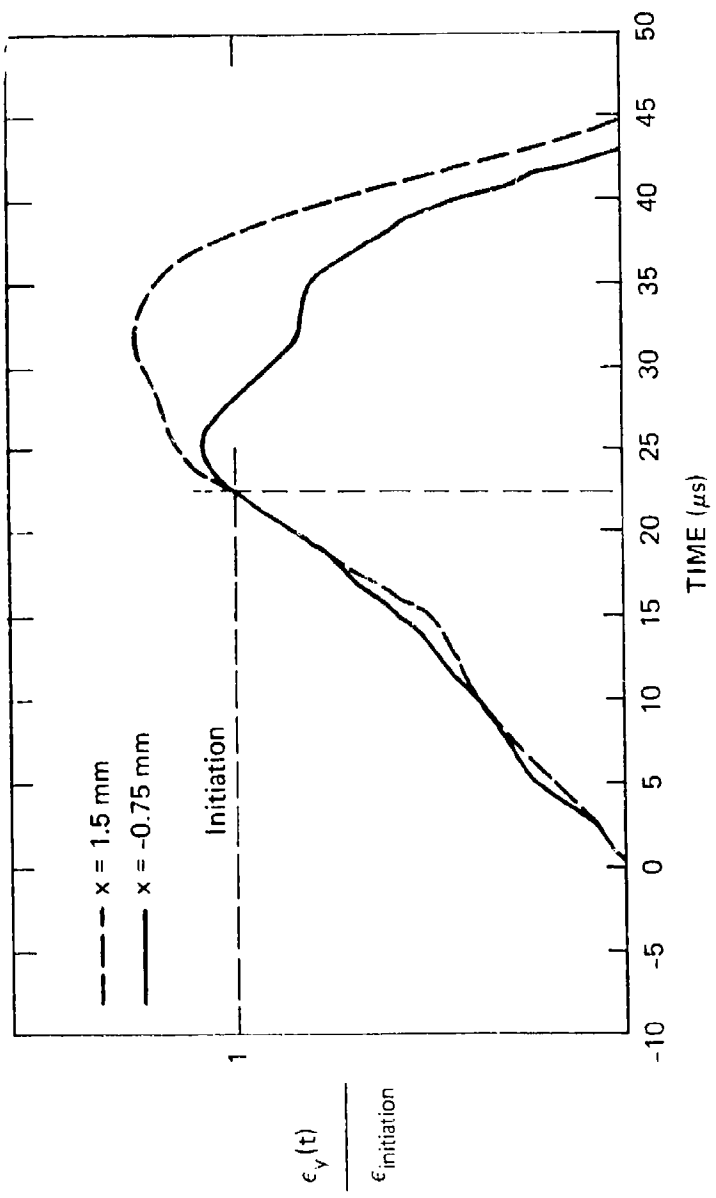


FIGURE C-7 NORMALIZED EXPERIMENTAL STRAIN HISTORY NEAR INITIAL CRACK TIP FOR TWO GAGE POSITIONS \times
Test at high impact velocity.

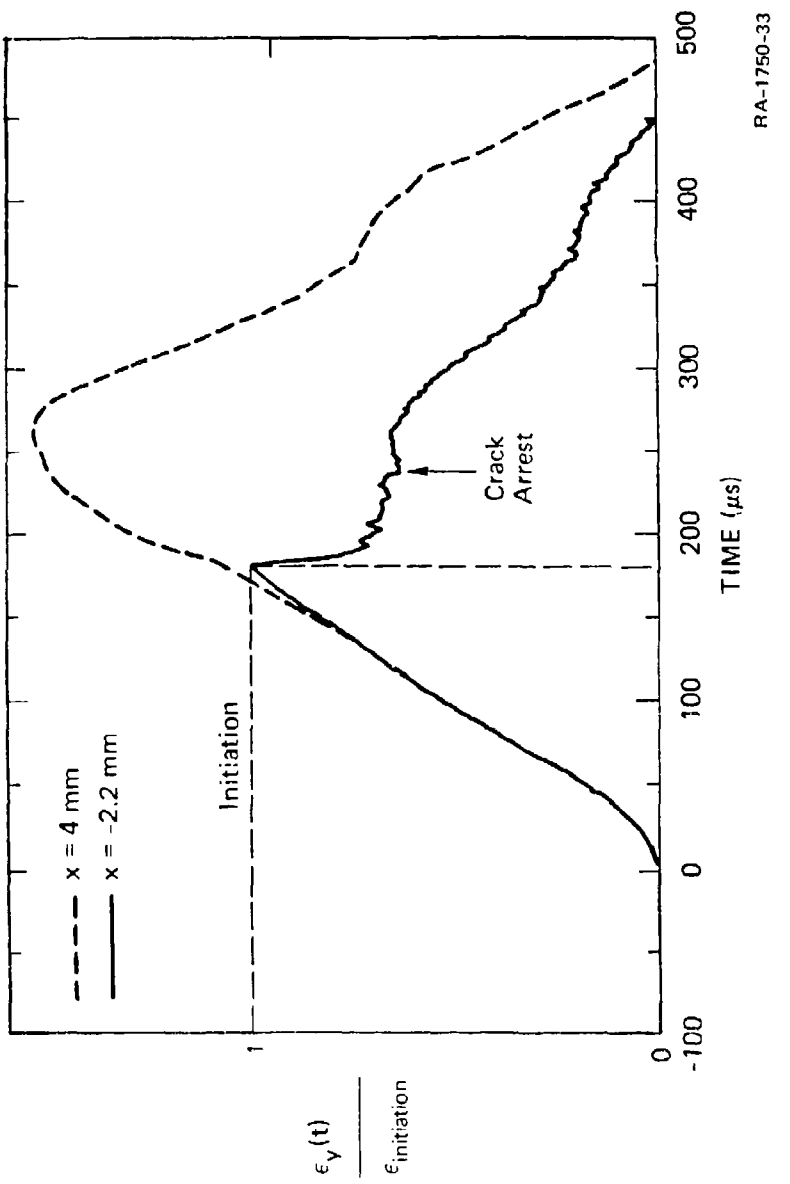
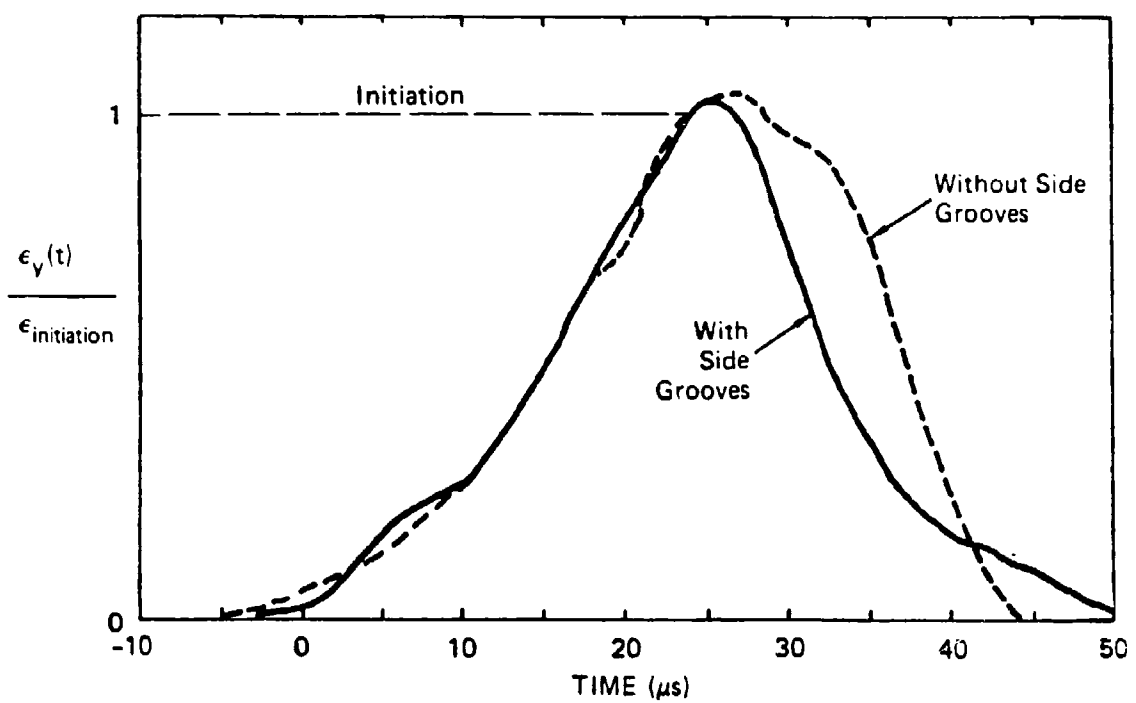


FIGURE C-8 NORMALIZED EXPERIMENTAL STRAIN HISTORY NEAR INITIAL CRACK TIP FOR TWO GAGE POSITIONS \times
Test at low impact velocity.

Another factor that may affect the strain history after crack initiation is plasticity in the crack tip region. In particular, the formation of small shear lips at the free surfaces of the specimen may affect the unloading of the crack tip strain gage. Indeed, when shear lips are present, they are invariably accompanied by a certain degree of crack tunneling so that the tip of the crack in the shear lip lags behind the tip of the crack at the center of the specimen. Therefore, shear lips represent unbroken material ligaments that may continue loading the strain gage, although most of the crack front has already passed the gage position.

To investigate this possibility, we performed 1PB experiments with small 4340 steel specimens. The material was heat treated to a hardness HRC 50. The specimens were 32 mm wide and 133 mm long, 13 mm thick, and had a crack length of 13 mm. Some of the specimens were provided with small side-grooves (0.5 mm wide, 1 mm deep) to suppress the formation of shear lips. In the rest of the specimens, which had smooth side surfaces, 1-mm-wide shear lips were formed upon fracturing. All the specimens were instrumented with a strain gage positioned 3 to 3.5 mm from the crack tip and as shown in Figure C-1. The static calibration method was used to obtain the stress intensity history from the strain records.

Figure C-9 compares the strain history records for side-grooved and ungrooved specimens. For the records shown, the gage position was about 0.3 mm behind the crack tip. The strain drops sooner in the side-grooved than in the ungrooved specimens, suggesting that the formation of even small shear lips may have a significant influence on the strain history after crack initiation. This influence may be direct or indirect. In the first case, the shear lips acts as a small tensile ligament behind the crack front that continues loading the strain gage. According to this explanation, the shear lip would affect the strain history but not the effective propagation toughness and the crack velocity. In the second case, the formation of the shear lips raises the apparent toughness of the material and slows the crack extension. Therefore, the



JA-2777-47A

FIGURE C-9 NORMALIZED EXPERIMENTAL STRAIN HISTORY NEAR THE INITIAL CRACK TIP FOR SIDE-GROOVED AND UNGROOVED SPECIMENS

strain record for the ungrooved specimen in Figure C-9 would drop off later than the strain record for the side-grooved specimen because there is a crack velocity difference in the two tests. Such a crack velocity difference has indeed been observed in experiments in which the average velocity during the first 9 mm of extension was measured with strain gages. Therefore, we conclude that the shear lips have an influence on the strain records, but that this influence reflects an actual rise in the effective propagation toughness. Plasticity at the crack tip may also affect the strain history by inducing residual strains which then prevent a complete unloading of the strain gage. Residual strains will occur particularly if the gage is mounted too close to the crack tip.

Higher order terms in the elasto-dynamic series expansion solution and transient conditions set up by stress waves could also affect the strain history after crack initiation. These effects can be studied only by detailed photoelastic experiments or by numerical simulations of the complete specimen.

CONCLUSIONS

Our analysis of the two strain gage methods of determining stress intensity factor histories in dynamic fracture tests indicates that both methods should give stress intensity estimates within 10% or better of the true value. The static calibration method and the singularity solution method give very consistent results that are within 5% of each other, provided the strain gage is positioned carefully. Therefore, the singularity solution method, which is simpler to implement, can be used with confidence. An angle of 90 degrees from the crack plane and a distance of 3 to 4 mm from the crack tip represent an optimum position for the strain gage, for specimens with length-over-width-ratios greater than 2.6 and widths down to 25 mm.

Experimental estimates of the first higher order term in the series expansion using multiple strain gages indicate that, with the optimum gage position, the influence of this term on the mode I stress intensity is less than 5% and can be neglected. However, for the mode II stress

intensity history, errors of about 35% have been observed for K_{II} by neglecting the effect of the first higher order term.

Simulations of strain histories near the crack tip after initiation show that, depending on the precise gage position and the material toughness, the strain can continue to rise significantly after initiation. Therefore, the instant of crack initiation does not always correspond to the maximum strain and must be determined by comparing the stress intensity history for the fracture curve with the reference stress intensity history (without a crack extension). Finally, the strain history simulations suggest that analysis of the strain history after initiation can provide estimates of the crack velocity and information about the material propagation toughness.

APPENDIX D

MODEL FOR ESTIMATING THE STRESS INTENSITY FACTOR AT THE TIP OF A RUNNING CRACK IN 1PBT

INTRODUCTION

Using the 1PBT to evaluate dynamic initiation fracture toughness relies on the interpretation of strain records from a strain gage placed near the crack tip. Therefore, in addition to evaluating the influence of the higher order terms of the singularity solution, as discussed in Appendix C, we must also understand how the strain history is affected by the position of the strain gage, the loading rate, the initial crack velocity, and the resistance of the material to dynamic crack extension.

To simulate the effect of these parameters on the strain gage records, we have developed a simple model of the 1PBT that allows us to estimate the stress intensity history at the stationary and the running crack tip for various loading rates or material toughness assumptions. From these estimates, we can evaluate the strain history at any given location near the crack tip and compare it with experimental records. Given the initial impact velocity and the crack velocity, the model can also make first order estimates of the propagation toughness without recourse to complex and expensive finite element or finite difference computations. This appendix describes the model and the assumptions on which it is based and compares model predictions with experimental results to demonstrate the validity and limits of the model.

BASIS FOR THE MODEL AND ASSUMPTIONS

The model of the 1PBT is based on experimental observations of the stress intensity history for specimens with different crack lengths and

on several assumptions regarding the dynamics of the specimen. First, we observe from experimental records that the stress intensity history for the LPBT has a smooth approximately sinusoidal shape, controlled mainly by the first mode of oscillation of the specimen. Because later oscillations are of smaller amplitude, they are of no interest in this discussion and we do not attempt to model them. Thus the stress intensity history can be characterized by a maximum amplitude, K_I^{\max} , and a duration T_0 . The dependence of these two parameters on specimen size and material and the impact velocity was discussed in Appendices A and B. In particular, K_I^{\max} is directly proportional to the impact velocity. Theoretical considerations and experimental observations also show that, during a significant part of the initial loading, the stress intensity history is independent of crack length, as illustrated in Figure D-1. We used this observation in developing the model.

We construct our model on the basis of the stress intensity history for a specimen with a stationary crack equal to the initial crack length. We first derive a model to predict the stress intensity history for specimens of the same size but with stationary cracks of lengths greater than the initial crack length. In doing so we assume that the shape of the stress intensity history for the various crack lengths is the same, with only K_I^{\max} and T_0 changing. Further, we assume that the stress intensity factor can be expressed in terms of the crack mouth opening displacement and the static compliance functions. We also make simplifying assumptions regarding the kinematic behavior of the specimen and use momentum considerations to calculate K_I^{\max} and T_0 for each crack length.

To estimate the stress intensity history at the extending crack tip we then assume that, after initiation, the crack mouth opening history can be expressed in terms of the crack mouth opening histories of specimens with stationary cracks of length equal to the current length of the extending crack. In estimating the stress intensity, we do not consider any interaction of stress waves reflected from the specimen

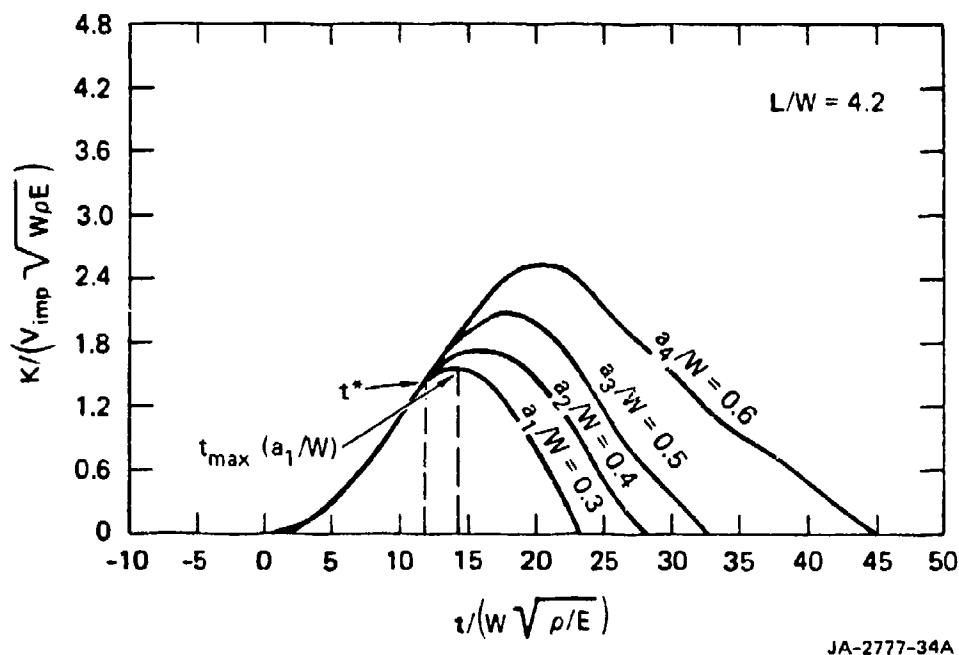


FIGURE D-1 NORMALIZED STRESS INTENSITY HISTORY FOR SPECIMENS WITH DIFFERENT CRACK LENGTH

boundaries with the crack tip. We do, however, consider material inertia effects at the crack tip; they are modeled using a linear approximation to the expression derived by Freund¹ for a crack extending in an infinite plate.

The proposed model is implemented on a desk top computer and calculates stress intensity and crack extension histories incrementally. A listing of the computer program is given at the end of this Appendix. Given the initial impact velocity, two approaches can be taken: either the crack velocity history is known and the resulting stress intensity history is calculated or the material toughness behavior is known and the resulting crack velocity history is calculated. The following sections give a step-by-step account of the model development.

PREDICTION OF THE STRESS INTENSITY HISTORY FOR SPECIMENS WITH STATIONARY CRACK LENGTH GREATER THAN THE INITIAL CRACK LENGTH

We start by assuming that, in a manner similar to the static case for the three-point-bend test, the stress intensity history $K_I^S(t)$ for the 1PBT with a stationary crack can be expressed in terms of the crack mouth opening as

$$K_I^S = \frac{V_{imp}}{V_{imp}^0} \delta_{max} (a/W) f\left(\frac{t}{T_0}\right) \frac{\sqrt{\pi}}{\sqrt{a}} \frac{F(a/W)}{V(a/W)} \quad (D-1)$$

where $F(a/W)$ and $V(a/W)$ are the static compliance functions relating the stress intensity and the crack mouth opening displacement, respectively, to the applied load. The term $f(t/T_0)$ is a shape function representing the shape of the stress intensity history for the specimen with the initial crack length. It is chosen to match the experimentally recorded stress intensity history as closely as possible, within practical limits, with a set of simple functions. The shape function has a maximum, and the time at which this maximum occurs is denoted t_{max} . As noted above, the experimental stress intensity histories for specimens of varying crack length have a common initial portion (Figure D-1). The time at which the stress intensity history for the specimen with the initial

crack length starts diverging from the other stress intensity histories is denoted t^* .

The term $\delta_{\max}(a/W)$ in equation (D-1) is an amplitude parameter that increases with crack length. The value of the amplitude parameter for the specimen with initial crack length is adjusted to match the experimental K_I^{\max} and is an input to the model. v_{imp}^0 is the impact velocity for which the reference stress intensity history for the specimen with initial crack length has been obtained. The product $\frac{v_{imp}}{v_{imp}^0} \delta_{\max}(a/W) f(t/T_0)$ represents the crack mouth opening history $\delta(t/a/W)$ or more precisely,

$$\delta(a/W, t) = \frac{4}{E'} \frac{v_{imp}}{v_{imp}^0} \delta_{\max}(a/W) f(t/T_0) \quad (D-2)$$

where E' is equal to E in plane stress and to $E/(1 - v^2)$ in plane strain.

From experimental observation, we have found that a shape function of the form

$$f\left(\frac{t}{T_0}\right) = \begin{cases} \frac{1}{2} \left[1 + \sin \frac{8\pi}{5T_0} \left(t - \frac{5T_0}{16} \right) \right] & 0 < t \leq 5/8 T_0 \\ \cos \frac{8\pi}{6T_0} \left(t - \frac{5}{8} T_0 \right) & \frac{5}{8} T_0 < t \leq T_0 \end{cases} \quad (D-3)$$

gives a suitable representation of the stress intensity history for a wide variety of specimen geometries. In equation (D-3), t_{\max} has been taken as $(5/8)T_0$. Also based on experimental observations, we assume that t^* is given in terms of T_0 as $(7/16)T_0$. In deriving the stress intensity histories for specimens with longer crack lengths, we will constrain all the curves to pass through this point. Further, we assume that the same shape function applies for every crack length, provided the duration T_0 is made a function of crack length.

Equation (D-1), together with the experimental observation that the initial portion of the stress intensity history is independent of crack length, implies that:

- (1) The crack mouth opening history must have the same shape function as the stress intensity history.
- (2) At a given time, the crack mouth opening must increase with increasing crack length, as illustrated in Figure D-2.

These points will be discussed further when comparing the model predictions with experimental results.

From the foregoing discussion, it follows that predicting the stress intensity history for specimens with stationary crack lengths longer than the initial crack length simply amounts to predicting the maximum amplitude $K_I^{\max}(V_{imp}, a/W)$, or equivalently the amplitude parameter $\delta_{\max}(V_{imp}, a/W)$, and the duration $T_o(a/W)$.

The condition that at time t^* all stress intensity histories must have the same value provides the first equation to calculate these two unknowns:

$$K^s(t^*, a_i/W) = K^s(t^*, a/W) \quad (D-4)$$

A second condition is derived from momentum considerations. We consider the specimen as made up of two rigid halves connected elastically at the crack plane, as shown in Figure D-3. Upon impact, each half of the specimen is imparted a translational velocity, $V_s(t)$, and a rotational velocity $\omega_s(t)$. Under these conditions, conservation of linear momentum requires that

$$mV_s(t) = \int_0^t F(t', a/W) dt' \quad (D-5)$$

where $F(t', a/W)$ is the force applied to the specimen by the impacting hammer and m is the mass of the specimen. Further, conservation of angular momentum requires that

$$\frac{mL^2}{12} \omega_s(t) = \int_0^t F(t', a/W) \frac{L}{2} dt' - \int_0^t M(t', a/W) dt' \quad (D-6)$$

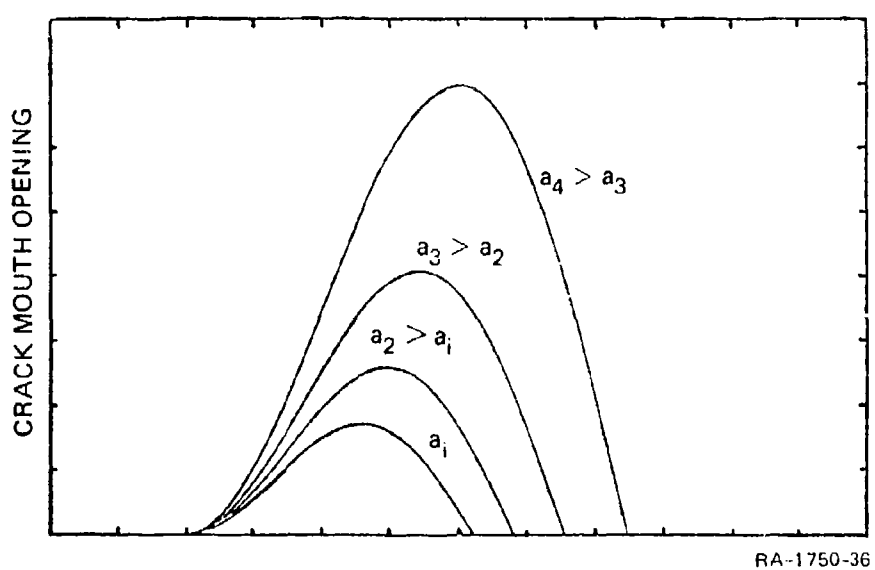
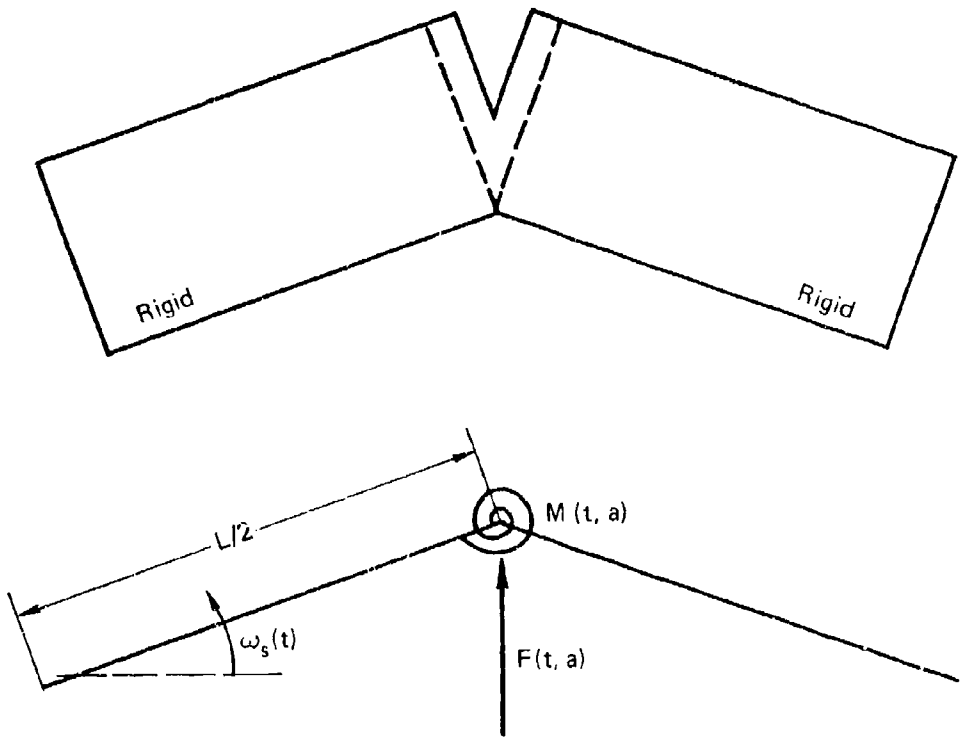


FIGURE D-2 SCHEMATIC OF CRACK MOUTH OPENING HISTORY FOR 1PB SPECIMENS WITH DIFFERENT CRACK LENGTHS



RA-1750-37

FIGURE D-3 SIMPLIFIED KINEMATIC MODEL OF 1PB SPECIMEN

where $M(t', a/W)$ is the resisting moment on the uncracked ligament and L is the specimen length.

At time t_{\max} , the whole specimen has the same uniform velocity $v_s(t_{\max})$ and $w_s(t_{\max}) = 0$. Thus, equations (D-5) and (D-6) become

$$\int_0^{t_{\max}} F(t', a/W) dt' = m v_s(t_{\max}) \quad (D-7)$$

and

$$\int_0^{t_{\max}} F(t', a/W) \frac{L}{2} dt' = \int_0^{t_{\max}} M(t', a/W) dt' \quad (D-8)$$

respectively. If we assume that $v_s(t_{\max})$ is a function of the initial impact velocity, only, and is independent of the crack length of the specimen, then equation D-8 can be rewritten

$$\int_0^{t_{\max}} M(t', a/W) dt' = \text{constant} \quad (D-9)$$

The assumption that $v_s(t_{\max})$ is independent of the specimen crack length implies, through equation (D-7), that the total momentum applied to the specimen up to the point of maximum stress intensity is constant and also independent of crack length. This result will be compared with experimental observations when discussing the model.

Finally, assuming that the moment on the crack plane ligament and the stress intensity factor can be directly related as in the quasi-static case, that is,

$$K_I^S(t, a/W) \sim M(t, a/W) F(a/W) \sqrt{\frac{a}{\pi}} \quad (D-10)$$

equation (D-9) reduces to

$$\int_0^{t_{\max}} \frac{K_I^S(t', a/W)}{F(a/W) \sqrt{\frac{a}{\pi}}} dt' = \text{constant} \quad (D-11)$$

In equations (D-10) and (D-11), we have used the static compliance function $F(a/W)$, which is consistent with the assumption underlying equations (D-1).

The constant on the right-hand side of equation (D-11) can be evaluated by integrating the stress intensity history of the specimen with the initial crack length. Thus, introducing $t_{\max} = \frac{5}{8} T_0$

$$\int_0^{5/8T_0(a/W)} \frac{K_I^S(t', a/W)}{F(a/W) \sqrt{\pi a}} dt' = \int_0^{5/8T_0(a_i/W)} \frac{K_I^S(t', a_i/W)}{F(a_i/W) \sqrt{\pi a_i}} dt'$$

(D-12)

Equations (D-4) and (D-12), combined with equations (D-1) and (D-3), provide the two equations with which to calculate $\delta_{\max}(a/W)$ and $T_0(a/W)$.

Having expressed $\delta_{\max}(a/W)$ and $T_0(a/W)$, we have completed modeling of the stress intensity history for specimens with stationary crack lengths larger than the initial crack length.

EVALUATION OF THE STRESS INTENSITY HISTORY AT THE RUNNING CRACK TIP

Once the material dynamic initiation fracture toughness has been exceeded in a LPBT experiment, the crack will start to propagate at a speed $\dot{a}(t)$. The energy to drive the propagating crack is supplied by the inertial bending of the specimen. Therefore, to evaluate the stress intensity at the extending crack tip, $K_I^P(t, a, \dot{a})$, we extend the approach taken in evaluating the stress intensity history at the stationary crack tip.

Again, we assume that the stress intensity can be expressed in terms of the crack mouth opening displacement as

$$K_I^P(t, a, \dot{a}) = \delta_{\max}(a/W) f\left(\frac{t}{T_0(a/W)}\right) \sqrt{\frac{\pi}{a}} \frac{F(a/W)}{V(a/W)} A\left(\frac{\dot{a}}{C_R}\right) \quad (D-13)$$

In the preceding equation, a is now the current crack length, updated for each time increment. The function $A(\dot{a}/C_R)$ is introduced to account in an approximate way for material inertial effects at the crack tip. Based on Freund's¹ analysis of a crack extending in an infinite plate at constant velocity, and following an approach proposed by Homma et al.,² we take

$$A(\dot{a}/C_R) = 1 - \frac{\dot{a}}{C_R} \quad (D-14)$$

where C_R is the Rayleigh wave speed.

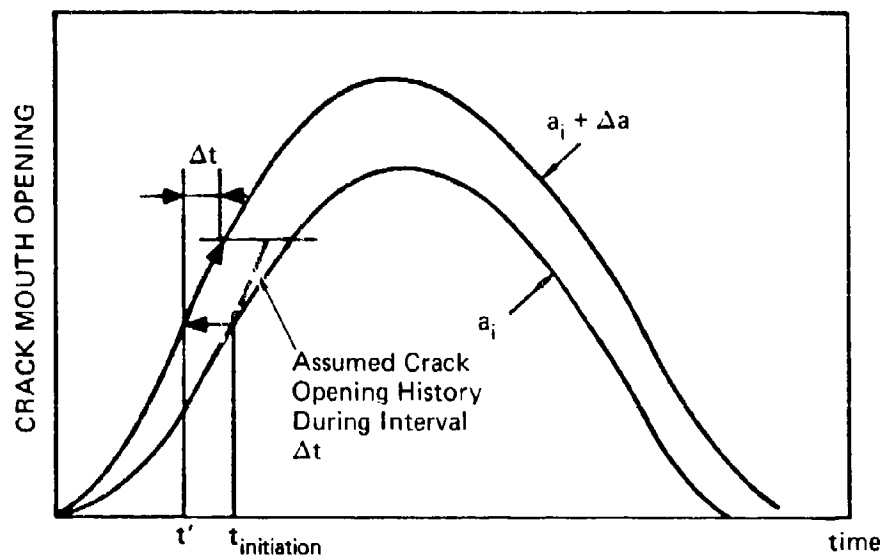
In writing equation (D-13), we assume that the stress intensity at the running crack tip can be expressed as a function of the current crack mouth opening displacement and of the static compliance functions evaluated for the current crack length. To evaluate the current crack mouth opening displacement, or equivalently the term $\delta_{\max}(a/W)f(t/T_0, a/W)$, we assume the behavior illustrated in Figure D-4. For each increment of time after initiation, the crack mouth opening displacement follows the displacement history for the specimen with stationary crack length equal to the current crack length.

If the crack velocity history is not given as an input to the simulation, it is calculated by equating the dynamic stress intensity factor to the propagation fracture toughness, that is,

$$K_I^P(t, a, \dot{a}) = K_{ID}(\Delta a, \dot{a}) \quad (D-15)$$

Here the propagation toughness behavior is assumed known and, for generality, is taken to depend on both the crack velocity and the amount of crack extension Δa .

Thus, at the end of each time step, the crack velocity and the crack length are updated. These values are then used to calculate $K_I^P(t, a, \dot{a})$ during the following time step. $\delta_{\max}(a/W)$ and $T_0(a/W)$ are evaluated, following the procedure described in the preceding section, for a specimen with a stationary crack length equal to the current crack



JA-2777-46A

FIGURE D-4 SCHEMATIC OF CRACK MOUTH OPENING BEHAVIOR ASSUMED IN 1PBT MODEL FOR SPECIMEN WITH PROPAGATING CRACK

length and then introduced in equation (D-13) to obtain $K_I^P(t, a, \dot{a})$. The process is repeated for the next time steps.

In simulations where the crack velocity history is not prescribed, the crack is allowed to extend as long as $K_I^P(t, a, \dot{a})$ exceeds $K_{ID}(\Delta a, \dot{a})$. However, $K_I^P(t, a, \dot{a})$ cannot increase arbitrarily. Depending on the impact velocity and the material toughness, inertial bending of the specimen may stop before the crack reaches the specimen boundary. Referring to the simplified model of Figure D-3, this is the case when the applied force $F(t, a/W)$ and the moment on the remaining ligament $M(t, a/W)$ have brought the specimen to an instantaneous uniform velocity. Consistent with the approach taken in the preceding section, we assume that the point of maximal inertial bending for the specimen with an extending crack is reached when the following condition is met:

$$\int_0^{t_{init}} \frac{K_I^S(t', a_1/W)}{F(a/W) \sqrt{\pi a_1}} dt' + \int_{t_{init}}^t \frac{K_I^P(t', a, \dot{a})}{A(\dot{a}/C_R) F(a/W) \sqrt{\pi a}} dt'$$

$$= \int_0^{5/8 T_o(a_1/W)} \frac{K_I^S(t', a_1/W) dt'}{F(a_1/W) \sqrt{\pi a_1}} \quad (D-16)$$

At each time step in the simulation, the left-hand side of equation (D-16) is evaluated, taking into account that now the crack length is also a function of time. When equation (D-16) is satisfied, the crack mouth opening $\delta_{max}(a/W)f(t/T_o(a/W))$ is made to decrease using the cosine expression in (D-3) for the shape function $f(t/T_o)$.

If the condition in (D-16) is not met before the crack has extended to an a/W value of 0.7, the calculation is stopped. Experimental observations³ and numerical results⁴ indicate that, once the crack extends beyond an a/W value of 0.7, the effect of the compressive zone under the impact point will significantly affect the propagation behavior. The effect of the compressive zone is not considered in our simple approach.

SIMULATION OF STRAINS IN THE VICINITY OF THE STATIONARY AND THE PROPAGATING CRACK

One of the objectives in developing the model of the 1PBT was to simulate the effect of crack extension on the strain records obtained with strain gages placed near the initial crack tip. Improved understanding of the factors affecting these records allows a better determination of the instant of crack initiation. A careful analysis of the drop in strain after crack initiation may also provide information about the resistance of the material to crack extension, as suggested by Böhme and Kalthoff.⁵

Knowing the stress intensity at the tip of the extending crack, we evaluate the strain history at two locations: near the initial crack tip and at a small distance from the crack plane on the path of the extending crack. These positions and their coordinates are shown in Figure D-5.

Simulation of Strain History Near the Initial Crack Tip

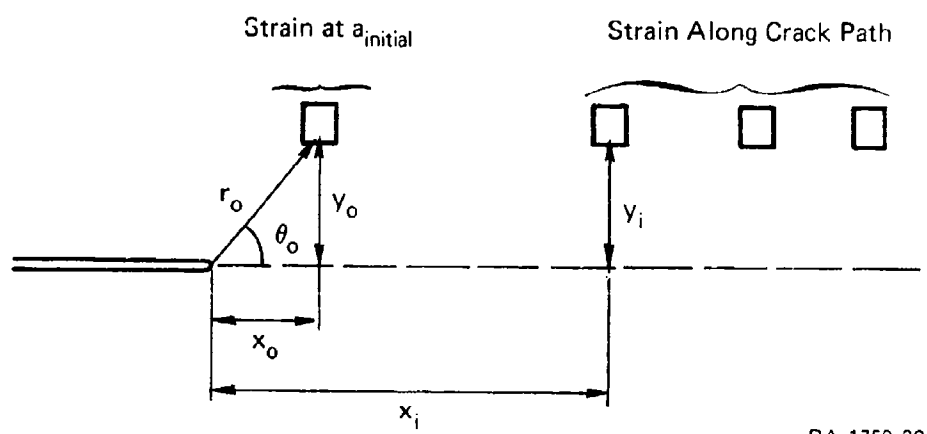
The strain in the direction y , normal to the crack plane, Figure D-5, is evaluated at a position representative of the strain gage position in the 1PBT. The position is defined by the polar coordinates r_o and θ_o with the coordinate system centered at the crack tip (Figure D-5).

The strain is then calculated using the singular term of the elastic solution for the fields at the stationary crack tip to relate the strain to the dynamic stress intensity factor evaluated with the 1PBT, that is,

$$\epsilon_y = \frac{1}{E} \frac{K_I(t)}{\sqrt{2\pi r}} [1 - v + (1 + v)\sin\theta \sin \frac{3}{2}\theta] \quad (D-17)$$

Up to the time of crack initiation, t_{init} , the polar coordinates r and θ are held constant. After crack initiation, they are updated to account for crack extension, with

$$r(t) = \sqrt{[r_o \cos\theta_o - \dot{a}(t - t_{init})]^2 + (r_o \sin\theta_o)^2} \quad (D-18)$$



RA-1750-39

FIGURE D-5 POSITIONS WHERE ϵ_y STRAIN IS EVALUATED AND DEFINITION OF COORDINATES

$$\theta(t) = \arctan \left[\frac{r_o \sin \theta_o}{(r_o \cos \theta_o - \dot{a}(t - t_{init}))} \right] \quad (D-19)$$

Note that using the solution for the stationary crack is no longer strictly correct after initiation because of crack velocity effects on the crack tip field. However, in the absence of transient solution for the accelerating crack, and given the relatively low crack velocities measured in the 1PBT, we believe that this approach gives a satisfying representation.

From equations (D-17) through (D-19), we see that the strain history at the gage location is controlled by the gage position with respect to the initial crack tip position, by the crack velocity, and by the dynamic stress intensity factor. Thus, different combinations of loading rates and material toughness will result in different strain histories. These effects can be simulated with the 1PBT model, and the results can be compared with experimental observations to draw conclusions about the early stage of crack extension.

Simulation of Strain History Along the Crack Path

The strain history at a distance x ahead of the initial crack tip and at a distance y above the crack plane (see Figure D-5) is also evaluated for comparison with experimental measurements. Again an analytical solution is used to relate the strain to the dynamic stress intensity factor at the extending crack tip. In this case we use the solution for a crack extending with a uniform velocity, \dot{a} , in an elastic material.^{6,7} Considering only the singular term of the series expansion and assuming plane stress, the strain in the y -direction is given by

$$\varepsilon_y = \frac{K_I(t, \dot{a})}{\sqrt{2\pi E}} C_1 \left[\frac{\cos \frac{\theta}{2}}{\sqrt{r_1}} (C_4 - v C_2) + \frac{\cos \frac{\theta}{2}}{\sqrt{r_2}} C_3 (1 + v) \right] \quad (D-20)$$

where

$$r_1 = \sqrt{x_i^2 + y_i^2 - \lambda_1^2} \quad \theta_1 = \arccos \frac{1}{r_1}$$

$$r_2 = \sqrt{x_i^2 + y_i^2 - \lambda_2^2} \quad \theta_2 = \arccos \frac{x_i}{r_2}$$

$$\lambda_1 = \sqrt{1 - (\frac{a}{c_1})^2} \quad \lambda_2 = \sqrt{1 - (\frac{a}{c_2})^2}$$

c_1 = plate wave speed (plane stress)

c_2 = shear wave speed

$$c_1 = \frac{1 + \lambda_2^2}{4 \lambda_1 \lambda_2 - (1 + \lambda_2^2)^2} \quad c_2 = (1 + 2 \lambda_1^2 - \lambda_2^2)$$

$$c_3 = \frac{4 \lambda_1 \lambda_2}{1 + \lambda_2^2} \quad c_4 = -(1 + \lambda_1^2)$$

Strain histories evaluated at several positions along the crack plane using different assumptions for the propagation toughness behavior K_{ID} can be compared with experimental strain gage measurements and conclusions can be drawn regarding the actual material propagation toughness.

VERIFICATIONS OF 1PBT MODEL

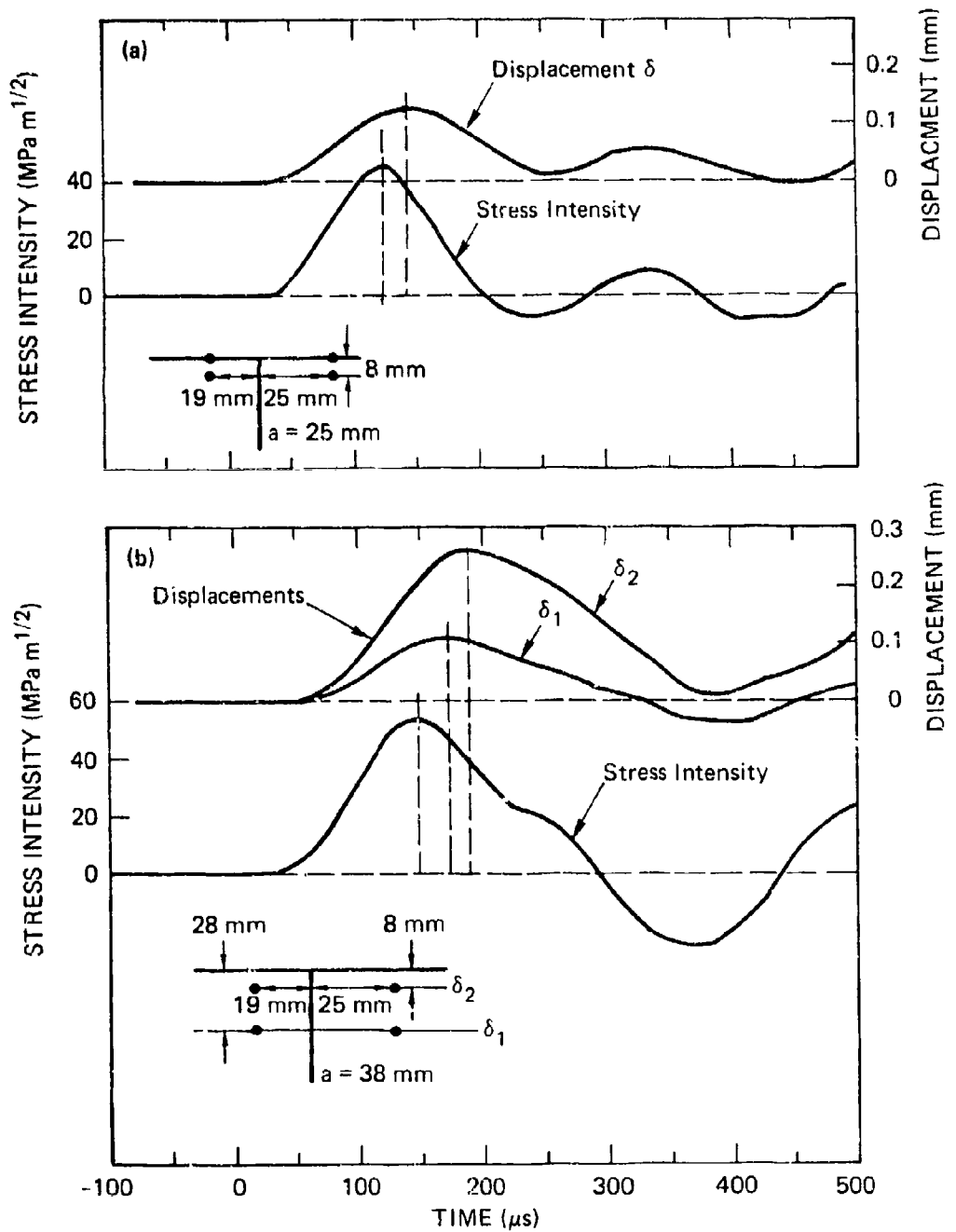
To evaluate the validity of the 1PBT model and of its underlying assumptions we have performed several comparisons with experimental results, which are presented below. Some of the experimental results also provide additional insight in the 1PBT specimen dynamics.

Crack Face Opening Displacement Histories

In the model it is assumed that the stress intensity at the crack tip is proportional to the crack mouth opening displacement, equation (D-1). To investigate this assumption, we measured crack face displacements in two 1PB specimens, using proprietary displacement transducers based on the Hall effect. The specimens were 267 mm long and 63 mm wide and had a/W ratios of 0.4 and 0.6. The specimen with the longer crack was instrumented with two transducers, whereas the specimen with the shorter crack was instrumented with a single transducer. The positions of the transducers are indicated in the inserts in Figure D-6.

Figure D-6 compares the results of the displacement measurements with the stress intensity history measured simultaneously in the specimen. The crack face displacement histories have the same general shape as the stress intensity history for the corresponding specimen, which is in agreement with the 1PBT model assumption. Comparison with the stress intensity history, however, reveals that the maximum in the first displacement oscillation occurs later than the maximum in the stress intensity curve. Further, the time delay between the maxima increases as the transducer distance from the crack tip increases, Figure D-6(b). These observations indicate that it takes a significant time for information to be transferred from the crack tip to the crack mouth. These results are consistent with the observation that, during early times after impact, specimens with the same inplane dimensions but different crack lengths have the same initial stress intensity history. The crack face displacement measurements also indicate that, for a given position from the specimen edge, the displacement increases with increasing crack length, as assumed in Figure D-2.

The displacement measurements demonstrate that the assumption made in the derivation of the 1PBT model is not strictly true; however they show that, in first approximation, the stress intensity history can be considered proportional to the crack face opening displacement some distance from the crack tip during the rising part of the loading.



RA-1750-40

FIGURE D-6 CRACK FACE DISPLACEMENT AND STRESS INTENSITY HISTORIES FOR SPECIMENS WITH DIFFERENT CRACK LENGTHS
 (a) $a/W = 0.4$; (b) $a/W = 0.6$ (inserts show transducer mounting location).

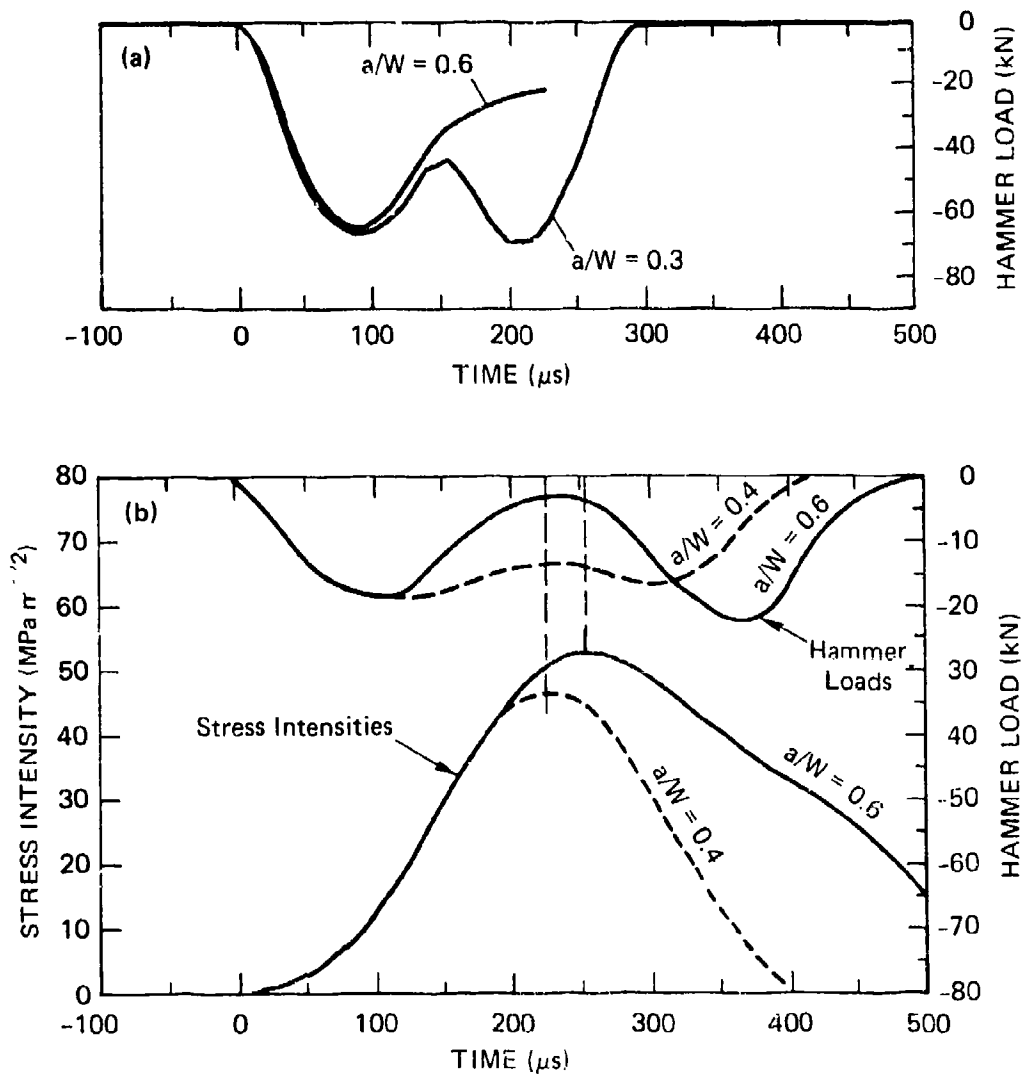
Comparison of Hammer Load History for Specimens of Different Crack Lengths

In deriving the 1PBT model, we also assumed that the total momentum transferred up to the maximum in the stress intensity curve is independent of the specimen crack length. Thus the time integral of the hammer load histories up to the maximum should be the same. To verify this point, we measured the hammer load for two sets of specimens with different crack lengths. The first two specimens were 229 mm long and 89 mm wide and had a/W ratios of 0.3 and 0.6. The hammer load histories for these two specimens are shown in Figure D-7(a). The other two specimens were 267 mm long and 63 mm wide with a/W ratios of 0.4 and 0.6. The hammer load histories and the stress intensity histories for these two specimens are plotted in Figure D-7(b). As for the displacement assumption, it is seen that the area under the hammer load curves is not strictly the same for specimens of two crack lengths, but that the differences are relatively small. Therefore, the assumption made in the model is, in first approximation, acceptable.

Comparison of Experimental and Predicted Stress Intensity Curves for Specimens with Different Stationary Crack Lengths

The procedure described above for predicting the stress intensity history of specimens of different stationary crack lengths was used to estimate the stress intensity history of small specimens (107 mm by 25.4 mm) with a/W ratios of 0.3, 0.4, 0.5, and 0.6. The stress intensity history for the specimen with the a/W = 0.3 was used as input for the estimate.

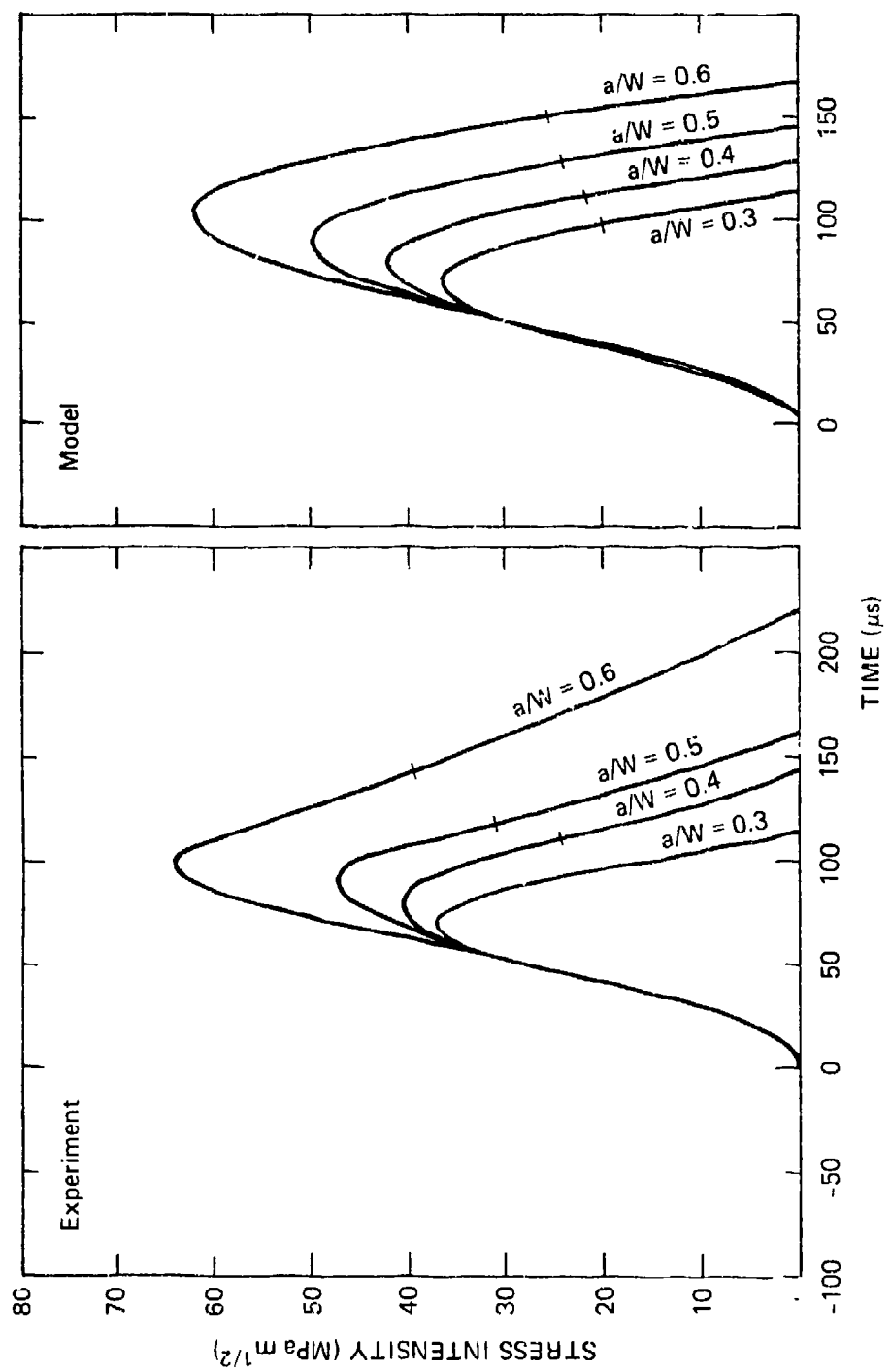
Figure D-8 compares the experimental results with the results of the simulation. The predicted maximum amplitudes and the time at which these amplitudes are reached agree well with the experimental results. The total duration of the stress intensity oscillations do not agree as well because at later times the oscillation mode in the specimens changes, which is not considered in the model. The good agreement between model



RA-1750-41

FIGURE D-7 HAMMER LOAD HISTORIES FOR TWO SPECIMEN GEOMETRIES
EACH WITH TWO DIFFERENT CRACK LENGTH

(a) $L = 229 \text{ mm}$, $W = 89 \text{ mm}$, $B = 9 \text{ mm}$; (b) $L = 267 \text{ mm}$, $W = 63 \text{ mm}$,
 $B = 13 \text{ mm}$)



RA-1750-42

FIGURE D-8 COMPARISON OF EXPERIMENTAL AND PREDICTED STRESS INTENSITY HISTORIES
FOR SPECIMENS OF DIFFERENT CRACK LENGTHS
($L = 107 \text{ mm}$, $W = 25 \text{ mm}$, $B = 13 \text{ mm}$.)

and experiment up to the point of maximum amplitude gives some confidence that the model simulates the essentials of the specimen dynamics.

Comparison of Experimental and Predicted Results for a Fracturing 1PB Specimen

A definitive verification of the simple 1PB model can only be made by comparing the model prediction for a running crack with experimental measurements of the stress intensity history or with numerical simulations of the test using finite element or finite difference codes. We have found in the literature the results of a single 1PB experiment for which the stress intensity history and the crack velocity were measured using the method of caustics for the initial part of crack extension.⁸ A finite difference simulation of the complete crack extension through the specimen is also available.⁴ The experiment was performed with an ARALDITE B specimen. For the simulation, the propagation toughness versus crack speed curve measured in separate experiments was used to govern the crack extension, and the predicted stress intensity and crack extension histories were compared with the experimental results. They were found in excellent agreement.

To test the 1PB model, we used the same approach, combining the experimental toughness versus velocity curve with the applied stress intensity estimated with the model to predict the stress intensity and crack extension histories. In addition to the toughness versus crack velocity curve, the 1PB model requires knowledge of the stress intensity curve for the specimen with a stationary crack of length equal to the initial crack length in the propagation experiment. This curve was estimated from the corresponding curve for a steel specimen, and the initial slope was adjusted to match the slope of the ARALDITE specimen measured in the experiment.

Figure D-9 compares the results of references 4 and 8 and of the stress intensity and crack velocity histories predicted by the 1PB model. During the initial portion of crack extension, the agreement is remarkably good, given the rather crude nature of the 1PB model. At

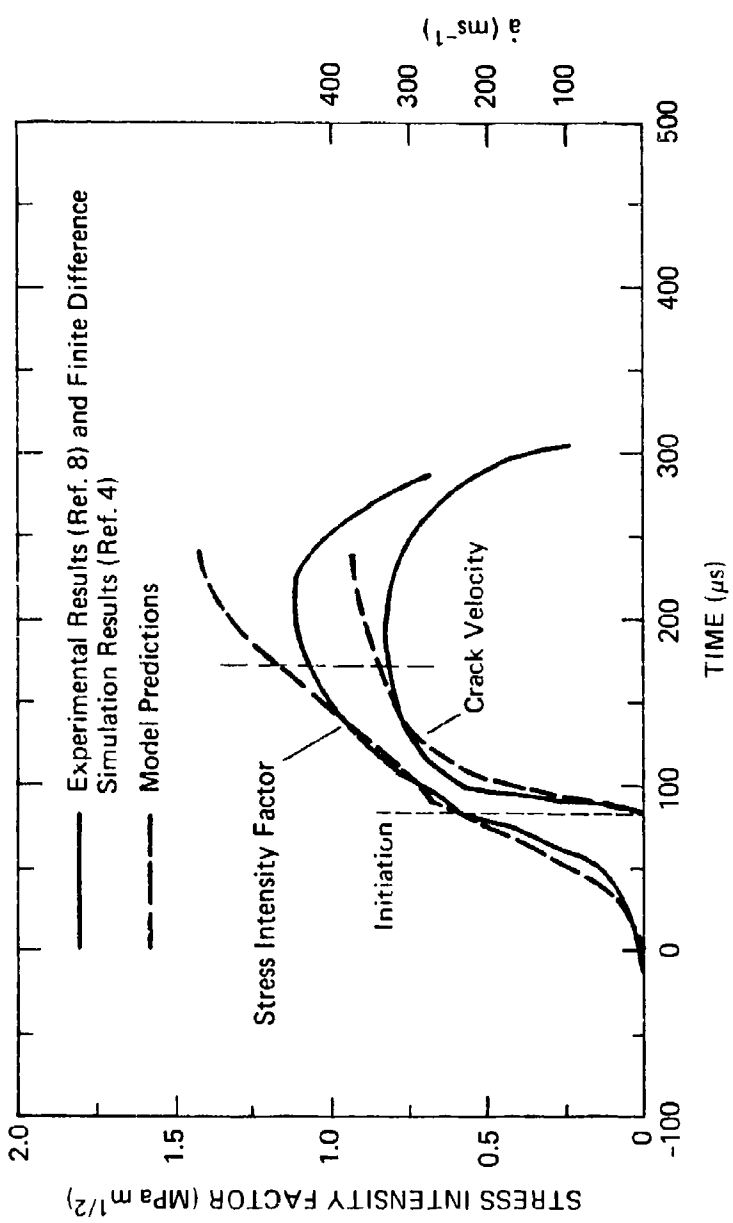


FIGURE D-9 COMPARISON OF 1PBT MODEL PREDICTIONS WITH FINITE DIFFERENCE SIMULATIONS AND EXPERIMENTAL RESULTS
(Material ARALDITE B.)

RA-1750-43

later times, the 1PB model overpredicts both the stress intensity amplitude and the crack velocity; no maximum had been reached at the time the calculation was terminated when a/W exceeded 0.7. This simulation suggests that the simple model of the 1PBT represents the phenomenon of the early part of crack extension correctly. At later times or for larger crack extension, the model does not perform as well and should be used with caution.

USES AND LIMITS OF THE 1PBT MODEL

The 1PBT model was developed to simulate the effect of crack extension on the strain history near the initial crack tip and to obtain engineering estimates of the propagation toughness without having to resort to expensive code calculations. The model is based on a series of simplifying assumptions and on the phenomenological understanding of the experiment. It is based on quasi-static considerations and does not take into account stress wave/crack tip interactions, which are known to be important at high crack velocities.

Experimental verification of the assumptions made in the model show that, although these assumptions are violated, they represent a reasonable first approximation. Further a direct comparison with experimental results and a full-blown computation show that the model approximates well the stress intensity history for specimens with different stationary crack lengths and gives a good approximation of the initial phase of crack extension. Therefore, the 1PBT model is well suited for the applications it was designed for. It has proved very useful in understanding what affects the strain history near the initial crack tip and in evaluating the transition from the stationary to the fast extending crack (Appendices C and G). It can also be used to estimate what specimen geometry and impact conditions should be chosen to achieve certain crack extension conditions in a given material.

Beyond these applications great care should be used. The results in Figure D-9 show that the model is not suited to making predictions for crack extension to large a/W values and that it provides only an estimate

of the stress intensity and crack velocity histories. Therefore, for longer crack extensions and for crack arrest, the model should at best be used to make qualitative comparison between various propagation behaviors.

REFERENCES FOR APPENDIX D

1. L. B. Freund, "Crack Propagation in an Elastic Solid Subjected to General Loading -I. Constant Rate of Extension," *J. Mech. Phys. Solids*, Vol. 20, pp. 129-140 (1972).
2. H. Homma, T. Ushiro, and H. Nakazawa, "Dynamic Crack Growth under Stress Wave Loading," *J. Mech. Phys. Solids*, Vol. 27, pp. 151-162 (1979).
3. W. Böhme, and J. F. Kalthoff, "Untersuchungen des Bruchverhaltens schlagbelasteter Dreipunktbiegeproben unter Einsatz verschiedener Messverfahrens der Spannungsanalyse," *VDI-Bericht*, Vol. 480, pp. 23-27 (1983).
4. H. Stöckl, and W. Böhme, "Numerische Simulation von Kerbschlagbiegeversuchen an Proben aus Araldit B und Stahl," *Fraunhofer-Institut für Werkstoffmechanik*, Report W 4/83 (September 1983).
5. W. Böhme and J. F. Kalthoff, "Der Einfluss der Probengroesse auf dynamische Effekte bei der K_{Id} -Bestimmung im Kerbschlagbiegetest," *Fraunhofer-Institut für Werkstoffmechanik*, Report W 3/83 (1983).
6. G. R. Irwin, R., "Constant Speed Semi-Infinite Tensile Crack Opened by a Line Force P, at a Distance b, from the Leading Edge of the Crack Tip," *Lehigh University Lecture Notes* (1968).
7. G. R. Irwin, "Series Representation of the Stress Field Around Constant Speed Cracks," *University of Maryland Lecture Notes* (1980).
8. J. F. Kalthoff, W. Böhme, and S. Winkler, "Analysis of Impact Fracture Phenomena by Means of the Shadow Optical Method of Caustics," presented at the VIIth International Conference SESA, Haifa, Israel, August 23-27, 1982.

1PBT MODEL: LISTING OF COMPUTER PROGRAMS

```

10 ! PROGRAM TO SIMULATE THE PROCESS OF CRACK INITIATION AND CRACK PROPAGATION
11 ! UNDER DYNAMIC LOADING CONDITIONS IN THE ONE-POINT-BEND SPECIMEN
12 !
13 ! THE PROGRAM CONTAINS A BEST APPROXIMATION OF THE EXPERIMENTALLY MEASURED
14 ! STRESS INTENSITY HISTORY FOR THE DYNAMIC LOADING OF THE STATIONARY CRACK
15 ! AND USES FREUND'S EXPRESSION FOR THE STRESS INTENSITY FACTOR AT THE TIP
16 ! OF THE RUNNING CRACK.
17 !
18 ! DURING PROPAGATION, THE CRACK SPEED IS EVALUATE USING HOMMA'S ET AL.
19 ! PROCEDURE
20 !
21 ! SEVERAL MATERIAL TOUGHNESS BEHAVIORS ARE INVESTIGATED AND CAN BE CHOSEN
22 ! FROM A MENU
23 !
24 ! DEFINITION OF MATERIAL PROPERTIES: Young IS YOUNG'S MODULUS, Mu IS
25 ! POISSON'S RATIO, Rho IS THE MASS DENSITY AND Cr IS THE RAYLEIGH
26 ! WAVE VELOCITY
27 !
28 ! Young=2.1E+11
29 ! Mu=.3
30 ! Rho=7800
31 ! Cr=(.87+1.12*Mu)/(1+Mu)*SQR(Young/2/(1+Mu)/Rho)
32 ! Cp=SQR(Young/Rho*(1-Mu)/(1-2*Mu))
33 ! Cs=SQR(Young/2/(1+Mu)/Rho)
34 !
35 ! OPTION BASE 1
36 ! DIM Velo(20)
37 ! PRINTER IS 1
38 ! INPUT "ENTER SCALE FACTOR FOR VELOCITY = ",Scvel
39 ! INPUT "SCALE FACTOR FOR TIME, (1 OR 10)",Sc
40 ! INPUT "SCALE FACTOR FOR K, (1 OR 10)",Sk
41 ! INPUT "SCALE FACTOR FOR STRAIN 6000/Scs",Scs
42 ! INPUT "PLOT FRAME ? (Y/N)",Cont$"
43 ! INPUT "PRINT DATA ? (Y = 1, N = 0)",Prinvar
44 ! PRINT "KCONT = ? (1, THEN K(t)-CURVE IS PLOTTED; OTHERWISE Epsiy(t) IS
45 ! PLOTTED )"
46 ! INPUT Kcont
47 ! IF Kcont<>1 THEN
48 !     PRINT "WHERE DO YOU WANT TO CALCULATE STRAIN ? (INITIAL CRACK : 0
49 !           ALONG CRACK PATH : 1"
50 !     INPUT Strplot
51 ! END IF
52 ! INPUT "NUMBER OF VELOCITY AVERAGING POINTS N ?",N
53 !
54 ! Step=30 ! CONTROLS TIME STEP IN THE CALCULATION
55 !
56 ! GEOMETRIC PARAMETERS FOR SPECIMEN
57 !
58 ! A0=.033    ! INITIAL CRACK LENGTH
59 ! W=8.89E-2   ! WIDTH
60 !
61 ! T0=2.05E-4 ! STRESS INTENSITY HISTORY DURATION
62 !
63 ! T1=T0
64 ! Impfac=1.537E+7 ! STRESS INTENSITY AMPLITUDE PARAMETER
65 ! X0=-8.E-4 ! X-COORDINATE OF POINT WHERE STRAIN IS EVALUATED
66 ! Y0=.005    ! Y-COORDINATE OF POINT WHERE STRAIN IS EVALUATED
67 !
68 !
69 !
70 !
71 !
72 !
73 !
74 !
75 !
76 !
77 !
78 !
79 !
80 !
81 !
82 !
83 !
84 !
85 !
86 !
87 !
88 !
89 !
90 !
91 !
92 !
93 !
94 !
95 !
96 !
97 !
98 !
99 !
100 !
101 !
102 !
103 !
104 !
105 !
106 !
107 !
108 !
109 !
110 !
111 !
112 !
113 !
114 !
115 !
116 !
117 !
118 !
119 !
120 !
121 !
122 !
123 !
124 !
125 !
126 !
127 !
128 !
129 !
130 !
131 !
132 !
133 !
134 !
135 !
136 !
137 !
138 !
139 !
140 !
141 !
142 !
143 !
144 !
145 !
146 !
147 !
148 !
149 !
150 !
151 !
152 !
153 !
154 !
155 !
156 !
157 !
158 !
159 !
160 !
161 !
162 !
163 !
164 !
165 !
166 !
167 !
168 !
169 !
170 !
171 !
172 !
173 !
174 !
175 !
176 !
177 !
178 !
179 !
180 !
181 !
182 !
183 !
184 !
185 !
186 !
187 !
188 !
189 !
190 !
191 !
192 !
193 !
194 !
195 !
196 !
197 !
198 !
199 !
200 !
201 !
202 !
203 !
204 !
205 !
206 !
207 !
208 !
209 !
210 !
211 !
212 !
213 !
214 !
215 !
216 !
217 !
218 !
219 !
220 !
221 !
222 !
223 !
224 !
225 !
226 !
227 !
228 !
229 !
230 !
231 !
232 !
233 !
234 !
235 !
236 !
237 !
238 !
239 !
240 !
241 !
242 !
243 !
244 !
245 !
246 !
247 !
248 !
249 !
250 !
251 !
252 !
253 !
254 !
255 !
256 !
257 !
258 !
259 !
260 !
261 !
262 !
263 !
264 !
265 !
266 !
267 !
268 !
269 !
270 !
271 !
272 !
273 !
274 !
275 !
276 !
277 !
278 !
279 !
280 !
281 !
282 !
283 !
284 !
285 !
286 !
287 !
288 !
289 !
290 !
291 !
292 !
293 !
294 !
295 !
296 !
297 !
298 !
299 !
300 !
301 !
302 !
303 !
304 !
305 !
306 !
307 !
308 !
309 !
310 !
311 !
312 !
313 !
314 !
315 !
316 !
317 !
318 !
319 !
320 !
321 !
322 !
323 !
324 !
325 !
326 !
327 !
328 !
329 !
330 !
331 !
332 !
333 !
334 !
335 !
336 !
337 !
338 !
339 !
340 !
341 !
342 !
343 !
344 !
345 !
346 !
347 !
348 !
349 !
350 !
351 !
352 !
353 !
354 !
355 !
356 !
357 !
358 !
359 !
360 !
361 !
362 !
363 !
364 !
365 !
366 !
367 !
368 !
369 !
370 !
371 !
372 !
373 !
374 !
375 !
376 !
377 !
378 !
379 !
380 !
381 !
382 !
383 !
384 !
385 !
386 !
387 !
388 !
389 !
390 !
391 !
392 !
393 !
394 !
395 !
396 !
397 !
398 !
399 !
400 !
401 !
402 !
403 !
404 !
405 !
406 !
407 !
408 !
409 !
410 !
411 !
412 !
413 !
414 !
415 !
416 !
417 !
418 !
419 !
420 !
421 !
422 !
423 !
424 !
425 !
426 !
427 !
428 !
429 !
430 !
431 !
432 !
433 !
434 !
435 !
436 !
437 !
438 !
439 !
440 !
441 !
442 !
443 !
444 !
445 !
446 !
447 !
448 !
449 !
450 !
451 !
452 !
453 !
454 !
455 !
456 !
457 !
458 !
459 !
460 !
461 !
462 !
463 !
464 !
465 !
466 !
467 !
468 !
469 !
470 !
471 !
472 !
473 !
474 !
475 !
476 !
477 !
478 !
479 !
480 !
481 !
482 !
483 !
484 !
485 !
486 !
487 !
488 !
489 !
490 !
491 !
492 !
493 !
494 !
495 !
496 !
497 !
498 !
499 !
500 !
501 !
502 !
503 !
504 !
505 !
506 !
507 !
508 !
509 !
510 !
511 !
512 !
513 !
514 !
515 !
516 !
517 !
518 !
519 !
520 !
521 !
522 !
523 !
524 !
525 !
526 !
527 !
528 !
529 !
530 !
531 !
532 !
533 !
534 !
535 !
536 !
537 !
538 !
539 !
540 !

```

```

550 Vt0=Impfac*Scvel ! COMBINED STRESS INTENSITY AMPLITUDE PARAMETER
560 !
570 !
580 !
590 !
600 PRINTER IS 705
610 !
620 !
630 ! COMPUTATION OF POLAR COORDINATES
640 X=X0
650 Y=Y0
660 R=SQR(X^2+Y^2)
670 IF X=0 THEN
680 Theta=PI/2
690 Theta1=Theta/PI*180
700 GOTO 790
710 END IF
720 IF X>0 THEN
730 Theta=ATN(Y/X)
740 Theta1=Theta/PI*180
750 GOTO 790
760 END IF
770 Theta=PI+ATN(Y/X)
780 Theta1=Theta/PI*180
790 GOSUB 2430
800 !
810 ! COMPUTATION OF STATIC COMPLIANCE AND STRESS INTENSITY FUNCTIONS FOR
820 ! SPECIMEN WITH INITIAL CRACK LENGTH
830 Faw0=1.09-1.735*A0/W+8.2*(A0/W)^2-14.18*(A0/W)^3+14.57*(A0/W)^4
840 Vaw0=.76-2.28*A0/W+3.87*(A0/W)^2-2.04*(A0/W)^3+.66/(1-A0/W)^2
850 K0=Vt0*Faw0/Vaw0/(A0^.5)*(1+SIN(PI/5))
860 !
870 Impulse0=5/16*T1*Vt0/A0/Vaw0 ! REFERENCE IMPULSE PARAMETER
880 !
890 ! Kid IS THE TOUGHNESS OF THE MATERIAL AT ANY TIME
900 !
910 ! Kidd IS THE INITIATION TOUGHNESS OF THE MATERIAL
920 !
930 Kidd=5.7E+7
940 !
950 PRINTER IS 1
960 !
970 ! INITIALIZATION OF VARIOUS VARIABLES
980 !
990 A=A0
1000 T1=T0
1010 T00=T0
1020 T=0
1030 Tt=0
1040 Vt=Vt0
1050 Velo=0
1060 Kid=Kidd
1070 FOR I=1 TO N
1080 Velo(I)=0
1090 NEXI I
1100 Skip=0
1110 Switch=0
1120 Impulse=0
1130!
1140!

```

```

1150! TIME ITERATIONS
1160!
1170!
1180 FOR I=0 TO 500*Step/Sc
1190 T=I*1.E-6/Step
1200 Tt=Tt+1.E-6/Step
1210 T0=T00
1220 Vt0-Vt
1230! DEFINITION OF F(A/W) AND V(A/W) FOR BEND SPECIMENS
1240!
1250 Faw=1.09-1.735*A/W+8.2*(A/W)^2-14.18*(A/W)^3+14.57*(A/W)^4
1260 Vaw=.76-2.28*A/W+3.87*(A/W)^2-2.04*(A/W)^3+.66/(1-A/W)^2
1270!
1280!
1290! CALCULATION OF K FOR BEND SPECIMENS
1300!
1310! UPDATE OF STRESS INTENSITY HISTORY DURATION
1320 IF Switch=1 THEN GOTO 1470
1330 T001=T1-5.E-7
1340 T001=(T001+T00)/2
1350 T00=T1/(1+SIN(PI/5))*Faw/Faw0*SQR(A/A0)*(1+SIN(8*PI/5/T001*(7/16*T1-5/16*T001)))
1360 IF ABS(T00-T001)<1.E-6 THEN GOTO 1380
1370 GOTO 1340
1380 Vt=K0/(1+SIN(8*PI/5/T00*(7/16*T1-5*T00/16)))/Faw*Vaw*A^.5
1390 Tt=ASN(Vt0/Vt*(1+SIN(8*PI/5/T0*(Tt-5*T0/16))-1)/(8*PI/5/T00)+5*T00/16
1400 Kt=.5*(1+SIN(8*PI/5/T00*(Tt-5*T0/16)))
1410 Impulse=Impulse+Vt*Kt/A/Vaw*1.E-6/Step ! CURRENT IMPULSE PARAMETER
1420 IF Impulse>=Impulse0 THEN
1430     Switch=1
1440     GOTO 1470
1450     END IF
1460     GOTO 1520
1470 IF Skip=1 THEN GOTO 1510
1480 Skip=1
1490 Vt=.5*(1+SIN(8*PI/5/T00*(Tt-5*T00/16)))*Vt
1500 Tt=5/8*T00
1510 Kt=COS(8*PI/6/T00*(Tt-5/8*T00))
1520 K=Vt*Kt*SQR(PI/A)*Faw/Vaw*(1-1.*Vel/Cr)
1530! K=Vt*Kt*SQR(PI/A)*Faw/Vaw
1540 GOTO 1570
1550!
1560!
1570 IF K<=0 AND T>T00/20 OR T>T00 THEN GOTO 2470
1580 IF K<Kidd AND Vel<1 THEN
1590     GOTO 2060
1600     END IF
1610!
1620!
1630!
1640! HERE WE CALCULATE THE CRACK VELOCITY Vel
1650!
1660 Kk=K/(1-1.*Vel/Cr)
1670! Kk=K
1680! DEFINITION OF THE PROPAGATION TOUGHNESS FUNCTION IS INTRODUCED HERE
1690!
1700 Kid=Kidd
1710!
1720! CALCULATION OF CRACK VELOCITY (AVERAGED OVER N ITERATIONS)
1730 FOR J=1 TO N-2
1740 Velo(N-J)=Velo(N-J-1)

```

```

1750 NEXT J
1760 Velo(1)=Vel
1770 Vel=(1-Kid/Kk)*1.00*Cr
1780 IF Vel<0 THEN Vel=0
1790 Vv=Vel
1800 FOR J=1 TO N-1
1810 Vv=Vv+Velo(J)
1820 NEXT J
1830 Vel=Vv/N
1840!
1850!
1860! HERE WE UPDATE THE CRACK LENGTH AND THE COORDINATES OF THE STRAIN GAGE
1870!
1880 A=A+Vel*1.E-6/Step
1890 IF A/W>.7 THEN GOTO 2470
1900 X=X-Vel*1.E-6/Step
1910 R=SQR(X^2+Y^2)
1920 IF X=0 THEN
1930   Theta=PI/2
1940   Theta1=Theta/PI*180
1950   GOTO 2030
1960 END IF
1970 IF X>0 THEN
1980   Theta=ATN(Y/X)
1990   GOTO 2020
2000 END IF
2010 Theta=PI+ATN(Y/X)
2020 Theta1=Theta/PI*180
2030!
2040! HERE WE CALCULATE THE STRAIN MEASURED BY THE STRAIN GAGE AT THE INITIAL
CRACK TIP
2050!
2060 IF Kcont=1 THEN GOTO 2370
2070 IF Strplot=1 THEN GOTO 2140
2080 H=1/(SQR(SIN(Theta))*COS(Theta/2)*(1+SIN(Theta/2)*SIN(3*Theta/2)-Mu*(1-
SIN(Theta/2)*SIN(3*Theta/2))))
2090 Epsiy=K/Young/H/SQR(2*PI*Y0)
2100 GOTO 2330
2110!
2120! HERE WE CACULATE THE STRAIN ALONG THE CRACK PATH
2130!
2140 IF Vel=0 THEN
2150   Epsiy=0
2160   GOTO 2330
2170 END IF
2180 L1=(1-(Vel/Cp)^2)^.5
2190 L2=(1-(Vel/Cs)^2)^.5
2200 C1=(1+L2^2)/(4*L1*L2-(1+L2^2)^2)
2210 C2=1+2*L1^2-L2^2
2220 C3=(4*L1*L2)/(1+L2^2)
2230 C4=-1+L2^2
2240 R1=SQR(X^2+L1^2*Y0^2)
2250 R2=SQR(X^2+L2^2*Y0^2)
2260 Cost1=X/R1
2270 Cost2=X/R2
2280 Rr=SQR(X^2+Y0^2)
2290 Theta=ACOS(X/Rr)
2300 Rz1=SQR(Cost1+1)/SQR(2*R1)
2310 Rz2=SQR(Cost2+1)/SQR(2*R2)
2320 Epsiy=C1*(Rz1*(C4-Mu*C2)+Rz2*(1+Mu)*C3)/Young/SQR(2*PI)*K
2330 IF Epsiy<0 AND Kcont<>1 THEN

```

```

2340 I=500/Sc*Step
2350 GOTO 2520
2360 END IF
2370 GOSUB 2820
2380 NEXT I
2390 GOTO 2470
2400!
2410! PLOTTING OF STRESS INTENSITY, CRACK VELOCITY AND STRAIN HISTORIES
2420!
2430 PRINT "IN:IP224,767,9764,7608;SP2;"
2440 PRINT "SC-200,600,-50,250;PA-100,230;DI;"
2450 PRINT "PU;PA 0.0;""
2460 RETURN
2470 INPUT "DO YOU WANT TO PLOT CRACK VELOCITY (Y=1,N=0)",Velcont
2480 IF Velcont=1 THEN
2490   PRINT "LT2;""
2500   GOTO 360
2510 END IF
2520 IF Cont$="N" THEN GOTO 2810
2530 PRINT "PU;PA-100,0;LT"
2540 FOR I=1 TO 12
2550 PRINT "PD; TL0.5,0;XT;PU;CP-2,-1.;LB";(-150+I*50)/Sc;"PA".-100+50*(I-1),
",0;PD;PR50,0;""
2560 NEXT I
2570 PRINT "PU;CP-2,-1;LB";500/Sc;"PA100,-23;LBTIME [microsecs.];PU;PA-100,0
;PD;""
2580 IF Kcont<>1 THEN GOTO 2640
2590 FOR I=1 TO 8
2600 PRINT "PD;TL0.5,0;YT;PU;CP-5-,5;LB";(I*10-10)*Sk;"PA-100.",25*I-25.";PD
;PR0.25;""
2610 NEXT I
2620 PRINT "PU CP-4,-0.5;LB";80*Sk;"PA-160.20;DI0,1;LBSTRESS INTENSITY FACTOR
[MPa-m1/2.];"
2630 GOTO 2680
2640 FOR I=1 TO 5
2650 PRINT "PD;TL0.5,0;YT;PU;CP-5-,5;LB";(I*600-600)*2/Sc;"PA-100.",40*I-40
,";PD;PR0.40;""
2660 NEXT I
2670 PRINT "PU CP-4,-0.5;LB";6000/Sc;"PA-160.38;DI0,1;LBSTRAIN [microstrain.
];"
2680 PRINT "PA-100,200;PD;""
2690 FOR I=1 TO 12
2700 PRINT "PD;TL0,0.5;XT;PR50,0;""
2710 NEXT I
2720 IF Kcont<>1 THEN GOTO 2770
2730 FOR I=1 TO 8
2740 PRINT "PD;TL0,0.5;YT;PR0,-25;""
2750 NEXT I
2760 GOTO 2800
2770 FOR I=1 TO 5
2780 PRINT "PD;TL0,0.5;YT;PR0,-40;""
2790 NEXT I
2800 PRINT "PU;PA0,0;""
2810 GOTO 3120
2820 PRINTER IS 705
2830 IF Kcont<>1 THEN GOTO 2920
2840 IF Kcont=1 AND Velcont=1 THEN
2850   PRINT "PD;PA",I*Sc/Step,"","Vel*2.5/10;""
2860   GOTO 2940
2870 END IF
2880 !

```

```
2890! PRINT "PD;PA",I*Sc/Step,".",Vt*Kt*2.5/1.E+6/Sk,;"  
2900 PRINT "PD;PA",I*Sc/Step,".",K*2.5/1.E+6/Sk,;"  
2910 GOTO 2940  
2920 IF Epsiy<0 THEN Epsiy=0  
2930 PRINT "PD;PA",I*Sc/Step,".",Epsiy/1.5E-5/2*Scs,;"  
2940 RETURN  
2950 PRINTER IS 1  
2960 END
```

Appendix E

CRACK INITIATION AND EXTENSION IN STEEL FOR SHORT LOADING TIMES

Paper appeared in the Proceedings of DYMAT '85, International Conference on Mechanical and Physical Behavior of Materials Under Dynamic Loading, Paris, September 2-5, 1985, les Editions de Physique, France, 1985, pp. C5-171 through C5-178.

CRACK INITIATION AND EXTENSION IN STEEL FOR SHORT LOADING TIMES

J.H. Giovanola

SRI International, 333 Ravenswood Avenue, Menlo Park, California 94025, U.S.A.

Résumé - On a étudié les conditions d'instabilité d'une fissure dans un acier à haute résistance pour des temps de charge courts (aussi courts que 25 μ s) en utilisant un essai dynamique de flexion avec mise en charge par inertie (flexion un point). On trouve que pour le domaine de vitesses de charge considéré, un critère de rupture incorporant le temps n'est pas nécessaire. Par contre la résistance à la propagation peut croître de façon marquée avec l'avance de la fissure, en raison de la formation de lèvres de cisaillement même faibles.

Abstract - The one-point bend impact test has been used to investigate crack instability conditions for short loading times (as short as 25 μ s) in high strength steel. It was found that, in the range of loading rates investigated, no time-modified fracture criterion need be invoked. The resistance to crack extension may, however, increase significantly with crack growth due to the formation of even small shear lips.

I - INTRODUCTION

In recent years, considerable attention has been given to the prediction of crack instability under high loading rates. It is now well understood that, because of inertia and stress wave effects, the stress intensity history for dynamically loaded cracks is often significantly different from the stress intensity history anticipated from quasi-static considerations /1-5/.

Further, several experimental results suggest that, for very rapid loading (a few microseconds or less), the classical quasi-static linear elastic fracture mechanics criterion for crack instability must be modified to account for microstructural rate effects /5-8/. On the basis of experiments for very short duration loads (less than 2.2 μ s), Kalthoff and Shockley /5/ postulated that cracks would become unstable only after the dynamic fracture toughness had been exceeded for a minimum time. Based on fracture tests with pulse loads of several durations (18 to 80 μ s), Homma et al. /6/ have estimated that, for AISI 4340 steel in the R_c 50 condition, the minimum time for fracture should be about 7 μ s. There is, however, some uncertainty regarding this value, because the fracture toughness reported in reference 6 is only about one half the value reported in the literature for similar loading rates. More recently, Ravi-Chandar and Knauss /7/ found that, when the time required to load a crack to instability in Homalite 100 is gradually decreased below 50 μ s, the stress intensity value at which the crack becomes unstable increases rapidly. For a loading time to fracture of 10 μ s, the stress intensity factor at instability is about twice the value when the loading time is 50 μ s or more. Kalthoff /8/ has rationalized this behavior by suggesting that a so-called incubation time is necessary to nucleate, grow, and coalesce microdefects ahead of the macrocrack. Conceptually, the incubation time is similar to the minimum time postulated by Kalthoff and Shockley /5/.

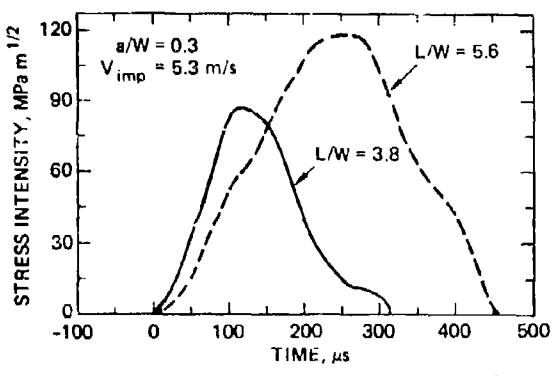
This work attempted to establish whether fracture incubation time has a significant influence on crack instability conditions in high strength steel at conventional

dynamic loading rates, that is, for fracture times down to 25 μ s. In evaluating the experimental crack initiation results, attention was also given to the conditions controlling the first increments of crack extension.

II - EXPERIMENTAL PROCEDURES

Investigation of the crack instability conditions for high loading rates requires detailed knowledge of the dynamic stress intensity history experienced by the crack tip. To obtain well-characterized stress intensity histories in which the loading rate could be easily varied, we used a novel experimental technique, the one-point bend impact test (1PBT) /9-11/.

The 1PBT uses a single-edge-cracked specimen and the same testing arrangement as a conventional three-point bend impact test, except that the end supports are removed. When the hammer strikes the specimen, the center portion of the specimen is accelerated away from the hammer, whereas the end portions of the specimen lag behind because of inertia. This causes the specimen to bend and to load the crack tip. The resulting stress intensity histories do not show the undesirable oscillations that often characterize the three-point bend impact test, but rather are smoothly varying, as shown in Figure 1 for two specimens with blunt notches and with different length-over-width ratios. The maximum stress intensity amplitude and the duration of loading are readily adjusted by changing the impact velocity and the specimen geometry, respectively. Varying these parameters in combination also allows the loading rate to be varied.



JA-2777-37

FIGURE 1 STRESS INTENSITY HISTORY FOR SPECIMEN USED IN DYNAMIC FRACTURE TESTS [Impact Velocity $V_{imp} = 5.3$ m/s; Specimen Dimensions Thickness $B = 13$ mm, Width $W = 64$ mm, Crack Length $a = 19$ mm; Length $L = 241$ mm (full line curve) and 356 mm (dashed line curve)]

The stress intensity histories in Figure 1 were obtained by measuring the crack tip strain intensification with a calibrated strain gage placed near the crack tip. The measured strain was then related to the applied stress intensity using a calibration factor, determined in an independent quasi-static three-point bend calibration experiment /12/. This method was also used for all the dynamic fracture experiments reported in this paper.

To investigate whether incubation time affects the dynamic crack instability condition, we performed a series of dynamic fracture experiments at three stress intensity rates (3.3×10^5 , 5×10^5 , and 3×10^6 MPa $\text{m}^{1/2} \text{s}^{-1}$), using the 1PBT. The material tested was AISI 4340 aircraft quality steel, quenched and tempered to a Rockwell hardness of 50. The specimens used for the tests at the low and intermediate stress intensity rates were 356 mm long, 64 mm wide, and 13 mm thick. The ratio of crack length to specimen width was 0.3 for the low rate tests and 0.4 for the intermediate rate tests. The lower loading rates were obtained by impacting the specimen at 3.5 and 5.3 m/s with a striker mounted on a Charpy pendulum machine. The specimens used for the tests at the high stress intensity rate were 241 mm long, 64 mm wide, and 13 mm thick. The ratio of crack length to specimen width was 0.3. The specimens were impacted at 50 m/s using a compressed air launcher to accelerate a steel striker plate. The reference stress intensity history for these specimens is shown in Figure 1. All specimens were fatigue-precracked according to ASTM standard E399, instrumented with a strain gage near the crack tip, and calibrated.

To complement the dynamic fracture tests, the quasi-static fracture toughness was measured in triplicate following the standard ASTM E399 procedure.

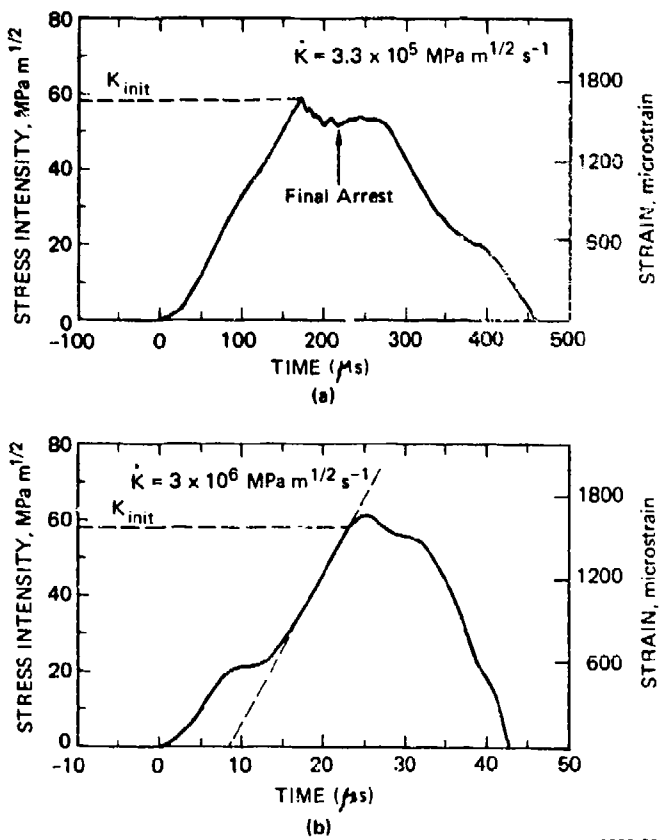
The effect of incubation time was tested as follows. In the tests at the low stress intensity rate, the specimens were impacted at a velocity sufficient to produce a maximum stress intensity slightly above the anticipated critical value. The loading times to fracture were about 100 μs , well above the anticipated incubation time. Thus, these tests provided a measure of the dynamic fracture toughness, K_{Id} . The high rate tests were designed to determine an eventual incubation time. In these tests the specimens were grossly overloaded by increasing the impact velocity. This resulted in times to fracture of 20 to 25 μs . Thus if fracture incubation time is important and of the order of several microseconds, we expected fracture to occur at significantly higher stress intensity values than the value measured in the low rate tests. The difference between the time at which the K_{Id} value was reached and the time of instability would provide an estimate of the incubation time. The intermediate rate tests provided additional data to monitor the influence of the loading rate on the value of the stress intensity factor at crack initiation.

III - EXPERIMENTAL RESULTS

Figure 2 shows typical stress intensity histories measured at the low and high loading rates. The point of crack initiation is also indicated. Since the stress intensity factor is calculated from a strain gage measurement, the curves in Figure 2 represent the true stress intensity history only up to the point of crack initiation. Beyond this point, the stress intensity at the running crack tip is no longer simply proportional to the recorded strain. Therefore, the corresponding strain scale is also given in Figure 2.

At the low and intermediate loading rates, crack initiation caused a clear drop in the measured strain; therefore, the point at which the stress intensity for initiation is evaluated can be easily determined. At the high loading rate, the strain history has a smoother appearance. A simulation of the effect of crack growth on the strain record (discussed in the next section) indicates that, depending on the strain gage position, the loading rate, and the crack growth behavior, a strain overshoot above the point of crack initiation is possible. Thus the point of initiation was chosen as the point of separation of the recorded strain history from a straight line fitted to the main portion of this curve, see Figure 2(b).

At the low loading rate, the crack started to propagate and then arrested after tunnelling 2 to 5 mm. The arrest point can be clearly seen in Figure 2(a). At the intermediate and high rates, the specimens fractured completely. In the low and intermediate rate tests, the jagged appearance of the strain records immediately after initiation suggests that crack extension occurred by a series of run-arrest events, Figure 2(a).



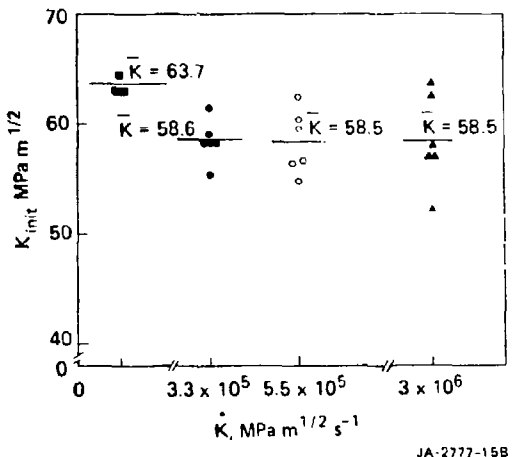
JA-2777-38

FIGURE 2 STRESS INTENSITY HISTORY FOR (a) LOW RATE TEST
(b) HIGH RATE TEST

The results of the static and dynamic fracture experiments are plotted in Figure 3 as ϵ a function of stress intensity rate. Although the scatter in data increases with loading rate, the average value of the dynamic initiation stress intensity factor K_{init} is essentially the same for the three elevated rates, about $58.5 \text{ MPa m}^{1/2}$, and only slightly (8%) lower than the static fracture toughness value of $63.7 \text{ MPa m}^{1/2}$.

IV - SIMULATION OF STRAIN RECORDS IN ONE-POINT BEND TESTS

To interpret the strain records obtained in the 1PBT correctly and to gain some insight in to the crack extension phase in the 1PBT, we developed a simple phenomenological model of the test to estimate the stress intensity at the stationary and running crack tip. It is only discussed briefly here; details are given elsewhere (see J. H. Giovanola, Poulter Laboratory Report, SRI International, in preparation). The model is based on the stress intensity history measurements for specimens with stationary cracks of various lengths. It assumes that the 1PBT is displacement controlled, with the first flexural mode of the specimen controlling the stress intensity at the crack tip. The model accounts for the effect of crack extension and for the effect of material inertia on the stress intensity at the



JA-2777-15B

FIGURE 3 SUMMARY OF FRACTURE TEST RESULTS
FOR FOUR STRESS INTENSITY RATES

crack tip. It is implemented on a microcomputer and calculates the stress intensity at regular small time intervals. During each time increment, the crack velocity is calculated using the current stress intensity and the current toughness value according to a procedure proposed by Homma et al. /13/. The current toughness is an adjustable variable of the model.

The strain records obtained in the LPBT can be simulated by calculating the stress intensity history with the model and by relating stress intensity and strain with the elastic singularity solution /14/. We studied the effect on the records of gage position with respect to the crack tip as well as the influence of different initiation and propagation fracture toughness assumptions.

We examined two postulated toughness behaviors. In one case, we assumed the material toughness K_{mat} was constant equal to the initiation toughness K_{Id}

In the other case, a toughness rising with crack extension was assumed, i.e.,

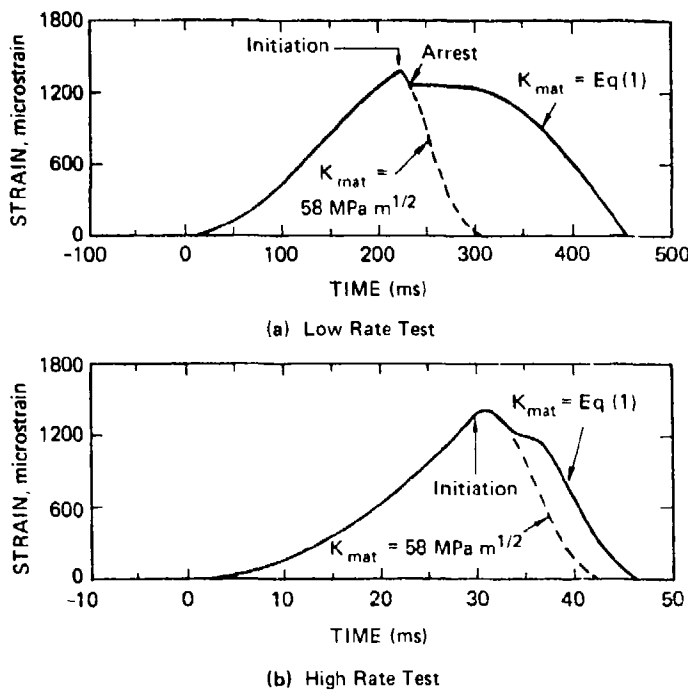
$$\begin{aligned} K_{mat} &= 58 && \text{for } \Delta a < 0.5 \\ K_{mat} &= 58 + 14(\Delta a - 0.5) && \text{for } 0.5 < \Delta a < 1.5 \\ K_{mat} &= 72 && \text{for } \Delta a > 1.5 \end{aligned} \quad (1)$$

where K_{mat} is in $\text{MPa m}^{1/2}$ and Δa is in mm.

Strain simulations for the low rate and high rate experiments are shown in Figure 4 for the two assumed toughness behaviors, using the classical fracture criterion for initiation and extension

$$K_{mat} = K_{appl} \quad (2)$$

where K_{appl} is the applied stress intensity.



JA-2777-39

FIGURE 4 SIMULATION OF EXPERIMENTAL STRAIN RECORDS
FOR TWO TOUGHNESS ASSUMPTIONS

The experimental strain records were simulated well by the model, provided expression (2) was used for the toughness. A constant toughness predicts a very rapid strain drop at the crack tip and an excessive arrested crack length. Expression (2) yields better agreement with the experimental strain profiles; the arrest crack length is somewhat underestimated. An optimum simulation of both strain profile and arrest crack length was achieved when slightly different resistance curve expressions were used for the low and the high rate experiments. Note that, as mentioned before, the strain in Figure 4(b) continues to rise beyond the point of crack initiation, irrespective of the toughness assumption.

V - DISCUSSION

The results of the dynamic fracture tests show that, within the range of loading rates studied, the stress intensity factor at initiation is $58.5 \text{ MPa m}^{1/2}$ and essentially constant. This value is about 92% of the static toughness and represents the dynamic initiation fracture toughness K_{Id} . This suggests that a fracture incubation time is unimportant for these loading rates. Further, our results imply that, if a fracture incubation time exists, it is much smaller than the times to fracture of 20 to 25 μs considered here.

These conclusions are consistent with estimates of the incubation time based on the kinetics of microstructural damage. Microdamage models /15,16/ based on a viscous damage growth law and calibrated with high rate experimental data indicate that the characteristic time for the nucleation and growth of microvoids and microcracks should be of the order of a microsecond. If the incubation time is interpreted as the time it takes for microvoids or microcracks to nucleate and grow at the crack tip, then it should be of the order of the characteristic time for these processes.

Our conclusions are also consistent with recent results obtained for a high strength steel by Kalthoff /17/. It was found that, down to fracture times of about 20 μ s, the stress intensity at initiation remains more or less constant. However, when the time to fracture was decreased to about 5 μ s, a sharp increase in the stress intensity at initiation was observed.

The simulation of the IPBT predicted initiation well using the classical initiation criterion $K_{app} = K_{Id}$. However, to simulate the strain records after initiation we had to postulate a rising dynamic toughness resistance curve. Such an assumption may be justified, considering that small shear lips (roughly 1 mm in width) were formed during the crack extension phase and that the arrested cracks in the low loading rate experiments had a thumbnail shape. Shear lips and a bowed crack front are known to increase the apparent toughness in static fracture tests. In additional experiments, in which the specimens had been side-grooved to suppress the formation of shear lips, the strain records dropped much more abruptly (as predicted by the simulations with a constant toughness) than in the experiments where shear lips formed, although the value of the stress intensity factor at initiation remained the same. These latter results, together with the simulations of the tests, therefore suggest that the formation of even small shear lips significantly affects the strain history recorded after crack initiation. The shear lip acts as an unbroken ligament that continues to load the strain gage as the crack extends. As a consequence, the shear lip may also considerably increase the material resistance to dynamic crack extension. This effect needs to be assessed more precisely, in particular to determine if it is sensitive to crack velocity.

VI - CONCLUSIONS

We conclude that, for fracture times in excess of 20 μ s, the crack initiation conditions for 4340 steel in the Rockwell hardness 50 (and probably for other similar high strength alloys) are not influenced by a fracture incubation time. Rather, our work indicates that the initiation conditions can be determined solely by using the classical concepts of fracture mechanics. In relatively thin sections, the resistance to dynamic crack extension may rise significantly due to the formation of shear lips and to crack tunnelling. In these situations the concept of resistance curve must be invoked to predict crack extension.

ACKNOWLEDGMENTS

This work was supported by the U.S. Air Force Office of Scientific Research under Contract AFOSR/F49620-81-K-007 and was monitored by Drs. Alan H. Rosenstein and Ivan L. Caplan. The author thanks Dr. D. A. Shockley, Project Supervisor, Dr. J. F. Kalthoff, and Dr. T. Kobayashi for helpful discussions during this study.

REFERENCES

- /1/ Mechanics of Fracture, Volume 4: Elastodynamic Crack Problems, Sih, G. C., Ed., Noordhoff International Publishing, Leyden (1977).
- /2/ Sih, G. C., Embley, G. T. and Ravera R. J., Int. J. Solids Structures 8 (1972) 977.
- /3/ Embley, G. T. and Sih, G. C., Proc. 12th Midwestern Mechanics Conference, 6 (1971); see also Sih, G. C., Handbook of Stress Intensity Factors, Institute of Fracture and Solid Mechanics, Lehigh University, Bethlehem, PA, p. 8.5.2-1 (1973).
- /4/ Freund, L. B., J. Mech. Phys. Solids 21 (1973) 47.
- /5/ Kalthoff, J. F. and Shockley, D. A. J. Appl. Phys. 48 (1977) 984.

/6/ Homma, H., Shockey, D. A. and Murayama, Y., J. Mech. Phys. Solids 31 (1983) 261.

/7/ Ravi-Chandar, K. and Knauss, W. G., unpublished data presented and discussed in reference 8.

/8/ Kalthoff, J. F., "On Some Current Problems in Experimental Fracture Dynamics, in Workshop on Dynamic Fracture, Knauss, W. G., Ravi-Chandar, K. and Rosakis, A. J., Eds., California Institute of Technology (1983), p. 11.

/9/ Kalthoff, J. F., Winkler, S., Bohme, W. and Shockey, D. A., Proceedings of the International Conference on the Dynamical Properties and Fracture Dynamics of Engineering Materials, Institute of Metallurgy, Czechoslovak Academy of Science, 61662 Brno Czechoslovakia (June 1983).

/10/ Kalthoff, J. F., Bohme, W. and Winkler, S., "Verfahren zum Bestimmen mechanischer Werkstoffkennwerte und Vorrichtung zur Durchfuhrung des Verfahrens," Patent Disclosure Deutsches Patentamt (June 1983).

/11/ Giovanola, J. H., Proceedings of ASTM 17th National Symposium of Fracture Mechanics, Albany, NY, (August 1984), to appear; see also Giovanola J. H., Poulter Laboratory Technical Report 005-84, SRI International (1984).

/12/ Loss, J. F., Hawthorne, J. R. and Griffis, C. A., "Fracture Toughness of Light Water Reactor Pressure Vessel Materials," Naval Research Laboratory Memorandum Report 3036 (April 1975).

/13/ Homma, H., Ushiro, T. and Nakazawa, H., J. Mech. Phys. Solids 27 (1979) 151.

/14/ Williams, M. L., J. Appl. Mech. 24 (1957) 109.

/15/ Curran, D. R., Seaman L. and Shockey, D. A. "Linking Dynamic Fracture to Microstructural Processes," in Shock Waves and High Strain Rate Phenomena in Metals: Concepts and Applications, Meyers, M. A. and L. E. Murr, Eds., Plenum Press, New York (1981) p. 129.

/16/ Seaman, L., Curran D. R., Murri, W. J., J. Appl. Mech., to appear; see also Seaman L., Poulter Laboratory Technical Report 001-80, SRI International (1980).

/17/ Kalthoff, J. F., Proceedings of the International Conference on Dynamic Fracture Mechanics, San Antonio, Texas (1984), to appear.

Appendix F

DYNAMIC MIXED-MODE CRACK INITIATION

INTRODUCTION

In numerous practical applications, cracks are not subjected to pure mode I loading, but rather to a combination of mode I and mode II loading. Mixed-mode loading particularly occurs under dynamic loading conditions where loading from reflected waves or from structural vibrations can be superimposed on the primary loads. In addition, the degree of mixed-mode loading strongly influences the crack propagation path. Therefore, we need to understand how mixed-mode loading conditions affect crack initiation and extension. Although several investigations have been performed for crack initiation under mixed-mode static loading, no consistent mixed-mode crack initiation theory is yet available. For the dynamic case, very few, if any, initiation data are available to evaluate mixed-mode crack initiation models.

The objectives of the work described in this appendix were to develop a testing technique capable of producing controlled dynamic mixed-mode loading conditions at a stationary crack tip and to generate dynamic mixed-mode initiation data in order to develop failure criterion. The significant progress made toward these objectives is described below.

DEVELOPMENT OF A METHOD TO PRODUCE CONTROLLED DYNAMIC MIXED-MODE LOADING CONDITIONS.

To produce controlled dynamic mixed-mode loading conditions, we chose to build on our experience with the inertia-loaded 1PBT specimen and to modify it to introduce a mode II loading component at the crack

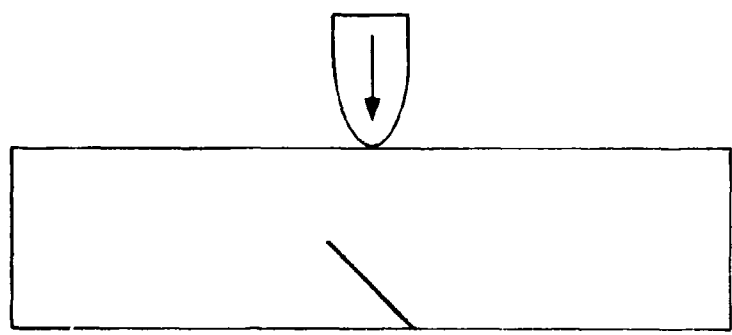
tip. Figure F-1 shows three configurations capable of producing dynamic mixed-mode loading. The configuration in Figure F-1(a) has been investigated by Barnes et al.¹ The configuration in Figure F-1(b) is a variation designed to preserve specimen symmetry. Variation in the mixed-mode ratio can be achieved by changing the inclination of the cracks with respect to the impact direction. The configurations in Figure F-1(a) and (b) both present the disadvantage that they make it difficult to introduce a controlled sharp fatigue crack. Therefore, we adopted the double-crack configuration shown in Figure F-1(c), which allows fatigue precracking in pure mode I in an easy way.

For all the work reported here we chose specimens 267 mm long and 63.5 mm wide. The mode I and mode II stress intensity factors were obtained from strain measurements near the crack tip using three strain gages mounted at angles of 45°, 90°, and 135°. The method is described in detail in Appendix C.

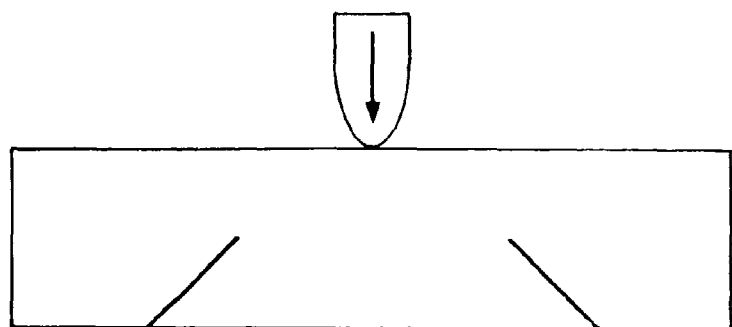
Double-Crack 1PBT Configuration

We investigated the double crack specimen response by performing calibration experiments on specimens with blunt notches to avoid crack initiation. Figure 2 shows the mode I and mode II stress intensity histories for the unsupported double-crack specimen later used in the fracture experiments for impact velocities of 1.7, 2.3, and 4.3 m s⁻¹. The crack length is 38 mm, and the distance between cracks, 2D, is 102 mm as shown in Figure F-1(c). Comparison of the stress intensity histories indicates that, as the impact velocity is increased, the mode of vibration that dominates the specimen response changes. This change is evidenced by the shorter duration of the mode I stress intensity history at 4.3 m s⁻¹ than at 2.3 m s⁻¹ and by the oscillations appearing on the

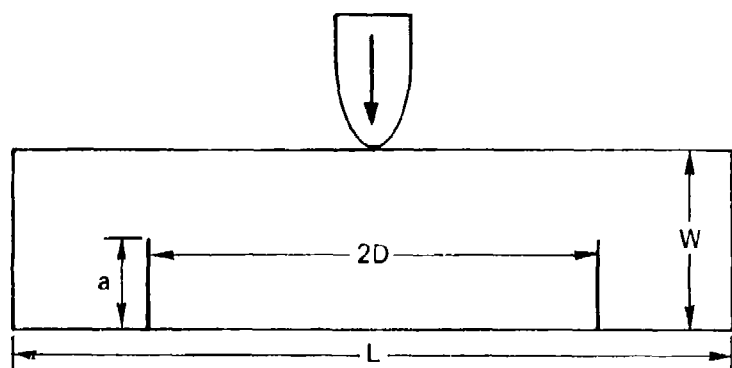
¹C. R. Barnes, J. Ahmad, and M. F. Kanninen, "Analysis of Mixed-Mode Crack Growth in a Ship Hull Material," Proceedings of the Army Symposium on Solid Mechanics, 1982-Critical Mechanics Problems in Systems Design, AMMRC-MS 82-4 (1982).



(a) Single Slanted Crack



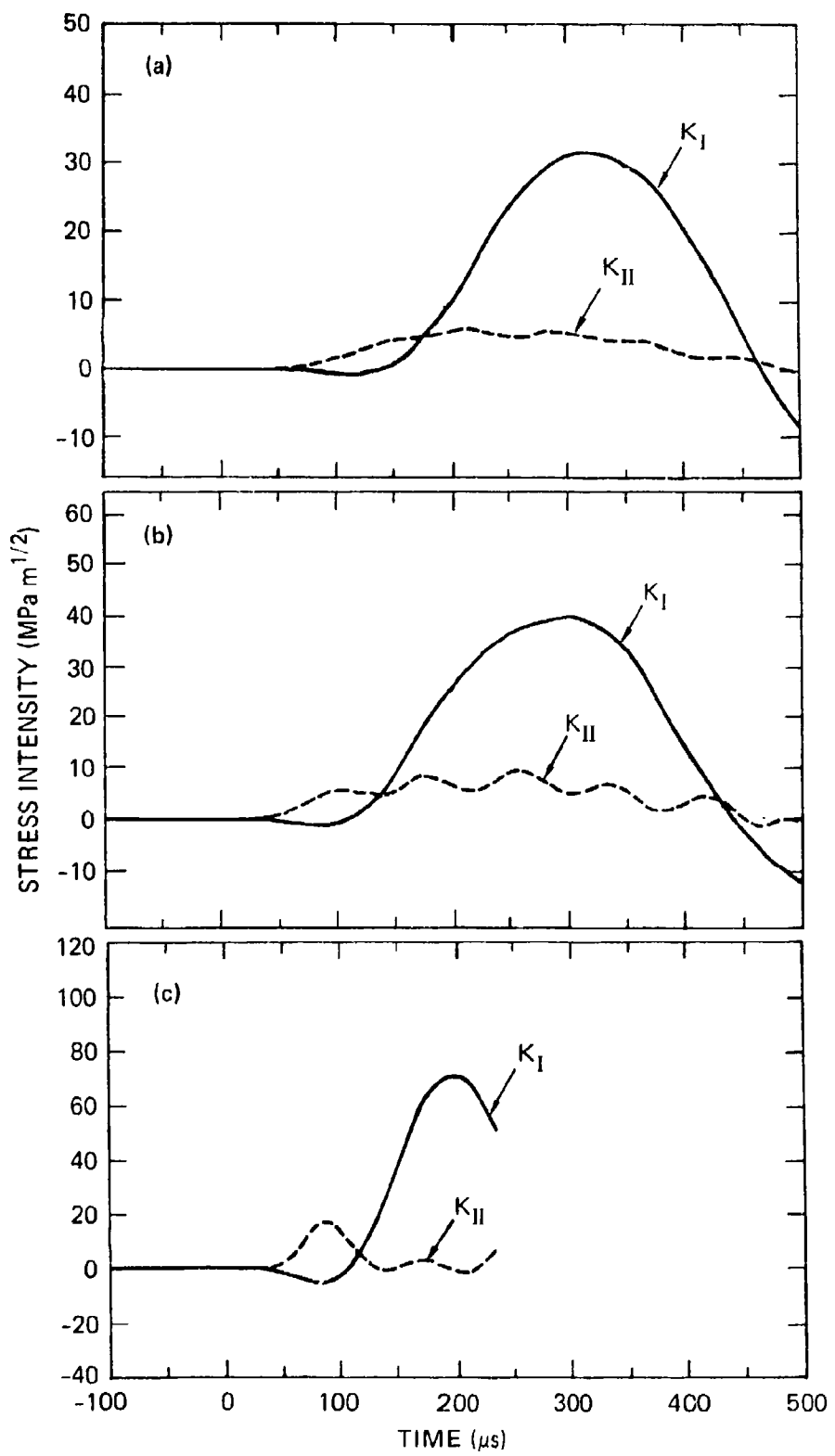
(b) Symmetric Slanted Crack



(c) Double Vertical Crack

RA-1750-70

FIGURE F-1 POSSIBLE SPECIMEN CONFIGURATIONS TO OBTAIN
MIXED-MODE LOADING IN 1PBT



RA-1750-73

FIGURE F-2 STRESS INTENSITY HISTORIES FOR 1PB DOUBLE-CRACK SPECIMEN
WITH $2D = 102 \text{ mm}$, $a/W = 0.6$

(a) $V_{imp} = 1.7 \text{ ms}^{-1}$, (b) $V_{imp} = 2.3 \text{ ms}^{-1}$, (c) $V_{imp} = 4.3 \text{ ms}^{-1}$.

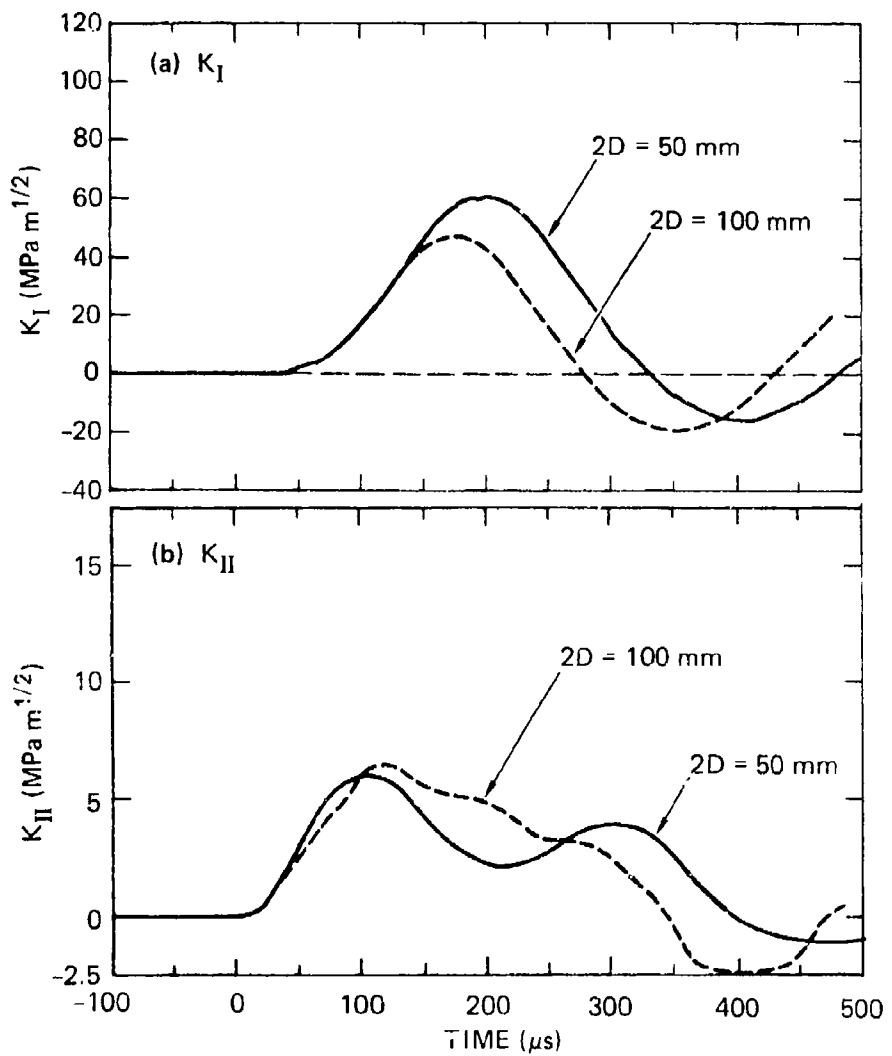
mode II stress intensity history for 2.3 m s^{-1} . The mechanism of this vibrational mode change is not yet understood. The later part of the stress intensity histories was not obtained at higher velocity because of triggering problems for the test at 4.3 m s^{-1} and because the specimen broke during the next calibration test at 12 m s^{-1} . The stress intensity calibrations of interest for the fracture tests are those obtained for impact velocities of 4.3 m s^{-1} and higher.

The calibration tests at 4.3 and 12 m s^{-1} demonstrated that, once the higher vibrational modes dominate the specimen response, no further change in the shape of the stress intensity history occurs. Further, the amplitudes of the stress intensity history scale proportionally to the impact velocity as is the case in the single crack 1PBT. Figure F-2(c) shows that, on impact, K_{II} first goes through a maximum and then drops back to essentially zero. K_I , however, becomes slightly negative at first (compressive load on the crack tip) and then has a sinusoidal history. Thus, K_I is either negative or small during the major portion of the K_{II} history.

We tested additional specimens to investigate how changing the crack length and the crack spacing affects the stress intensity histories. For these additional calibration experiments no changes in the dominant vibrational mode were observed for impact velocities up to 4.3 m s^{-1} , and we presume that no change will occur for higher velocities.

Figure F-3 shows the effect of varying the distance $2D$ between cracks from 50 to 100 mm keeping the crack length constant at 19 mm . For the K_I histories in Figure F-3(a), the time scales have been shifted by about $20 \mu\text{s}$ with respect to each other, and for the K_{II} histories in Figure F-3(b), they have been shifted by about $8 \mu\text{s}$ to account for the difference in arrival time at the crack tip of the flexural and shear waves, respectively, caused by the difference in crack spacing.

The early part of the K_I histories is the same for both crack positions, except that K_I becomes slightly negative at first for the specimen with the larger value of $2D$. They start diverging once the stress waves reflected at the far end of the specimen reach the crack



RA-1750-75

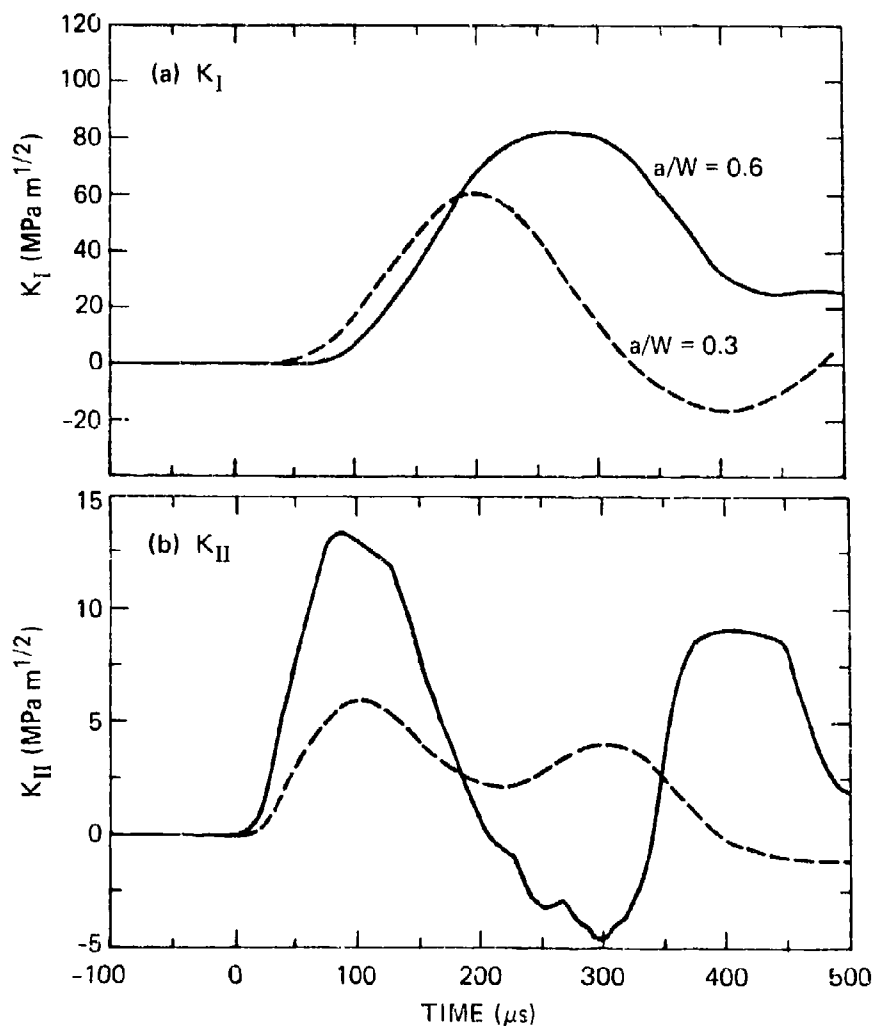
FIGURE F-3 STRESS INTENSITY HISTORIES FOR DOUBLE-CRACK 1PB SPECIMENS WITH DIFFERENT CRACK SPACINGS $2D$ ($a/W = 0.3$, $V_{\text{imp}} = 4.3 \text{ ms}^{-1}$)

farthest from the specimen mid-plane. The K_I history for this crack has a shorter oscillation duration and a lower maximum amplitude than the one for the crack closest to the crack plane.

The K_{II} histories in Figure F-3(b) are essentially the same for both crack spacings at early times, with small differences at later times when the K_I histories also start to diverge. In the two cases, the mode II stress intensity amplitudes are small.

Figure F-4 illustrates the influence of varying the crack length on the stress intensity histories, keeping the crack spacing constant (50 mm). In this Figure, the time origin corresponds to the time of impact, and the stress intensity histories have not been shifted with respect to each other. For reasons not yet understood, the mode I stress intensity for the shorter crack rises earlier than the stress intensity for the longer crack, although the initial slope is the same. Both the duration and the maximum amplitude of the K_I history increase with crack length. The shape of the early times of the K_{II} histories is similar for both crack lengths, with the amplitude increasing with crack length. At later time the K_{II} histories differ, probably because of the different flexural behaviors.

The calibration results presented above demonstrate that, although some features of the mode I stress intensity histories are anticipated based on the results of the single crack 1PBT, the dynamic response of the double-crack test is more complicated and will require further studies to understand the coupling between shear and flexural deformation. The calibration results also illustrate an important characteristic of dynamic mixed-mode loading, namely, that the mixed-mode ratio K_{II}/K_I varies continuously, but not necessarily monotonically with time. This variation makes the interpretation of dynamic mixed-mode initiation tests more complicated, because possible loading history effects must be taken into account. However, the variation of the K_{II}/K_I ratio with time offers, in principle, a simple mean of varying the degree of mixed-mode at initiation by varying the impact velocity.



RA-1750-76

FIGURE F-4 STRESS INTENSITY HISTORIES FOR DOUBLE-CRACK 1PB SPECIMENS WITH DIFFERENT CRACK LENGTHS ($2D = 50 \text{ mm}$, $V_{\text{imp}} = 4.3 \text{ ms}^{-1}$)

The calibration results of Figure 2 further show that a significant mode II loading component can be produced with the double-crack one-point-bend. With impact velocities of 30 m s^{-1} , maximum amplitudes of $54 \text{ MPa m}^{1/2}$ have been achieved in mixed-mode fracture experiments. These values, however, proved too small to initiate a crack under mainly mode II conditions, and there is a limit to raising the impact velocity to obtain higher stress intensity values because, beyond a certain velocity, a large plastic indent develops under the hammer. Moreover, the maximum K_{II} amplitude occurs when K_I is either compressive or zero. In turn, the mode II loading decreases to zero while the mode I loading becomes significant. Thus the test configuration in Figure F-1(c) produces loading conditions in which the mode I and the mode II loading are essentially decoupled.

The configuration of Figure F-1(c) must be modified to increase the maximum achievable K_{II} amplitude and to obtain larger K_{II}/K_I ratios at stress intensity levels close to the material mode I and mode II toughnesses and for reasonable impact velocities.

Modified Double-Crack 1PB Configuration

To achieve higher mode II stress intensity amplitudes, at least three solutions are possible. The first solution is to increase the crack length, keeping the specimen width constant. A second solution is to use a wider hammer plate to minimize the plastic indentation and permit higher impact velocities. We also anticipate that this solution will induce a sharper acceleration of a larger portion of the center part of the specimen and hence a higher shear force on the uncracked ligament and a higher K_{II} amplitude. The third solution is to increase the specimen inertia between the crack and the far end of the specimen either by increasing the thickness of the specimen in this area or by adding ballast plates. These solutions have not been tested in this investigation.

To achieve higher mixed-mode ratios at higher stress intensity levels, at least two solutions are feasible. The first solution is to

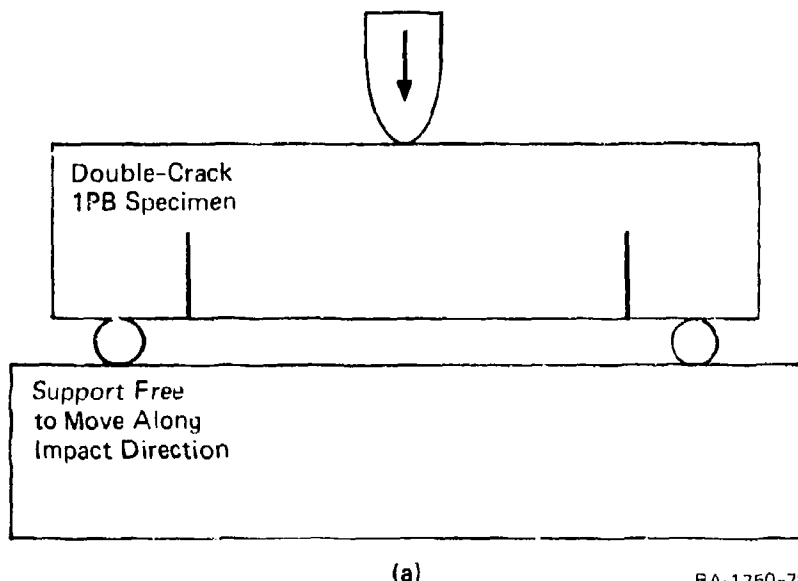
control the amount of mode I loading by statically prestressing the specimen. This solution presents the additional advantage of eliminating the compressive mode I loading component, which complicates interpretation of the fracture experiments.

The second solution is to introduce a delayed shear loading at the time in the loading history when the mode I loading becomes important. This delay can be achieved by using unrestrained end supports that are free to move with the specimens once they are impacted, as shown in Figure F-5(a). At early times after the hammer impact, the double-crack specimen does not interact with the supports and the stress intensity histories are similar to the histories shown in Figure F-2. Later, however, the specimen comes in contact with the unrestrained supports, which transmit renewed inertial shear loading on the uncracked ligament. Although we have not investigated this point, the amplitude of the second shear loading could be adjusted to a certain extent by varying the support position with respect to the crack position.

To perform our mixed-mode fracture experiments, we used a combination of static prestressing and additional inertial shear loading by unrestrained supports. The experimental arrangement is shown in Figure F-5(b). The specimen is loaded statically in three-point-bend by means of a support plate and a yoke. The amount of prestressing can be adjusted with the screw positioned opposite the impact point. The whole prestressed specimen assembly is supported in the air launcher apparatus used for the experiments in a way that permits free movement in the direction parallel to the impact direction. The effect of the prestressing and of the prestressing fixture on the stress intensity histories is illustrated in the results of the fracture experiments presented below.

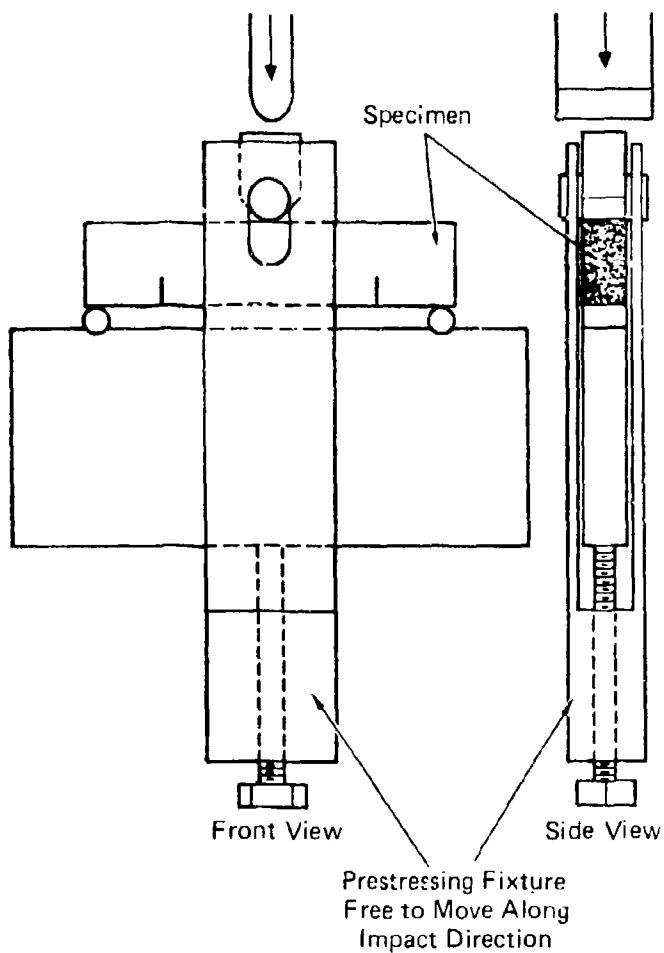
DYNAMIC MIXED-MODE EXPERIMENTS

We used the experimental arrangement described in the previous paragraph to perform dynamic mixed-mode experiments. One of the two notches of the specimen was fatigue-precracked, whereas the other had a



(a)

RA-1750-78



(b)

JA-2777-44A

FIGURE F-5 ARRANGEMENTS TO CONTROL MIXED-MODE RATIO

- (a) Unrestrained support arrangement,
- (b) Combined prestress and unrestrained support arrangement.

root radius of approximately 0.125 mm. The total length of the sharp crack was the same as the length of the blunt notch, 38 mm. The material in these tests was the same as in the rest of the program, aircraft quality 4340 steel, quenched and tempered to HRC 50. The amount of prestress measured in terms of the mode I stress-intensity factor was varied from $K_I^{\text{Stat}} = 0$ to a level equal to the maximum amplitude applied during fatigue precracking, i.e., 60% of the dynamic mode I fracture toughness, 58 MPa $\text{m}^{1/2}$.

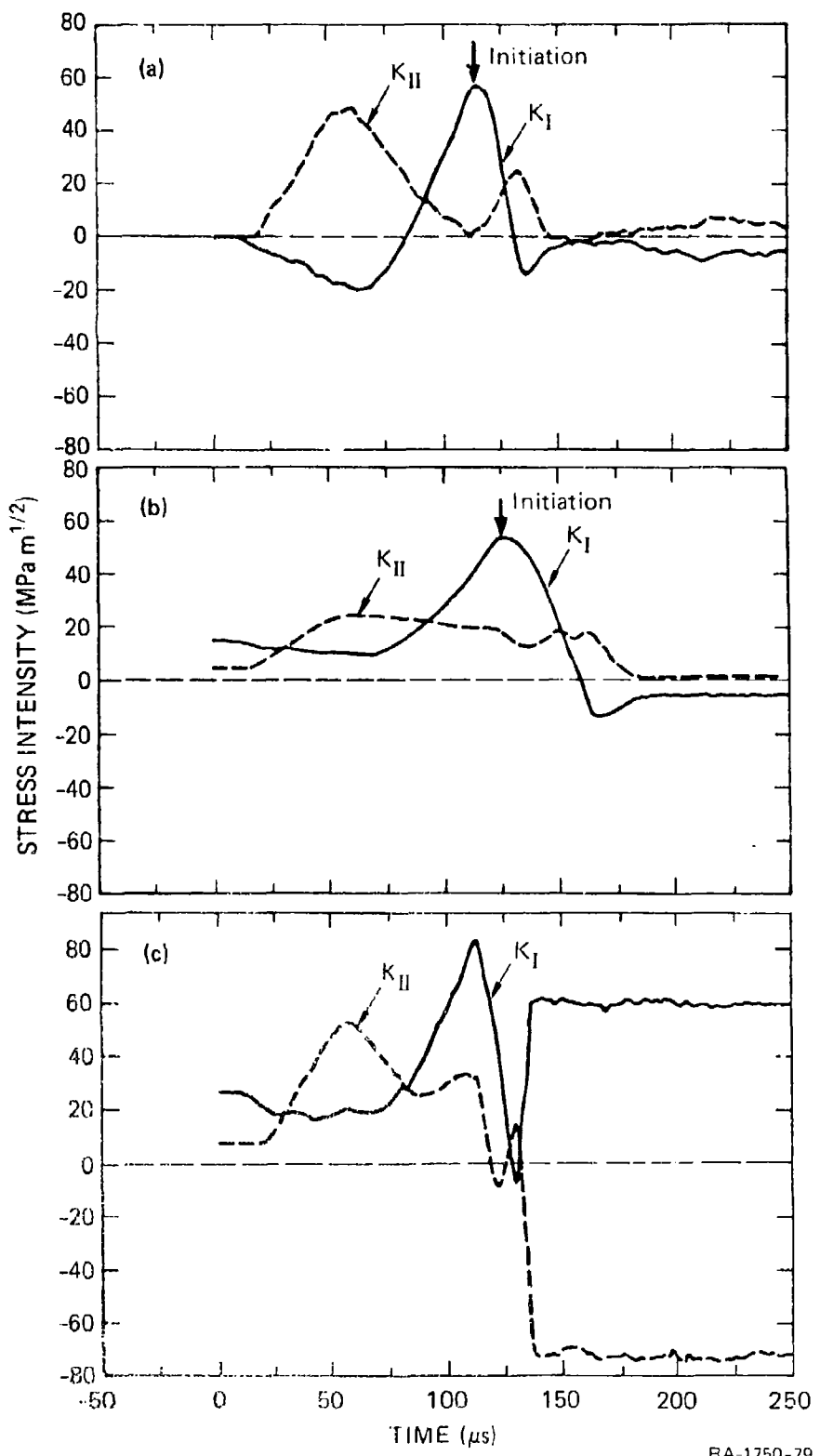
Figure F-6 shows the stress intensity histories for three tests with different levels of prestress (specimens MMF-2, MMF-6, and MMF-8). These histories were calculated from the records of three strain gages placed near the crack tip (see Appendix C). The point of crack initiation is defined, by analogy with the pure mode I dynamic fracture initiation, as the point where the mode I stress intensity history departs significantly from the tangent to the rising portion of the curve. The impact velocities for each test are indicated in the figure. Tests performed under essentially the same conditions demonstrated that the fracture initiation conditions as well as the crack extension path are reproducible.

The results of the dynamic mixed-mode initiation experiments are summarized in Table F-1 and Figure F-7. Figure F-7 plots K_{II} , normalized by the dynamic initiation toughness K_{Id} , as a function of K_I also normalized by K_{Id} . Solid circles represent conditions under which crack initiation occurred; open circles represent mixed-mode loading states that were traversed during the dynamic experiments without causing the crack to extend. Three loading paths, corresponding to the stress intensity histories in Figure F-6, are indicated by the dashed lines. The open triangles represent initial prestress conditions used in the tests, and the single solid triangle indicates a value of the static mode II initiation toughness for 4340 steel (HRC 50), reported by Shah.²

²R. C. Shah, "Fracture under Combined Modes in 4340 Steel," ASTM-STP 560, pp. 29-52 (1974).

Table F-1
RESULTS OF MIXED-MODE FRACTURE EXPERIMENTS

<u>Test No.</u>	<u>Configuration</u>	<u>K_I [MPa m^{1/2}]</u>	<u>Fracture At K_{II} [MPa m^{1/2}]</u>	<u>K_I/K_{II}</u>	<u>Max K_{II}</u>	<u>Angle of Crack Extension</u>
MMF-1	No Prestress	54.3	11.0	0.2	44.3	49°
MMF-2	No Prestress	56	0	0	49.0	10°
MMF-3	No Prestress	54	3	0.06	34.5	3° ~ 9°
MMF-4	No Prestress	63.4	32.4	0.51	41.4	35°
MMF-5	No Prestress	63.5	27.6	0.43	35.9	35°
MMF-6	No Prestress	53.8	18	0.34	25.5	18° + 5°
MMF-7	No Prestress	98	31	0.32	53.2	25° + 33°
MMF-8	No Prestress	82.7	31.7	0.38	52.4	41° + 59°



RA-1750-79

FIGURE F-6 STRESS INTENSITY HISTORIES FOR THREE MIXED-MODE FRACTURE EXPERIMENTS

- (a) $V_{imp} = 15 \text{ ms}^{-1}$ no prestress
- (b) $V_{imp} = 8.1 \text{ ms}^{-1}$ prestress, $K_I = 15 \text{ MPa m}^{1/2}$, $K_{II} = 5 \text{ MPa m}^{1/2}$
- (c) $V_{imp} = 21 \text{ ms}^{-1}$ prestress, $K_I = 26 \text{ MPa m}^{1/2}$, $K_{II} = 8 \text{ MPa m}^{1/2}$

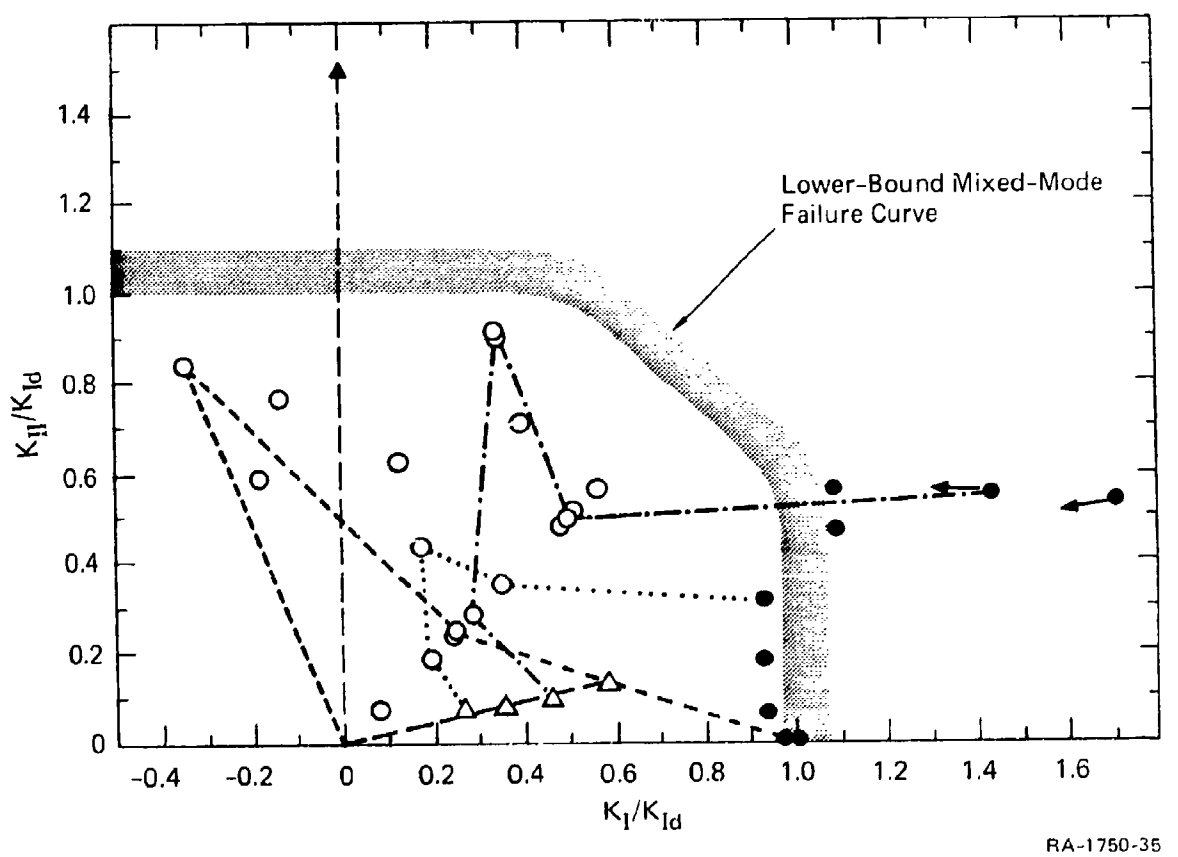


FIGURE F-7 RESULTS OF DYNAMIC MIXED-MODE FRACTURE EXPERIMENTS ON 4340 STEEL

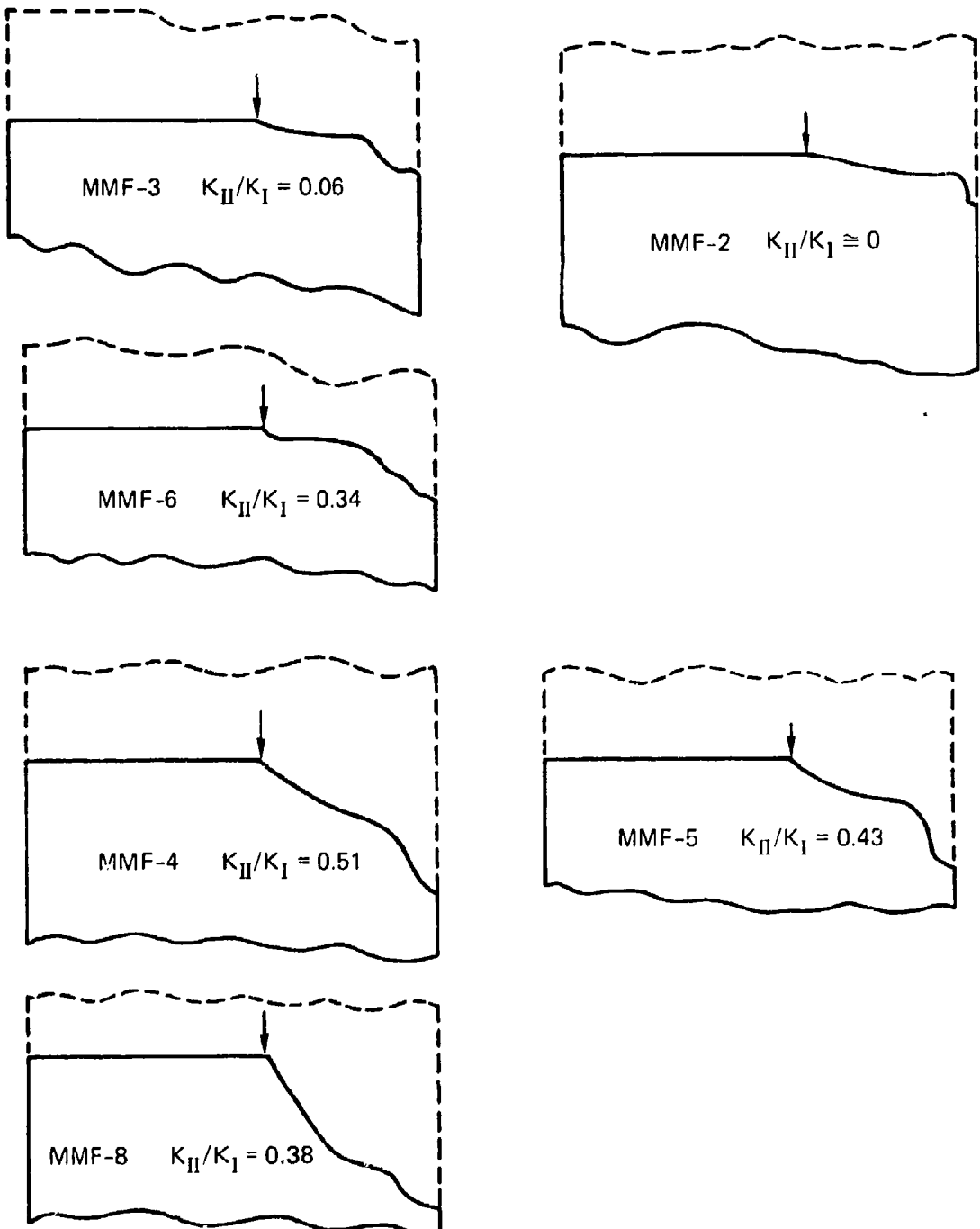
The shaded band in Figure F-7 is a tentative lower bound mixed-mode failure curve that will be discussed below.

Figure F-7 presents dynamic initiation data for mixed-mode ratios K_{II}/K_I up to 0.5. Most of the initiation data points fall around a vertical line $K_I/K_{Id} = 1$, except for the two points on the far right of the figure. This results suggests that, under relatively mild mixed-mode conditions, dynamic crack initiation is essentially controlled by the mode I stress intensity amplitude. The two failures that occurred at K_I values significantly larger than the dynamic mode I fracture toughness (specimens MMF-7 and MMF-8) represent specimens that were tested at higher impact velocity than other specimens with comparable mixed-mode ratios. The significance of these two data points will be discussed below.

Figure F-8 illustrates the crack path for each of the specimens tested, except of specimens MMF-1 and MMF-7, which had a rough and uneven crack path. With the exception of specimen MMF-8, the initial crack propagation angle appears to increase with the mixed-mode ratio at initiation. The propagation angle changed rapidly in some specimens, reflecting the changing mixed-mode condition at the extending crack tip.

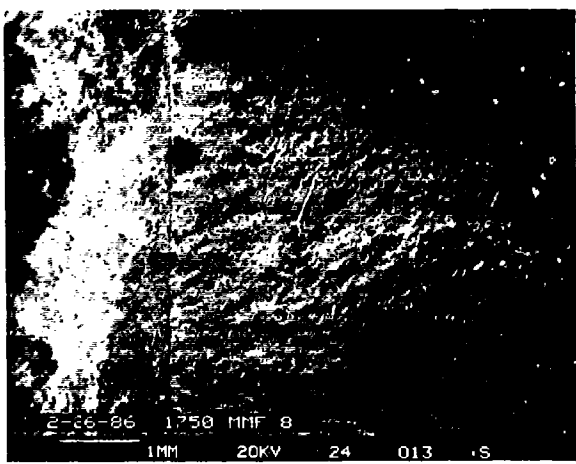
For most specimens, the macroscopic fracture surface appearance was very similar to the fracture surface appearance in pure mode I experiments. However, in experiment MMF-7 and particularly in experiment MMF-8, the fracture surface has a much rougher appearance than in the other specimens. Preliminary scanning electron microscope observations confirm these differences.

Figure F-9 compares the fracture surface of specimen MMF-8, Figure F-9(a) and (b), with the fracture surface of specimen MMF-5, Figure F-9(c). Specimen MMF-8 has a narrow region near the fatigue crack tip of relatively smooth appearance, which corresponds to a region of failure by ductile growth of small voids. Beyond this narrow band, the fracture surface is very rough and displays large inclined steps Figure F-9(a). A view of this area at higher magnification, Figure F-9(b), suggests that the inclined steps may correspond to grains that have pulled out along

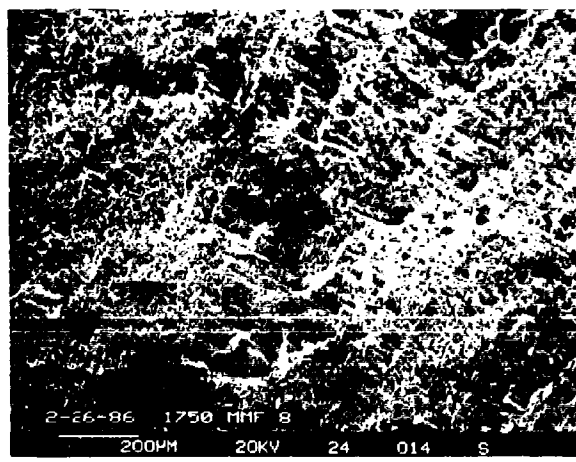


RA-1750-82

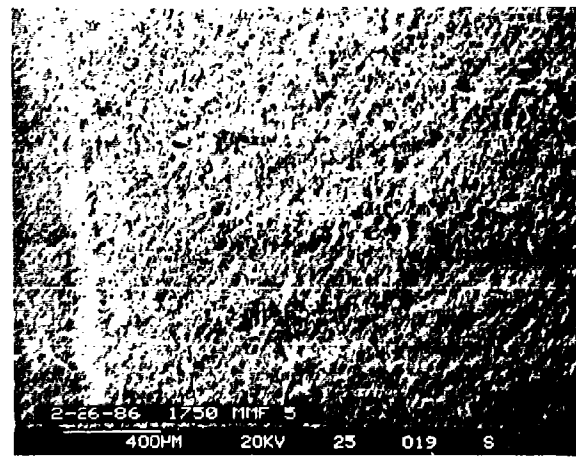
FIGURE F-8 CRACK PATH IN MIXED-MODE FRACTURE SPECIMENS
(Arrows indicate initial crack tip position.)



(a)



(b)



(c)

RP-1750-83

FIGURE F-9 FRACTURE SURFACE OF MIXED-MODE SPECIMENS

(a) and (b) Specimen MMF-8, (c) Specimen MMF-5

grain boundaries. In contrast, such steps are not visible on the fracture surface of specimen MMF-5, except for a few limited occurrences, Figure F-9(c). Note, however, that the difference in fracture surface appearance arises only about 1 mm away from the initial fatigue crack front; therefore, it can be argued that the fracture surface appearance reflects differences in crack propagation behavior and not difference in crack initiation behavior.

DISCUSSION OF DYNAMIC MIXED-MODE FRACTURE EXPERIMENTS AND CONCLUSIONS

The dynamic mixed-mode fracture data presented here represent the first set of results obtained with a new experimental technique; therefore, they must be analyzed with caution before conclusions can be drawn. One of the limitations of the results is the small number of specimens tested and the restricted range of mixed-mode ratios investigated. A more serious limitation is that the strain gage technique for measuring the K_I and K_{II} histories at the stationary crack tip has not been assessed against another experimental technique or against numerical simulations. Although the stress intensity histories measured with the strain gage technique qualitatively agree with histories anticipated from simple specimen dynamic considerations, an assessment against other methods is necessary to gain full confidence in the strain gage technique.

Another limitation of the approach taken in this investigation is the detection of crack initiation under mixed-mode conditions. As for the pure mode I experiments, we have determined the instant of crack initiation based on the strain history measured by the gage mounted 90° from the crack plane and immediately above the crack tip. A sharp drop in the strain signal recorded by this gage has been interpreted as an indication of crack initiation. However, in contrast to the pure mode I case, we have not yet investigated how crack extension under mixed-mode conditions affects the strain signals after initiation. For small mixed-mode ratios, the initial angle of crack extension is small, and crack extension will probably affect the strain histories in a manner similar

to the pure mode I case. As the degree of mixed-mode and the initial angle of crack extension increase, the crack front will tend to move toward, rather than away from, the strain gages. Immediately after initiation, this may at first cause a rise in the strain measured by the 90° gage. As a consequence, the time of crack initiation and the value of K_I would be overpredicted. This argument seems borne out by our experimental data, which show that the K_I values at initiation increase with the initial angle of crack extension. In particular, the very high values of K_I measured for tests MMF-7 and MMF-8 maybe due to this extension effect. Therefore, we strongly suspect that the data points on the far right in Figure F-7 should be moved toward the line $K_I/K_{Id} = 1$, as indicated by the small arrows in the figure.

A final comment on the mixed-mode experiments concerns the number of parameters that must to be considered when interpreting the fracture results. At least three factors may influence the dynamic mixed-mode initiation results: the loading history, the mixed-mode ratio at initiation, and the loading rate. With the test method we used (as probably with any other dynamic mixed-mode test method), it is not possible to vary these three factors independently. This limitation may make it difficult to make an unambiguous interpretation of the results.

Bearing in mind the above limitations, we can draw the following conclusions from the present dynamic mixed-mode fracture investigation.

- (1) We have demonstrated the applicability of a simple experimental technique for obtaining dynamic mixed-mode crack initiation data. The technique permits us to initiate cracks with dynamic mixed-mode ratios K_{II}/K_I varying between 0 and 0.5. The dependence of the stress intensity history on crack length and position and on impact velocity has been established. From these results, we have proposed modifications to achieve mixed-mode ratios at crack initiation larger than 0.5.
- (2) The dynamic mixed-mode crack initiation data generated for the range $K_{II}/K_I = 0$ to 0.5 show that, for this range of mixed mode ratios, crack initiation is essentially controlled by the mode I stress intensity and that it occurs when $K_I = K_{Id}$, the pure mode I initiation toughness.

- (3) Based on the points of the K_I - K_{II} plane traversed during the fracture experiments for which no failure occurred, we can draw a tentative lower bound mixed-mode failure curve for 4340 steel HRC 50 (Figure F-7). The pure mode II dynamic toughness K_{IId} is at least equal to the pure mode I initiation toughness K_{Id} ; i.e., $K_{IId} > 58 \text{ MPa m}^{1/2}$. Assuming that K_{IId} has the same rate sensitivity as K_{Id} , which is very low, and taking for the static mode II fracture toughness the value reported by Shah,² 88 MPa $\text{m}^{1/2}$, we estimate that K_{IId} should be about 85 MPa $\text{m}^{1/2}$. This value is consistent with the proposed lower bound failure curve.
- (4) We have observed a significant difference in the fracture surface appearance both macroscopically and microscopically, in the specimens with the largest overall crack propagation angle. These specimens are also the specimens that were tested at the highest impact velocities. This result suggests that the micromechanism of dynamic mixed-mode crack extension is affected either by the degree of mixed-mode or by the crack velocity or by both factors.

For future studies, we recommend that the dynamics of the double-crack specimen configuration be further investigated to answer some of the questions in this study. The methods proposed to increase the achievable mode II component of loading should be tried, and a procedure for a more reliable detection of crack initiation should be developed. Simply placing the strain gages on the exterior face of the crack may prove adequate; with this arrangement, the extending crack will move away from the gages instead of toward them. More mixed-mode initiation data should then be generated with the improved experimental procedure to augment and verify the failure curve obtained in this study.

Appendix G

INVESTIGATION OF THE INITIAL PHASE OF DYNAMIC CRACK EXTENSION FOR IMPACT LOADING CONDITIONS

INTRODUCTION

The relationship between dynamic initiation and propagation toughnesses is an important aspect of dynamic fracture from the fundamental as well as the practical point of view. Initiation and propagation are not two separate processes but two phases of one continuous process controlled by the same microdamage mechanisms. Therefore, from a fundamental point of view, a complete understanding of dynamic fracture will be achieved only if a unique model can be developed that consistently explains experimental observations for both dynamic crack initiation and propagation. In addition, interpretation of dynamic initiation behavior at very high loading rates may also hinge on understanding the initial phase of crack extension. From a practical point of view, an understanding of the relationship between dynamic initiation and propagation toughnesses may open the possibility for obtaining estimates of the propagation toughness from values of the dynamic initiation toughnesses, which are significantly easier to measure.

Few studies have focused on the initial part of dynamic crack extension immediately following initiation.¹ Most dynamic crack propagation studies have been conducted on cracks initiated at blunt notches under quasi-static loading conditions. In many practical cases,

¹K. Ravi-Chandar and W. G. Knauss, "An Experimental Investigation into Dynamic Fracture: I. Crack Initiation and Arrest," *Int. J. Fract.*, Vol. 25, pp. 247-262 (1984).

however, running cracks will initiate from sharp precursor fatigue cracks and the loading conditions will be dynamic. This latter situation differs significantly from the situation of a crack initiated from a notch under quasi-static loading. When the crack initiates at a blunt notch, the energy release rate immediately after initiation is much greater than the critical energy release rate for initiation from a sharp crack, and also much greater than the rate of energy absorbed in fracture during the first increments of crack growth. As a consequence, the crack is overdriven by the excess strain energy stored in the specimen and accelerates very rapidly to a more or less steady state velocity.

If the crack is initiated from a sharp fatigue crack, however, the energy release rate at initiation is smaller and more closely comparable to the rate of fracture energy that can be dissipated by the material. The crack is not significantly overdriven and there maybe a smoother transition from the stationary crack to the propagating crack. Limited attention has been given to this short transient phase. A dynamic fracture investigation under these conditions permits a continuous observation of crack initiation and the subsequent early phase of crack extension, and it allows a direct comparison of dynamic initiation and propagation toughnesses.

For the preceding reasons, we studied the dynamic propagation of cracks initiated from sharp cracks in the 1PBT in order to relate dynamic initiation and propagation toughnesses. This Appendix reports on the results of this investigation and on their implications for understanding dynamic fracture. Using three methods, we showed that the propagation toughness increases significantly above the dynamic initiation toughness over the first increments of crack growth. This behavior is attributed to a resistance curve effect caused by the formation of small shear lips and by the development of a curved crack front.

MATERIAL INVESTIGATION AND EXPERIMENTAL PROCEDURE

The material used in this investigation was AISI aircraft quality 4340 steel quenched and tempered to HRC50. Two batches of material were studied: 9.5-mm-thick plates and 12.7-mm-thick plates.

For each batch of material, the static and the dynamic fracture toughnesses were measured, the latter by means of the 1PBT. The results are summarized in Table G-1. The point of dynamic crack initiation was determined from the near crack tip strain records by means of the tangent-to-the-loading-curve method discussed in Appendices B and C. The results for each of the two thicknesses of material will be discussed separately. More data were obtained for the 9.5-mm-thick material; the data from the 12.7-mm-thick material were used as a complement to assess the effect of the specimen thickness on the results.

Table G-1

STATIC AND DYNAMIC FRACTURE TOUGHNESS

<u>Specimen Thickness (mm)</u>	<u>K_{Id} (MPa m^{1/2})</u>	<u>K_{Ic} (MPa m^{1/2})</u>
9.5	63.8 ± 6	59.9 ± 5
12.7	58.5 ± 5	63.7

Three methods were used to estimate the dynamic propagation toughness and to relate it to the initiation toughness: crack jump experiments, strain record analysis, and direct strain gage measurements. In the first method we performed a series of experiments in which the impact velocity was gradually increased to produce controlled amounts of crack extension. These experiments are termed crack jump experiments (CJ). By simulating these experiments with the 1 PBT model described in Appendix D, we assessed the crack extension

behavior over short propagation distances after initiation. The specimens used in the CJ experiments were 98.5 mm long, 38.1 mm wide, 9.5 mm thick, and had a crack length over width ratio of 0.3. The stress intensity history for this specimen geometry and a nonpropagating crack is shown in Figure G-1 for an impact velocity of 5.3 m s^{-1} . It is seen that a stress intensity pulse shorter than $90 \mu\text{s}$ can be obtained; this short pulse combined with varying the impact velocity (and hence the amplitude K_I^{Max}) permits a precise control of the crack jump distance. In the CJ experiments, some of the specimens were subjected to a single impact, each specimen at a different impact velocity, to produce a different amount of crack extension. In these experiments, crack extension was detected by inspecting the near crack tip strain records.

As the crack jump distance decreases, it becomes increasingly difficult to detect crack initiation from the strain records. To attempt to circumvent this difficulty, we subjected the remainder of the specimens to multiple impacts, starting at low velocity and gradually increasing it to bracket as closely as possible crack initiation. After each impact, the specimens were inspected for signs of crack initiation by a compliance measurement method or by replicating the crack tip region with acetate tape and observing the replica with a light microscope. Although neither technique gave satisfactory results, we were able to produce crack extension increments as small as $50 \mu\text{m}$ in the multiple impact experiments.

In addition to the small 98.5-mm specimens, one larger specimen (203 by 98 by 9.5 mm, $a/W = 0.35$) was also tested to determine the influence of the specimen size and consequently the stress intensity pulse duration on the crack jump behavior.

Ten CJ experiments were performed. After the tests, the crack jump specimens were subjected to low amplitude fatigue loading to mark the position of the arrested crack front, and they were broken open. Crack extension was then measured on the fracture surface using scanning electron or optical microscopy.

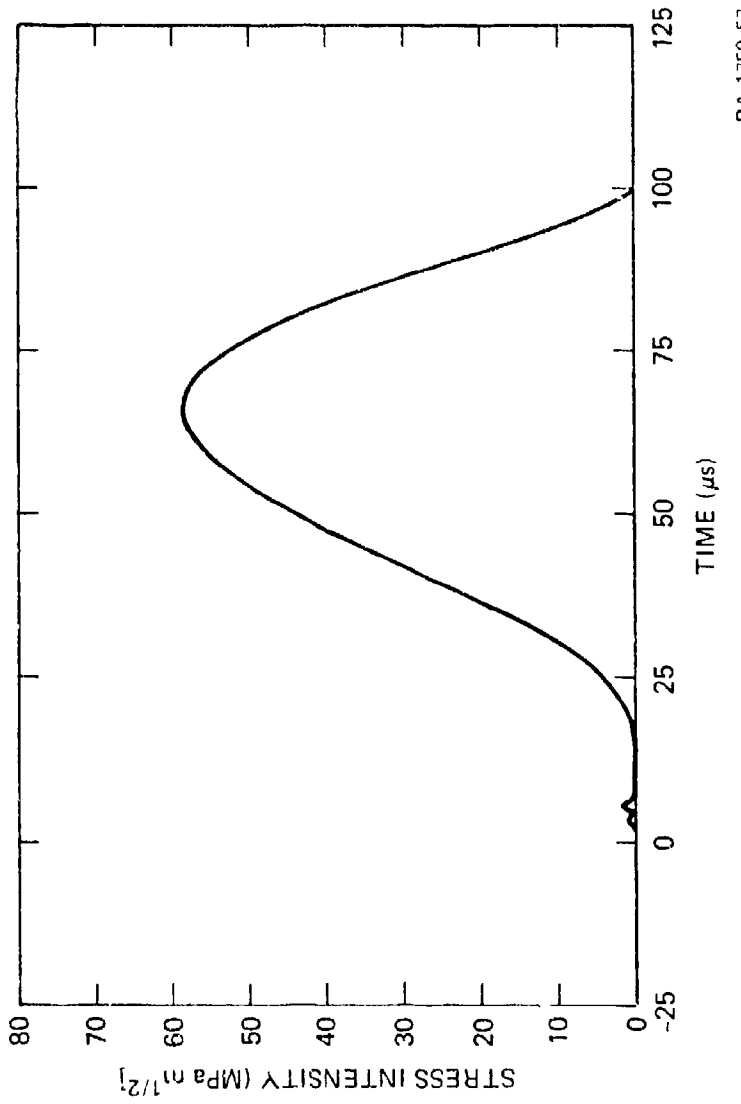


FIGURE G-1 STRESS INTENSITY HISTORY FOR CRACK JUMP SPECIMEN

WITH STATIONARY CRACK
Impact velocity $V_{\text{imp}} = 5.3 \text{ ms}^{-1}$.

RA-1750-57

The second technique used to investigate the first increments of crack extension after initiation was to analyze the strain history records beyond the point of crack initiation. In Appendix C we showed that estimates of the crack speed and of the propagation toughness can be obtained from a careful analysis of the experimental strain histories. We applied this approach to the records obtained during the 1PBT performed to obtain the dynamic initiation toughness data reported in Table G-1 and to the records obtained in the CJ experiments. We compared the experimental strain records with strain history simulations performed using the simple 1PBT model using different propagation toughness hypotheses to draw conclusions regarding the actual toughness behavior.

In the third technique, to provide additional verification of these conclusions, we performed one 1PBT crack extension experiment in which the specimen was instrumented with four strain gages spaced evenly along the crack path. From the strain gage records, we determined the crack velocity and the applied dynamic stress intensity factor, using the elastodynamic solution for a crack extending in an infinite solid at a constant velocity. Details of this method are presented in Appendix H.

In all the experiments discussed in this Appendix, small shear lips formed during crack extension. Observation of arrested cracks indicated that the crack shape gradually changed from the essentially straight fatigue crack to a strongly curved crack front after 3 mm or so of extension.

RESULTS OF CRACK JUMP EXPERIMENTS

The results of the CJ experiments are summarized in Figure G-2. The crack jump distance is plotted as a function of the maximum stress intensity K_{IMax}^{appl} that would have been applied to the specimen had the crack not extended. Because K_{IMax}^{appl} is proportional to the impact velocity, it can easily be calculated from the reference curve in Figure G-1, knowing the impact velocity for the experiment during which the crack jump occurred. K_{IMax}^{appl} represents a measure of how hard the crack was driven during the experiment, although it is not a direct measure of

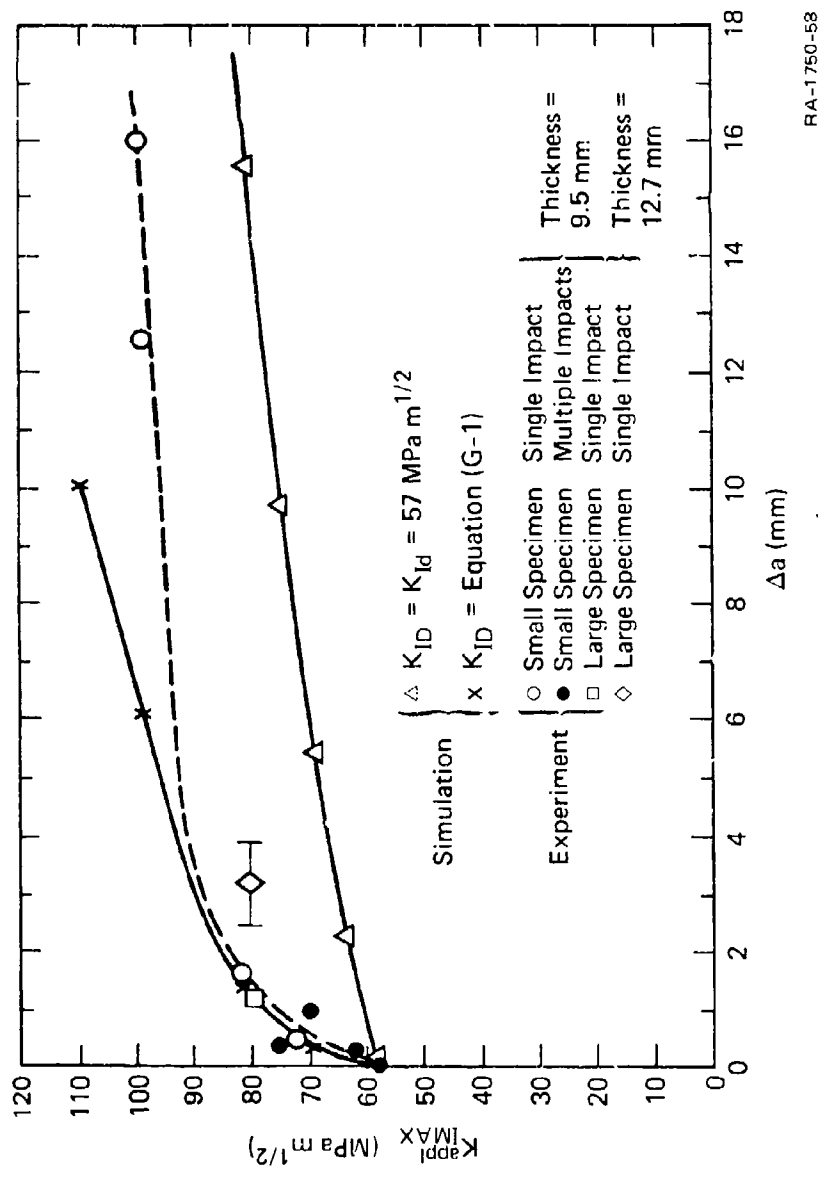


FIGURE G-2 RESULTS OF CRACK JUMP EXPERIMENTS AND COMPARISON WITH 1PBT MODEL SIMULATIONS

the stress intensity at the propagating crack tip. However, if the crack jump distance is much smaller than the specimen width, the stress intensity history for the specimen with the stationary crack provides an estimate of the stress intensity history experienced by the extending crack.

Figure G-2 shows that, initially, a large increase in K_{IMax}^{appl} , and hence in impact velocity is required to produce a small increase in crack jump distance. Beyond a K_{IMax}^{appl} value of about $80 \text{ MPa m}^{1/2}$, the trend is reversed and small increases of K_{IMax}^{appl} above $80 \text{ MPa m}^{1/2}$ cause comparatively large crack jumps. The smallest crack extension detected in the CJ experiments was $50 \mu\text{m}$, for a K_{IMax}^{appl} of $58 \text{ MPa m}^{1/2}$. From this observation, we conclude that crack initiation must occur around $57 \text{ MPa m}^{1/2}$.

Note that data points for specimens that have undergone multiple impacts fall on the same curve as specimens impacted only once.

Figure G-2 is reminiscent of the resistance curves of static fracture mechanics, which plot the increase in toughness as a function of crack extension. However, it could be argued that the shape of the curve in Figure G-2 is simply a result of the loading history at the crack tip. That is, for K_{IMax}^{appl} values only slightly over the value of the initiation toughness, the crack is loaded only long enough to propagate a very small distance before it is unloaded by the one-point-bend specimen bending back after reaching its maximum inertial deflection. If this was the case, changing the stress intensity duration, by changing the specimen size, and keeping K_{IMax}^{appl} the same would change the resulting crack jump distance. Figure G-2 shows that this is not the case because the data point for a geometrically similar specimen but scaled up in size by a factor of 2.3 falls on the same curve as the data points for smaller specimens. Therefore Figure G-2 suggests that the propagation toughness increases significantly above the initiation toughness level as the crack extends a short distance.

This conclusion is further supported by predictions of the crack jump distance as a function of the K_{IMax}^{appl} obtained with the simple 1PBT

model, assuming two behaviors for the propagation toughness. In one case, the propagation toughness was assumed constant equal to the initial toughness, $K_{ID} = K_{Id} = 57 \text{ MPa m}^{1/2}$. In the other case, K_{ID} was assumed to depend both on the crack velocity \dot{a} and the amount of crack extension Δa and to have the form

$$K_{ID} = 57 \cdot 10^6 (1 + 526 \Delta a) + f(\dot{a}) \quad 0 < \Delta a < 0.5 \text{ mm}$$

(G-1)

$$K_{ID} = 72 \cdot 10^6 (1 + 89 (\Delta a - 0.5 \cdot 10^{-3})) + f(\dot{a}) \quad 0.5 \text{ mm} < \Delta a < 2 \text{ mm}$$

$$K_{ID} = 81.6 \cdot 10^6 + f(\dot{a}) \quad \Delta a > 2 \text{ mm}$$

where

$$f(\dot{a}) = 40703 \dot{a} - 275 \dot{a}^2 + 0.2094 \dot{a}^3 + 0.00155 \dot{a}^4$$

Bearing in mind the limitations of the simple IPBT model, comparison of the experimental data and the simulations shows that the experimental results fall much closer to the predictions based on equation (G-1) which assumes an increase in toughness with both crack length and crack velocity than to the predictions based on the constant propagation toughness assumption, although for longer crack jumps, the crack jump distance is underpredicted when using equation (G-1).

RESULTS OF STRAIN RECORD ANALYSIS

The normalized strain gage records for several IPB experiments are plotted in Figures G-3 and G-4. Figure G-3 shows the records for three crack jump experiments in which the crack arrested after less than 2 mm extension. The records in Figure G-3(a) and G-3(b) were obtained from small specimens (Specimens CJ7 and CJ5, respectively), whereas the data

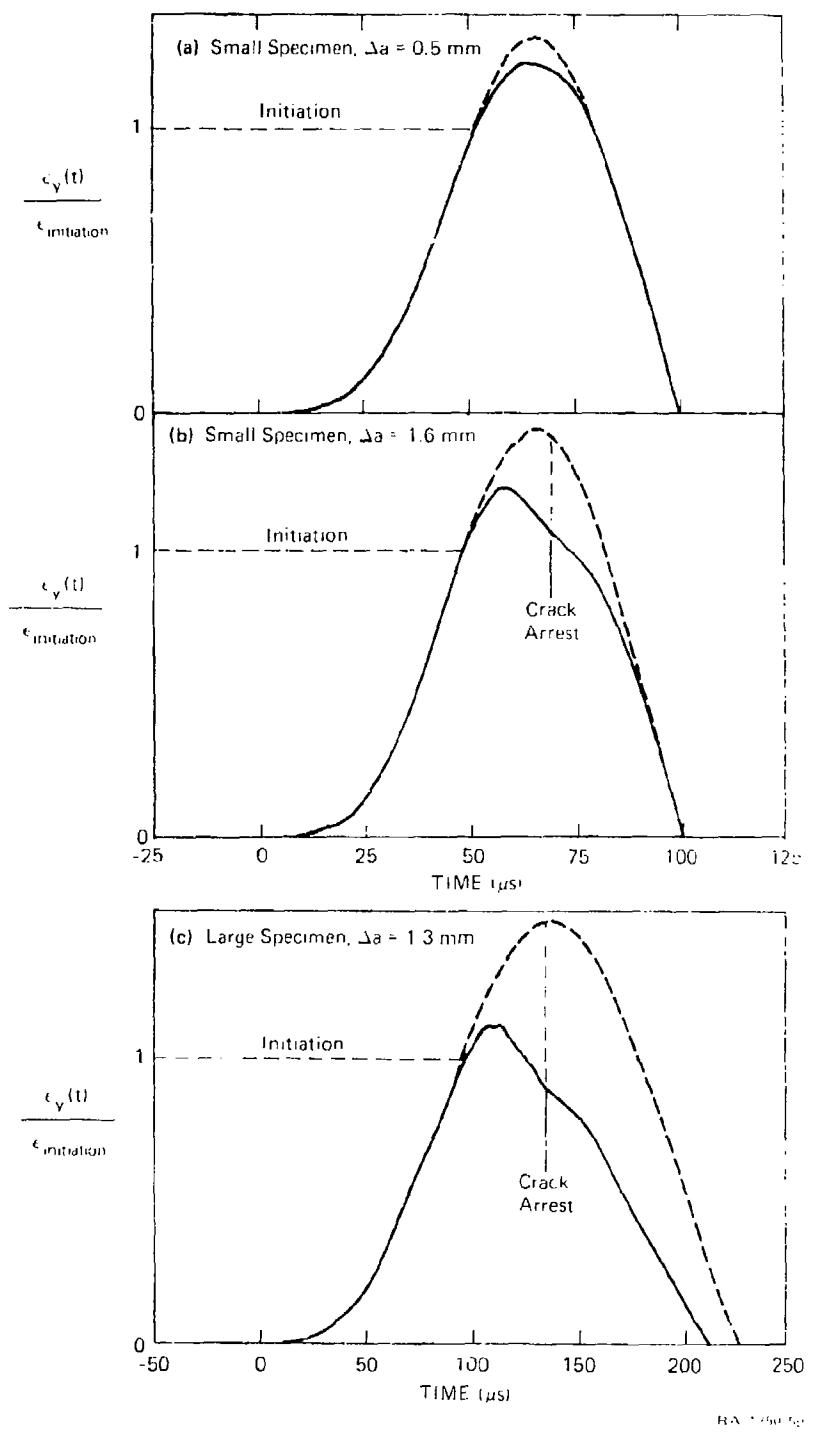
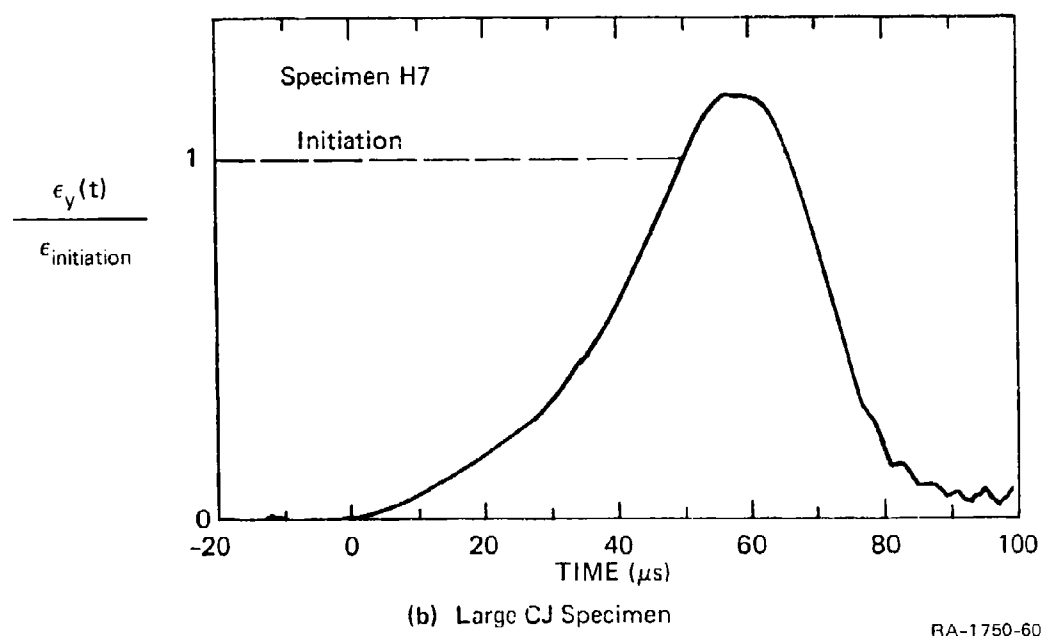
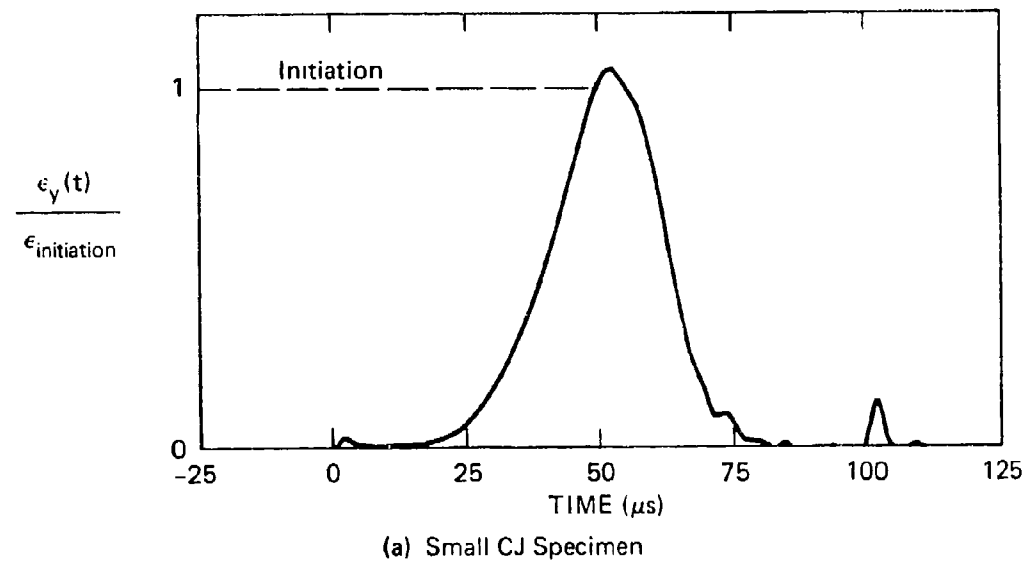


FIGURE G-3 NORMALIZED STRAIN HISTORIES FOR CJ EXPERIMENTS



RA-1750-60

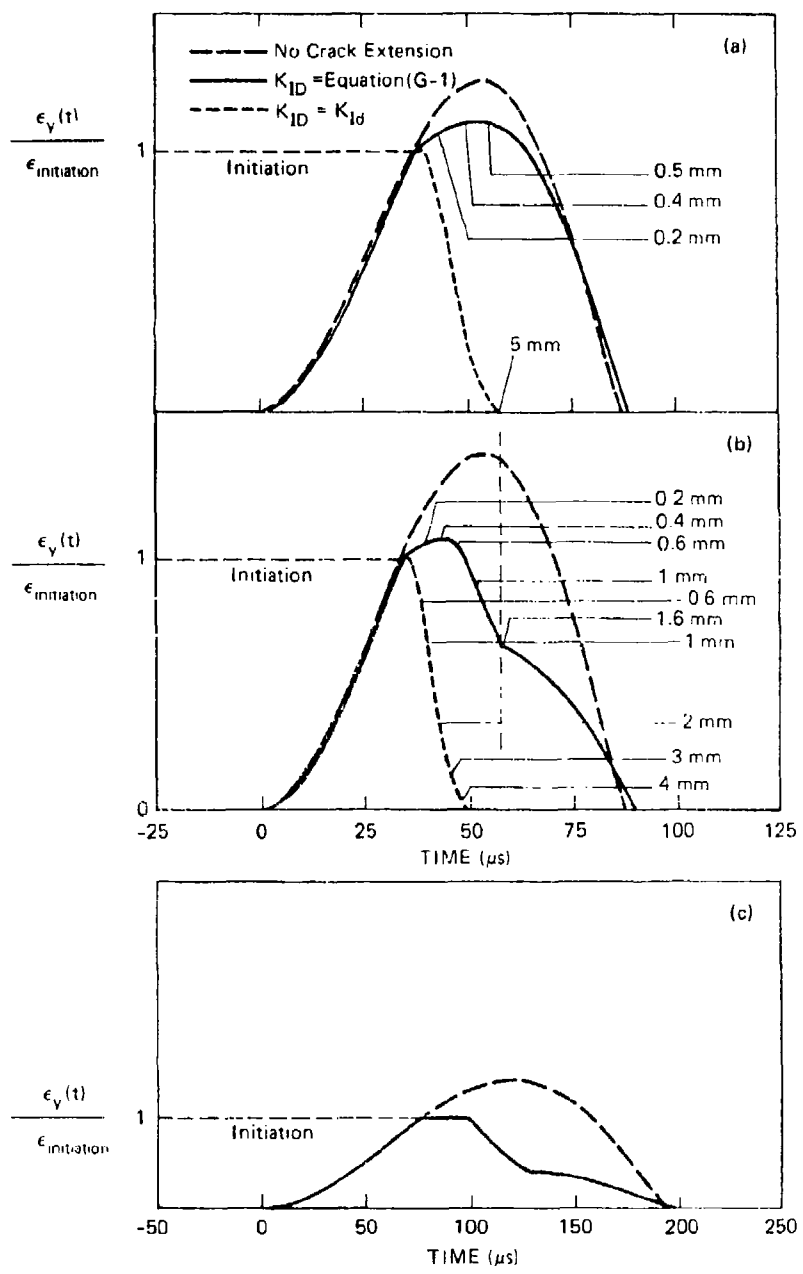
FIGURE G-4 NORMALIZED STRAIN HISTORIES FOR COMPLETELY FRACTURED SPECIMENS

in Figure G-3(c) were obtained from a large specimen (Specimen H1). Figure G-4 shows the stress intensity records for 1PB experiments in which the specimens were completely broken. Figure G-4(a) shows the record for a small specimen (C6) and Figures G-4(b) shows the record for a large specimen (H7) used to determine the dynamic initiation toughness data in Table G-1. Figure G-3 also plots the strain history that would have resulted had the crack not propagated. The horizontal dashed line represents the strain level at which the crack initiates (corresponding to a stress intensity of $57 \text{ MPa m}^{1/2}$).

Simulations of the strain records for the experiments illustrated in Figures G-3 and G-4 are presented in Figures G-5 and G-6, respectively. These simulations were performed with the simple 1PBT model assuming the same two toughness behaviors as for the simulations in Figure G-2. For each simulation, the strain was calculated at the position of the strain gage in the corresponding experiment. On some simulated strain records, we have indicated the amount of crack extension associated with given amounts of strain drop. This value can be used to estimate the crack velocity from the experimental strain records.

In the test from which the strain history in Figure G-3(a) was obtained, the crack extended by 0.5 mm, which is probably the smallest crack growth increment that can be detected based on the strain records. It causes a very mild flattening of the top part of the strain history curve. Further, the strain level continues to rise significantly above the crack initiation level. This rise is also observed in Figures G-3(b) and G-3(c), where the instant of crack arrest can be established as a point of inflection in the decreasing part of the strain records. Comparison of the time of arrest and the time at which the dashed curves are maximum suggests that arrest occurred when the maximum in applied stress intensity was reached.

Comparison of the experimental records and the strain simulations based on Equation (G-1) shows good agreement in the general shape of the strain histories (Figures G-3 and G-5 and Figures G-4 and G-6). In particular, the duration between the time of crack initiation (i.e., time



RA-1750-61

FIGURE G-5 SIMULATION OF NORMALIZED STRAIN HISTORIES FOR CJ EXPERIMENTS SHOWN IN FIGURE G-3

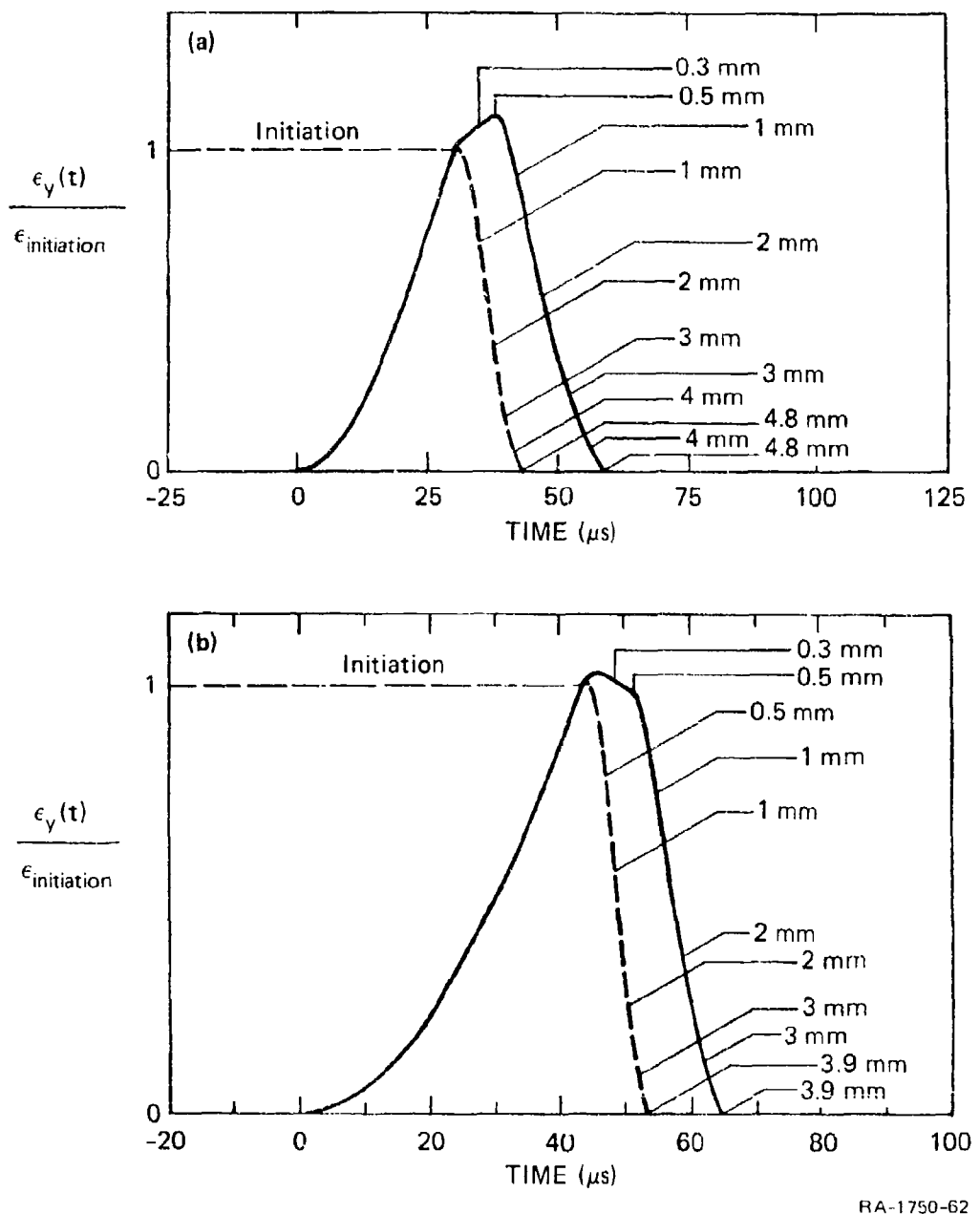


FIGURE G-6 SIMULATION OF NORMALIZED STRAIN HISTORIES FOR FRACTURE EXPERIMENTS SHOWN IN FIGURE G-4

when $K_I = 57 \text{ MPa m}^{1/2}$) and the time of crack arrest or the time at which the strain becomes zero is well predicted. The only exception is Figure G-6(b), which underestimates the time required for the strain to drop to zero in Figure G-4(b).

The good qualitative agreement between experimental data and simulations shows that the interpretation of the strain records is correct, particularly in identifying the inflection in the unloading portion as the point of crack arrest. Moreover, the fact that simulations using a constant propagation toughness equal to the initiation toughness do not represent the experimental strain records suggest that that assumption is incorrect. Rather an increasing propagation toughness must be assumed.

We can estimate the average crack velocity during the first millimeters of crack extension by comparing the results of simulation and experiments. Indeed, as discussed in Appendix C and illustrated in Figure G-6, for a given strain measurement location, the distance that the crack must extend to relax the strain to zero is essentially constant. For a given experiment, this distance can be estimated from the strain simulations. Then, by measuring the time from initiation to the point where the experimental strain drops to zero, we can estimate the average crack velocity.

The average crack velocities estimated for several tests are given in Table G-2, together with average velocities for the experiments in Figure G-3(b) and G-3(c). The latter data were obtained by dividing the crack jump distance measured after the test by the time between initiation and arrest measured on the experimental records. Table G-2 also gives the loading rate to crack initiation and $K_{I\text{Max}}^{\text{appl}}$ for each test. The results in Table G-2 show that the initial average velocities in all the tests are low, not exceeding 250 m s^{-1} . A more detailed look at the strain history records and simulations indicates that crack extension is even slower during the first 0.5 mm or so, and then accelerates to velocity about double the average velocity.

Table G-2

AVERAGE CRACK VELOCITIES FOR FIRST MILLIMETERS OF CRACK EXTENSION

Specimen	$\dot{K}_1 (\text{MPa m}^{1/2} \text{s}^{-1})$	$K_{\text{IMAX}}^{\text{App1}} (\text{MPa m}^{1/2})$	$\dot{a}_{\text{av}} (\text{m s}^{-1})$	$\dot{a}_1 (\text{m s}^{-1})$
H1	10^6	80	34	38
H7	1.9×10^6	220	130	190
CJ5	2.5×10^6	81	76	109
CJ6	2.85×10^6	99	192	253
CJ1	5.7×10^6	280	247	400

Estimates of the crack velocity, \dot{a}_1 , after the first 0.5 mm of extension and up to the point where the strain has dropped to zero are given in the last column of Table G-2. The very low average crack velocities for tests H1 and CJ5 indicate that, in these experiments, the crack was extending under dynamically stable conditions; that is, the driving force applied to the crack tip by the bending specimen was always equal to the material resistance and had to continuously increase to maintain crack extension. Once the driving force reached its maximum, the crack arrested.

RESULTS OF DIRECT K_{ID} AND \dot{a} MEASUREMENTS

One specimen (Specimen H7) instrumented with four strain gages placed along the crack path was tested in 1PB. The strain records are shown in Figure G-7, where the strain history from four gages have been

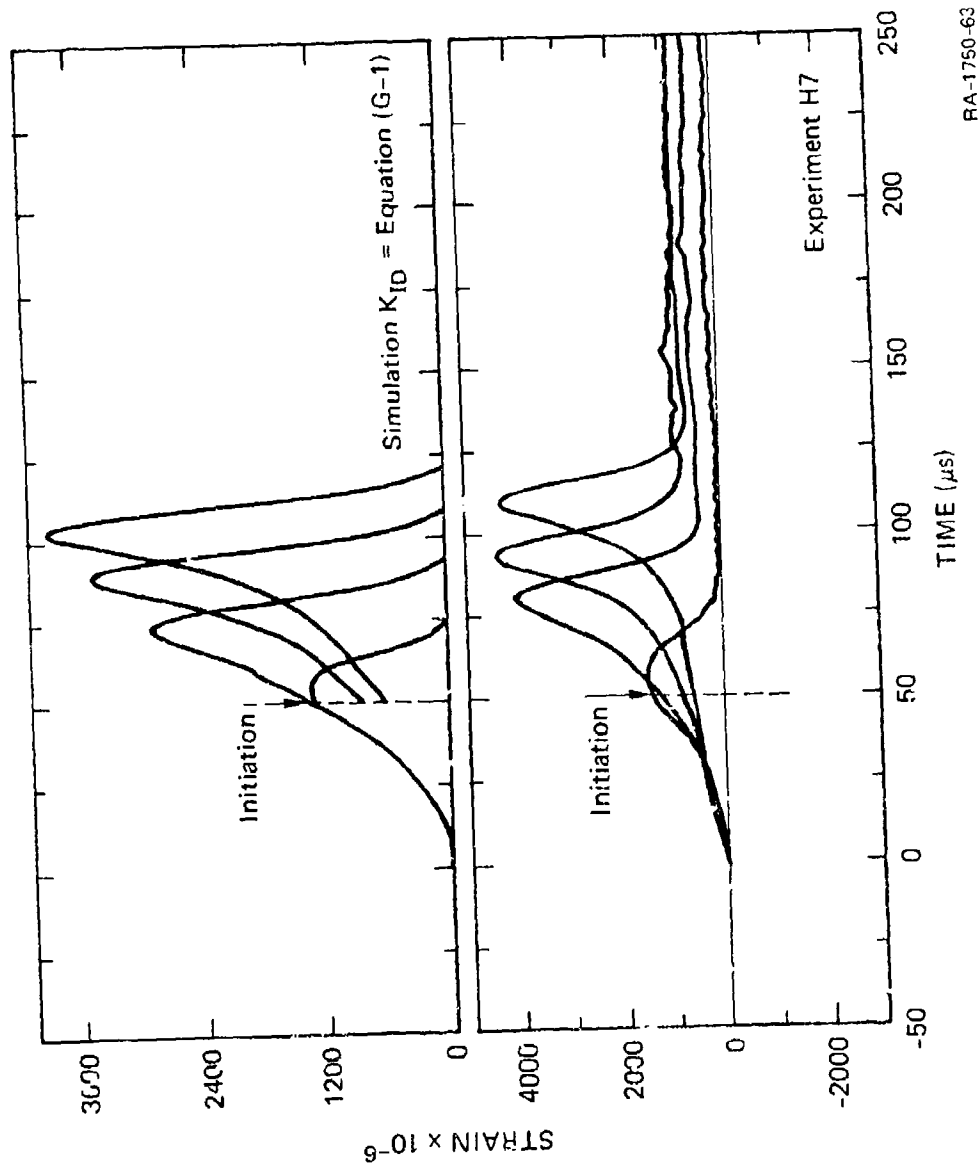


FIGURE G-7 COMPARISON OF EXPERIMENTAL AND SIMULATED STRAIN HISTORIES IN SPECIMEN H7

referred to the same initial time and superimposed on the same time scale. Strains in the vicinity of the running crack tip are much higher than the strain near the initial crack tip, although the gages were placed further away. Residual strain is also significant for the gages placed along the crack path. Note that, according to the elastodynamic solution for an extending crack, the maximum in the strain history does not occur when the running crack tip is immediately underneath the gage; rather, the strain is maximum while the crack is still approaching the gage and the line connecting the crack tip to the center of the gage makes an angle of 70 degrees with the crack plane. This distinction is important for correct evaluation of the crack velocity immediately after initiation.

Figure G-7 also shows the results of a simulation of the experiment, using the propagation toughness behavior given by equation (G-1). Although the position of the simulated peaks in strain do not match perfectly with the experimental data and their amplitude is smaller, the agreement between simulation and experiment is qualitatively good. A simulation with a constant propagation toughness equal to the initiation toughness is unable to reproduce any of the experimental strain features. This again suggests that the propagation toughness increases rapidly over the first millimeters of crack extension.

From the strain gage data, we determined the average crack velocity between two strain gages and the dynamic stress intensity factor at the propagating crack tip. The velocity results are plotted in Figure G-8 as a function of the crack extension Δa . The symbols in the figure represent the average crack velocities, and the horizontal lines represent the interval over which they were measured. The strain gage measurements yield an average velocity over the first 3 to 4 mm of 120 m s^{-1} , which is in very good agreement with the estimate of the crack velocity based on the drop-off of the strain near the initial crack tip (see Table G-2, Specimen H7). This result demonstrates that the latter procedure is legitimate.

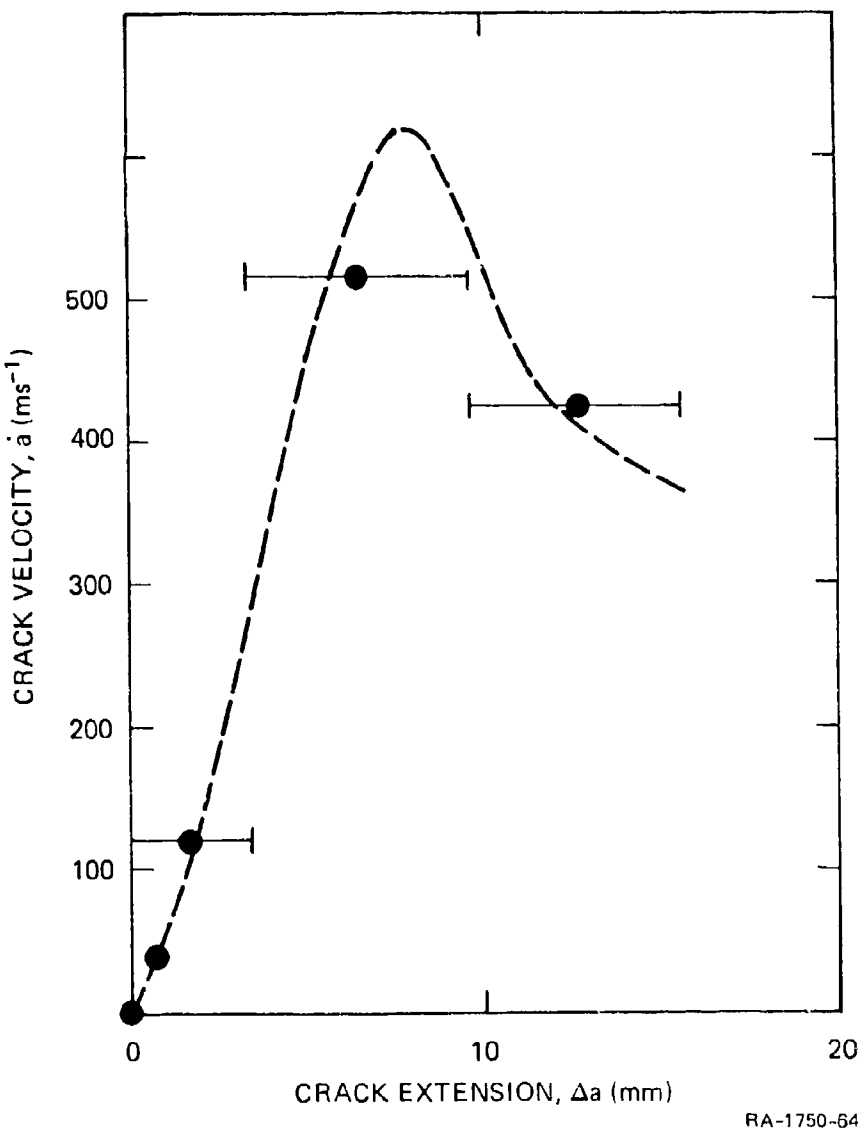
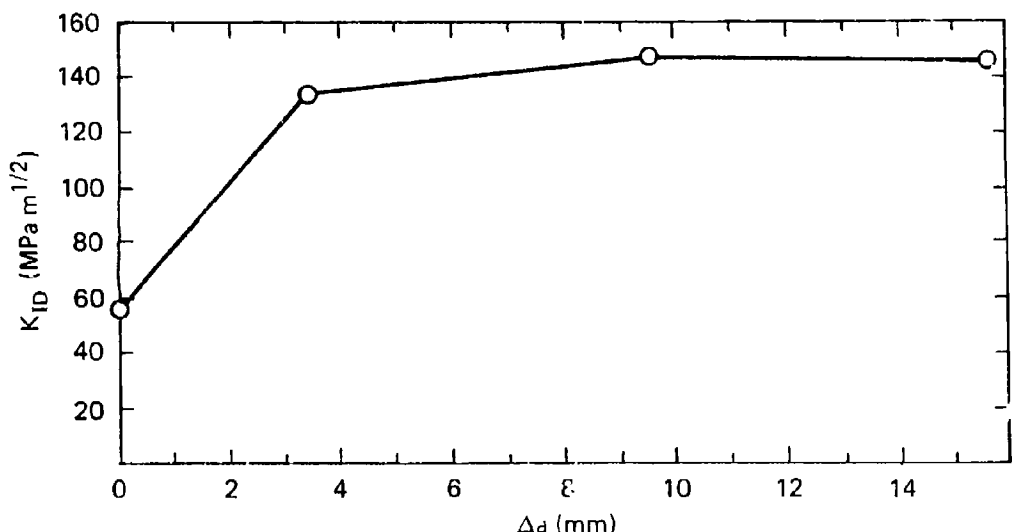
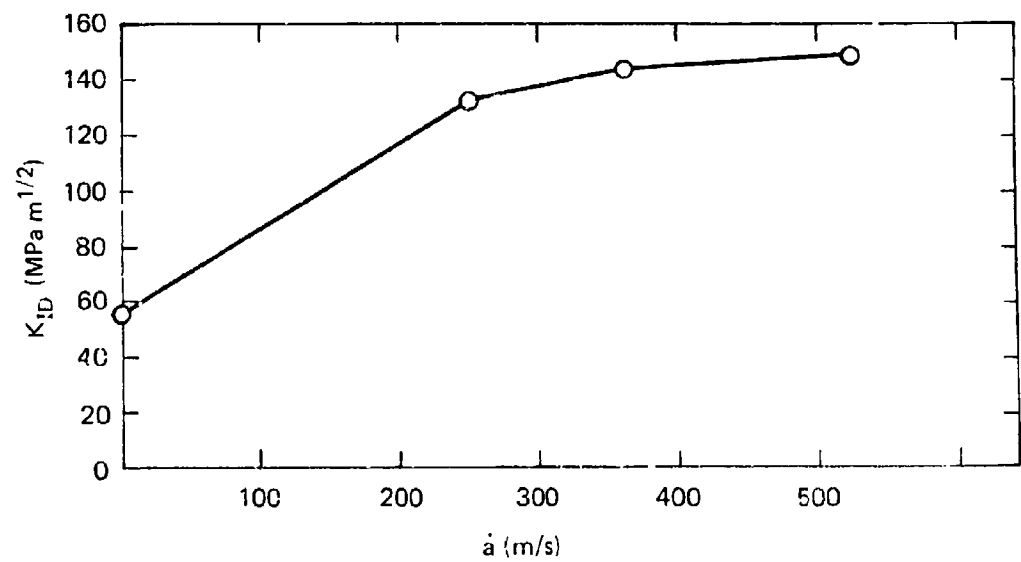


FIGURE G-8 CRACK VELOCITY \dot{a} AS A FUNCTION OF CRACK EXTENSION Δa FOR TEST H7



(a) Propagation Toughness K_{ID} as a Function
of Crack Extension Δa



(b) Propagation Toughness K_{ID} as a Function
of Crack Velocity \dot{a}

RA-1750-65

FIGURE G-9 PROPAGATION TOUGHNESS MEASURED IN TEST H7

The stress intensity values calculated from the strain gage data are plotted in Figure G-9(a) as a function of position and in Figure G-9(b) as a function of crack velocity. For the latter plot, the crack velocity was estimated from the fitted curve in Figure G-8. Over the velocity range of Figure G-9(b), the stress intensity does not vary markedly. Assuming that the stress intensity at the running crack tip can be equated to the propagation toughness, Figure G-9(b) shows that the propagation toughness measured by the strain gage method is more than twice the initiation toughness. This conclusion is also suggested by the simulation shown in Figure G-7. To obtain the high strain values along the crack path observed in the experiment, high propagation toughness values must also be assumed.

ADDITIONAL RESULTS FOR THICKER SPECIMENS

To assess the influence of specimen thickness and small shear lips on the dynamic crack propagation behavior, we present the results of experiments with thicker (12.7 mm thick) and side-grooved specimens. Most of the data were obtained during the LPBT crack initiation experiments discussed in Appendices A and E and include the near crack tip strain history records for three loading rates. In addition, we compare the results for tests on specimens with small side-grooves (0.5 mm wide, 1 mm deep) introduced to suppress the formation of shear lips, with the results for smooth specimens.

Figure G-10 shows the strain history records for a specimen loaded at a low stress intensity rate (3.2×10^5 MPa $m^{1/2}$). In these experiments, the crack initiated, extended 2.5 to 4 mm, and arrested. Figure G-10 also shows the strain history that the specimen would have experienced had the crack not propagate. The arrested crack profile, diagrammed in Figure G-11, shows that a significant amount of crack tunneling occurred and that the crack did not extend at all at the specimen edges. Upon subsequent rapid fracturing of the specimen, narrow shear lips (1 mm) developed along the edges.

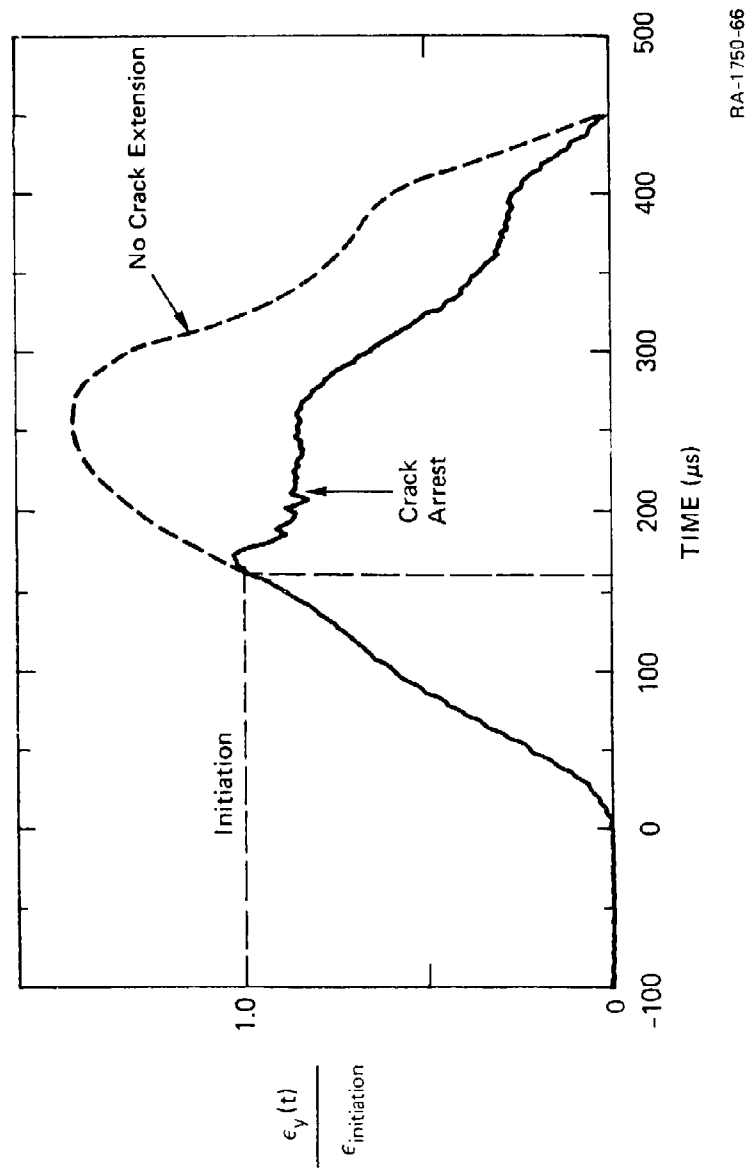
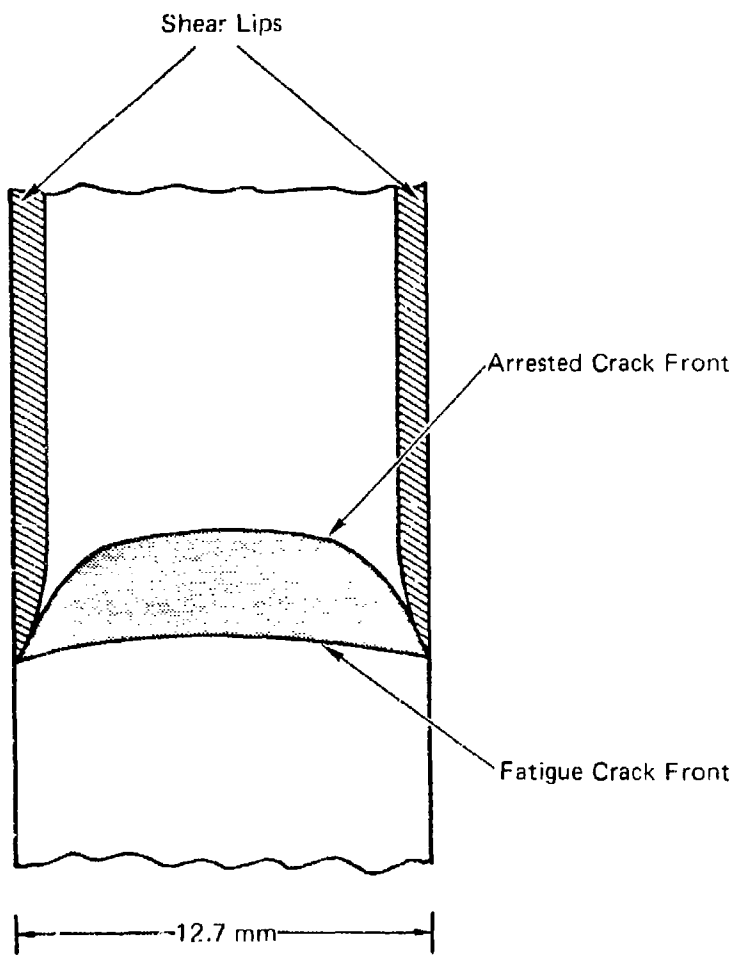


FIGURE G-10 NORMALIZED STRAIN HISTORY FOR 12.7-mm-THICK SPECIMEN
LOADED AT LOW RATE



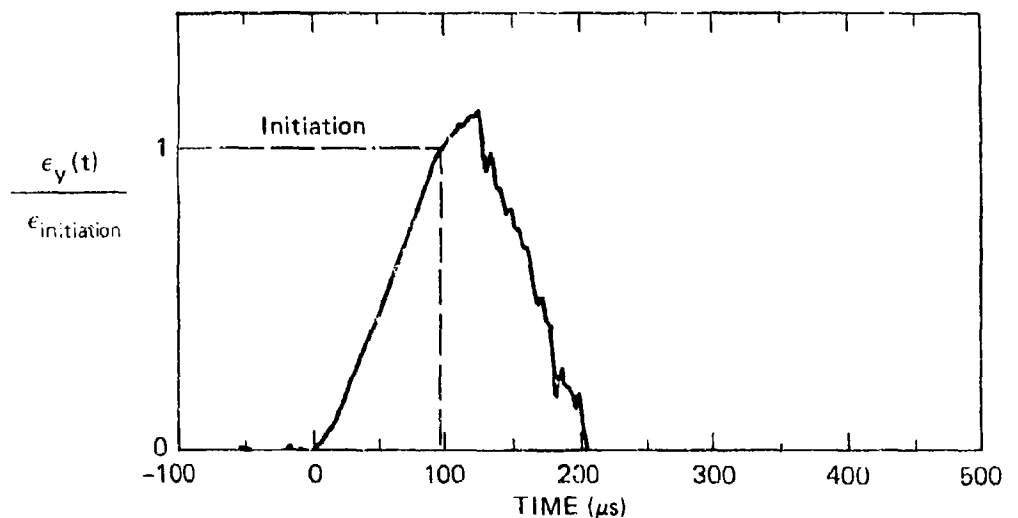
JA-2777-43

FIGURE G-11 ARRESTED CRACK SHAPE AND SHEAR LIPS

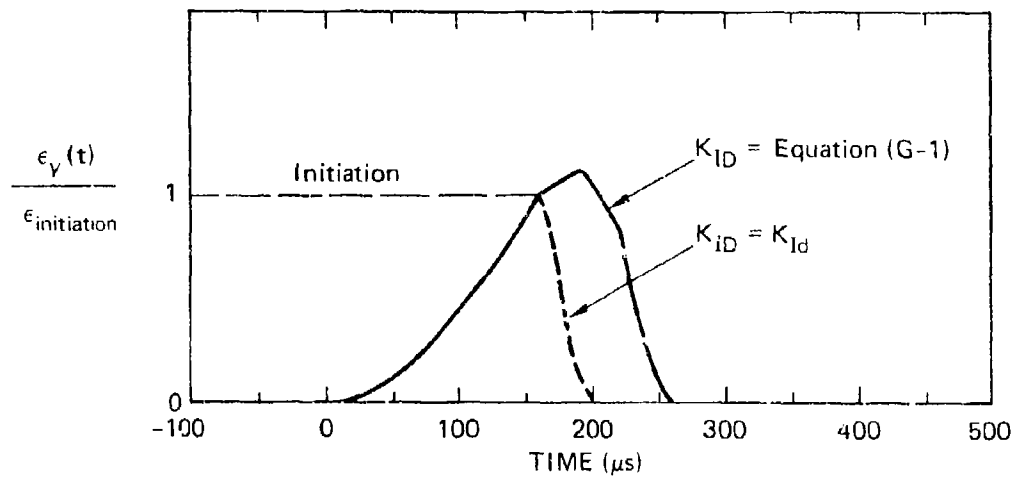
The serrated strain history during unloading suggests that crack extension occurred by a series of small jumps and arrests. Average crack speeds can be calculated from the arrested crack length, measured on the fracture surface, and from the time from initiation to final crack arrest, measured on the strain history records. The average velocities are between 60 and 110 m s^{-1} . Because of the reloading time between incremental jumps, the actual crack velocities are higher than the average velocities. Corrected crack velocity values are between 110 and 130 m s^{-1} .

Figure G-12(a) shows the normalized strain history record for a specimen loaded at an intermediate stress intensity rate of $5.5 \times 10^5 \text{ MPa m}^{1/2} \text{ s}^{-1}$. $K_{\text{IMax}}^{\text{appl}}$ in these tests was approximately $140 \text{ MPa m}^{1/2}$ and the specimens fractured completely during the tests. Figure G-12(b) shows strain simulations for the case corresponding to Figure G-12(a) and for two toughness assumptions. In one case the propagation toughness is assumed constant equal to the initiation toughness; in the other case it varies according to equation (G-1).

The serrated appearance of the unloading portion of the strain history again suggests that the crack extended by a series of jumps and arrests. Comparison of the experimental records with the strain simulation shows that the simulation with a constant toughness assumption predicts a much more rapid strain drop than is observed in reality. A simulation using equation (G-1) predicts a strain history that resembles the experimental one more closely, although the jumps and arrests are not reproduced. In particular, the simulation predicts an average crack velocity during the unloading portion of the strain history of about 120 m s^{-1} . This compares well with the velocities calculated from the experimental records assuming (based on the indication of the simulation) that the crack has extended by approximately 9 mm when the strain has dropped to zero. Because of the run-arrest nature of the crack extension, these estimates represent lower bounds for the crack velocity. Corrected crack velocities are about 170 m s^{-1} .



(a) Experimental Record



(b) Simulation

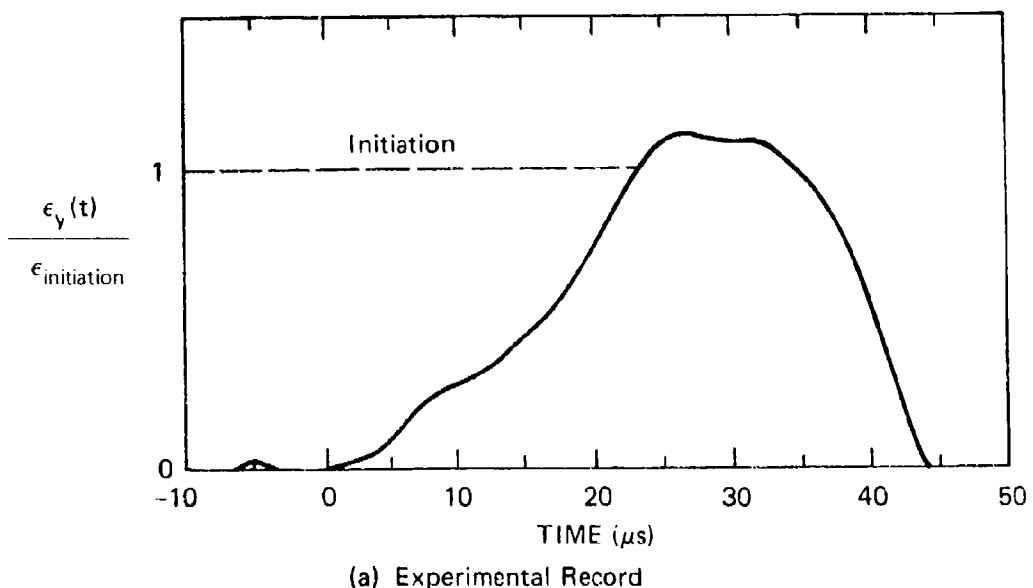
RA-1750-67

FIGURE G-12 NORMALIZED STRAIN HISTORY FOR 12.7-mm-THICK SPECIMEN
LOADED AT INTERMEDIATE RATE

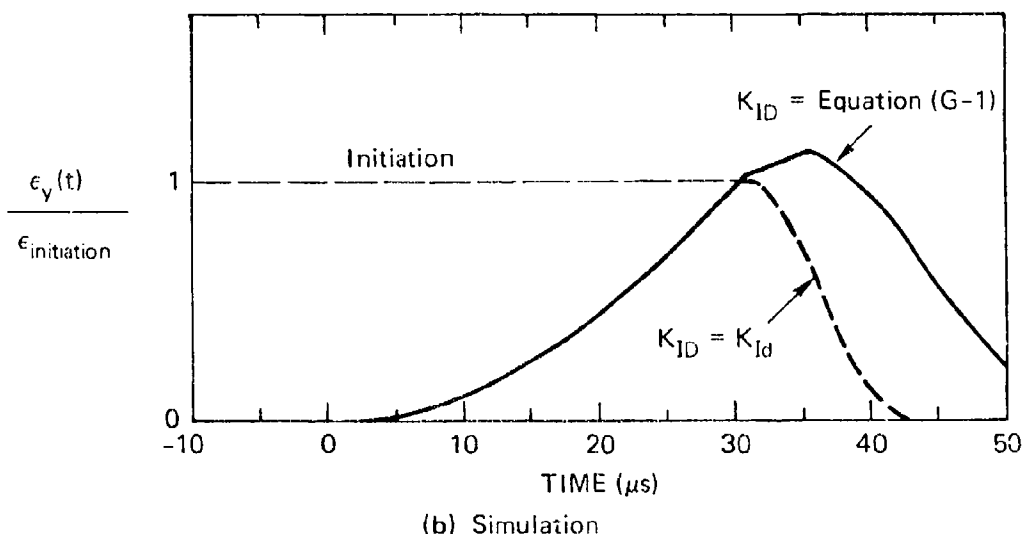
Figure G-13(a) shows a normalized strain history record for an experiment at high loading rate (3×10^6 MPa $\text{m}^{1/2} \text{s}^{-1}$). This strain history is much smoother than the records in Figures G-10 and G-12, suggesting that crack extension was continuous. Also, the strain does not drop significantly during the first 10 μs after initiation. Simulations of the high loading rate experiments in Figure G-13(b) indicate that, for a constant propagation toughness equal to the initiation toughness, the strain should drop much more rapidly. A simulation using equation (G-1) predicts a strain history resembling more closely the experimental one. From the comparison of the simulation and the experimental records, we estimate that the crack extended first at a very slow speed of about 100 m s^{-1} and then rapidly accelerated to about 500 m s^{-1} .

The observation of crack tunneling and the small but not negligible shear lips on the fracture surfaces raises the possibility that the crack front geometry and the shear lips may affect the strain history and the overall crack extension behavior. To investigate this possibility, we performed experiments on smooth and side-grooved specimens of identical shape and under the same loading conditions. The specimens were instrumented with a strain gage at the fatigue precrack tip and with an additional strain gage positioned 9 mm away from the crack tip along the prospective crack path. The second strain gage determined the average crack velocity immediately after crack initiation. A static calibration of the strain gages at the fatigue crack tip was performed to relate the strain history to the stress intensity history. For the side-grooved specimens, a thickness correction factor was introduced to account for the effect of the side grooves.

Figure G-14 shows strain histories near the fatigue crack tip for a smooth and for a side-grooved specimen. After crack initiation, the curves show a definite difference in shape. For the smooth specimen, the strain first decreases very gradually before it rapidly drops off. For the side-grooved specimen, the strain drops off immediately, suggesting a higher initial crack velocity when shear lips are suppressed.



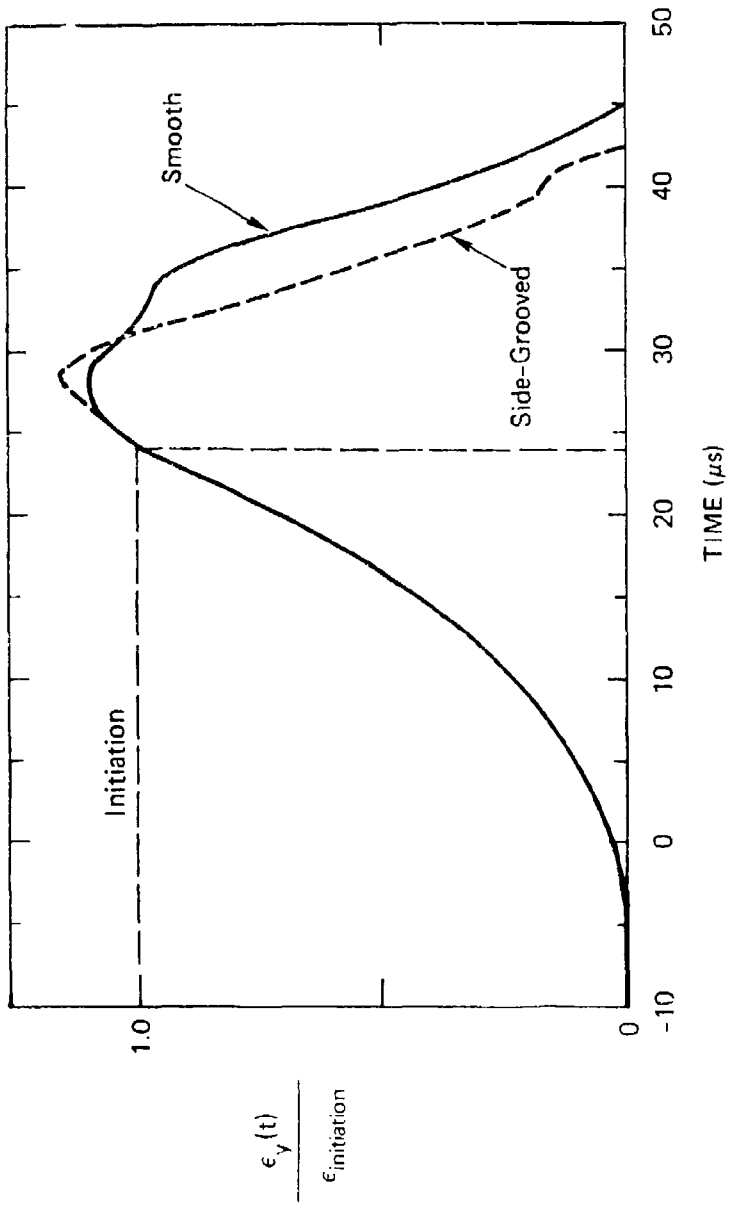
(a) Experimental Record



(b) Simulation

RA-1750-68

FIGURE G-13 NORMALIZED STRAIN HISTORY FOR 12.7-mm-THICK SPECIMEN
LOADED AT HIGH RATE



RA-1750-69

FIGURE G-14 NORMALIZED STRAIN HISTORY FOR SMOOTH AND SIDE-GROOVED SPECIMENS

Measurements of the average crack velocity with strain gages supports this interpretation with an average crack velocity of 360 m s^{-1} in the side-grooved specimen and 270 m s^{-1} in the smooth specimen. However, the rate of the rapid dropoff in the smooth and side-grooved specimens is the same, indicating similar crack velocities during this part of the crack extension. Therefore, the measured difference in the average crack velocity appears essentially due to the very slow initial crack velocity in the smooth specimen. In turn, this indicates that the resistance to crack propagation increases significantly above the initiation toughness level as the crack extends. Strain history simulations for the experiments of Figure G-13 show that a significant increase in propagation toughness above the initiation toughness must be postulated to duplicate the experimental results for the smooth specimen.

In summary, the experiments with 12.7-mm material have provided the following results. The crack velocity in the IPB tests increases with the loading rate. At lower loading rates (3.2×10^5 and $5.5 \times 10^6 \text{ MPa m}^{1/2} \text{ s}^{-1}$), crack extension is discontinuous and proceeds by a series of small crack jumps and arrests. Estimates of the average crack speed range from 130 m s^{-1} at a loading rate of $3.2 \times 10^5 \text{ MPa m}^{1/2} \text{ s}^{-1}$ to 170 m s^{-1} at a loading rate of $5.5 \times 10^6 \text{ MPa m}^{1/2} \text{ s}^{-1}$ to 500 m s^{-1} for the highest loading rate of $3 \times 10^6 \text{ MPa m}^{1/2} \text{ s}^{-1}$. Simulations of the strain histories indicate that the propagation toughness must be increased significantly ($20 \text{ MPa m}^{1/2}$ or more) above the initiation level during the first millimeters of crack growth to reproduce the observed crack speeds. Finally, the experiments with smooth and side-grooved specimens demonstrate that the formation of even small shear lips markedly affects the crack propagation behavior.

DISCUSSION

All the experimental results discussed above together with the strain history simulations show that, immediately after initiation, the crack extension resistance increases above the crack initiation toughness level. The crack jump experiments indicate that an increase in toughness of over $20 \text{ MPa m}^{1/2}$ occurs during the first 2 mm of crack extension.

Direct measurements with strain gages yield a propagation toughness of $140 \text{ MPa m}^{1/2}$ at a crack speed of about 400 m s^{-1} (Figure G-9), which is over twice the value of the initiation toughness. These observed increases in propagation toughness may be a function of at least two parameters: the amount of crack extension Δa and the crack velocity.

Most of the dynamic crack propagation work has focused on the relationship between crack velocity and propagation toughness K_{ID} .^{2,3} Although it is generally admitted that K_{ID} is a unique, increasing function of the crack velocity, it is unlikely that the increase in toughness observed in the crack jump experiments is due to crack velocity effects. First, the velocities measured in the crack jump experiments are low, whereas significant increases in K_{ID} for high strength steels are generally observed above 500 m s^{-1} only. Second, specimens having different crack velocities displayed the same behavior in the crack jump experiments (specimens CJ5 and H1 in Table G-2).

Therefore, we conclude that the initial increase in the propagation toughness above the initiation value in the 9.8-mm-thick material is a function of the amount of crack extension Δa . In other words, there is a resistance curve effect in the dynamic case as is often observed in static fracture experiments. The crack jump experiments and their simulations indicate that K_{ID} increases from the value of $57 \text{ MPa m}^{1/2}$ at initiation to $81 \text{ MPa m}^{1/2}$ after 2 mm of extension. They further suggest that, beyond this steady state value, K_{ID} does not depend significantly on the amount of crack extension. We presume that, as the crack extends and the crack speed increases, the dependence on the velocity becomes

²T. Kobayashi and J. W. Dally, "Dynamic Photoelastic Determination of the \dot{a} -K Relation for 4340 Steel," Crack Arrest Methodology and Applications, ASTM STP 711, G. T. Hahn and M. F. Kanninen, Eds. (American Society for Testing and Materials, 1980), pp. 189-210.

³A. J. Rosakis, J. Duffy, and L. B. Freund, "The Determination of Dynamic Fracture Toughness of AISI 4340 Steel by the Shadow Spot Method," *J. Mech. Phys. Solids*, Vol. 23, pp. 443-460 (1984).

more important and contributes to raise the propagation toughness further. Evidence for this behavior is provided by the direct measurements of the propagation toughness with strain gages shown in Figure G-9 which indicate values of $140 \text{ MPa m}^{1/2}$.

Therefore, the experiments with the 9.8-mm-thick specimens indicate that the propagation toughness depends both on the amount of crack extension and on the crack velocity. Equation (G-1), which was used for the strain simulations, is a crude attempt to represent and quantify this dependence. It was chosen, based on the experimental results, to represent all the data with a single toughness behavior. In particular, the dependence on the amount of crack extension was determined by fitting linear segments to the $K_{\text{Max}}^{\text{appl}}$ versus Δa curve of Figure G-2. Due to the limitations of the IFBT model, complete agreement with all the experimental results cannot be expected, particularly for the larger crack propagation distances. However, we believe that the simulations are adequate for predicting the early stage of crack extension and for qualitatively assessing the overall crack propagation behavior.

The crack propagation results for the 9.8-mm-thick specimens are in contrast with several published results for very similar materials, which indicate that the propagation toughness is a unique monotonic function of the crack velocity, which is essentially equal to the initiation toughness up to crack velocities of 500 m s^{-1} or more.^{2,3} However, other publications also report values of the propagation toughness in 4340 steel that are significantly larger than the initiation toughness at crack velocities as low as 80 m s^{-1} .^{4,5}

The results of the experiments on 12.7-mm-thick, smooth and side-grooved specimens provide the basis for a tentative explanation of the

⁴G. T. Hahn, R. C. Hoagland, A. R. Rosenfield, and R. Sejnoha, "Rapid Crack Propagation in a High Strength Steel," Met. Trans. Vol. 5, pp. 475-482 (1974).

⁵S. J. Hudak, R. J. Dexter, J. H. Fitzgerald, and M. F. Kanninen, "The Influence of Specimen Boundary Conditions on the Fracture Toughness of Running Cracks," Eng. Fract. Mech., Vol. 23, pp. 201-213 (1986).

observed propagation toughness behavior. The smooth 12.7-mm specimens displayed crack jump distances for a given $K_{I\text{Max}}^{\text{appl}}$ that were markedly larger than in the 9.8-mm-thick specimens, indicating that the dependence of the propagation toughness on the amount of crack extension is a function of the specimen thickness. Moreover, side-grooved specimens showed a markedly lower resistance to crack extension during the first millimeter of crack growth than the smooth specimens in which small shear lips formed. This was evidenced by the difference in the crack speed in the two types of specimens.

Based on these observations and on the curved shape of the arrested crack front, we believe that the rise in propagation toughness during the first increments of crack extension is due to the gradual change in the crack front geometry as it moves forward into the specimen and to the formation of small shear lips. These changes are in turn caused by the difference of constraint at the center of the specimen compared to the edges. Further the overall constraint level will be lower in the 9.8-mm specimen than in the 12.7-mm specimens, which would explain the observed difference in crack jump distance.

Additional evidence for this interpretation is provided by limited fractographic observations. Aside from the shape of the arrested crack front and the formation of shear lips, macroscopic fractographic observations reveal differences in the markings left on the fracture surface by the propagating crack in side grooved and smooth specimens. In the former, a pattern of lines more or less parallel to the specimen edges is observed on the fracture surface, whereas in the latter the lines strongly curve toward the edges. This curved pattern suggests that, near the edges, the crack propagates almost perpendicularly to the overall direction of crack propagation. This strong curvature of the crack front, which is essentially pinned down by the unbroken material in the shear lip, will without doubt affect the apparent propagation toughness.

Therefore, our investigation shows that part of the difference between the dynamic initiation and propagation toughness is due to a geometrical and a structural effect associated with changes in constraint along a propagating crack front and to the formation of small shear lips. This explanation is consistent with the observations of Hahn, et. al.⁴

Practical conclusions can be drawn from the results reported here. First, unless the thickness of the fractured specimen or part is large, there will be a resistance curve effect, even in the dynamic case, due to changes in the crack front geometry during the early part of crack extension. Because of this resistance curve effect, a rising applied stress intensity is required to drive the crack at a significant speed. In other words, there is the possibility for dynamic stable crack extension over very short distances. Second, our results show that the thicknesses sufficient to obtain valid dynamic initiation toughness values may not be sufficient for obtaining thickness-independent propagation toughness data. Third, because of the three-dimensional nature of the crack propagation process, caution should be applied in interpreting experimental data obtained from surface measurements. Finally, the results presented here have demonstrated that the strain history record obtained from a strain gage placed near the initial crack tip can be successfully analyzed to obtain crack velocity estimates and at least a qualitative assessment of the propagation toughness.

Appendix H

INVESTIGATION OF DYNAMIC CRACK EXTENSION BY MEANS OF HEAT OF FRACTURE MEASUREMENTS

This appendix reports on a series of crack extension experiments in which the crack was initiated from a blunt notch by quasi-static loading. The first objective of these experiments was to measure the dynamic propagation toughness for approximately steady crack velocity conditions (in contrast to the work reported in Appendix G, where we were interested in the transient regime immediately following initiation). The second objective of the experiments was to compare, by means of independent measurements, the energy delivered to the crack tip and the energy absorbed during crack propagation. The third objective was to evaluate several experimental techniques for measuring the dynamic propagation toughness: thermal measurement techniques with thermistors or thermocouples and a strain gage technique.

For reasons that will be discussed below, a direct comparison between energy delivered to the crack tip and energy absorbed could not be performed from the experiments. However, the experiments yielded propagation toughness values consistent with the values reported in Appendix G and highlighted several advantages and limitations of the experimental techniques we used.

PRINCIPLES OF THE EXPERIMENTS

During the experiments described in this Appendix, we intended to measure the applied dynamic stress intensity, $K_I^{dyn}(t)$, by means of strain gages and to derive the dynamic propagation toughness, $K_{ID}(\dot{a})$, from temperature measurements obtained using thermocouples and thermistors. The principles of these two approaches are summarized below.

Dynamic Stress Intensity Measurements

With reference to Figure H-1, the elastic stress field at the tip of a fast running crack in an infinite plate is given by the expressions:

$$\sigma_y = \frac{K_I^{\text{dyn}}}{\sqrt{2\pi r}} \phi_y(\beta, k, \theta) \quad (\text{H-1})$$
$$\sigma_x = \frac{K_I^{\text{dyn}}}{\sqrt{2\pi r}} \phi_x(\beta, k, \theta)$$

where ϕ_x and ϕ_y are nondimensional functions, $\beta = \dot{a}/c_1$, $k = (1 - 2\nu)/(2 - 2\nu) = C_t/C_1$, and \dot{a} , C_1 , and C_t are the crack velocity, the longitudinal wave velocity and the transverse wave velocity, respectively. ν is Poisson's ratio and r and θ are polar coordinates attached to the crack tip. Assuming plane stress conditions, the strain in the y direction is given by

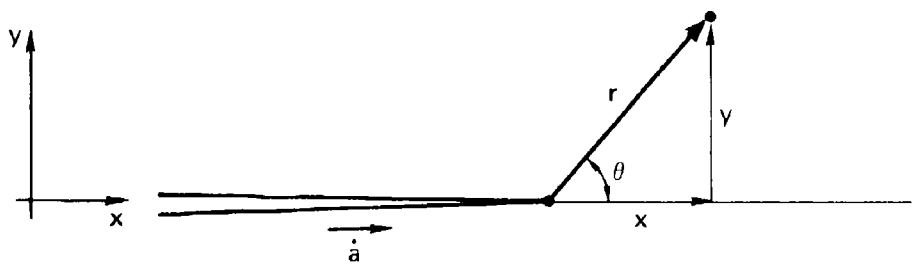
$$\epsilon_y = \frac{1}{E} (\sigma_y - v\sigma_x) \quad (\text{H-2})$$

As the crack tip approaches a material point located a fixed distance y from the crack plane, the strain ϵ_y at that point rises, reaches a maximum ϵ_y^{max} , and decreases. Denoting r_{max} and θ_{max} the moving coordinates of the material point when ϵ_y reaches its maximum ϵ_y^{max} and combining equations (H-1) and (H-2) yields

$$\epsilon_y^{\text{max}} = \frac{1}{E} \frac{K_I^{\text{dyn}}}{\sqrt{2\pi r_{\text{max}}}} [\phi_y(\beta, k, \theta_{\text{max}}) - v\phi_x(\beta, k, \theta_{\text{max}})] \quad (\text{H-3})$$

By rearranging (H-3) and substituting $r_{\text{max}} = y/\sin \theta_{\text{max}}$, we can express the dynamic stress intensity factor as

$$K_I^{\text{dyn}} = \epsilon_y^{\text{max}} E \sqrt{2\pi y} / H(\beta, k, \theta_{\text{max}}) \quad (\text{H-4})$$



RA-1750-44

FIGURE H-1 COORDINATES AT A RUNNING CRACK TIP

where $H(\beta, k, \theta_{\max}) = \sqrt{\sin \theta_{\max}} [\phi_y(\beta, k, \theta_{\max}) - v\phi_x(\beta, k, \theta_{\max})]$.

θ_{\max} can be obtained by differentiating the expression for ϵ_y with respect to θ and is a function of crack velocity and Poisson's ratio. As tabulated in Table H-1, the values of θ_{\max} over the range of interest for a/C_t and v ($a/C_t = 0$ to 0.6 and $v = 0.1$ to 0.49) vary only between 69° and 73° . The function $H(\beta, k, \theta_{\max})$ is plotted in Figure H-2.

Thus it is seen from equation (H-4), that, if the crack velocity a and the strain ϵ_y at a small distance y from the crack plane are known, say, from strain gage measurements, the stress intensity factor can easily be determined. The crack velocity can be estimated by measuring the time interval between the peak strains recorded by two neighboring gages placed at a known distance from each other along the crack path. By mounting a series of strain gages parallel to the specimen center line, we can measure a K_I^{dyn} -a history at regular intervals as the crack propagates. This approach was taken in the present experiments.

The strain gage method of measuring $K_I^{\text{dyn}}(t)$ is based on two limiting assumptions. First, it uses the analytical solution for a crack extending at a constant velocity in an infinite plate, and therefore, it does not account for the effect on the crack tip field of stress waves reflected at the boundaries. For a finite geometry, it has been shown³ that stress waves emanating from the extending crack tip, reflecting at the boundaries, and returning to the crack tip can cause significant changes in the instantaneous stress intensity factor and result in a transient change in the crack velocity. The second limitation of the strain gage method is that it considers only the singular term of the series expansion for the crack tip fields. However, in finite size specimens, higher order terms may also be important.⁴ An additional limitation is the restricted number of measurement positions, which obviously limits the ability to measure rapid transients in crack velocity and stress intensity factor. Therefore, this technique must be used with caution.

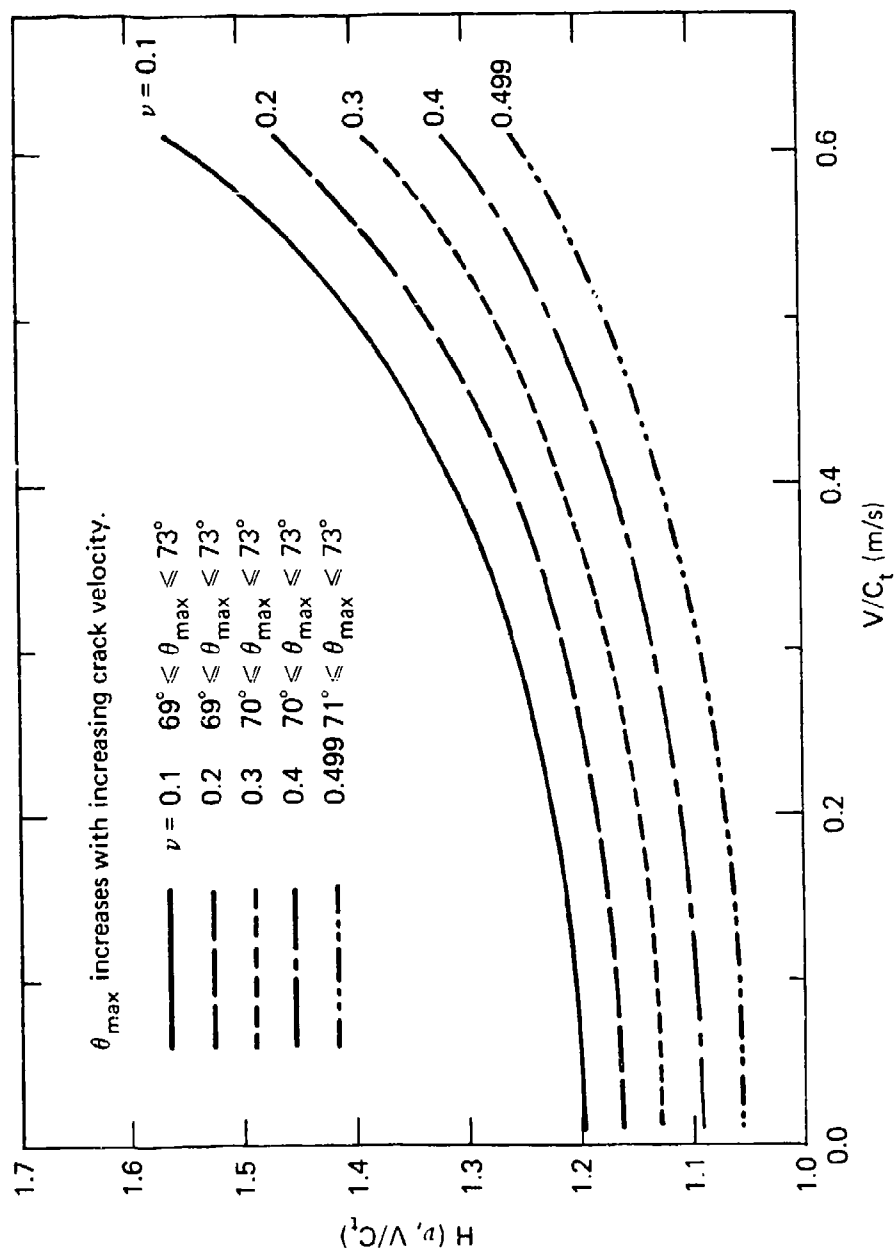


FIGURE H-2 NONDIMENSIONAL FUNCTION H USED IN CALCULATING K_I^{dyn}
FROM STRAIN GAGE MEASUREMENTS

RA-1750-45

Table H-1 Angle θ_{\max} for Maximum Strain ϵ_y^{\max}

V/C_t	$\nu_1 = 0.1$	$\nu = 0.2$	$\nu = 0.3$	$\nu = 0.4$	$\nu = 0.49$
0.01	69.0	69.0	70.0	70.0	71.0
	69.0	69.0	70.0	70.0	71.0
	69.0	69.0	70.0	70.0	71.0
	69.0	69.0	70.0	70.0	71.0
	69.0	69.0	70.0	70.0	71.0
	69.0	69.0	70.0	70.0	71.0
	69.0	69.0	70.0	70.0	71.0
	69.0	69.0	70.0	70.0	71.0
	69.0	69.0	70.0	70.0	71.0
	69.0	69.0	70.0	70.0	71.0
0.1	69.0	69.0	70.0	70.0	71.0
	69.0	69.0	70.0	70.0	71.0
	69.0	70.0	70.0	70.0	71.0
	69.0	70.0	70.0	70.0	71.0
	69.0	70.0	70.0	70.0	71.0
	69.0	70.0	70.0	70.0	71.0
	69.0	70.0	70.0	70.0	71.0
	69.0	70.0	70.0	70.0	71.0
	69.0	70.0	70.0	70.0	71.0
	69.0	70.0	70.0	70.0	71.0
0.2	69.0	70.0	70.0	70.0	71.0
	69.0	70.0	70.0	70.0	71.0
	69.0	70.0	70.0	70.0	71.0
	69.0	70.0	70.0	70.0	71.0
	69.0	70.0	70.0	70.0	71.0
	69.0	70.0	70.0	70.0	71.0
	69.0	70.0	70.0	70.0	71.0
	69.0	70.0	70.0	70.0	71.0
	69.0	70.0	70.0	70.0	71.0
	69.0	70.0	70.0	70.0	71.0
0.3	70.0	70.0	71.0	71.0	71.0
	70.0	70.0	71.0	71.0	71.0
	70.0	70.0	71.0	71.0	71.0
	70.0	70.0	71.0	71.0	71.0
	70.0	70.0	71.0	71.0	71.0
	70.0	70.0	71.0	71.0	71.0
	70.0	70.0	71.0	71.0	71.0
	70.0	70.0	71.0	71.0	71.0
	70.0	70.0	71.0	71.0	71.0
	70.0	70.0	71.0	71.0	71.0
0.4	70.0	70.0	71.0	71.0	71.0
	71.0	71.0	71.0	71.0	71.0
	71.0	71.0	71.0	71.0	71.0
	71.0	71.0	71.0	71.0	71.0
	71.0	71.0	71.0	71.0	71.0
	71.0	71.0	71.0	71.0	71.0
	71.0	71.0	71.0	71.0	71.0
	71.0	71.0	71.0	71.0	71.0
	71.0	71.0	71.0	71.0	71.0
	71.0	71.0	71.0	71.0	71.0
0.5	72.0	72.0	72.0	72.0	72.0
	72.0	72.0	72.0	72.0	72.0
	72.0	72.0	72.0	72.0	72.0
	72.0	72.0	72.0	72.0	72.0
	72.0	72.0	72.0	72.0	72.0
	72.0	72.0	72.0	72.0	72.0
	72.0	72.0	72.0	72.0	72.0
	72.0	72.0	72.0	72.0	72.0
	72.0	72.0	72.0	72.0	72.0
	72.0	72.0	72.0	72.0	72.0
0.6	73.0	73.0	73.0	73.0	73.0
	73.0	73.0	73.0	73.0	73.0

RA-1750-56

Dynamic Propagation Toughness Measurements

The dynamic fracture toughness of the propagating cracks was derived from the temperatures measured on the specimen surface near the running crack. Nearly all the energy absorbed by a propagating crack is absorbed by plastic flow of material in a relatively small (compared with specimen dimensions) volume in the vicinity of the crack tip. Therefore, the fracture toughness associated with the propagating crack is determined by the plastic energy expended at the crack tip. Taylor and Quinney⁵ showed that for metals nearly all the plastic energy is dissipated as heat. Heat generated at a running crack tip flows away from the crack plane into both halves of the specimen, causing small transient temperature elevations. If the temperature history of material near a running crack can be measured, the heat energy and hence the plastic energy and the propagation toughness can be calculated by solving the appropriate heat flow equation.

Thermocouples and thermistors were used in these experiments to measure near-crack-tip temperature histories. This method was used first by Wells⁶ and later improved and applied by several other investigators.⁷⁻¹⁰

To obtain the heat generated by the propagating crack Q and the dynamic fracture toughness K_{ID} , we used the measured maximum temperature values ΔT_{max} and the solution of the one-dimensional heat flow equation for an instantaneous heat source.¹¹⁻¹³

$$Q = \Delta T_{max} y \sqrt{2\pi e} \rho c = \frac{K_{ID}^2}{E} \quad (H-5)$$

where y is the distance between the fracture surface and the temperature transducer, $e = 2.718$, and ρ , c , and E are the mass density, the specific heat, and Young's modulus, respectively.

The adequacy of the models used for interpreting the experiments and the measurements error for the strain and temperature data are discussed along with the results.

EXPERIMENTAL PROCEDURES

Six transversally wedge-loaded compact tension (CT) specimens were prepared from a commercial aircraft quality 4340 steel plate. The rough machined specimens were heat-treated to HRC 50 and then ground to the final dimensions and tolerances shown in Figure H-3. The loading hole and the starter notch were put in by electrodischarge machining. Chevrons of varying acuity were introduced at the bottom of the notch using a thin grinding wheel.

Each specimen was instrumented with four miniature strain gages evenly spread along the anticipated crack path and about 1/8 inch from the specimen center line (Figure H-3). These strain gages measured the crack velocity as well as the applied dynamic stress intensity factor K_I^{dyn} at the running crack tip. In addition to the strain gages, two thermocouples and four thermistors were mounted on each specimen. The active junction of the thermocouples consisted of a 0.2-mm constantan wire spot-welded to the specimen a few millimeters away from the crack path. Another constantan wire, spot welded in a corner of the specimen away from the crack, acted as reference junction. The thermistors (Siemens K19) were less than 0.4 mm in diameter and were held on the specimen with heat conducting paste.

The precise positions of the temperature sensors on the specimen varied from test to test, but they were more or less evenly spaced along the crack path at a distance not exceeding 10 mm. In some cases one thermocouple and one thermistor were mounted as close to each other as possible so that they would see essentially the same temperature history. This arrangement made a direct comparison of the two types of transducers possible.

During loading of the specimen, the crack mouth opening displacement (CMOD) was measured using a clip gage.

Figure H-4 diagrams the electronic circuitry that was used to process and record the signals from the various transducers. The strain gage signals were recorded on dual-channel digital oscilloscopes with a

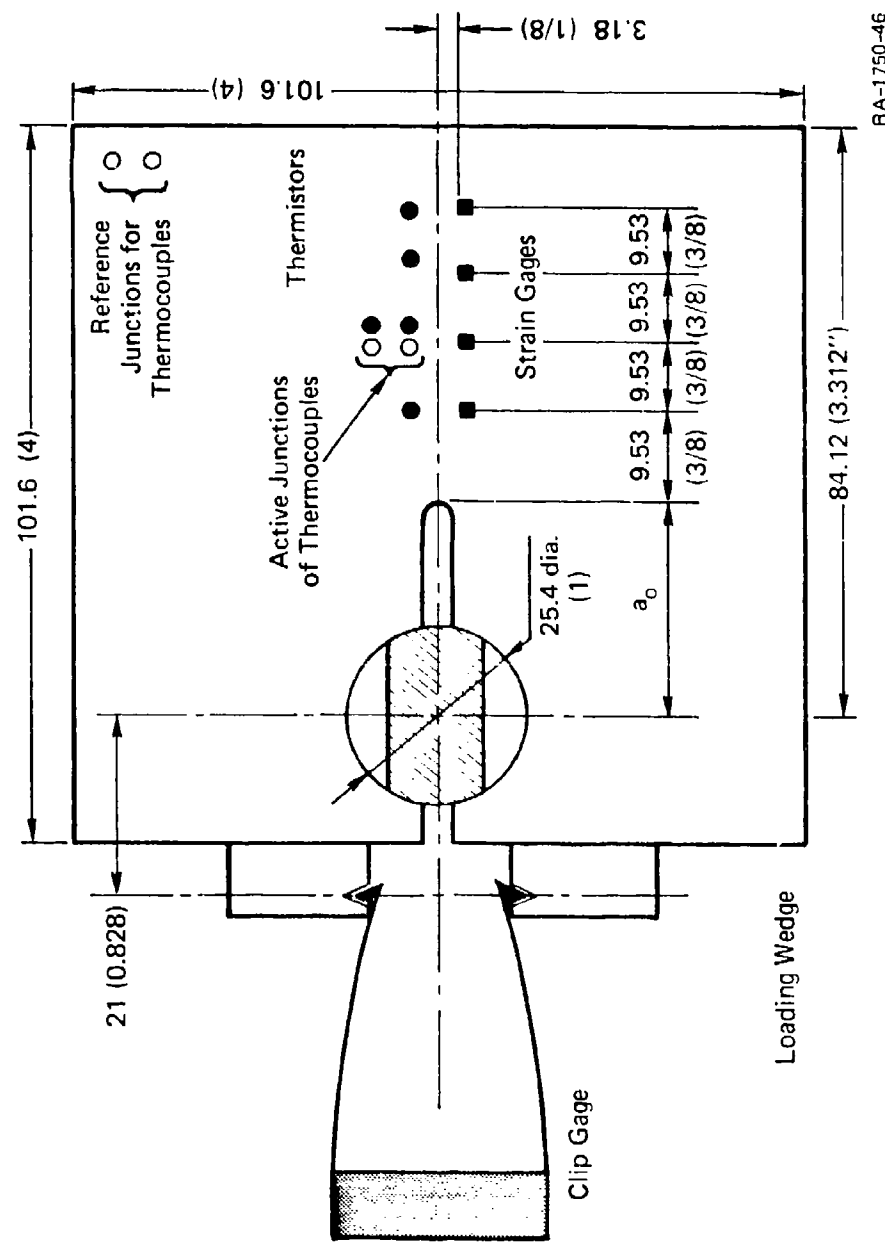
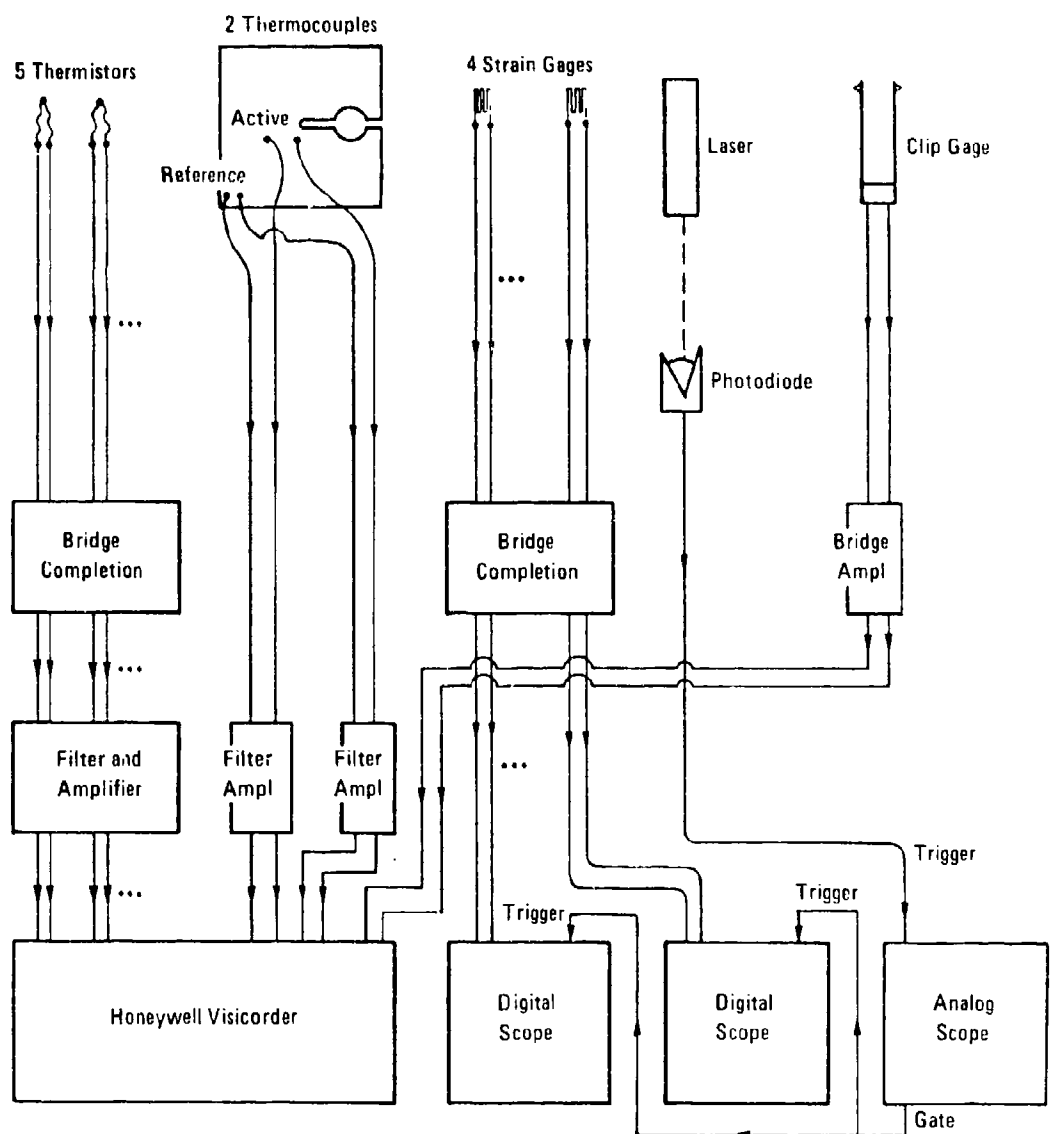


FIGURE H-3 CRACK PROPAGATION SPECIMEN DIMENSIONS IN mm (inch)
AND INSTRUMENTATION



RA-1750-47

FIGURE H-4 ELECTRONIC INSTRUMENTATION FOR CRACK PROPAGATION EXPERIMENTS

1-ms time window. The temperature histories were recorded on a Honeywell eight-beam strip chart recorder. During loading, the CMOD was also recorded on the strip chart recorder.

To trigger the oscilloscopes, we used a laser beam directed at a spot a few millimeters ahead of the specimen starter notch and reflected by the polished specimen surface onto a photodiode. When the crack becomes unstable, it displaces a small plastic zone around its moving tip. As the plastic zone crosses the laser beam, it deflects it away from the photodiode and the voltage change at the photodiode output triggers the oscilloscopes.

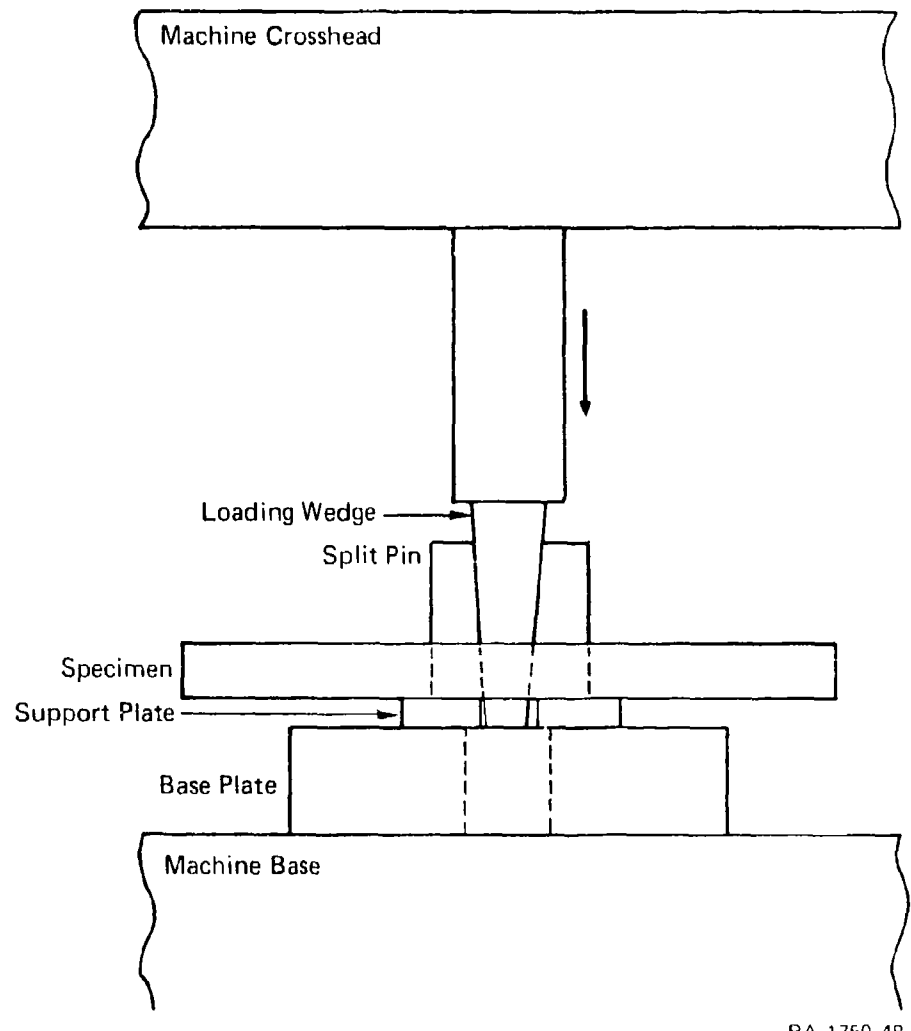
After checking that the response of the thermistors was linear in the temperature range of interest, we calibrated the thermistors against a thermocouple of known temperature sensitivity. A similar procedure was used to calibrate the thermocouples.

The specimens were loaded to fracture in a 10-kips screw-driven Instron universal testing machine. The loading arrangement is shown in Figure H-5. Two support steel plates were inserted between the two halves of the split-pin and the base plate to prevent any axial loading of the specimen and to suppress friction at the specimen support plate interface. For all the experiments, the machine cross-head speed was 8 mm s^{-1} . At this cross-head rate, loading to fracture took less than 2 seconds.

The testing machine was manually operated. Due to the slow reaction time of the operator and the inertia in the loading train, it took about half a second for the cross-head to stop after the instability and crack arrest events. As discussed below this delay in interrupting the specimen loading after the test was completed is significant for interpretation of the test results.

EXPERIMENTAL RESULTS

Two of the six experiments that were performed gave a complete set of strain and temperacure measurements (specimens CT3 and CT6). For one



RA 1750-48

FIGURE H-5 LOADING ARRANGEMENT FOR CRACK PROPAGATION EXPERIMENTS

specimen (CT1), the strain gage signals could not be recorded because the sensitivity of the oscilloscopes was improperly set. For two other specimens (CT4 and CT5), the strain gage data were lost because of trigger problems. Finally, for specimen CT2, there was a first initiation at a relatively low K_{IQ} ; then the crack arrested, reinitiated upon further loading, and arrested again after a total extension of only 24 mm. The multiple initiations rendered the interpretation of the temperature data impossible. Small shear lips formed in all six specimens tested. The width and height of the shear lip were about 1.5 mm near the initial notch and tapered to about 1 mm in the arrest region.

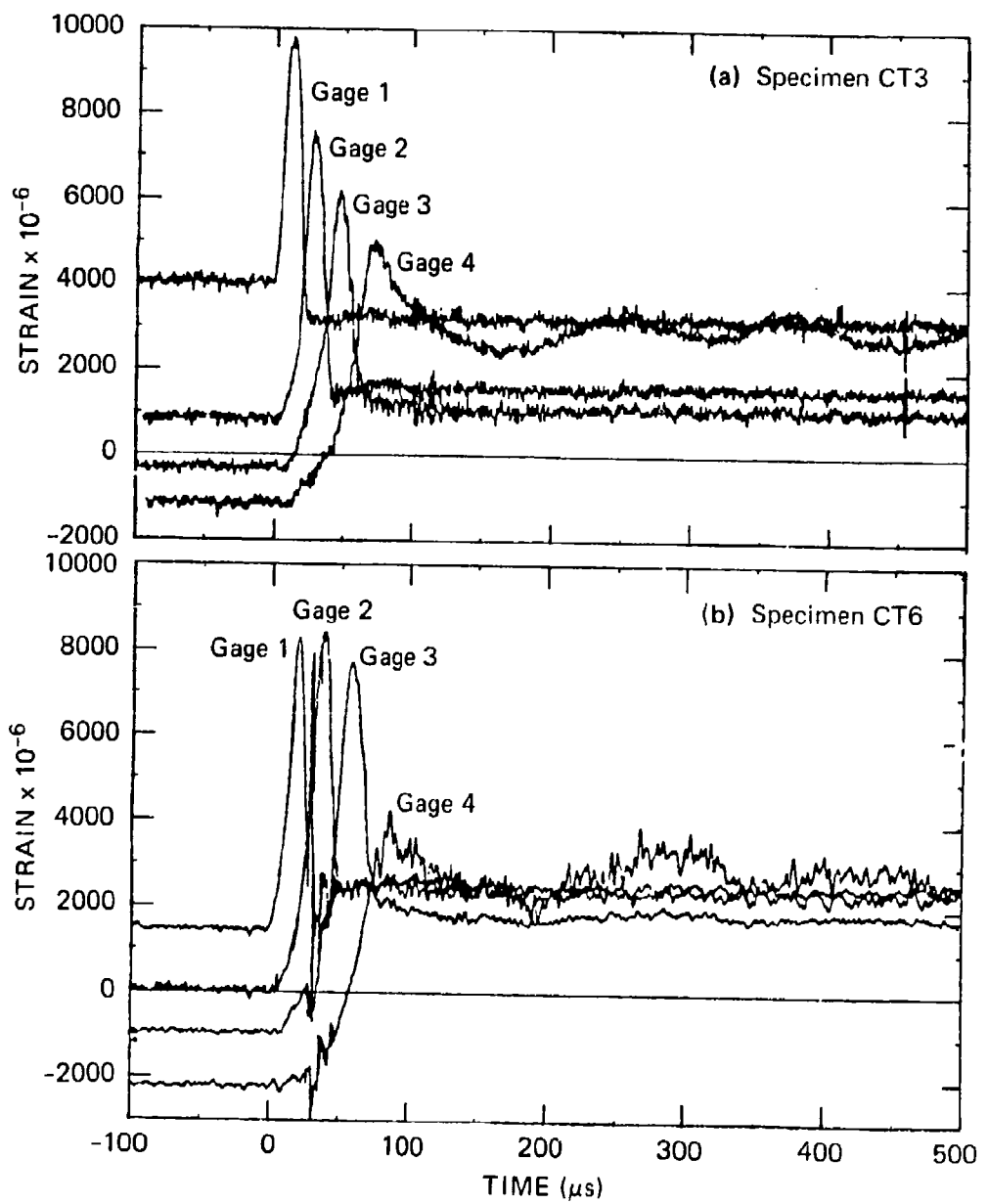
The K_{IQ} 's and arrest crack lengths for all six specimens are given in Table H-2. Tests CT3 through CT6 have similar K_{IQ} values and arrest crack lengths. Based on this observation and on the work of Hoagland et al.,¹⁴ we concluded that all four specimens had about the same crack propagation history. Thus the propagation toughness data obtained in tests CT4 and CT5 can be evaluated using the strain histories and crack velocities measured in tests CT3 and CT6.

Figure H-6 plots the strain histories obtained with the four strain gages in tests CT3 and CT6. In each plot, the strain gage signals have been superimposed in such a way that they have the same strain baseline and the same time base. The strain histories for the two experiments are very similar. The observable differences between the strain histories in tests CT3 and CT6 occur because the row of evenly spaced strain gages was positioned further away from the original notch in test CT6 than in test CT3.

The sharp strain peaks are caused by the passage of the crack tip near the strain gage. The signals from gage 4 in both test have a different shape than the signals from gages 1 to 3 because in both tests strain gage 4 was located very close to the arrested crack tip. Also, the strain histories for gage 4 do not have a sharp peak, the strain does not decrease to zero after going through the maximum, and there is a significant oscillation in the late time strain history. This oscillation indicates that, after crack arrest, the material in the

Table H-2
EXPERIMENTAL PARAMETERS FOR SIX WEDGE-LOADED COMPACT TENSION TESTS

Test #	Initial Crack Length (mm)	K_{IQ} (MPa $\sqrt{\text{m}}$)	Arrest Crack Length (mm)	Δa (mm)
CT1	34.6	394	80.0	45.4
CT2	33.6	190	57.8	24.2
CT3	33.1	284	71.7	38.6
CT4	33.9	306	76.5	42.6
CT5	32.5	265	77.2	44.7
CT6	34.4	288	74.4	40.0



RA-1750-49

FIGURE H-6 STRAIN HISTORIES ALONG CRACK PATHS

region of the arrested crack tip continues to be loaded by the vibrating specimen.

The propagation time from one gage location to the other can be directly measured in Figure H-6 as the time difference between successive peaks. Using the singularity solution to estimate the position of the crack tip with respect to the gage position at the time of the strain maximum, we can estimate the crack velocity. The strain signals before the sharp peaks give a measure of the strain in the specimen during quasi-static loading before crack extension, and the signals after the sharp peaks show the residual strains after crack propagation. Figure H-6 shows that the maximum strains measured by gages 1, 2, and 3 were very large (in excess of 6000 microstrains) and that significant residual stresses were left in the wake of the crack (in excess of 1000 microstrains). These high strain values suggest that the material at or near the gage location (about 3 mm from the crack plane) may have yielded. This result is consistent with the estimate of the radius of the plastic zone of about 2 mm based on the shear lip size.

Figure H-7 plots the crack velocity profiles as a function of crack position obtained from the strain gage measurements in tests CT3 and CT6. Estimates for the crack velocity profiles in tests CT4 and CT5 are also indicated in the figure. These estimates were obtained in the following way. Because the K_{IQ} values and the arrested crack length were similar in all the tests, we assumed that the crack velocity profiles from tests CT3 and CT6 would also apply to tests CT4 and CT5. The assumed initial velocity was slightly raised or lowered to account for the differences in K_{IQ} . The velocity curves of test CT3 (for test CT5) and CT6 (for test CT4) were then displaced to fit through the points $\Delta a = 0$, $\dot{a} = \dot{a}_{init}$ and $\Delta a = \Delta a_{ar}$, $\dot{a} = 0$. The crack velocity profiles of Figure H-7 were used in plotting the stress intensity and propagation toughness data measured with the strain gages, the thermocouples, and the thermistors.

Figures H-8 and H-9 show temperature histories recorded near the crack plane in tests CT3 and CT6, respectively. The dashed vertical

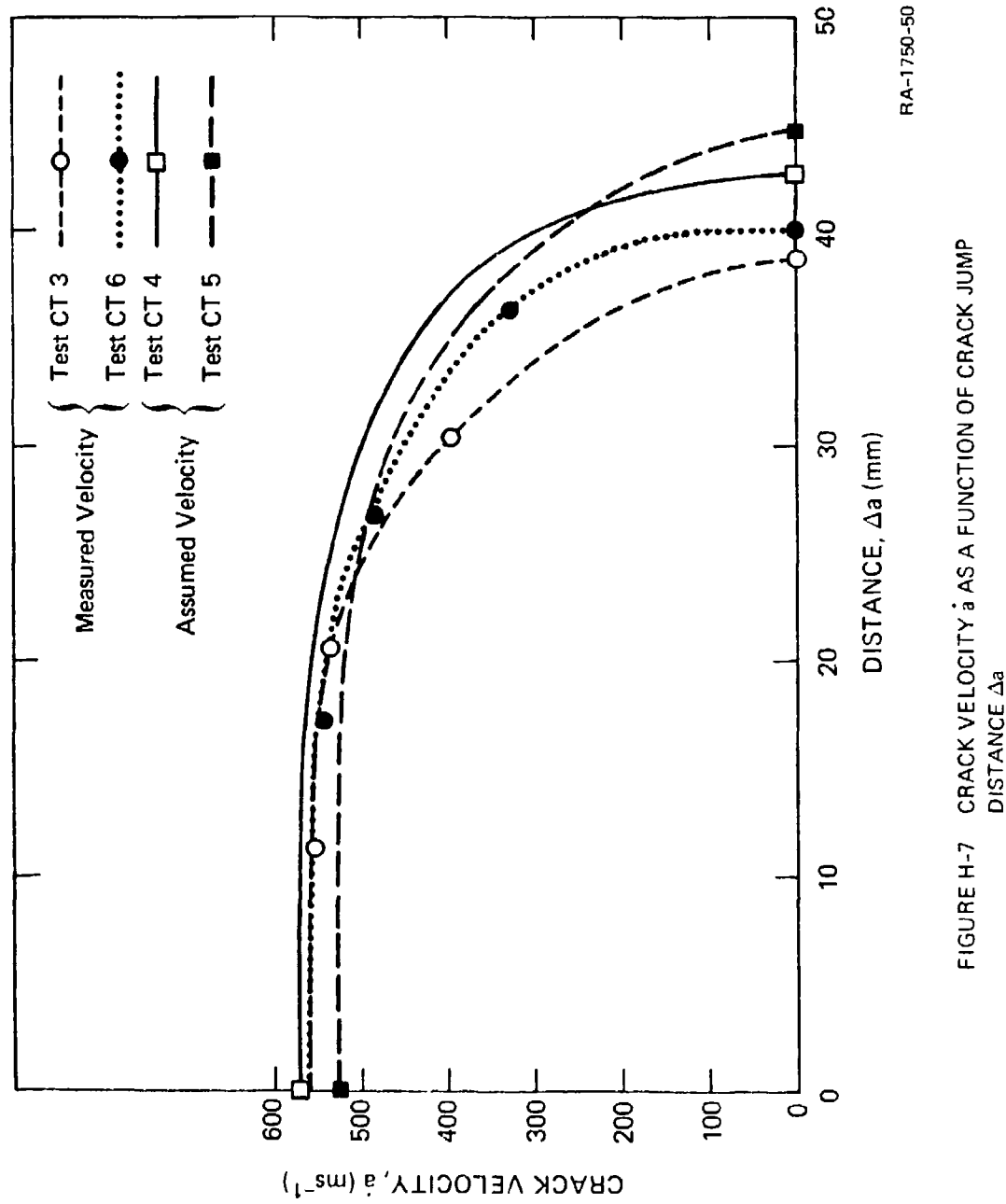
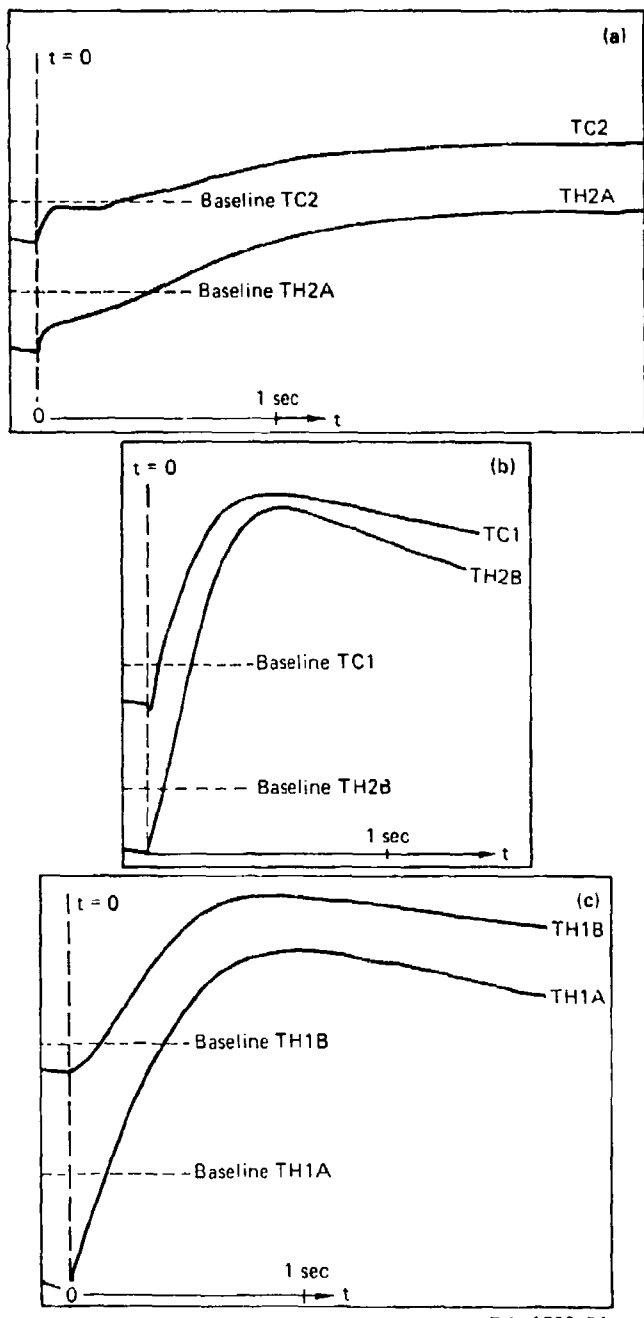
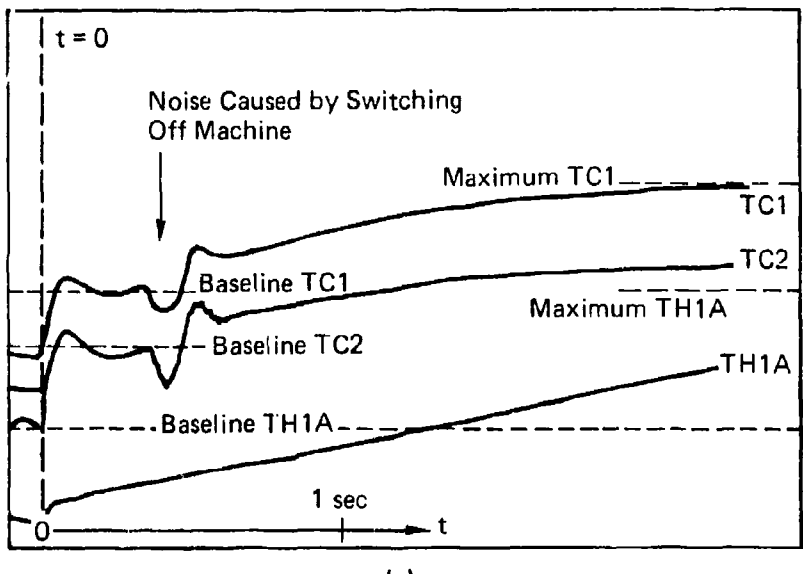


FIGURE H-7 CRACK VELOCITY \dot{a} AS A FUNCTION OF CRACK JUMP
DISTANCE Δa

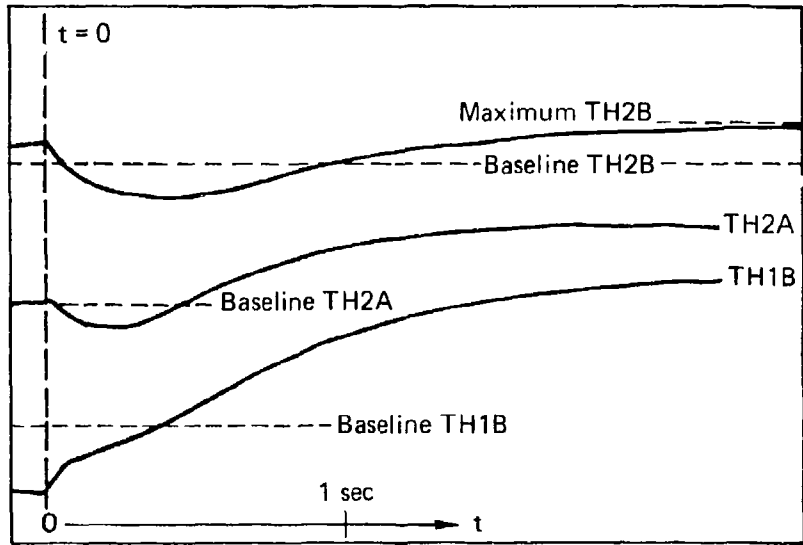


RA-1750-51

FIGURE H-8 TEMPERATURE HISTORIES FOR SPECIMEN CT3
(TH = Thermistors, TC = Thermocouples)



(a)



(b)

RA-1750-52

FIGURE H-9 TEMPERATURE HISTORIES FOR SPECIMEN CTG
(TH = Thermistors, TC = Thermocouples)

lines in the figures indicate the instant of crack initiation. After crack extension and arrest, simple one-dimensional heat flow considerations show that the temperature at the transducer location should gradually rise, pass through a maximum, and then slowly decrease as the specimen reaches thermal equilibrium. The amplitude of the temperature maximum is a function of the position of the transducer and of the intensity of the heat source (equation H-5).

During quasi-static loading of the specimens, the temperature transducers register a temperature change that is linear with time (portion of the temperature histories to the left of the vertical dashed lines). This temperature change is associated with the thermoelastic effect in the specimen, which causes cooling of the material at points where the mean stress is tensile and heating at points where the mean stress is compressive. If the loading is fast enough, this temperature change occurs quasi-adiabatically, and it is reversible once the elastic stress is relieved by the passage of the crack. Thus after crack arrest, the temperature is expected to go back to the base-line value almost instantaneously, before gradually rising because of heat flow from the fracture surface.

Figures H-8 and H-9 indicate that, although for the thermocouples the recovery of the thermoelastic temperature excursion is relatively fast and complete, Figure H-8(a) and (b), and Figure H-9(a), this is not the case for the thermistors, which in some instances show considerable delay and only partial temperature recovery. The reasons for this behavior are not entirely clear. It may be due to poor heat conduction of the cement used for mounting the thermistors or to residual stresses that prevent complete material unloading after the passage of the crack and hence complete temperature recovery.

Another anomalous temperature behavior is evidenced in Figure H-9(b), where the temperature histories measured by thermistors TH2A and TH2B first decrease after the fracture event, go through a minimum, and then increase as expected from heat flow considerations. This behavior is characteristic of the transducers placed near the arrested crack tip

region and is due to the thermoelastic effect. After crack extension and arrest, the loading machine was stopped manually by the operator. Therefore, a delay of 0.5 to 1 second occurred between crack arrest and shut-off of the loading machine. Because high displacement rates were used to drive the wedge (to minimize heat flow caused by the nonequilibrium thermoelastic temperature distribution during loading), this small delay is sufficient to permit reloading of the arrested crack tip, which in turn results in thermoelastic cooling of the material in the crack tip region that is under tensile stress. The thermoelastic cooling is superimposed on the temperature elevation due to heat flow from the crack plane and makes interpretation of the temperature histories impossible. Therefore, the temperature data from such records have been discarded.

The stress intensity factor K_I^{dyn} was calculated from the strain gage data using equation (H-3). The propagation toughness was calculated from the temperature data using equation (H-5) and from the maximum temperature amplitude ΔT_{\max} , defined as the difference between the maximum in the temperature history and the baseline temperature just before the test. Because the thermoelastic temperature excursion was not always recovered, this definition yields a lower bound for the propagation toughness. The propagation toughness values calculated with equation (H-5) were also corrected to account for the finite width of the plastic zone. The correction is necessary because, as evidenced by the shear lips at the specimen edge, the plastic zone is about 4 mm. Thus, the distance from the temperature transducer to the crack plane can no longer be considered large compared with the width of the instantaneous heat source. To correct the propagation toughness values, we calculated the temperature history at various distances from the heat source for the case of an instantaneous line heat source and for the case of an instantaneous heat source distributed uniformly over a width $2r_y$. The total heat dissipation per unit crack area was assumed the same in both calculations. Figure H-10 compares the results for a calculation assuming a heat source width $2r_y$ of 4 mm with the results for a line heat source. The history of temperature elevation, normalized by the heat

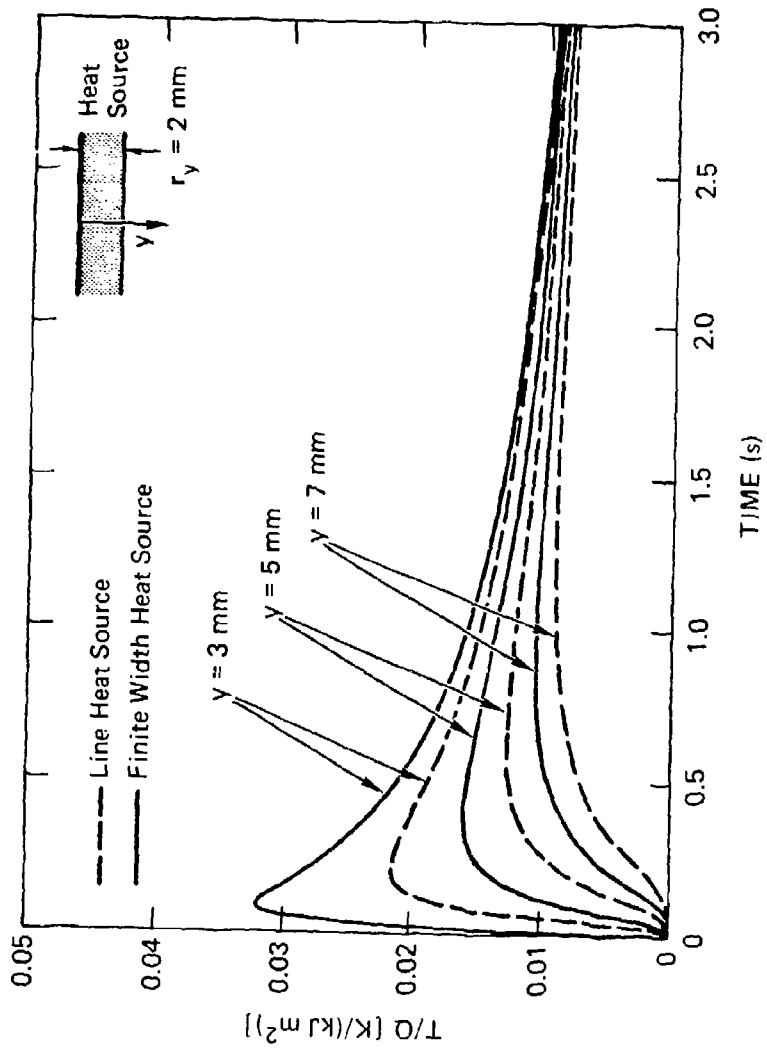


FIGURE H-10 NORMALIZED TEMPERATURE HISTORIES AT SEVERAL LOCATIONS y
FOR LINE HEAT SOURCE AND FINITE WIDTH HEAT SOURCE ($r_y = 2 \text{ mm}$)

RA-1750-53

source amplitude Q , is plotted for several distances from the center of the heat source. At a given point and for a given value of Q , use of the line heat source model predicts a lower temperature elevation than the finite width heat source. Conversely, use of a given temperature elevation with the line heat source model predicts a higher value of Q than the use of the same temperature elevation with the finite width heat source model. The correction factor for the appropriate measurement distance for each temperature transducer was calculated from the differences in T/Q -amplitude in Figure H-10 and applied to the Q values calculated with equation (H-5).

The stress intensity values calculated from the strain gage data and the propagation toughness values calculated from the temperature data are plotted in Figure H-11 as a function of crack velocity and in Figure H-12 as a function of distance from the original crack tip. Also plotted in Figure H-12 is a curve giving the statically calculated stress intensity factor as a function of crack length for initial conditions representative of those in test CT3 through CT6 (crack opening displacement at initiation = 1.7 mm, $a_0/W_0 = 0.402$). The value K_{ID} shown in Figures H-11 and H-12 represents the dynamic initiation toughness measured independently with the one-point-bend test for the particular batch of 4340 steel used for the CT crack extension experiments.

In Figure H-11, the K_I^{dyn} values obtained from strain gage measurements lie significantly above the K_{ID} data obtained from the temperature measurements. The K_{ID} data show a large scatter and most of the data are grouped in the velocity range 500 to 600 $m s^{-1}$ because of the elimination of the data points affected by the post-arrest thermoelastic effect. In Figure H-12, the K_I^{dyn} data again lie well above the K_{ID} data but also above the static curve. This result contradicts previously published results, which show that during the early part of crack extension K_I^{dyn} is below K_I^{stat} and at later times the opposite situation prevails.¹⁵ However, the K_{ID} values show the expected trend, first falling below the static curve and then approaching or crossing the static curve close to the arrest crack length. Note that

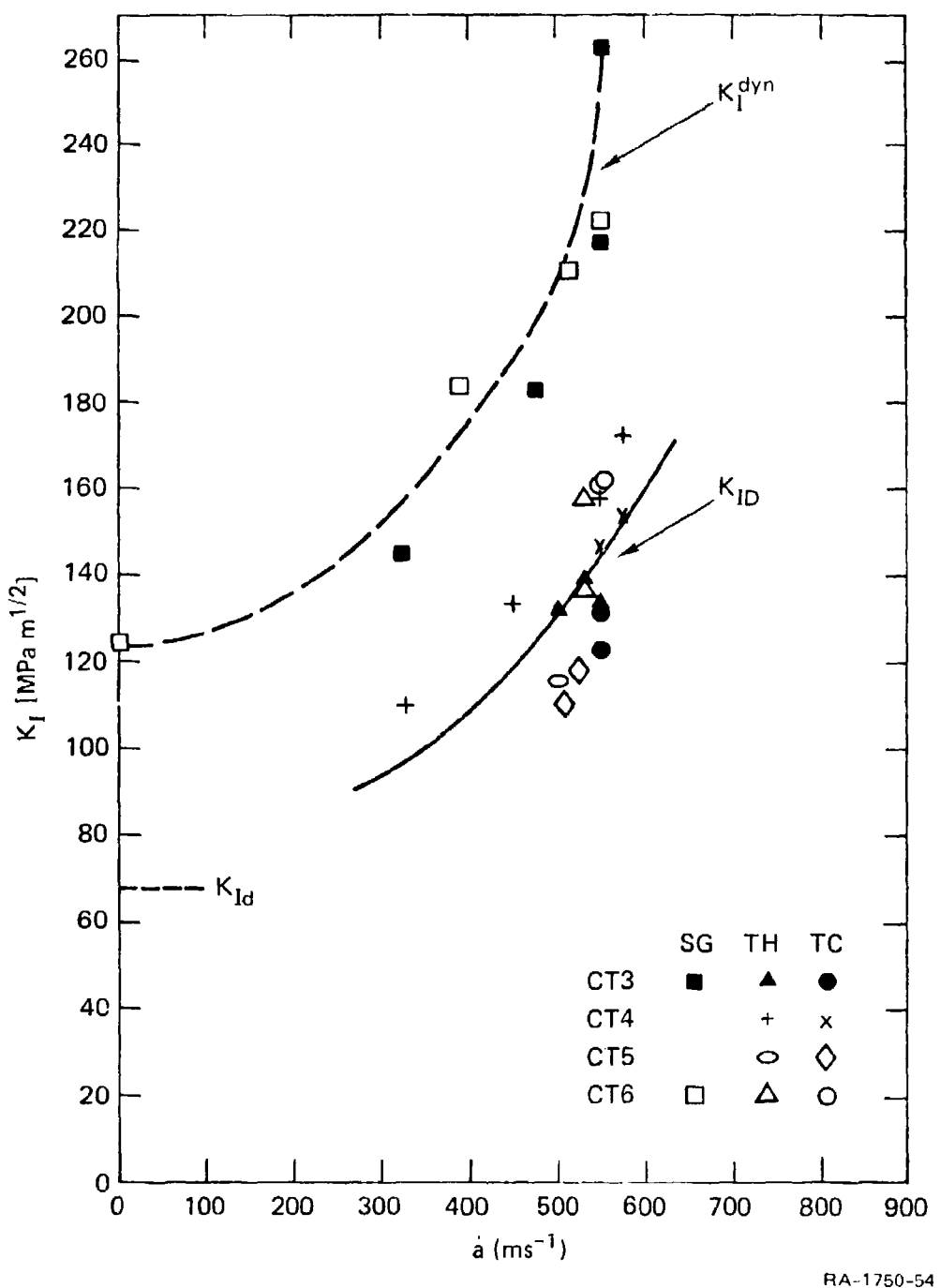


FIGURE H-11 K_I^{dyn} AND K_{ID} AS A FUNCTION OF CRACK VELOCITY \dot{a}

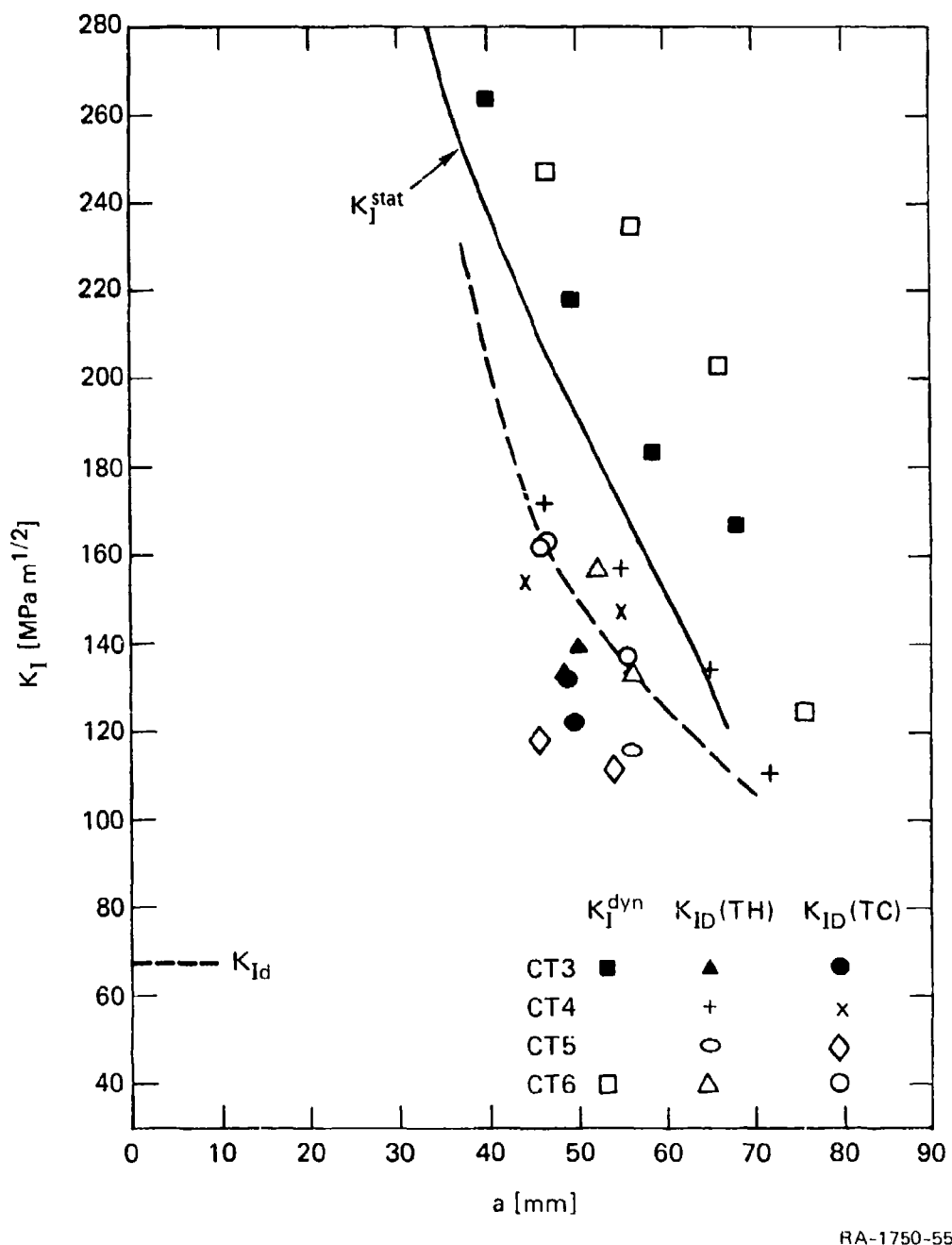


FIGURE H-12 K_I^{stat} , K_I^{dyn} , AND K_{ID} AS A FUNCTION OF CRACK LENGTH

the K_{ID} and the K_I^{dyn} measured in the CT experiments are much higher than the dynamic initiation toughness K_{Id} .

The objective in using two types of temperature sensors for the thermal measurements was to evaluate the relative advantages of thermocouples and thermistors. Table H-3 compares the results of pairs of thermocouple-thermistors positioned at the same location. In each case the general shape of the temperature history pairs agree well (see Figures H-8 and H-9). There is, however, a systematic difference in the maximum temperature amplitude that results in a systematic difference in the K_{ID} values. Thus, the K_{ID} values obtained from the thermistor measurement are lower than the K_{ID} values obtained from the thermocouple measurements. The reason for this systematic difference has not been established. Note that because the toughness depends on the square root of the temperature, the differences in propagation toughness estimates are relatively small compared with the temperature differences.

DISCUSSION AND CONCLUSIONS

The propagation toughness measured in the present experiments is much higher than expected from published data for similar materials^{16,17} or from comparisons with the dynamic initiation toughness. This high value of the propagation toughness is associated with a large plastic zone, which affects our ability to measure the applied stress intensity factor K_I^{dyn} using strain gages. Indeed, the high strains measured during the experiments (Figure H-6) and the large residual strains measured after crack arrest demonstrate that the material at and near the strain gage locations (3 mm from the crack plane) was deformed beyond the elastic limit. Therefore, the proposed approach of using the elastodynamic solution to obtain the stress intensity applied at the running crack tip cannot be used, and the values calculated with equation (H-4) are gross overestimates because they do not account for plasticity. This discrepancy is further demonstrated in Figure H-12 where the K_I^{dyn} values calculated from the strain gage measurements are greater than the K_I^{stat} values. It is physically impossible for K_I^{dyn}

Table H-3
COMPARISON OF THERMISTOR (TH) AND THERMCOPPLE (TC) DATA

<u>Test</u>	<u>Transducer #</u>	<u>Distance from Crack Plane y (mm)</u>	<u>Distance Along Crack from Original Notch Δa (mm)</u>	<u>ΔT_{max} (°C)</u>	<u>Propagation Toughness Difference K_ITH - K_I^{TC} = ΔK_{ID} (MPa m^{1/2})</u>
CT3	TH2B	2.6	48.6	3.40	13
	TC1	2.6	49.5	2.82	
CT4	TH2A	6.8	50.0	1.09	8
	TC2	7.1	49.1	0.93	
CT5	TH1A	5.0	46.6	2.42	18
	TC1	5.0	44.4	2.05	
CT6	TH1B	7.7	55.0	1.25	12
	TC2	7.5	54.8	1.15	
CT5	TH1B	4.5	55.8	1.28	4
	TC2	4.6	54.3	1.19	
CT6	TH1A	7.7	46.6	1.25	0
	TC1	8.0	45.6	1.25	

to be greater than K_I^{stat} because, during the early part of crack extension, part of the energy released must be used to overcome the inertia of the specimen and hence cannot be delivered to the crack tip.

Although the strain gage measurements failed to provide K_I^{dyn} values because of plasticity, they are still usable to determine the crack velocity. The main limitation on the crack velocity measurements during the CT experiments is that they are performed at a limited number of locations and give average crack velocity values. This limitation is more important when using small specimens because in these specimens the velocity gradients are larger. Further, the strain gages cannot detect rapid transients in the crack velocity caused by stress waves reflected from the boundaries and impinging on the crack tip. Again we expect that these transients would be more pronounced in small specimens than in larger specimens. However, because the average crack velocities measured during the experiments never exceeded 600 m s^{-1} , we think that the stress wave-crack tip interactions may have been small in the CT experiments.

Thus we conclude that the strain gage method gives reliable first-order estimates of the crack velocity, but is not suited for studying details of the crack tip dynamic unless an impractical high number of gages are used. With respect to the CT crack extension experiments, tests CT3 and CT6 yielded consistent crack velocity data in the range where most of the temperature measurements were performed, although insufficient data were available to characterize precisely the deceleration phase (Figure H-7).

In contrast to the strain gage technique, the heat of fracture approach to measuring propagation toughness is independent of constitutive assumptions for the material and can be used even in the presence of plasticity. In the case of significant plastic deformation at the crack tip, however, the finite width of the heat source must be taken into account when reducing the temperature data. We did this in the present study, but for the sake of simplicity, we assumed a uniform intensity of the heat source over the plastic zone width. This uniformity is not true in reality because plastic strains decay rapidly

with the distance from the crack tip; hence plastic dissipation is most intense at the crack tip and decreases as the boundary of the plastic zone is approached. The assumption of uniform heat source intensity will cause an underestimate of the propagation toughness.

The heat of fracture approach is based on a one-dimensional heat flow interpretation of the experimental data. This interpretation implies that energy dissipation at the crack tip is the same over large distances of crack extension. Assuming that the propagation toughness is a function of the crack velocity, the crack velocity must be constant through the region where the temperature measurements are performed. This requirement was met for most of the data points, except those taken near the arrested crack tip.

The heat of fracture approach is a surface measurement and it measures the dissipation in the plane stress plastic zone. As a consequence, it may overestimate the plane-strain propagation toughness, particularly when significant shear lips are formed. This point can be assessed by comparing the K_{ID} values obtained from transducers placed at various distances from the crack plane. If the heat dissipation at the surface, is significantly different from that in the interior, there will be a three-dimensional heat flow field after crack extension. Temperature transducers placed farther from the crack plane will be affected differently than transducers placed closer to the crack tip. In our experiments, the transducers that were placed 3 mm and 7 mm from the crack plane gave results that are within 10% suggesting that there are no strong three dimensional effects. In addition the potential overestimate caused by the surface measurements is at least partially offset by the underestimate introduced by the finite width heat source correction and by the definition of the maximum temperature elevation caused by crack extension.

A final comment about the heat of fracture approach concerns the type of transducers most appropriate for this type of experiments. Thermistors have a better resolution than thermocouples, but they are more difficult to use because they have a nonlinear response for large

temperature fluctuations and because they are more difficult to bond to the specimen. This interfacing difficulty appears to affect their time response. Comparison of the performance of the thermistors and the thermocouples in our experiments indicates a systematic difference (20% or less in the temperature measurements) between the results of the two transducer types that could not be explained. Beside the difference in the absolute amplitudes, the temperature histories agreed very well, with the thermocouple displaying a faster time response. For this reason and because of their ease of application, thermocouples should be used in future heat of fracture experiments.

In summary, the CT crack extension experiments failed to provide K_I^{dyn} measurements because a large plastic zone at the crack tip invalidated the assumption underlying the strain gage approach. However, reliable estimates of the propagation toughness K_{ID} were obtained with the heat of fracture approach. First-order estimates of the crack velocity during the steady-state crack extension phase were obtained from the strain gage measurements with an error bound of $\pm 50 \text{ m s}^{-1}$.

The propagation toughness measured in the 12.7-mm-thick CT specimens varied between $172 \text{ MPa m}^{1/2}$ at a crack speed of 575 m s^{-1} and $110 \text{ MPa m}^{1/2}$ at a crack speed of 330 m s^{-1} with an estimated scatter of $\pm 30 \text{ MPa m}^{1/2}$. These values are more than twice the value of the dynamic initiation toughness K_{Id} and they are also significantly higher than the values reported by Kobayashi and Dally¹⁶ and Rosakis et al.¹⁷ However, other investigations of 4340 steel, in a comparable hardness condition and for comparable crack velocities, have also yielded high propagation toughness values.^{18,19} Furthermore, the propagation toughness values obtained with the heat of fracture measurements are consistent with the values reported in Appendix G. As discussed in Appendix G, and following the work of Hahn et al.,¹⁸ we think that the large increase in toughness above the initiation toughness is caused by the formation of shear lips and by the associated curvature of the extending crack front. Apparently, the resistance to crack extension is much more sensitive to the degree of constraint than the resistance to crack initiation. Also,

the toughness-crack velocity relationship may depend on the initiation conditions (such as the initial notch root radius) because the size of the plastic zone will affect the size of the shear lips along the extending crack path, over distances that are significant compared with the initial plastic zone size.

REFERENCES FOR APPENDIX H

1. K. B. Broberg, "The Propagation of a Brittle Crack," *Arkiv Fyhsik*, Vol. 18, p. 159 (1960).
2. W. Klemm, "Uer das Spannungsfeld eines schnellaufenden Risses," Ph.D. Dissertation, Universität Karlsruhe (1977).
3. A. J. Rosakis, and Zehnder, "On the Dynamic Fracture of Structural Metals," *Int. J. Fracture*, Vol. 27, pp. 169-186 (1985).
4. W. L. Fourney, R. Chona, and R. J. Sanford, "Dynamic Crack Growth in Polymers," in Workshop on Dynamic Fracture, W. G. Knauss, K. Ravichandar, and A. J. Rosakis, Eds. (California Institute of Technology, 1983), pp. 75-99.
5. G. I. Taylor and H. Quinney, H., "The Latent Energy Remaining in a Metal After Cold Working," *Proc. Roy. Soc. Vol. A143*, p. 307 (1934). See also, "The Scientific Papers of Sir Geoffrey Ingram Taylor," in Mechanics of Solids, Vol. 1, G. Batchelor, Ed. (Cambridge University Press, 1958) p. 310.
6. A. A. Wells, "The Mechanics of Notch Brittle Fracture," *Welding Res.* Vol. 7, pp. 34v-56v (1953).
7. W. Döll, "Thermische Wirkung der Bruchvorgänge in Polymethylmethacrylat," *Wiss. Bericht 3/67 des Ernst-Mach-Instituts, Freiburg i. Br.* and "Untersuchungen zum Bruchvorgang von verschiedenen molaren Polymethylmethacrylat," Dissertation at the University of Karlsruhe (1974).
8. R. Weichert, and K. Schönert, "Die Wärmetonung des Bruches in Eisen und ihre Abhängigkeit von der Ausbreitungsgeschwindigkeit," *Chem. Ing. Technik*, Vol. 11, pp. 295-300 (1969). See also "Heat Generation at the Tip of a Moving Crack," *J. Mech. Phys.*, Vol. 26 pp. 151-161 (1978).
9. W. Klemm and J. F. Kalthoff, "Simultane Messung des dynamischen Spannungsintensitätsfaktors und der dynamischen Bruchzähigkeit für schnellaufende Risse in Stahl," Deutscher Verband für Materialprüfung (DVM), Sitzung AK, Bruchvorgänge, Stuttgart (October 1979).

10. C. Zimmerman, W. Klemm, and K. Schönert, "Dynamic Energy Release Rate and Fracture Heat in Polymethylmethacrylate (PMMA) and High-Strength Steel" Eng. Fracture Mechanics, Vol. 20, pp. 777-782 (1984).
11. R. Weichert, "Untersuchungen zur Temperatur an der Bruchspitze," Ph.D. Dissertation, Universitat Karlsruhe (1976).
12. D. Rosenthal, "The Theory of Moving Sources of Heat and Its Application of Metal Treatments," Trans. ASME, Vol. 68, pp. 849-866 (1946).
13. H. S. Carslaw and J. C. Jaeger, Conduction of Heat in Solids (Oxford, 1959).
14. R. G. Hoagland, P. C. Gehlen, A. R. Rosenfield, M. E. Kanninen, and G. T. Hahn, "Proposed Tentative Method of Test for Fast Fracture Toughness and Crack Arrest," Appendix B of Prospects for a Cooperative Test Program on Crack Arrest Toughness Measurement, ASTM E 24.03.04 (Crack Arrest Task Group, American Society for Testing and Materials, Philadelphia, 1977).
15. J. F. Kalthoff, J. Beinert, S. Winkler, and W. Klemm, "Experimental Analysis of Dynamic Effects in Different Crack Arrest Test Specimens," Crack Arrest Methodology and Applications, ASTM STP 711, G. T. Hahn and M. F. Kanninen, Eds. (American Society for Testing and Materials, 1980), pp. 109-127.
16. T. Kobayashi, and J. W. Dally, "Dynamic Photoelastic Determination of the Δ -K Relation for 4340 Alloy Steel," Crack Arrest Methodology and Applications, ASTM STP 711, G. T. Hahn and M. F. Kanninen, Eds. (American Society for Testing and Materials, 1980), pp. 189-210.
17. A. J. Rosakis, J. Duffy, and L. B. Freund, "The Determination of Dynamic Fracture Toughness of AISI 4340 Steel by the Shadow Spot Method," J. Mech. Phys. Solids, Vol. 32, pp. 443-460 (1984).
18. G. T. Hahn, R. G. Hoagland, A. R. Rosenfield, and R. Sejnoha, "Rapid Crack Propagation in a High Strength Steel," Met. Trans. Vol. 5, pp. 475-482 (1974).
19. S. J. Hudak, R. J. Dexter, J. H. Fitzgerald, and M. F. Kanninen, "The Influence of Specimen Boundary Conditions on the Fracture Toughness of Running Cracks," Eng. Fract. Mech., Vol. 23, pp. 201-213 (1986).